UNIVERSIDAD POLITÉCNICA DE MADRID
Escuela Técnica Superior de Ingeniería Aeronáutica y del Espacio

Generation of Spectral Representations of Urban Wind Fields From LES and Experimental Databases for Aeroelastic Simulations of Wind Turbines

DOCTORAL THESIS

Submitted for the degree of Doctor by:

Mohanad Elagamy
Master of Science in Computational Mechanics, Swansea University

Madrid, 2023

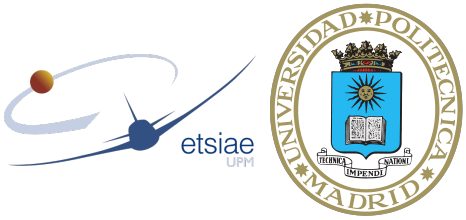

UNIVERSIDAD POLITÉCNICA DE MADRID
Escuela Técnica Superior de Ingeniería Aeronáutica y del Espacio

Doctoral Degree in Aerospace Engineering

Generation of Spectral Representations of Urban Wind Fields From LES and Experimental Databases for Aeroelastic Simulations of Wind Turbines

DOCTORAL THESIS

Submitted for the degree of Doctor by:

Mohanad Elagamy
Master of Science in Computational Mechanics, Swansea University

Under the supervision of:
Dr. Cristóbal José Gallego Castillo
Dr. Alvaro Cuerva Tejero

Madrid, 2023

Title: Generation of Spectral Representations of Urban Wind Fields From LES and Experimental Databases for Aeroelastic Simulations of Wind Turbines

Author: Mohanad Elagamy

Doctoral Programme: Aerospace Engineering

Thesis Supervision:

Dr. Cristóbal José Gallego Castillo, Associate professor (Profesor Contratado Doctor), UPM (co-supervisor)

Dr. Alvaro Cuerva Tejero, Professor (Profesor Titular de Universidad), UPM (co-supervisor)

External Reviewers:

Thesis Defense Committee:

Thesis Defense Date:

This research has received funding from the European Union's Horizon 2020 research and innovation programme under the Marie Skłodowska-Curie project zEPHYR: Towards a more efficient exploitation of on-shore and urban wind energy resources, with grant agreement No 860101.

To my wife and my family

Acknowledgement

I would like to express my gratitude to Dr. Cristóbal José Gallego Castillo and Dr. Alvaro Cuerva Tejero, my thesis supervisors and mentors, for their continuous support, guidance, and insight. The completion of this thesis would not have been possible without their moral and educational support. I appreciate their availability when needed and complete guidance to overcome many obstacles faced during this thesis. I really admire the way they initiated and mapped the workflow; it saved a lot of time and, in my opinion, was the key to producing prestigious work.

I would also like to show my gratitude to all my peers and colleagues at UPM and in the zEPHYR project. They were all supportive when needed and willing to sincerely help when asked for. Their advice and suggestions created an enjoyable working environment. I would like to show my appreciation for the continuous support from my research team at UPM, including Dr. Sergio Avila-Sanchez, Dr. Oscar Lopez-Garcia, and Mr. Ricardo Fernández. I am privileged to have worked with them. Nevertheless, I never would have been able to realize my goal without the kind and sincere help of numerous individuals and organizations.

I would like to sincerely thank CESVIMA and the Department of Aircraft and Aerospace Vehicles of UPM for their support in providing computer resources and space for this research.

Lastly, I would not forget to thank my beloved family, especially my wife and my parents, for their unconditional love and support during this whole journey. Although this work took place abroad from home, their warm wishes and encouraging words empowered me the most. I would like to dedicate my thesis to my family and my close friends.

Abstract

The increase in demand for renewable energy has led to a need to assess various types of sites, particularly urban areas, for wind turbine installation. Small wind turbines in urban environments require minimal space, and they can be installed in proximity to high electricity demand regions. However, existing aeroelastic design standards (IEC 61400-2) developed for open terrains may lead to inaccurate results due to the distinct wind field characteristics of urban environments. The present thesis proposes the use of large eddy simulation to characterize the urban wind field statistics to be used in the generation of synthetic wind velocity fields to be used in the aeroelastic simulation of wind turbines operating in urban environments, to contribute, in the future, to the updating of the design standards of urban wind turbines. Spectral representation methods and sequential methods were employed for the synthesis of urban wind fields, with a particular focus on the autoregressive and vector autoregressive models. As a novelty, these models were developed to include second-order statistical information described in the frequency domain as they typically utilize inputs described in the time domain. This is done through the use of the relation of poles and the autoregressive spectrum, as well as the exploitation of the connection between eigenvalues of the companion matrix of the vector autoregressive of order one representation and the vector autoregressive spectra. Von Karman and Mann turbulence models were employed as target spectra to assess the proposed approaches.

A large eddy simulation analysis was conducted to replicate an experimental study of a particular urban area flow case, a single high-rise building exposed to a turbulent inflow representative of Eurocode terrain category II. The conducted large eddy simulation study was used to provide second-order statistics of the wind field at three locations: the rooftop of the high-rise building along a vertical line at its center, a plane parallel to the wind direction in the middle of the rooftop, and a plane perpendicular to the wind direction also situated in the middle of the rooftop. The provided statistical information at the three locations were used to synthesize urban wind fields using the spectra-based vector autoregressive approach, the covariance-based vector autoregressive approach, and the spectral representation method, respectively. The results demonstrate that both the spectral representation methods and the sequential methods are capable of reproducing the statistical targets of highly non-homogeneous and anisotropic wind fields, and the non-Gaussianity nature of the urban wind field which has been accounted for by applying the quantile-to-quantile transformations of the histograms of the velocity components. However, each approach possesses distinct advantages. The covariance-based methods present a good capability in reproducing target covariances and variances of random processes that represent the wind velocity field, while the spectra-based approaches reproduce well target spectra. The choice of method should be based on the specific requirements of the synthetic wind field's intended application.

Resumen

El aumento en la demanda de energía renovable ha llevado a la necesidad de evaluar varios considerar diferentes tipos de emplazamientos, especialmente en áreas urbanas, para la instalación de aerogeneradores. Los Pequeños Aerogeneradores en entornos urbanos requieren un espacio mínimo y pueden ser instalados cerca de regiones con alta demanda de energía. Sin embargo, las normas de diseño existentes (IEC 61400-2) desarrolladas para terrenos abiertos pueden llevar a resultados inexactos debido a las características particulares del campo de viento en entornos urbanos. La presente tesis propone utilizar la simulación de grandes escalas para caracterizar las estadísticas del campo de viento urbano que son necesarias para general campos de viento sintético que puedan ser utilizados en la simulación aeroelástica de aerogeneradores operando en estos entornos con objecto de contribuir, en un futuro, a la actualización de las normas de diseño de aerogeneradores para ser utilizados en emplazemintos urbanos. Se han empleado Métodos de Representación Espectral y métodos secuenciales para la síntesis de campos de viento urbanos, con un enfoque particular en los modelos autorregresivo y autorregresivo vectorial. Estos modelos se han desarrollado para incluir información estadística de segundo orden descrita en el dominio de frecuencia, ya que normalmente utilizan entradas descritas en el dominio del tiempo. Esto se ha logrado mediante el uso de la relación de polos y el espectro autorregresivo, así como la explotación de la conexión entre los autovalores de la matriz compañera de la representación autorregresivo vectorial de orden uno y los espectros autorregresivo vectorial. Se han empleado los modelos de turbulencia de Von Karman y Mann para obtener un espectro objetivo y evaluar los enfoques propuestos.

Se ha llevado a cabo un análsis simulación de grandes escalas para replicar un estudio experimental de un caso particular en una zona urbana, un solo edificio de gran altura expuesto a un campo de velocidad turbulenta representativa de la categoría de terreno II del Eurocódigo. El estudio simulación de grandes escalas realizado se ha utilizado para determinar estadísticas de segundo orden del campo de viento en tres ubicaciones: en la azotea del edificio de gran altura a o largo de una línea vertical localizada en su centro, en un plano paralelo a la dirección del viento en el centro de la azotea y en un plano perpendicular a la dirección del viento, también ubicado en el centro de la azotea. La información estadística obtenida en las tres ubicaciones se ha utilizado para sintetizar el campo de viento urbano utilizando el enfoque autorregresivo vectorial basado en espectros, el enfoque autorregresivo vectorial basado en covarianzas y el enfoque métodos de representación espectral, respectivamente. Los resultados demuestran que tanto los enfoques métodos de representación espectral como los métodos secuenciales son capaces de reproducir las características estadísticas de segundo orden, en dos puntos y dos instantes, de campos de viento altamente no homogéneos y anisotrópos, así como la naturaleza no gaussiana del campo de viento urbano, que puede tenerse en cuenta aplicando técnicas de transformación de cuantil-a-cuantil de las correspondientes histogramas. Las metodologías de síntesis analizadas presentan ventajas características. De este modo, los métodos basados en covarianzas tienen una buena capacidad para reproducir las covarianzas y las varianzas de los procesos aleatorios que representan los campos de velocidad de viento urbano, mientras que los enfoques basados en espectros reproducen bien los espectros objetivos.

La elección del método debe basarse en los requisitos específicos de la aplicación prevista del campo de viento sintético.

Contents

List of Figures

List of Tables

Abbreviations

ABL Atmospheric Boundary Layer

AIJ Architectural Institute of Japan

AR AutoRegressive

ARMA AutoRegressive Moving Average

BC Boundary Condition

BR Blockage Ratio

CCF Cross-Covariance Function

CDF Cumulative Distribution Function

CEDVAL Compilation of Experimental Data for VALidation of microscale dispersion model

CFD Computational Fluid Dynamics

CG Cristobal Gallego et al.

CMF Covariance Matrix Function

CPSDM Cross Power Spectral Density Matrix

DNS Direct Numerical Simulation

DTFT Discrete-Time Fourier Transform

EGBO Enhanced Gradient Based Optimization method

FT Fourier Transform

FFT Fast Fourier Transform

HAWTs Horizontal Axis Wind Turbines

HRB High-Rise Building

HWA Hot-Wire Anemometer

IC Initial Condition

IEC International Electrotechnical Commission

JCR Journal Citation Reports

K-M Krenk-Møller

LES Large Eddy Simulations

MA Moving Average

MSE Mean Square Error

NG Numerical Generation

NS Navier-Stokes equations

NTM Normal Turbulence Model

OCEAN Optimal CPSDM fitting through Eigen Analysis

PISO Pressure Implicit with Splitting of Operators

PPA Pole-Placement Approach

PSD Power Spectral Density

RANS Reynolds-averaged Navier-Stokes

RP Random Process

RUB Ruhr-Universität Bochum

RV Random Variable

SGS Subgrid-Scale

SIMPLE Semi-Implicit Method for Pressure-Linked Equations

SRM Spectral Representation Method

SM Sequential Method

SVT Spectral Velocity Tensor

SWT Small Wind Turbine

TKE Turbulence Kinetic Energy

TFTH Taylor's Frozen Turbulence Hypothesis

UBL Urban Boundary Layer

UCL Urban Canopy Layer

UPM Universidad Politécnica de Madrid

URANS Unsteady Reynolds Averaged Navier Stokes

VAR Vector Autoregressive

vK von Karman

VKI von Karman Institute

VMA Vector Moving Average

WALE Wall-Adapting Local Eddy-viscosity

WRF Weather Research and Forecasting

WSS Wide Sense Stationary

WSS-RP Wide Sense Stationary Random Process

WT Wind Turbine

Y-W Yule-Walker

List of Symbols

Greek Symbols

α	realization number index	$[-]$
α_w	wind direction	$[^\circ]$
α_e	power law profile exponent	$[-]$
Δ_0	thickness of the first mesh layer	[m]
$\Delta\omega$	angular frequency step	[rad s^{-1}]
Δt	time step	[s]
Δx	spatial step in $x-$direction	[m]
Δz	spatial step in $z-$direction	[m]
ε_t	random variable (white noise)	[m s^{-1}]
$\boldsymbol{\varepsilon}_t$	random variable vector	[m s^{-1}]
η	kolmogorov length scale	[m]
γ	a constant of value 5/6	$[-]$
γ_s	the mean inclination angle during the analyzed period	$[^\circ]$
γ_l	autocovariance function in terms of lag index l	[m^2 s^{-2}]
$\gamma_{ii}(\tau)$	autocovariance function in terms of time lag τ for $i-$velocity component	[m^2 s^{-2}]
$\mathring{\gamma}_l$	non-dimensional autocovariance function	$[-]$
Γ	anisotropy parameter in Mann's turbulence model	$[-]$
$\boldsymbol{\Gamma}_l$	covariance matrix function at time lag index l	[m^2 s^{-2}]
λ^r	real eigenvalue	$[-]$
λ^c	complex eigenvalue	$[-]$
ν	kinematic viscosity	[m^2 s^{-1}]
ν_{air}	kinematic viscosity of air	[m^2 s^{-1}]
ν_i	random variable at time t_i	$[-]$
ω	angular frequency	[rad s^{-1}]

φ_s	mean wind direction during the evaluated period	[°]
φ_i	unrestricted AR regression coefficient	[−]
$\mathbf{\Phi}(k)$	spectral velocity tensor	[$m^3\ s^{-2}$]
$\mathbf{\Phi}_*$	companion matrix of AR/VAR model	[−]
$\mathbf{\Phi}_m$	unrestricted VAR regression matrix coefficient	[−]
$\mathbf{\Psi}_i$	regression coefficient matrix of VMA	[−]
ρ	density	[kg m^{-3}]
σ	unrestricted AR noise coefficient	[−]
σ_i	standard deviation for $i-$velocity component	[$m\ s^{-1}$]
σ_{ij}	ij component in the noise coefficient matrix $\mathbf{\Sigma}$	[−]
σ_c^2	characteristics variance	[$m^2\ s^{-2}$]
$\mathbf{\Sigma}$	unrestricted VAR noise coefficient matrix	[−]
τ	time lag	[s]
τ_e	eddy lifetime	[s]
τ_{ij}	subgrid-scale stress tensor	[Pa]
θ_λ	phase angle of eigenvalues	[°]
θ_P	phase angle of poles	[°]

Roman Symbols

a_{j_i}	restricted AR regression coefficient	[−]
$\boldsymbol{A}_{j_i}$	restricted VAR regression matrix coefficient	[−]
b	restricted AR noise coefficient	[−]
$\boldsymbol{B}$	restricted VAR noise coefficient matrix	[−]
D	building width	[m]
$\boldsymbol{D}$	diagonal eigenvalues matrix	[−]
$E(k)$	three dimensional energy spectrum	[$m\ s^{-2}$]
f	frequency	[Hz]
$F(k)$	one-dimensional spectrum	[$m\ s^{-2}$]
$f(r)$	non-dimensional longitudinal correlation function	[−]
h	number of variates in a VAR model	[−]
H	building height	[m]
$H(\mathrm{z})$	transfer function in terms of the z−domain	[−]

i	imaginary unit	$[-]$
$\mathbf{i}$	a unit vector in the $x-$direction	$[-]$
I_i	turbulence intensity for $i-$velocity component	$[-]$
$\boldsymbol{I}$	identity matrix	$[-]$
$\mathbf{j}$	$\mathbf{j}$ vector containing selected regression terms in AR/VAR model	$[-]$
$\boldsymbol{J}$	backward identity matrix	$[-]$
k	magnitude of the wavenumber vector	$[\mathrm{rad\ m^{-1}}]$
$\mathring{k}$	non-dimensional wavenumber	$[-]$
k_1	longitudinal component of wavenumber vector	$[\mathrm{rad\ m^{-1}}]$
$\boldsymbol{k}$	wavenumber vector $[k_1, k_2, k_3]$	$[\mathrm{rad\ m^{-1}}]$
l	lag index	$[-]$
$\mathbf{l}$	$\mathbf{l}$ vector containing selected lags for ACF/CMF	$[-]$
L	length scale	$[\mathrm{m}]$
L_i	length of computational domain in $i-$direction	$[\mathrm{m}]$
L^i_j	integral length scale for $i-$direction and $j-$velocity component	$[\mathrm{m}]$
N_i	number of grid points in $i-$direction	$[-]$
N_m	number of modes considered in VSED	$[-]$
N_{P^r}	number of real poles	$[-]$
N_{P^c}	number of complex conjugated poles	$[-]$
N_{λ^r}	number of real eigenvalues	$[-]$
N_{λ^c}	number of complex eigenvalues	$[-]$
$\tilde{p}^r$	filtered pressure	$[\mathrm{Pa}]$
P^r	real poles	$[-]$
P^c	complex conjugate poles	$[-]$
p	AR/VAR model order	$[-]$
q	MA/VMA model order	$[-]$
r	separation distance between two points	$[\mathrm{m}]$
$\mathring{r}$	non-dimensional separation distance between two points	$[-]$
$r_{_P}$	radial location of poles	$[-]$
r_λ	radial location of eigenvalues	$[-]$
$\boldsymbol{r}$	spatial separation vector	$[\mathrm{m}]$
Re	Reynolds number	$[-]$
S	mean wind speed	$[\mathrm{m\ s^{-1}}]$
S_{ii}	auto-power spectral density for $i-$velocity component	$[\mathrm{m^2\ s^{-2}\ Hz^{-1}}]$
$\mathring{S}_{ii}$	non-dimensional auto-power spectral density	$[-]$
$\boldsymbol{S}$	cross-power spectral density matrix	$[\mathrm{m^2\ s^{-2}\ Hz^{-1}}]$

Sk_i	skewness of the $i-$velocity component	$[\mathrm{m}^3\ \mathrm{s}^{-3}]$
T	simulation time stamp	[s]
T_i	integral time scale for $i-$velocity component	[s]
$\overline{u_{iso}^2}$	isotropic variance	$[\mathrm{m}^2\ \mathrm{s}^{-2}]$
$\tilde{u}$	longitudinal velocity component	$[\mathrm{m\ s}^{-1}]$
u	fluctuation of longitudinal velocity component	$[\mathrm{m\ s}^{-1}]$
$\tilde{u}_i^r$	filtered velocity component in the direction x_i	$[\mathrm{m\ s}^{-1}]$
$\boldsymbol{u}(\mathbf{x}, t; \alpha)$	3V-4D random process vector	$[\mathrm{m\ s}^{-1}]$
$\boldsymbol{u}(t; \alpha)$ or $\boldsymbol{u}_t$	MV-1D random process vector	$[\mathrm{m\ s}^{-1}]$
U	mean value of the longitudinal velocity component $\tilde{u}$	$[\mathrm{m\ s}^{-1}]$
U^{T}	time average of the longitudinal velocity component $\tilde{u}$	$[\mathrm{m\ s}^{-1}]$
U_∞	free wind speed	$[\mathrm{m\ s}^{-1}]$
$\tilde{v}$	lateral velocity component	$[\mathrm{m\ s}^{-1}]$
v	fluctuation of lateral velocity component	$[\mathrm{m\ s}^{-1}]$
V	mean value of the lateral velocity component $\tilde{v}$	$[\mathrm{m\ s}^{-1}]$
$\boldsymbol{v}$	eigenvector	$[-]$
$\boldsymbol{v}^r$	real eigenvector	$[-]$
$\boldsymbol{v}^c$	complex eigenvector	$[-]$
λ	eigenvalue	$[-]$
$\boldsymbol{V}$	right eigenvectors matrix	$[-]$
$\tilde{w}$	vertical velocity component	$[\mathrm{m\ s}^{-1}]$
w	fluctuation of vertical velocity component	$[\mathrm{m\ s}^{-1}]$
W	mean value of the vertical velocity component $\tilde{w}$	$[\mathrm{m\ s}^{-1}]$
$\mathbf{x}$	spatial coordinates vector (x, y, z)	[m]
$\mathbf{x}_\perp$	spatial coordinates vector on a plane perpendicular to the wind flow	[m]
coh_i	spatial coherence function for $i-$ velocity component	$[-]$
y^+	y-plus value	$[-]$
z^*	vertical distance from the building rooftop	[m]

Superscript

AR	autoregressive
Img	imaginary
Mann	Mann model
Re	real
t	target
VAR	vector autoregressive
vK	von Karman model
VMA	vector moving average

Subscript

iso	isotropic
max	maximum value
min	minimum value
ref	reference

Operators

$K_n(\cdot)$	modified Bessel function of the second kind of order n
$\det(\cdot)$	determinant
$\mathrm{E}[\cdot]$ or $\overline{(\cdot)}$	ensemble mean
$\mathcal{F}[\cdot]$	Fourier transform
$\mathcal{F}^{-1}[\cdot]$	inverse Fourier transform
$\Gamma(\cdot)$	gamma function
$(\cdot)^H$	Hermitian transpose
$(\cdot)^{-1}$	inverse
$\mathrm{Img}\{\cdot\}$	imaginary part
$\mathrm{P}_{i,n}(\cdot)$	n^{th}-order PDF of the RP i
$\mathrm{Re}\{\cdot\}$	real part
$(\cdot)^T$	transpose
$\mathrm{vec}(\cdot)$	vectorization

Chapter 1

Introduction

1.1 Motivation for research

This Doctoral Thesis has been carried out within the framework of a European research project called zEPHYR. This project has received funding from the European Union Horizon 2020 research and innovation programme under the Marie Skłodowska-Curie grant agreement number 860101. The zEPHYR project is aimed at improving the assessment of wind turbine performance operating in complex terrain and urban environments. With this regard, one of the objectives of the zEPHYR project is to provide three benchmarks: large wind turbine, complex terrain, and urban canopy benchmarks.

Within the zEPHYR framework, the UPM group has been responsible for the part that deals with the synthetic generation of atmospheric wind fields in urban environments. The inputs for this research project are numerical simulations and field measurements obtained by researchers and partners within the zEPHYR project. The synthetic turbulent wind field generated is provided to other researchers in the zEPHYR project to perform aeroelastic simulations of wind turbines.

Wind Turbines (WTs) are designed for safety, durability, and performance according to the International Electrotechnical Commission (IEC) standard 61400 series (IEC 61400-1, 2019; IEC 61400-2, 2019). The system is required to be simulated during a set of load cases determined by IEC standards. This is essential for studying the loads acting on the WTs and analyzing the performance of the WTs. Moreover, the study of the noise emitted by WTs to ensure that the noise level is within acceptable limits is necessary. To acquire the dynamic forces acting on WTs, numerical simulations of turbulent wind fields are required. Solving the Navier-Stokes (NS) equations describing the Atmospheric Boundary Layer (ABL) (Pope, 2000) using high-fidelity numerical approaches such as Direct Numerical Simulation (DNS) and Large Eddy Simulation (LES) is currently infeasible due to their high computational cost requirements for a complete aeroelastic designing process of WTs. Additionally, these simulations are highly sensitive to the Initial Conditions (ICs) and Boundary Conditions (BCs). An alternative approach is utilizing Numeric Generation (NG) (Kleinhans et al., 2009) to generate synthetic turbulent wind fields. NG uses predefined statistical features of actual

wind fields to generate the synthetic turbulent wind field. One of the main advantages of NG is the low computational cost required, compared to DNS and LES, for generating numerous synthetic samples (realizations) of wind fields with prescribed statistical features. With this proposed, synthetic wind fields are naturally modeled as multi dimensional- multi variate random processes .

Currently, the range of installation sites of onshore wind turbines is expanding from conventional open terrains to include the built environments (KC et al., 2019). The wind flow characteristics in built environments are rather different from those corresponding to the flow field, which is naturally developed over flat and open terrains. Small Wind Turbines (SWTs) are expanding to be installed in urban areas; thus, understanding the flow characteristics in urban areas is crucial as simulations of turbulent wind velocity fields are required to evaluate dynamic loads on wind turbines during different wind events (Stathopoulos et al., 2018). SWT must be tested under the wind conditions defined by IEC standards (IEC 61400-2, 2019). The IEC 61400-2 provides a description of the mean velocity and the turbulence intensity using the Normal Turbulence Model (NTM), which is used for the aeroelastic design of SWT mounted over building roofs in built environments. However, this description is based on data obtained for open and flat terrains (Forsyth et al., 2018; KC et al., 2019). The NTM does not incorporate the influence of the shape or the arrangement of structures in urban areas on the wind flow. Additionally, it excludes the effect of the wind direction on the wind field characteristics. These parameters have a significant impact on both the mean velocity and the turbulence intensity of the wind field. Therefore, the NTM of the IEC 61400-2 might lead to inaccurate prediction of the dynamic loads acting on the SWT (Evans et al., 2017; Forsyth et al., 2018). The IEC 61400-2 standard uses von Karman (vK) (Von Karman, 1948) and Kaimal (J. Kaimal et al., 1972) models to characterize the spectrum of urban wind fields and provide it to the NG approach as inputs for synthesizing wind fields. The applicability of these model in the urban environment has been questioned. For instance, it was observed that both the vK and Kaimal models underestimate the 3-velocity spectra measured in a field measurement conducted by (Tabrizi et al., 2015). This could be due to the fact that the parameters used in these models are not suitable for built environments. Hence, the synthesized urban wind field inadequately captures the statistical information represented in actual urban wind fields, consequently, leading to an inaccurate representation of the loads experienced by the SWT in built areas. The statistical characteristics of wind fields in urban areas are influenced by various parameters such as the shape and the height of structures, the arrangement of set of buildings, wind direction (Feigenwinter et al., 1999; Abohela et al., 2013; Tabrizi et al., 2015; Peng et al., 2020; Vita et al., 2020). The integral length scales of velocity components are affected by buildings (Christen et al., 2007; Vita et al., 2020). The mean streamwise velocity is accelerated above the rooftop of buildings (Peng et al., 2020). Additionally, the highest turbulence intensity range is observed close to the roof surface (Peng et al., 2020), where it can reach values higher than 45% as it was observed in field measurements in various cities done by (Forsyth et al., 2018).

The current situation is that wind turbines are being designed according to the IEC 61400-2 standard (IEC 61400-2, 2019), which were developed from the experience achieved in open and flat terrains data but are then installed in built environments, resulting in issues related to performance and safety. The results are underestimated loads, performance degradation,

and low energy yield (Smith et al., 2012; KC et al., 2019). Moreover, in the worst-case scenario, it will lead to the destruction of the wind turbine due to excessive fatigue loads. Thus, the SWT design standard needs to be completed by including more realistic urban wind conditions as there are affecting factors that need to be considered, such as surrounding structures, terrain roughness, interacting airflows, or street canyon effects. All these factors lead to having highly non-stationary, non-homogeneous, non-Gaussian and anisotropic wind fields (Ricciardelli & Polimeno, 2006). Until now, the urban wind field has not been rigorously characterized, although this characterization is required for generating synthetic turbulent wind fields well fitted to the urban environment.

In this thesis, the main aim is to investigate approaches for characterizing urban wind fields and to implement algorithms capable of generating synthetic turbulent wind fields useful for aeroelatic simulations of SWT in the urban environment. To address the issue of using the IEC 61400-2 to obtain statistical information to characterize urban wind fields, this work proposes using LES simulations to provide the statistical information (second-order statistics) of wind fields in urban areas. Using a high-fidelity approach such as LES to generate the statistical features of urban wind fields will lead to a better characterization of urban wind fields. By providing these statistical information to the NG, the generated synthetic urban wind field will represent well actual urban wind fields. Consequently, the dynamic loads acting on SWTs in urban areas will be better represented, ensuring the structural safety and good performance of SWTs. In this thesis, a LES study was conducted to provide two times-two points second-order statistics of urban wind field required by the NG approaches, ensuring their capability of dealing with a complex flow such as urban wind flow, which is highly non-homogeneous, non-Gaussian and non-stationary. Additionally, the non-Gaussianity distribution of the wind field is reproduced by utilizing the quantile-to-quantile transformation of the corresponding probability distribution functions of the velocity components. Note that matching the non-Gaussian distributions of the random process entails the alignment of all the statistical "auto" moments, including third-order, fourth-order and beyond.

1.2 Aim of research and objectives

As stated, the main objective of the present research is to propose improved methodologies able to generate reliable synthetic wind fields in complex situations such as urban environments. This is done by using NG, which requires two times-two points second-order statistical information of the actual wind field to provide the wind velocity field in the rotor plane with proper spatial and time resolution. The statistical methods commonly used for synthetic wind field generation are the Spectral Representation Method (SRM) (Veers, 1988; Mann, 1998) and the Sequential Method (SM) (Krenk & Møller, 2019; Gallego-Castillo et al., 2022). The objective of this work is to improve and apply these statistical methods with second-order statistical information of actual urban wind fields acquired from LES simulation as inputs. To this end, the major accomplishments of this thesis are:

- Extending the SM, which is typically based on deterministic inputs defined in the time domain (Covariance Matrix Function (CMF)), to cope with frequency domain inputs

(Cross-Power Spectral Density Matrix (CPSDM)). This extended algorithm optimally calibrates the parameters of the SM through an optimization process.

- Designing efficient algorithms for NG of urban synthetic wind velocity fields. These algorithms take into account the non-homogeneous and non-Gaussian characteristics of the wind fields in urban environments.
- Providing appropriate LES of urban wind fields. These databases are employed to implement a random process analysis aimed at identifying representative mean wind velocity field patterns and representative CMF and CPSDM.
- Providing to other researchers within the zEPHYR project the obtained urban synthetic wind velocity fields as inputs for aeroelastic simulations of wind turbines in urban environments.

These accomplishments have been fulfilled within the framework of the zEPHYR project. Various collaborations with other researchers within the project were achieved. A 3-month secondment was done at the von Karman Institute (VKI) in Belgium with the objective of developing computational tools for estimating CPSDM and CMF from raw data. Additionally, the performance of the implemented in-house code of the Weather Research and Forecasting (WRF)-LES to reproduce the time-varying turbulence spatial structures was analyzed during the aforementioned secondment. The WRF-LES in-house code was used by the other researchers within the zEPHYR project to simulate WTs in flat and complex terrains. This secondment led to a better understanding of the computation of the statistical characteristics of wind fields, which was beneficial during analyzing the statistical features of urban wind fields obtained from the conducted LES simulation.

The methodologies introduced within this thesis have been implemented in MATLAB and are available as part of the "mVARbox" toolbox. Additionally, the findings of this research and the collaboration with the other researchers within the zEPHYR project have led to the following publications:

Journals

- Elagamy, M., Tiwari, N. Gallego-Castillo, C., Cuerva-Tejero, A., Lopez-Garcia, O., & Avila-Sanchez, S (2023). Large eddy simulation of the flow around a high-rise building with special focus on the two-points two-times second order statistics of the velocity field. (Elagamy et al., n.d.) (**under review**).
- Elagamy, M., Gallego-Castillo, C., Cuerva-Tejero, A., Lopez-Garcia, O., & Avila-Sanchez, S (2023). Eigenanalysis of vector autoregressive model for optimal fitting of a predefined cross power spectral density matrix: Application to numeric generation of stationary homogeneous isotropic/anisotropic turbulent wind fields. Journal of Wind Engineering and Industrial Aerodynamics, 238 , 105420 (Elagamy et al., 2023).
- Gallego-Castillo, C., Cuerva-Tejero, A., Elagamy, M., Lopez-Garcia, O., & Avila-Sanchez, S. (2021). A tutorial on reproducing a predefined autocovariance function through AR models: application to stationary homogeneous isotropic turbulence. Stochastic Environmental Research and Risk Assessment, 36,1–26. (Gallego-Castillo et al., 2022)

Conferences

- Gallego-Castillo, C., Elagamy, M., Cuerva-Tejero, A., Lopez-Garcia, O., & Avila-Sanchez, S. (2024, May). Synthesis of realistic non-homogeneous non-gaussian turbulent wind fields. In TORQUE conference. Florence, Italy. (Accepted-to be published) (Gallego-Castillo et al., 2024).
- Elagamy, M., Kale, B., Gallego-Castillo, C., Cuerva-Tejero, A., Buckingham, S., van Beeck, J., Lopez-Garcia, O., & Avila-Sanchez, S. (2022). Statistical characteristics of turbulent wind inflow obtained from WRF-LES simulations for the SWiFT test site. In 18th European academy of wind energy conference (PhD seminar). Bruges, Belgium: November (Elagamy et al., 2022).
- Elagamy, M., Gallego-Castillo, C., Cuerva-Tejero, A., Lopez-Garcia, O., & Avila-Sanchez, S. (2021). Optimal autoregressive models for synthetic generation of turbulence. Implications of reproducing the spectrum or the autocovariance function. In 17th European Academy of Wind Energy Conference (PhD seminar). Porto, Portugal: November (Elagamy et al., 2021a).
- Elagamy, M., Gallego-Castillo, C., Cuerva-Tejero, A., Lopez-Garcia, O., & Avila-Sanchez, S. (2021). Restricted Autoregressive Models For Synthetic Generation of Stationary Homogeneous Isotropic Turbulence. A Methodology Based on Multi-point Spectrum Fitting. 17th International Conference of Computational Methods in Sciences and Engineering (ICCMSE) (Elagamy et al., 2021b).

1.3 Thesis outline

This thesis is organized as a coherent and logically structured document, addressing the objectives presented in Section 1.2. Some sections are parts of original research papers, which were submitted to conferences and journals. At the beginning of each chapter, a disclosure is provided if part or the whole chapter has been published by the author in a conference or a journal.

As depicted in Figure 1.1, the chapters in this thesis are arranged as follows. In Chapter 2, preliminary definitions and basic concepts are introduced. The description of wind velocity fields from a probabilistic perspective and the relevant simplification assumptions are enumerated. The generation of synthetic wind fields using statistical methods from second-order statistics is briefly introduced. A literature review of the current available statistical information of urban wind field is provided. Additionally, a review of the current studies done by various researchers to analyze the urban wind field is presented.

In Chapter 3, an introduction to AutoRegressive (AR) model is presented. The definition of theoretical AutoCovariance Function (ACF) and auto-Power Spectral Density (PSD) of an AR model is defined. The state-of-the-art approaches for computing the AR model parameters from predefined ACF are elaborated. Additionally, their merits and demerits are analyzed. A proposed methodology is presented to compute AR model parameters from a predefined PSD.

A case study is presented, where the vK turbulence model is used to generate a target ACF and a target PSD to be utilized with both ACF and PSD-based approaches.

In Chapter 4, the generation of synthetic wind fields using the Vector AutoRegressive (VAR) model is presented. The theoretical CMF and CPSDM of a VAR model are defined. Additionally, the VAR(1) representation of a high-order VAR model is illustrated. The evaluation of the VAR model parameters from a predefined CMF is explained, with the challenges of calculating the VAR CMF being addressed. An extension of the proposed approach for computing the model parameters from predefined statistics in the frequency domain is presented. A test case analyzed with the proposed approach is treated.

In Chapter 5, the conducted LES study for a High-Rise Building (HRB) to analyze urban wind fields is described. Preliminary definitions of the statistical characteristics of turbulent wind velocity are introduced. The reference wind tunnel experiment and the reference LES simulation that were used in the presented work are presented. The SRM for synthetic generation of the turbulent wind inflow field at the domain inlet, based on the Mann's US-SVT Model, is illustrated. The LES setup is presented, including the process for selecting the Mann model parameters, which produces a synthetic turbulence field at the domain inlet, which gives rise to the best match of the undisturbed inflow characteristics at the HRB location. The assessment of the conducted LES simulation by comparing it to the reference experiment and LES simulations is shown. The results of the two-points two-times second-order statistics over the HRB rooftop are shown and analyzed.

In Chapter 6, statistical characteristics of the wind field over the HRB acquired from the conducted LES study are used as inputs for the SRM and SMs. The objective of this chapter is to apply various statistical methods for the synthesis of wind fields in the context of urban environments, which are characterized by high non-homogeneity, non-Gaussianity and anisotropy. An overview of the synthesis process using Veers-Shinzouka approach combined with the application of eigen-decomposition of CPSDM is presented. A computationally efficient SM, CMF-based approach is illustrated. The application of quantile-to-quantile transformation to generate non-Gaussian wind fields through SM is detailed. Three instances of the synthesis of urban wind fields are discussed. These case studies involve synthesis along a vertical line, a vertical plane perpendicular to the mean speed direction and another vertical plane parallel to the mean speed direction. The synthesis approaches employed in these cases are the SM CPSDM-based approach, SM CMF-based approach and Veers-Shinzouka for each case, respectively.

Finally, conclusions concerning the presented work are drawn in Chapter 7.

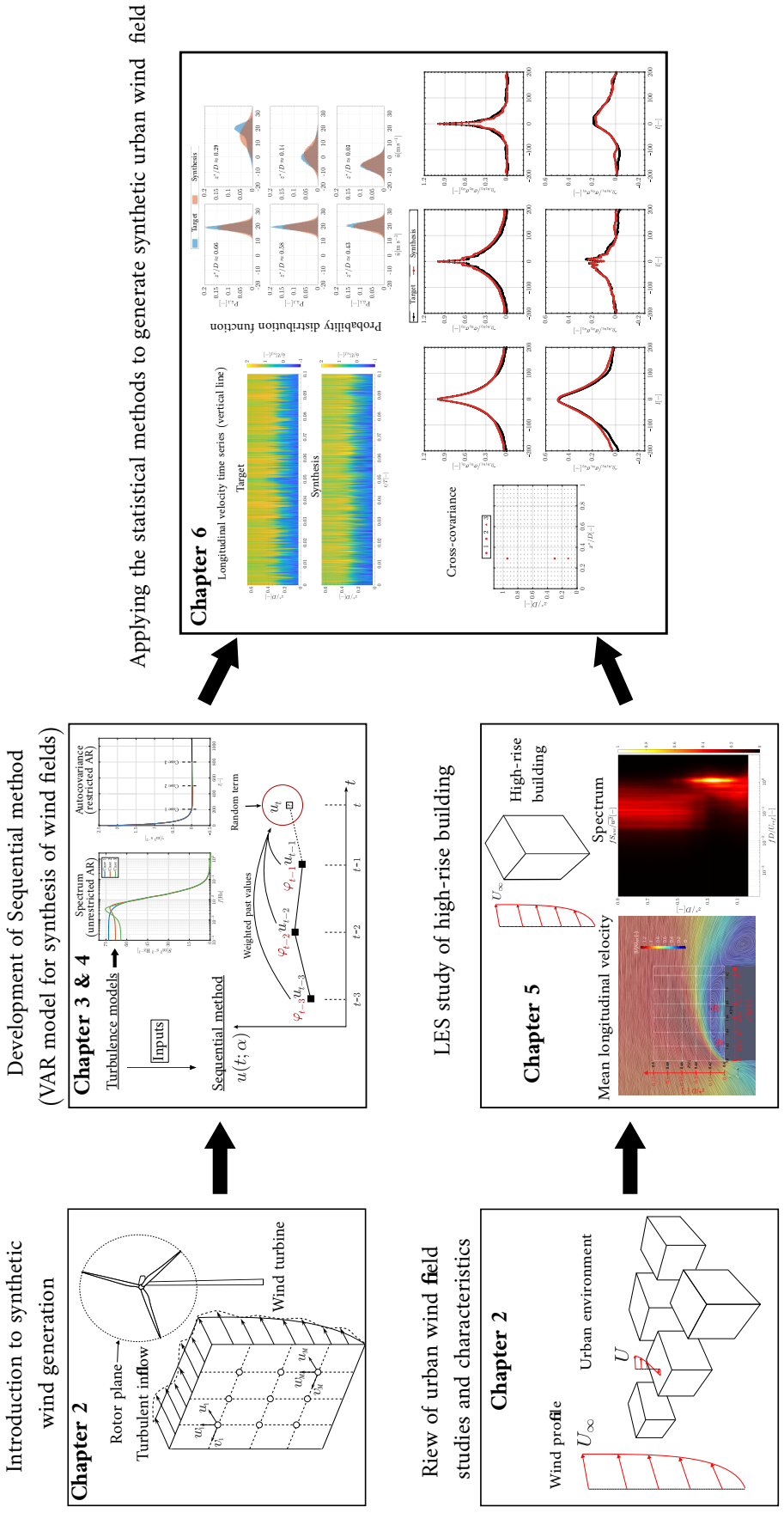

Figure 1.1: A diagram showing the thesis outline.

Chapter 2

Literature and methodology background

The objective of this chapter is to present an overview of the probabilistic description of turbulent wind fields and provide a general understanding of the synthetic generation of wind fields by using numeric generation.

Additionally, this chapter includes a comprehensive review of the current available information about the statistical characteristics of turbulent wind fields in urban environments. Moreover, it provides an examination of existing measurements and Computational Fluid Dynamics (CFD) simulation studies undertaken to gain insights into the wind flow in urban environments.

2.1 Preliminary definitions and basic concepts

This section aims to introduce a description of different definitions and concepts utilized throughout this work.

2.1.1 Probabilistic description of wind velocity field

The highly complex non-linear dynamics that dominate atmospheric flows, along with the huge range of spatial and time scales involved in such flows, make unavoidable the use of statistical tools in their modeling and/or analysis. A deterministic approach to resolve the evolution of the atmospheric velocity field by utilizing DNS is conceptually possible, based on the well-defined mathematical physical model configured by the NS equations (Pope, 2000). However, the high sensitivity of the solution with respect to small changes in both Initial Conditions (ICs) and Boundary Conditions (BCs) (Lorenz, 1963) invites to treat them by considering certain degree of uncertainty in the statement of the problem. Moreover, this approach is currently unfeasible for flows with high Reynolds number due to the enormous computational cost required, which makes it highly practical to generate mathematical-physical models for directly resolving the evolution of average values of the

velocity field (ensemble mean velocity fields), in the case of Unsteady Reynolds Averaged Navier Stokes (URANS) or spatially filtered velocity fields in the case of LES. Similarly to the DNS, the LES is computationally expensive to be used for a complete aeroelastic design and certification process of wind turbines. Furthermore, URANS provides reasonable results with low computational cost, although for more information about the wind flow field (detail spatial structure and time dependence of the velocity field), LES and DNS are needed to be used. Consequently, adopting a probabilistic description of the wind velocity field is essential.

The statistical analysis of atmospheric velocity fields, both in the space-time domain or in the vector wavenumber-angular frequency domain, is crucial to gain an understating of the spatial and temporal structures of the flow with relevance, for instance, for the dynamic response of systems operating in the ABL. In this context, adopting a rigorous probabilistic description of the wind velocity field is essential. The velocity field is, therefore, treated as a three-Variate/four-Dimensional (3V-4D) Random Process (RP) $\tilde{u}_i(\mathbf{x}, t; \alpha)$, where $i = 1, 2, 3$ indicates the three velocity components in a given reference system, $\mathbf{x}$ is the position vector, t is time and $\alpha \in \mathbb{N}^+$ is the sample (realization) index. Indeed, once the theoretical framework of RPs is established to analyze wind fields, the statistical characteristics of that wind field can be characterized by conducting statistical analysis over a sufficiently high number of realizations. One crucial concept is that the RP has statistical properties that are easy to handle, interpret and relate to the dynamic response of systems operating in the ABL.

One of the most important statistical properties of the RP $\tilde{u}_i(\mathbf{x}, t; \alpha)$ is the ensemble mean. To comprehend the significance of the ensemble mean, consider the scenario of conducting N runs in a wind tunnel with the same initial and boundary conditions, resulting in the generation of turbulent wind fields $\tilde{\boldsymbol{u}}(\mathbf{x}, t; \alpha)$ with $\alpha = 1, \ldots, N$. The presence of an uncontrollable perturbation in initial or/and boundary conditions introduces variability in the generated wind field $\tilde{\boldsymbol{u}}(\mathbf{x}, t; \alpha)$ since the turbulent flow fields are acutely sensitive to perturbations (Pope, 2000). Therefore, for a given time $t^{'}$, $\tilde{\boldsymbol{u}}(\mathbf{x}, t^{'}; \alpha_a) \neq \tilde{\boldsymbol{u}}(\mathbf{x}, t^{'}; \alpha_b)$ for $a \neq b$, as shown in Figure 2.1. In this context, the three components of the ensemble mean vector $\boldsymbol{U}(\mathbf{x}, t)$ are defined as:

$$U_i(\mathbf{x}, t) = \mathrm{E}[\tilde{u}_i(\mathbf{x}, t; \alpha)] = \lim_{N \to \infty} \frac{1}{N} \sum_{\alpha=1}^{N} \tilde{u}_i(\mathbf{x}, t; \alpha), \tag{2.1}$$

where $\mathrm{E}[\cdot] = \overline{(\cdot)}$ is the ensemble mean. Following the establishment of the definition of the ensemble mean, the fluctuation of turbulent wind fields, $u_i(\mathbf{x}, t; \alpha)$, is defined as:

$$u_i(\mathbf{x}, t; \alpha) = \tilde{u}_i(\mathbf{x}, t; \alpha) - U_i(\mathbf{x}, t) \tag{2.2}$$

Note that the ensemble mean wind velocity field $U_i(\mathbf{x}, t)$ is deterministic, although it is space-time dependent, whilst the fluctuation field $u_i(\mathbf{x}, t; \alpha)$ is a 3V-4D RP (with zero mean by definition).

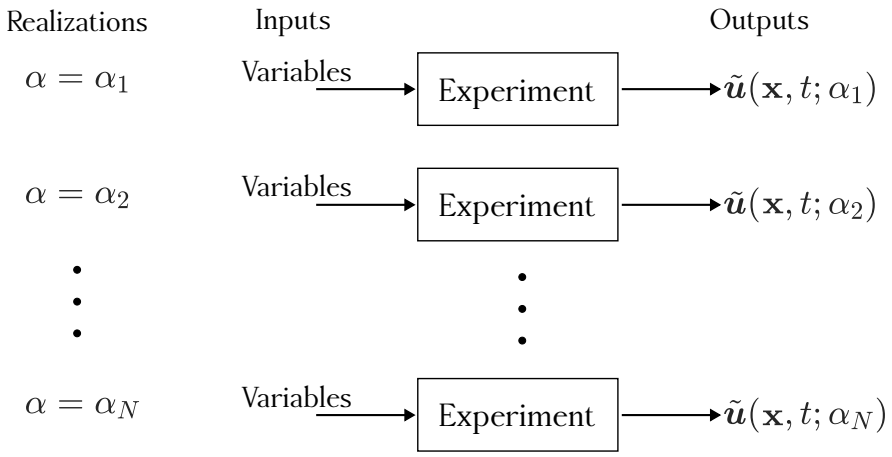

Figure 2.1: Experiment with fixed input variables and uncontrollable perturbations, resulting in the generation of turbulent wind field, $\tilde{\boldsymbol{u}}(\mathbf{x}, t; \alpha)$, which depends on the realization α.

To completely characterize a RP from a statistical point of view, consider a simplified case where only the $u-$velocity component of the turbulent wind field fluctuation at a given point is analyzed. This velocity component fluctuation can be represented by a 1V-1D RP $u(t; \alpha)$ formed by N realizations, as shown in Figure 2.2. A Random Variable (RV) at a given time t_i, $\nu_i = u(t_i, \alpha)$ is characterized by a Probability Distribution Function (PDF) $\mathrm{P}_{u,1}(\nu_i, t_i)$ (the subindex of $\mathrm{P}_{u,1}$ refers to the first-order probability of the RP $u(t; \alpha)$), as shown in Figure 2.2. The $\mathrm{P}_{u,1}$ of a RV lacks joint information about the RV at two or more times. Therefore, to fully characterize the 1V-1D RP $u(t; \alpha)$, it is required to know the infinite hierarchical set of Joint Probability Distribution Functions (JPDFs) (Lumley, 2007),

$$\begin{cases} \mathrm{P}_{u,1}(\nu_1, t_1), \\ \mathrm{P}_{u,2}(\nu_1, t_1; \nu_2, t_2), \\ \vdots \\ \mathrm{P}_{u,n}(\nu_1, t_1; ....; \nu_n, t_n), \end{cases} \tag{2.3}$$

where $\mathrm{P}_{u,n}(\nu_1, t_1; ....; \nu_n, t_n)$ is the n^{th}-order PDF of the RP. However, acquiring the JPDFs for all instants of time is usually unfeasible from a practical point of view. Therefore, in most of the cases, at least in the statement of models for synthetic generation of wind velocity fields from statistical descriptions that will be presented afterward, only the statistical information contained in $\mathrm{P}_{u,1}(\nu_1, t_1)$ and $\mathrm{P}_{u,2}(\nu_1, t_1; \nu_2, t_2)$ is used. Similarly, only the information contained at one point (time) and two-points (two-times) second-order moments are generally considered. It is worth mentioning that if a RP $u_i(\mathbf{x}, t; \alpha)$ is assumed to be Gaussian, then the JPDFs, expressed in Equation (2.3), describing the RP is fully characterized, from a statistical point of view, by the mean velocity field $U_i(\mathbf{x}, t)$ and the two-points two-times covariance tensor (see expression 2.6) (Pope, 2000). However, the actual atmospheric velocity fields are found to be non-Gaussian; indeed, certain statistical parameters that quantify the non-Gaussianity of the atmospheric velocity field could be correlated with the loading state of wind turbines. Certain controversy exists among recent studies that identify differences in the wind turbine

dynamic response affected by Gaussian and non-Gaussian wind fields (Schottler et al., 2017) and those that do not identify such differences (Berg et al., 2016).

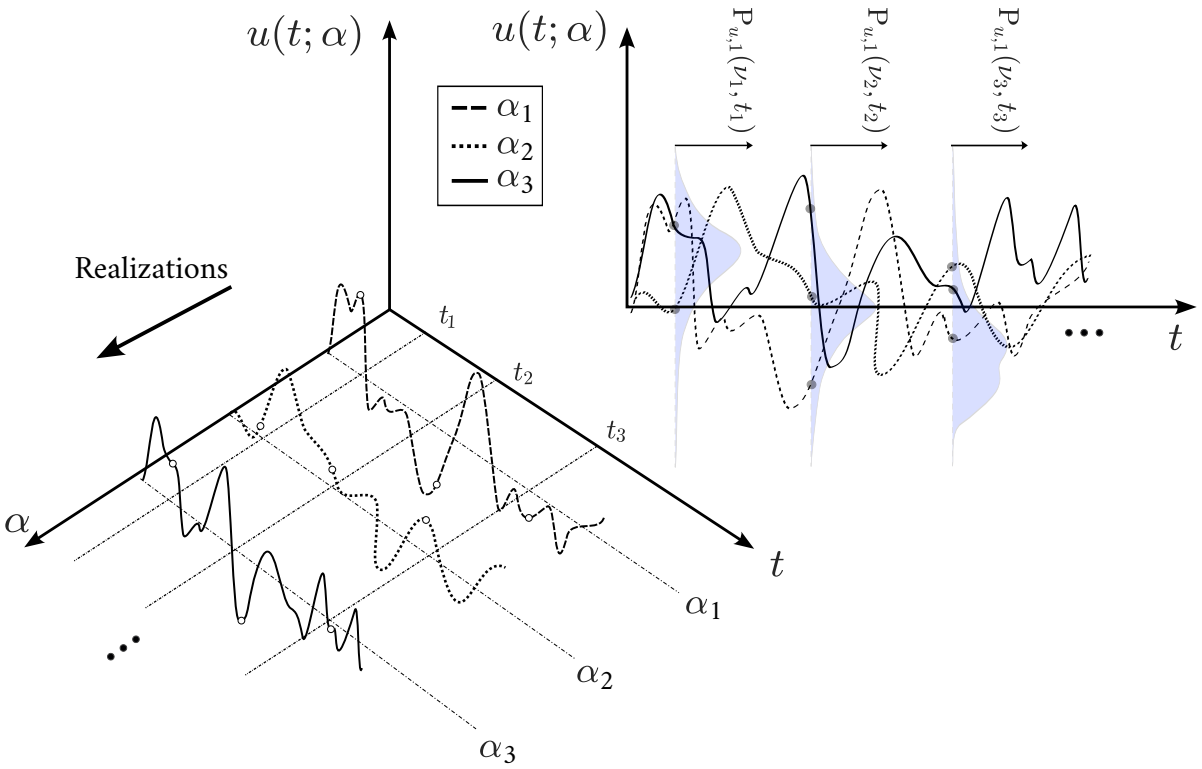

Figure 2.2: Representation of multiple realizations of a 1V-1D RP $u(t;\alpha)$ and the PDF of RVs at various time instants t_i.

To assess the covariance between two RVs at two time instants t_1 and t_2, the two-times second-order moment for the considered 1V-1D RP fluctuation, $\gamma_{uu}(t_1, t_2)$, is evaluated as:

$$\gamma_{uu}(t_1, t_2) = \mathrm{E}[u^*(t_1;\alpha)u(t_2;\alpha)] = \lim_{N\to\infty} \frac{1}{N} \sum_{\alpha=1}^{N} [u^*(t_1;\alpha)u(t_2;\alpha)], \tag{2.4}$$

where subscript $(\cdot)^*$ refers to the complex conjugate. For the case $t_1 = t_2 = t$, the one-time second-order moment is expressed as

$$\gamma_{uu}(t) = \mathrm{E}[u^*(t;\alpha)u(t;\alpha)] = \lim_{N\to\infty} \frac{1}{N} \sum_{\alpha=1}^{N} [u^*(t;\alpha)u(t;\alpha)], \tag{2.5}$$

where $\gamma_u(t)$ [$\mathrm{m}^2/\mathrm{s}^2$] is the variance of the RP $u(t;\alpha)$. By extending the two-times second-order moments, expressed in Equation (2.4), of the 1V-1D RP to the 3V-4D RP, the two points-two times covariance tensor for the complete RP fluctuation $\boldsymbol{u}(\mathbf{x}, t;\alpha)$, $\gamma_{ij}(\mathbf{x}_1, t_1, \mathbf{x}_2, t_2) \in \mathbb{R}^{3\times3}$, is defined as:

$$\gamma_{ij}(\mathbf{x}_1, t_1, \mathbf{x}_2, t_2) = \lim_{N\to\infty} \frac{1}{N} \sum_{\alpha=1}^{N} [u_i^*(\mathbf{x}_1, t_1;\alpha)u_j(\mathbf{x}_2, t_2;\alpha)]. \tag{2.6}$$

The two points-two times covariance tensor, $\gamma_{ij}(\mathbf{x}_1, t_1, \mathbf{x}_2, t_2)$, represented in Equation (2.6), contains the statistical information required by most of the models for synthetic generation of wind velocity fields from statistical descriptions (at least for the models which assume Gaussian RP). The information contained in the tensor $\gamma_{ij}(\mathbf{x}_1, t_1, \mathbf{x}_2, t_2)$ is often represented in the vector wavenumber-angular frequency domain through a 4D-Fourier Transform (FT), after considering the change of variables $\mathbf{x}_1 = \mathbf{x}$, $t_1 = t$, $\mathbf{x}_2 = \mathbf{x} + \boldsymbol{r}$ and $t_2 = t + \tau$, as

$$\Phi_{ij}(\mathbf{x}, t, \boldsymbol{k}, \omega) = \frac{1}{(2\pi)^4} \int_{-\infty}^{\infty} \gamma_{ij}(\mathbf{x}, t, \boldsymbol{r}, \tau) \exp(-\mathrm{i}\boldsymbol{k} \cdot \boldsymbol{r}) \exp(-i\omega\tau) d\boldsymbol{k} d\omega, \tag{2.7}$$

where $\Phi_{ij}(\mathbf{x}, t, \boldsymbol{k}, \omega) \in \mathbb{C}^{3\times3}$ is the Spectral Velocity Tensor (SVT) (Wyngaard, 2010), $\mathrm{i} = \sqrt{-1}$ is the imaginary unit, τ is the time lag, $\boldsymbol{r}$ is the spatial separation vector, $\boldsymbol{k} = [k_1, k_2, k_3]^T$ is the wavenumber vector and $\int_{-\infty}^{\infty} d\boldsymbol{k} d\omega = \int_{-\infty}^{\infty} \int_{-\infty}^{\infty} \int_{-\infty}^{\infty} \int_{-\infty}^{\infty} dk_1 dk_2 dk_3 d\omega$. Thus, from Equation (2.7), the SVT and the two-points two-times covariance tensors are Fourier pairs.

In practical situations, the wind velocity vector is known in M points over a grid parallel to the rotor plane of a WT, as shown in Figure 2.3. Therefore, the 3V-4D RP, $\boldsymbol{u}(\mathbf{x}_p, t; \alpha)$; $p = 1, ..., M$, is reorganized in a $3M$V-1D RP $\boldsymbol{u}(t; \alpha) = [u(\mathbf{x}_1, t; \alpha), v(\mathbf{x}_1, t; \alpha), w(\mathbf{x}_1, t; \alpha), ..., u(\mathbf{x}_M, t; \alpha), v(\mathbf{x}_M, t; \alpha), w(\mathbf{x}_M, t; \alpha)]^T$.The notation employed for the 3V-4D RP entails $\boldsymbol{u}(\mathbf{x}_p, t; \alpha)$ to represent a function of both space $\boldsymbol{x}$ and time t, whereas in the MV-1D RP, $\boldsymbol{u}(t; \alpha)$ signifies a function solely dependent on time t. The statistical information contained in the two-points two-times covariance tensor $\gamma_{ij}(\mathbf{x}_1, t_1, \mathbf{x}_2, t_2)$ or its Fourier pair $\Phi_{ij}(\mathbf{x}, t, \boldsymbol{k}, \omega)$ is represented in the so-called two-times covariance matrix $\gamma_{rs}(t, \tau) \in \mathbb{R}^{3M\times3M}$, for $r, s = 1, \ldots, 3M$,

$$\begin{aligned} \gamma_{rs}(t, \tau) &= \mathrm{E}[u_r^*(t; \alpha) u_s(t + \tau; \alpha)] \\ &= \lim_{N\to\infty} \frac{1}{N} \sum_{\alpha=1}^{N} [u_r^*(t; \alpha) u_s(t + \tau; \alpha)], \end{aligned} \tag{2.8}$$

or its Fourier pair, the spectrum $S_{rs}(t, \omega) \in \mathbb{C}^{3M\times3M}$, for $r, s = 1, \ldots, 3M$, given by

$$S_{rs}(t, \omega) = \frac{1}{2\pi} \int_{-\infty}^{\infty} \gamma_{rs}(t, \tau) \exp(-\mathrm{i}\omega\tau) d\tau. \tag{2.9}$$

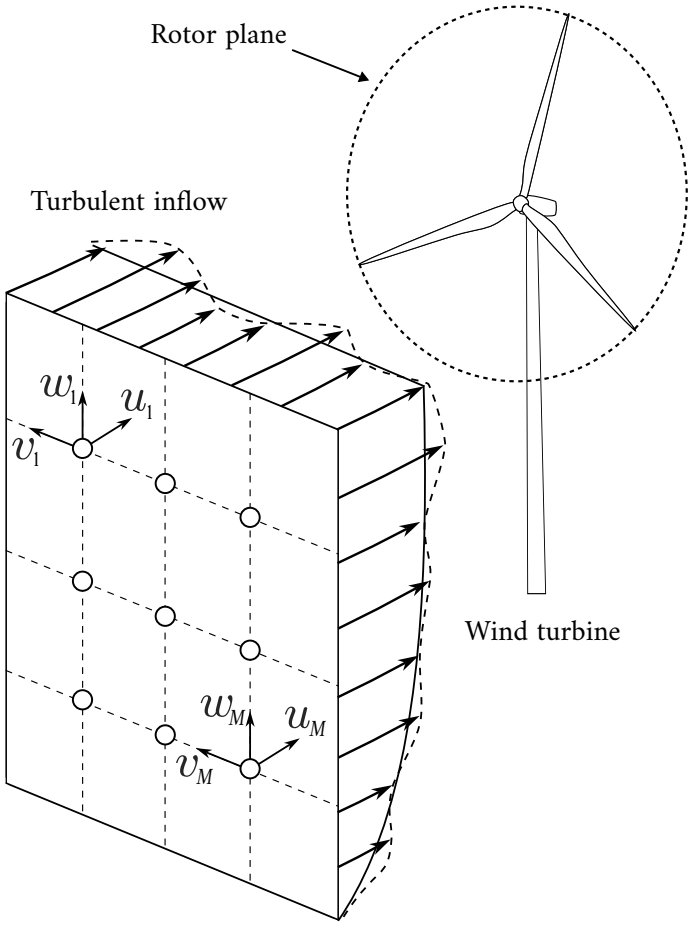

Figure 2.3: Turbulent wind field on a plane parallel to the rotor plane of the wind turbine.

2.1.2 Stationarity, homogeneity, isotropy and ergodicity

The RP $\tilde{\boldsymbol{u}}(\mathbf{x}, t; \alpha)$ is called Weak Sense Stationary-RP (WSS-RP), in a statistical sense, when the RP presents an ensemble mean, a one-point one-time covariance tensor, and a two-points two-times covariance tensor which are independent of time t. Consequently, the two-points two-times covariance tensor is dependent on the time lag, τ.

$$\tilde{u}_i(\mathbf{x}, t; \alpha) \xrightarrow{\text{WSS-RP}} \begin{cases} \dfrac{\partial U_i(\mathbf{x}, t)}{\partial t} = 0, \text{ thus, } U_i(\mathbf{x}, t) \equiv U_i(\mathbf{x}), \\ \\ \dfrac{\partial \gamma_{ij}(\mathbf{x}, t, \boldsymbol{r}, \tau)}{\partial t} = 0, \text{ thus, } \gamma_{ij}(\mathbf{x}, t, \boldsymbol{r}, \tau) \equiv \gamma_{ij}(\mathbf{x}, \boldsymbol{r}, \tau), \end{cases} \tag{2.10}$$

where the subindex $i, j = 1, 2, 3$ and they refer to the three velocity components.

Similarly, the ensemble mean, the one-point one-time covariance tensor and the two-points two-times covariance tensor of a RP can be independent of the spatial coordinates $\mathbf{x}$, which in that case is referred to as a Homogeneous-RP (H-RP) in the three spatial directions. Thus,

the two-points two-times covariance tensor is dependent on the spatial separation vector, $\boldsymbol{r}$. Note that homogeneity can be fulfilled along one, two, or three-space directions.

$$\tilde{u}_i(\mathbf{x},t;\alpha) \xrightarrow{\text{H-RP}} \begin{cases} \dfrac{\partial U_i(\mathbf{x},t)}{\partial \mathbf{x}} = 0, \text{ thus, } U_i(\mathbf{x},t) \equiv U_i(t), \\ \\ \dfrac{\partial \gamma_{ij}(\mathbf{x},t,\boldsymbol{r},\tau)}{\partial \mathbf{x}} = 0, \text{ thus, } \gamma_{ij}(\mathbf{x},t,\boldsymbol{r},\tau) \equiv \gamma_{ij}(t,\boldsymbol{r},\tau), \end{cases} \tag{2.11}$$

where the subindex $i,j = 1,2,3$ and they refer to the three velocity components.

For H-WSS-RP, the complexity of computing the SVT, represented in Equation (2.7), is significantly reduced. This is attributed to the 4D-FT of the two-points two-times covariance tensor being valid for the entire space-time domain, abolishing the need to compute it for all points $\mathbf{x}$ and times t. Therefore, the computation of SVT for a 3V-4D RP is reduced to the following:

$$\Phi_{ij}(\boldsymbol{k},\omega) = \frac{1}{(2\pi)^4} \int_{-\infty}^{\infty} \gamma_{ij}(\boldsymbol{r},\tau) \exp(-\mathrm{i}\boldsymbol{k}\cdot\boldsymbol{r}) \exp(-\mathrm{i}\omega\tau) d\boldsymbol{k} d\omega. \tag{2.12}$$

Similarly, the computational requirement for evaluating the CPSDM $S_{rs}(\omega)$, for $r,s = 1,\ldots,3M$, for a MV-1D RP is reduced to the following:

$$S_{rs}(\omega) = \frac{1}{2\pi} \int_{-\infty}^{\infty} \gamma_{rs}(\tau) \exp(-\mathrm{i}\omega\tau) d\tau. \tag{2.13}$$

In some cases, the flow velocity field has statistical properties that are independent of translation, rotation, and reflection of the coordinate axes in which the components of the velocity field are expressed. In such cases, the flow velocity field is called isotropic. Isotropy leads to relevant simplifications of the form of the covariance tensor and SVTs.

So far, all the previously described statistical characteristics have been defined upon the utilization of ensemble averaging. However, in practice, only a limited number of realizations (one or a few realizations) are typically available to compute these statistical features of wind fields. In such cases, the ergodicity assumption becomes valuable, allowing for the replacement of ensemble averaging with time averaging over a single realization. For example, under this assumption the ensemble mean of a WSS-SP $\tilde{u}_i(\mathbf{x},t;\alpha)$ is computed as follows:

$$U(\mathbf{x}) = \mathrm{E}\left[\tilde{u}(\mathbf{x},t;\alpha)\right] = \lim_{T\to\infty} U^{\mathrm{T}}\left(\mathbf{x},t,T;\alpha\right), \tag{2.14}$$

where $U^{\mathrm{T}}\left(\mathbf{x},t,T;\alpha\right)$ is evaluated as

$$U^{\mathrm{T}}(\mathbf{x},t,T;\alpha) = \frac{1}{T} \int_0^T \tilde{u}\left(\mathbf{x},t+t';\alpha\right) \mathrm{d}t'. \tag{2.15}$$

It is worth noting that the ergodicity assumption holds for the first and second-order statistics when stationarity is assumed up to the fourth-order statistics (Marple Jr & Carey, 2019). Note that in the analysis in the proceedings chapters, ergodicity is assumed, and the ensemble mean and the second-order statistics are estimated and evaluated using time averages.

The actual ABL velocity fields are hardly stationary in the wide sense, nor homogeneous nor isotropic. The spatial and time dependency in the ABL flow dynamics is introduced due to the

terrain surface roughness, the strength of the geostrophic wind, the earth's rotation (Coriolis effect), and the atmosphere's thermal behavior (atmospheric stability condition). Gaussianity, stationarity, homogeneity and isotropy are statistical properties that, although hardly found in actual atmospheric flows, lead to relevant simplifications in the mathematical tractability of the problem of numerical generation of velocity fields from statistical descriptions. Relaxing such simplifying assumptions leads to synthetic velocity fields more representative of the actual ones with a high complexity and computational cost.

Note that, in the following sections, the stationary two-times second order moment, $\gamma_{rs}(\tau)$, will be referred to as ACF for $r = s$ and Cross-Covariance Function (CCF) for $r \neq s$. Both the ACF and CCF are components of the CMF. The Fourier pair of the stationary ACF and CMF will be referred to as the PSD and CPSDM, respectively.

2.1.3 Taylor Frozen Turbulence Hypothesis

For stationary and homogeneous flow in x-direction, Taylor Frozen Turbulence Hypothesis (TFTH) (Taylor, 1938) states that the velocity fluctuation field, $\boldsymbol{u}(\mathbf{x}_\perp, t; \alpha)$, at spatial point $\mathbf{x}_\perp$ and time instance t is equivalent to the velocity fluctuation at spatial point $\mathbf{x}_\perp - Ut\mathbf{i}$ and at time $t = 0$ (J. C. Kaimal & Finnigan, 1994)(where U is the eddy's convection mean streamwise speed). Therefore, the wind velocity fluctuation, $\boldsymbol{u}(\mathbf{x}_\perp, t; \alpha)$, is computed as follows:

$$u_i(\mathbf{x}_\perp, t, \alpha) = u_i(\mathbf{x}_\perp - Ut\mathbf{i}, 0, \alpha), \tag{2.16}$$

where $\mathbf{i}$ refers to a unit vector in the $x-$direction. TFTH assumes that the eddy lifetime is much longer than the time required to reach the sensor shown in Figure 2.4; thus, the turbulent wind field is frozen in time. Note that this assumption is applicable for flows with low turbulence intensity (the velocity fluctuation is small compared to the mean wind speed) (Wyngaard, 2010).

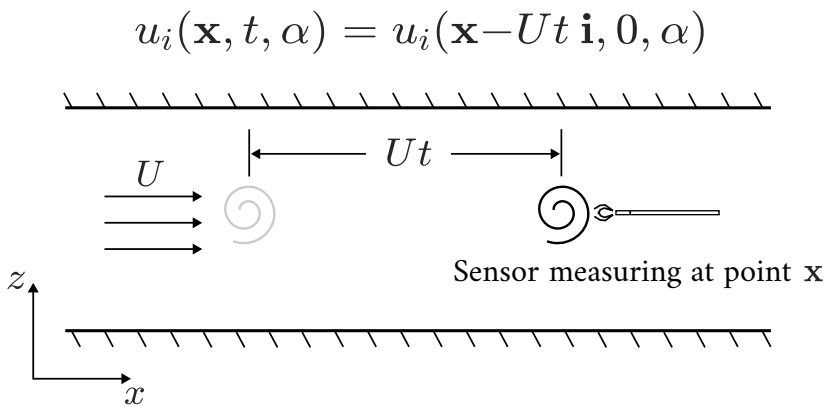

Figure 2.4: Representation of the TFTH idea. An eddy convected by a mean wind speed U and its eddy lifetime is much longer than the time required to reach the measuring point $\mathbf{x}$ at a horizontal distance Ut.

The TFTH allows to establish a relationship between temporal measurements acquired at a

specific point and spatial patterns in space in the flow convection direction. This is achieved through the transformation $x = Ut$. Additionally, the representation of the eddies in the frequency domain can be converted and represented in the longitudinal wavenumber domain through the transformation $k_1 = 2\pi f/U$ (J. Kaimal et al., 1972; J. C. Kaimal & Finnigan, 1994).

2.1.4 Practical considerations for a discrete and finite random process

A RP is characterized as a set of RVs that are generated in a sequential manner over a finite time period T. The RP is referred to as a continuous RP when the set of RVs is continuous in time. Whilst, for a discrete in time series of RVs, the RP is called a discrete RP. For a discrete RP with a sampling time $\Delta t = t_{i+1} - t_i$, a series of M RVs at time $t_1, t_2, \ldots, t_M$ is referred to as $u_{t_1}, u_{t_2}, \ldots, u_{t_M}$. Note that for notation simplicity, in the subsequent sections, the 1V-1D RPs $u(t;\alpha)$ and hV-1D RPs $\boldsymbol{u}(t;\alpha)$ will be referred to as u_t and $\boldsymbol{u}_t$, respectively. For a stationary process, the ACF of the discrete RP is also discrete in the lag domain and can be expressed in terms of a lag $l = \tau/\Delta t$, where τ is the time lag. Thus, the discrete ACF, γ_l for $l = 0, 1, \ldots$, is expressed as

$$\gamma_l = \mathrm{E}[u_t u_{t-l}] = \gamma(\tau = l\Delta t), \tag{2.17}$$

and its Fourier pair, one-sided PSD in terms of the frequency, f, or the angular frequency, $\omega = 2\pi f$, can be calculated from the DTFT of the discrete ACF as follows (Wiener-Khintchine Theorem (Marple Jr & Carey, 2019)):

$$S(f) = \mathcal{F}[\gamma_l] = 2\sum_{l=-\infty}^{\infty} \gamma_l \exp(-\mathrm{i}2\pi f l \Delta t), \qquad 0 \le f \le f_{\max}, \tag{2.18}$$

or

$$S(\omega) = \mathcal{F}[\gamma_l] = \frac{1}{\pi}\sum_{l=-\infty}^{\infty} \gamma_l \exp(-\mathrm{i}\omega\tau)d\tau, \qquad 0 \le \omega \le \omega_{\max}, \tag{2.19}$$

where $f_{\max}$ and $\omega_{\max}$ represent the maximum frequency and maximum angular frequency, respectively. The maximum frequency $f_{\max}$ is determined by the sampling time Δt, and it can be expressed as $f_{\max} = 1/2\Delta t$. It is worth mentioning that high values of sampling time Δt could introduce a rise in the PSD at high frequencies, a phenomenon referred to as "aliasing" (Meirovitch, 1986; Lathi, 2005). Additionally, the set of RVs is generated over a finite time period T instead of a long an infinite time period. The finite time period is can be considered as an infinite time period multiplied by a rectangular window; this operation is called "windowing" (Marple Jr & Carey, 2019). As a result of the windowing process, a distorted PSD will be obtained from the FT of this multiplication, employing the convolution theorem. This distortion caused by the windowing process is referred to as "leakage" (Lyons, 2010).

2.2 Synthetic turbulent wind fields generation

The numerical simulation of turbulent wind fields is required for calculating the forces acting on wind turbines during different wind events as a part of the design and certification process of the machines. To ensure the safe operation of a wind turbine, the system must be simulated under conditions specified by the IEC 61400 standards (IEC 61400-1, 2019; IEC 61400-2, 2019). The most precise way to simulate turbulent wind fields is by utilizing DNS to solve the NS equations of an atmospheric flow (Pope, 2000). However, this approach is currently unfeasible due to the enormous computational cost required to accurately represent the energy transference, from large scales ($L \sim 10^3$ [m] in the atmosphere boundary layer) down to the smallest scales ($\eta \sim 10^{-3}$ [m], Kolmogorov scale) (Wyngaard, 2010). Additionally, there are physical limitations, such as unknown ICs and BCs of the corresponding partial differential equations. Similarly, LES is computationally expensive to be used for a complete aeroelastic design and certification process of wind turbines. URANS is computationally less expensive than the high-fidelity approaches DNS and LES. However, it does not provide time-space revolved instantaneous wind velocity fields, but their ensemble mean (El Bahlouli et al., 2019).

An alternative approach, known as NG (Kleinhans et al., 2009), is utilized to generate synthetic turbulent wind fields (Mann, 1998; Di Paola & Zingales, 2008; Kareem, 2008; Cottone & Di Paola, 2011; Krenk, 2011; Benowitz & Deodatis, 2015; Li et al., 2017a; Krenk & Møller, 2019). NG uses statistical information gathered from actual wind fields to generate synthetic realizations of a turbulent wind field, which reproduces, in the ensemble sense, the statistical features of the predefined wind fields. Over several decades, the NG approach has been applied to synthesis wind fields used as inputs to assess the forces exerted on structures by the turbulent wind inflow (Reed & Scanlan, 1983; Veers, 1988; Li & Kareem, 1990, 1993; Di Paola & Gullo, 2001; Di Paola & Zingales, 2008; Kareem, 2008; H. Wang et al., 2012; Benowitz & Deodatis, 2015; Li et al., 2017b; Krenk & Møller, 2019). Also, NG has been used for the synthetic generation of turbulent inflow for LES studies (di Mare et al., 2006; Huang et al., 2010; Castro & Paz, 2013; Shur et al., 2014; Aboshosha et al., 2015; Castro et al., 2017; Melaku & Bitsuamlak, 2021). One of the main benefits of employing NG for generating synthetic turbulent inflow in LES is that it can contribute to reduce the upstream region of the computational domain, as it eliminates the need for utilizing roughness cubes and barriers to generate enough developed turbulence at the test section (Vita et al., 2020). Additionally, there is no requirement for the utilization of a precursor computational domain to acquire the desired turbulent inflow (Bazdidi-Tehrani et al., 2016; Vasaturo et al., 2018). The NG has also been used in different scientific engineering fields, such as ocean wave modeling (P. Spanos, 1983; Samii & Vandiver, 1984), earthquake ground motions modeling (Chang et al., 1981; Deodatis & Shinozuka, 1988), to synthesize realizations of a RP.

Various approaches can be employed in the NG for synthetic generation of realizations of a RP (Kleinhans et al., 2009); however, the most used methods in the NG of wind fields are the so-called Spectral Representation Methods (SRMs) (Shinozuka, 1971; Veers, 1988; Mann, 1998) and Sequential Methods (SMs) (M. P. Mignolet & Spanos, 1992; P. D. Spanos & Mignolet, 1992; Krenk & Møller, 2019). The SRMs were formally proposed by Shinozuka (Shinozuka, 1971, 1972) and they are theoretically supported by the Spectral Representation

Theorem (SRT) (Grigoriu, 2002). In the SRT, a 1V-1D real WSS-RP with zero mean, $u(t;\alpha)$, with the ACF $\gamma_u(\tau)$ and its Fourier pair, the PSD, $S_{uu}(\omega)$, is presented as a series of weighted trigonometric functions as shown in Figure 2.5 and it is defined as follows:

$$u(t;\alpha) = \lim_{N\to\infty} \sum_{k=1}^{N} \hat{u}_k \cos[\omega_k t + \phi_k(\alpha)], \tag{2.20}$$

where $\hat{u}_k$ are deterministic coefficients known in terms of $S_{uu}(\omega_k)$, $\omega_k \in [\omega_{\min}, \omega_{\max}]$ are deterministic angular frequencies ($\omega_k = (k-1)\Delta\omega$, where $\Delta\omega$ is the angular frequency step of the evenly spaced interval $[\omega_{\min}, \omega_{\max}]$) and $\phi_k(\alpha)$ are independent RVs uniformly distributed within the interval $[-\pi, \pi]$.

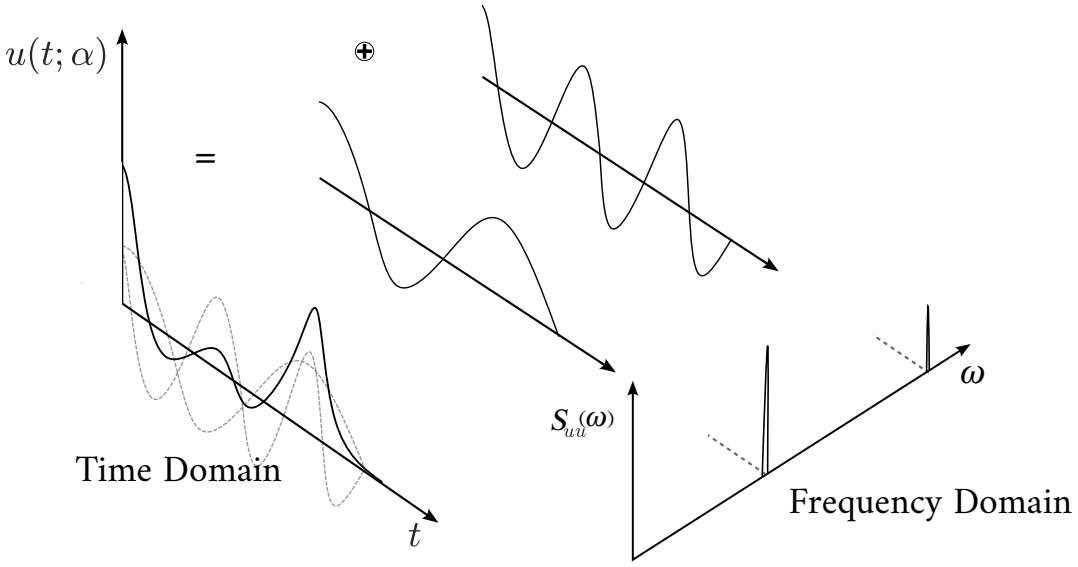

Figure 2.5: The visualization of the concept of SRM as summation of series of weighted cosine functions, where each cosine function is associated with a specific frequency in the frequency domain.

The SRMs can be applied to generate multivariate, multidimensional, or multivariate-multidimensional RPs, representing the wind velocity fluctuation vector at various points in space (Veers, 1988; Mann, 1998; Benowitz & Deodatis, 2015; Patruno & Ricci, 2017; H. Wang & Wu, 2018; J. Chen et al., 2018; Huo et al., 2018; Zhao & Huang, 2020). To improve the computational cost of the simulations, the FFT is employed to compute the summation of trigonometric functions in the SRMs. However, simulating multivariate and/or multidimensional wind fields over a large period of time requires a considerable amount of memory (Samaras et al., 1985; Li & Kareem, 1993; X. Chen & Kareem, 2002). In the SRMs, the Cholesky decomposition of the CPSDM is applied to evaluate the deterministic coefficients required to simulate stationary wind fields (Shinozuka & Jan, 1972; Li & Kareem, 1993; Veers, 1988; Li & Kareem, 1995; Mann, 1998) and non-stationary wind fields (Li &

Kareem, 1991, 1997). However, attention has been focused on the Schur decomposition as it avoids the challenges associated with the Cholesky decomposition. This includes issues like having eigenvalues close to zero but manifest negative values due to numerical issues during the CPSDM computation (Shinozuka et al., 1990; Di Paola & Gullo, 2001). The approaches proposed by (Veers, 1988; Mann, 1998) are the most utilized implementations of SRM in the wind energy community. The Mann approach is based in the SVT, whereas the Veer-Shinozuka approach is based in the CPSDM. A comparison between both approaches is well presented in (Gallego-Castillo et al., 2020). In Equation (2.20), the 1V-1D RP of the (Veers, 1988) approach is presented. Whilst, the (Mann, 1998) approach is illustrated in Section 5.3.3.

In the context of SM, the generation of synthetic wind fields is based on time series linear models, such as AR models, Moving Average (MA) models, and AutoRegressive Moving Average (ARMA) models and their vector versions (VAR, VMA, and VARMA) (Samaras et al., 1985; Li & Kareem, 1990; M. P. Mignolet & Spanos, 1992; P. D. Spanos & Mignolet, 1992; Takalo et al., 2005; Hytti et al., 2006; Krenk & Møller, 2019; Gallego-Castillo et al., 2022). Under this framework, any value of the time series can be expressed as a combination of weighted past values, plus a weighted random term as shown in Figure 2.6. These weights are referred to as the parameters of the model. Developing efficient calibration techniques for the parameters of a model is the main challenge (Krenk & Møller, 2019). Although SRMs are most widely used in wind energy applications, SMs present advantages in certain aspects compared to SRMs. For instance, the simulation of the wind velocity components in SM can be restarted from a small amount of stored data as only the model parameters need to be stored (Krenk & Møller, 2019; Gallego-Castillo et al., 2022). Furthermore, there are theoretical expressions for the CMF and the CPSDM for a model, which can be computed from the model parameters (Tsay, 2013; Box et al., 2016). This allows to directly compare the target CMF (or target CPSDM) and the theoretical CMF (or theoretical CPSDM) to check the reliability of the model in reproducing the predefined (target) two-points two-times statistical characteristics of the wind field rather than using the sample CMF and CPSDM obtained from realizations of the process.

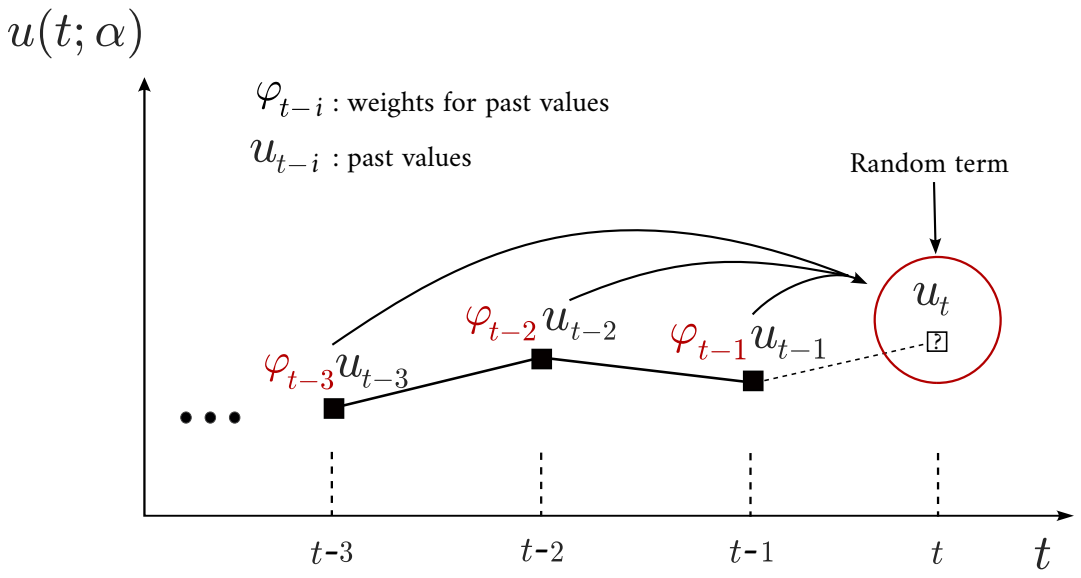

Figure 2.6: The visualization of the concept of SMs (AR), as summation of weighted past values plus a random term.

In this work, the AR/VAR model is selected as the computational burden for calibrating the AR/VAR model parameters is less compared to MA/VMA and ARMA/VARMA models (Marple Jr & Carey, 2019). Moreover, the AR/VAR model can be calibrated to present PSDs for the longitudinal, lateral, and vertical velocity components, with sharp peaks with no deep nulls (Marple Jr & Carey, 2019), which is convenient for reproducing the characteristics of realistic turbulent wind fields. In Sections 3.1 and 4.1, the AR and VAR models are discussed in detail. Various calibration techniques for the parameters of the AR model and its vector form VAR are discussed in the mentioned sections. The calibration techniques based on a predefined CMF (P. D. Spanos & Hansen, 1981; Reed & Scanlan, 1983; P. D. Spanos, 1983; Samaras et al., 1985; Krenk & Møller, 2019; Gallego-Castillo et al., 2022, 2024) and a predefined CPDSM (M. Mignolet & Spanos, 1987; Elagamy et al., 2023) are illustrated for generating stationary synthetic wind fields, presenting the advantages and disadvantages of each approach.

2.3 Wind field in urban areas and current studies

In this section, two literature reviews are presented. The first review provides an insight of the existing studies, both numerical and experimental, conducted in urban areas. The second review focuses on the available statistical information concerning wind fields within built environments.

2.3.1 A review: numerical and experimental studies of urban flows

The global climate crisis urges us to rapidly replace fossil energy sources with renewable sources. This requires massive installation of renewable capacity. In this context, the urban environment has several advantages connected with distributed renewable generation. Small wind turbine (SWT) technology is gaining popularity as it reduces some of the barriers associated with large-scale wind farms (Musial & Ram, 2010). However, the insufficient comprehension of the wind field characteristics in urban areas resulted in inadequate safety measures for the SWTs and poor performance (Smith et al., 2012; KC et al., 2019). The wind flow characteristics in the built environment are rather different from the flow field developed over flat and open terrains (J. C. Kaimal & Finnigan, 1994) since, in general, the local airflow patterns are significantly influenced by the non-homogeneous roughness of the urban area (Ricciardelli & Polimeno, 2006), and in particular, the wind field is strongly affected by the presence of buildings in their vicinity. Understanding the flow characteristics in urban areas is crucial to ensure the structural safety of the SWTs and improve their performance (Stathopoulos et al., 2018).

The comprehension of wind fields in built environments can be achieved by employing experimental and numerical approaches. Numerous research studies have been conducted to investigate wind fields in urban environments using both strategies. With this regard, the Architectural Institute of Japan (AIJ, 2007) and the Compilation of Experimental Data for Validation of microscale dispersion models (CEDVAL, 2006) provide numerical and experimental data for understanding wind flows around a single building or clusters of buildings. It is worth mentioning that these studies are primarily focused on the evaluation of wind conditions at the pedestrian level. Field measurements were conducted in Oklahoma City in the United States, wherein measurements were taken at various locations within the city, both at the pedestrian and building level (Nelson et al., 2004, 2007a, 2007b). The aim of these field measurements was to understand the wind patterns over an urban area and how they are influenced by wind direction variations. (Fortuniak & Pawlak, 2015) analyzed the turbulence spectra and cross spectra of wind field over Łódź in Poland. (Fortuniak & Pawlak, 2015) showed that the spectra and cross spectra of urban wind velocity components have similar characteristics to the spectra and cross spectra of the wind velocity components over a homogeneous flat terrain described by (J. Kaimal et al., 1972) for the Kansas experiment. However, some features, such as peaks, can appear in the spectra of urban wind fields due to some phenomena (Nelson et al., 2007a; Vita et al., 2020), such as conical vortex, which takes place in built environments. Furthermore, (Tabrizi et al., 2015) analyzed the influence of wind direction on spectra at the rooftop of a warehouse at Port Kennedy in Western Australia. Also, (Christen et al., 2007) showed that the integral length scale is affected by obstacles such as buildings. Additional research on understanding the urban wind field using wind tunnel and field measurements can be found in (Brook, 1972; Rotach, 1991; Feigenwinter et al., 1999; Roth, 2000; Christen et al., 2007; Peng et al., 2020).

Various researchers have used the numerical approach, CFD, to characterize the the urban airflow at the rooftop of buildings. (Micallef & Van Bussel, 2018; Stathopoulos et al., 2018; Toja-Silva et al., 2018; KC et al., 2019) provide detailed reviews of these studies. (Abohela et al., 2013) examined the influence of building height, urban configuration as well as the

shape of the rooftop on the wind flow characteristics over the rooftop. (Toja-Silva et al., 2015) studied the impact of the roof shapes on the turbulence intensity and mean velocity over a building roof. The investigations conducted in the previous studies were done by utilizing the RANS approach, which can resolve relevant characteristics of the mean wind field (Vita, 2020). However, for a deeper understanding of the urban wind field characteristics as well as having more accurate and reliable results, high-fidelity numerical approaches such as LES are required (Blocken, 2015, 2018). There are studies that have utilized LES for simulating wind fields over built environments, although their primary focus has been on the dispersion of pollutants (Merlier et al., 2019) and assessing pedestrian comfort (Tolias et al., 2018a; Jacob & Sagaut, 2018). (Kono et al., 2016) investigated the wind field over the rooftop of isolated buildings, analyzing the effect of wind direction and horizontal aspect ratio of a building on the wind resources at the rooftop.

Most of the mentioned studies offer limited information about the wind flow characteristics at the rooftop. In particular, they lack providing a full description of the two-points two-times second-order statistics of the wind velocity components, either in the frequency domain (cross-spectra) or in the time domain (cross-covariances), including the spectra at different height levels and/or spatial coherence of the velocity components, which are essential as they impact the wind loads applied on the wind turbines (Dimitrov et al., 2017). To fill that research gap, (Šarkić Glumac et al., 2018a; Hemida et al., 2020; Vita et al., 2020) conducted wind tunnel experiments to analyze the wind flow at the rooftop of an isolated building and a group of buildings. Moreover, they investigated the impact of different rooftop shapes and the influence of changing the inflow wind direction on the wind field around the buildings. (Hemida et al., 2020) analyzed the velocity and pressure fields over the isolated building, whilst (Šarkić Glumac et al., 2018a) focused on the cluster effect. (Vita et al., 2020) provided a more comprehensive description of the wind field at several possible locations for the SWT at the rooftop, which was also compared with a LES simulation done by (Vita, 2020). Furthermore, (Vranešević et al., 2022) utilized LES simulations to understand the flow pattern around the isolated building and compared the results with experimental measurements provided by (Šarkić Glumac et al., 2018a; Hemida et al., 2020; Vita et al., 2020).

In this work, a LES analysis was conducted (see Chapter 5) to replicate the experiments on an isolated High-Rise Building (HRB) from (Šarkić Glumac et al., 2018a; Hemida et al., 2020; Vita et al., 2020), with the aim to resolve the two point-two times second-order statistics of the wind velocity components over the HRB rooftop to be used as the deterministic inputs for the SRM and SM to generate synthetic wind fields representative of the urban environment.

2.3.2 A review: urban boundary layer and statistical characteristics of urban wind field

The boundary layer developed over urban environments is affected by the non-homogeneous roughness of the urban area (Ricciardelli & Polimeno, 2006). The statistical characteristics of wind fields in the ABL that develop over urban areas differ compared to those that develop over a homogeneous rough surface (J. C. Kaimal & Finnigan, 1994). In urban environments, the wind flow exhibits complex flow features such as acceleration regions, separation bubbles

formed over the rooftop and wake deficit on the leeward side of buildings. The wind field characteristics in urban areas can be influenced by various parameters, such as the building heights, the shape of rooftops, urban configuration, and the heterogeneity of the urban environment (Ricciardelli & Polimeno, 2006; Nelson et al., 2007a; Abohela et al., 2013; Peng et al., 2020; Vita et al., 2020). The ABL region where the influence of the urban environment is called Urban Boundary Layer (UBL) (Oke, 1987). Furthermore, the distance from the ground level to the highest building is defined as Urban Canopy Layer (UCL) (Micallef & Van Bussel, 2018) and it is shown in Figure 2.7.

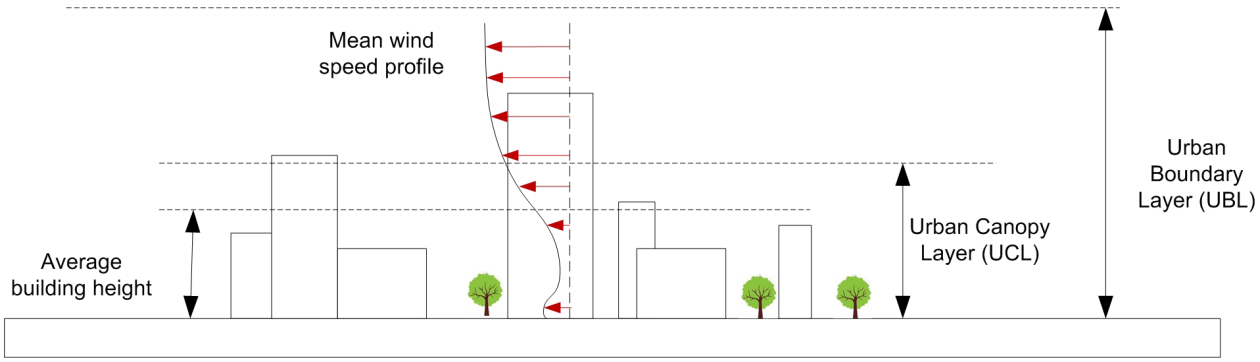

Figure 2.7: Urban wind profile depicting the UCL and the UBL (Figure acquired from (Micallef & Van Bussel, 2018)).

In response to global climate changes, the renewable energy market for energy production is increasing, although some delays were encountered during the period from 2020 to 2022 due to the COVID-19 pandemic restrictions (IEA, 2023). A total of 255 GW wind power capacity had successfully been installed in Europe by the end of 2022, comprising 88% onshore and 12% offshore wind turbines (ETIPWind, 2023). The European Commission's plan for clean and sustainable energy production, known as REPowerEU, aims to reach 440 GW of wind energy production by the year 2030 (ETIPWind, 2023). Currently, the SWT technology is gaining attraction as SWTs avoid certain challenges linked to large-scale wind farms (Musial & Ram, 2010). Some of the main barriers encountered by large-scale wind farms are the requirement of available large sites, power loss during the power transmissions and distributions to the consumers, high maintenance costs, and grid power efficiency issues (Musial & Ram, 2010). The preference for urban environments as installation sites for SWTs arises from their compact space requirements and their ability to provide energy close to the location where it is needed (Stathopoulos et al., 2018). However, there are technological and socio-political challenges that must be addressed when considering the installation of SWT in urban areas (Stathopoulos et al., 2018; IRENA, 2020; Kirkegaard et al., 2023).

As mentioned above, one of the challenges that needs to be addressed involves comprehending the flow characteristics in urban areas as simulations of turbulent wind velocity fields are required to evaluate dynamic loads on a wind turbine during different wind events. SWTs must be tested under the wind conditions defined by IEC (IEC 61400-2, 2019) standards. The IEC 61400-2 provides a description of the mean velocity and the turbulence intensity using the NTM, which are used for the aeroelastic design of SWT mounted over building

roofs in built environments. However, this description is based on data obtained for open and flat terrains. Therefore, this could lead to ill-prediction of the dynamics loads on the SWT as urban airflows are characterized by high levels of turbulence and frequent variations in wind direction (Nelson et al., 2004; Eliasson et al., 2006; Ricciardelli & Polimeno, 2006; Nelson et al., 2007a, 2007b). The IEC 61400-2 standard uses vK (Von Karman, 1948) and Kaimal (J. Kaimal et al., 1972) turbulence models to model the second-order statistics of urban wind fields. This literature review summarizes the investigation conducted by several authors concerning the urban flow statistical characteristics. Additionally, the suitability of vK and Kaimal models to describe the second-order statistical properties of urban wind fields is examined.

General information about the statistical characteristics of urban wind fields

The mean longitudinal velocity increases over the rooftop of buildings. (Peng et al., 2020) conducted a wind tunnel experiment and measured the mean wind speed profiles at various locations over a building roof (see Figure 4 in (Peng et al., 2020)). In Figure 2.8, the normalized mean longitudinal velocity profiles, U/U_{ref} (where U_{ref}, is the flow reference velocity at the same height in the undisturbed flow case), is shown at two locations from the conducted experiment. Similar mean longitudinal velocity profiles were obtained for the other rooftop locations indicated in Figure 2.8. The mean $u-$velocity component value increases with increasing the distance from the roof height until it reaches a maximum value surpassing the reference value. Subsequently, it recovers the to undisturbed flow velocity component value. Similar profiles were reproduced in RANS simulations done by (Abohela et al., 2013).

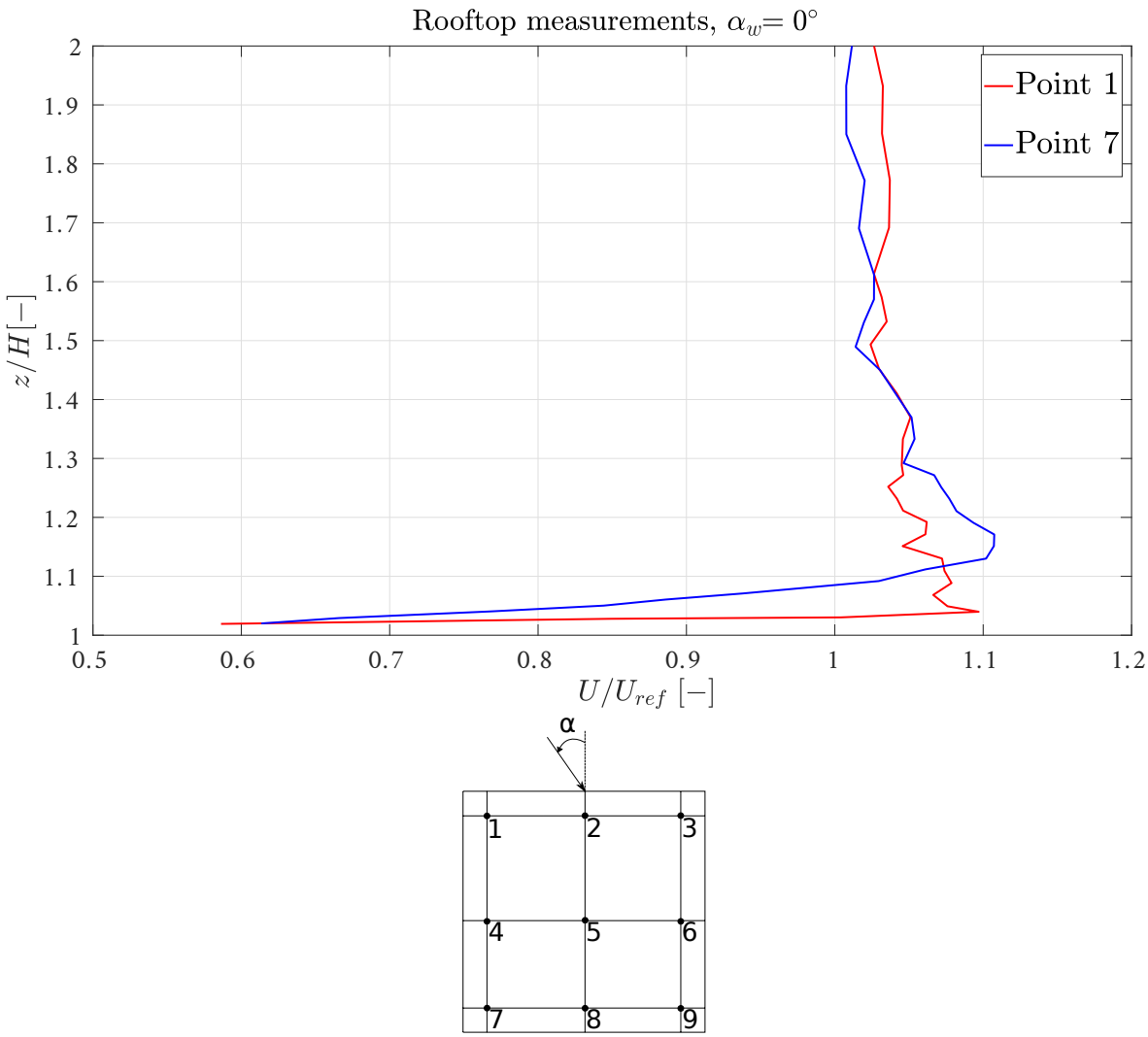

Figure 2.8: Normalized mean $u-$velocity profile, U/U_{ref}, over a flat rooftop, at points 1 and 7, for wind direction $\alpha_w = 0°$ (Figure adapted from (Peng et al., 2020)). H is the height of the building.

For various roof shapes, the highest longitudinal turbulence intensity, I_u, values over a building rooftop was observed within the range $1 < z/H < 1.3$ (where H is the building height) in 3D steady Reynolds-averaged Navier-Stokes (RANS) simulations conducted by (Abohela et al., 2013). Whilst, (Peng et al., 2020) obtained the highest I_u value within the range $1 < z/H < 1.2$, from wind tunnel measurements conducted on a flat roof of a building, as shown in Figure 2.9. The $I_{u,\max}$ was obtained in the range $1 < z/H < 1.3$, and for $z/H > 1.3$, it steadily returns to the value of turbulence intensity for undisturbed flow, similarly as the mean profile. However, this pattern is affected by the wind direction, as shown in Figure 2.9. A study done over a flat rooftop by (Vita et al., 2020), showed that for $z/H > 1.2$, the I_u presents a relatively similar magnitude to the vertical turbulence intensity I_w, which is a partial indicator of higher levels of isotropy. However, for $z/H < 1.2$, the I_u was remarkably higher than the I_w, which demonstrates that for this region the turbulence is rather anisotropic.

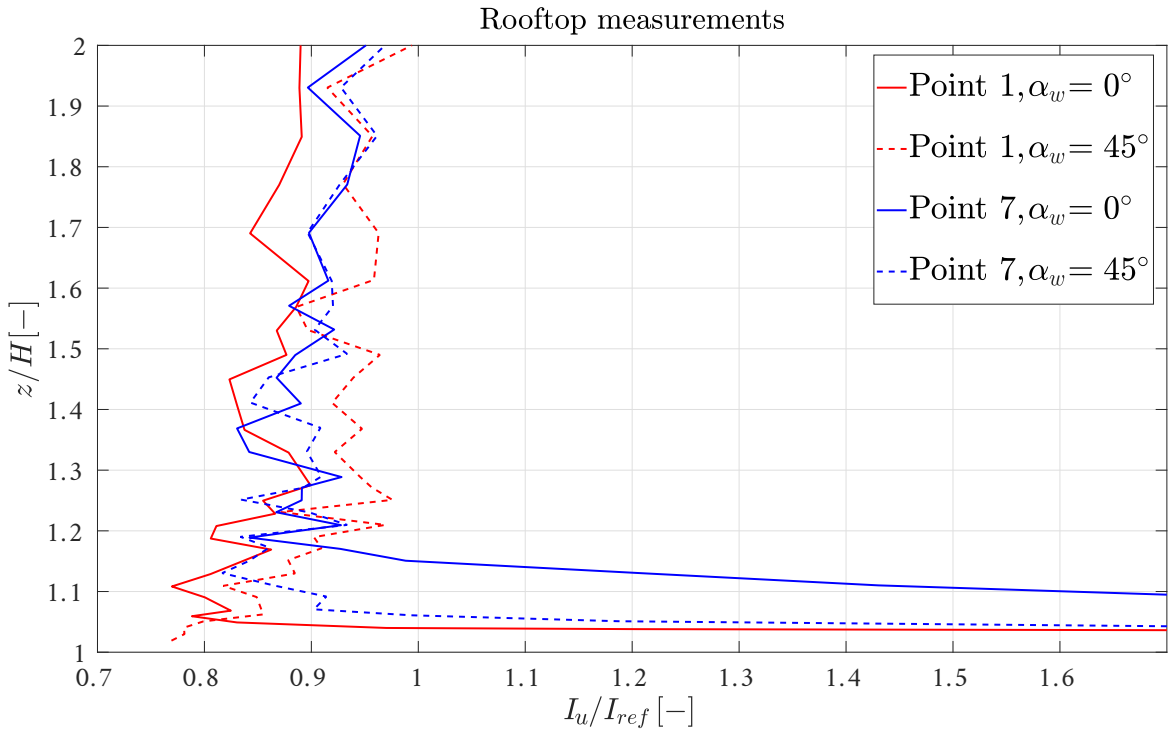

Figure 2.9: Normalized longitudinal intensity I_u/I_{ref}, obtained from wind tunnel measurements, at point 1 and 7 over a rooftop, for wind directions $\alpha_w = 0°, 45°$ (Figure adapted from (Peng et al., 2020)).

(Brook, 1972; Feigenwinter et al., 1999) showed the normalized longitudinal, lateral and vertical spectra, $fS_{ii}/\overline{i^2}$, for $i = u, v$ and w, using field measurements. There are some general characteristics in the normalized spectra for the three velocity components obtained in built environments in these case studies. The normalized longitudinal spectrum was characterized by a slope of $-2/3$ in the inertial subrange, and the normalized lateral and vertical spectra approached this slope at higher frequencies, as shown in Figure 2.10. The same characteristic of the spectra was observed in studies done by (Nelson et al., 2007b; Vogel, 2009; Fischer et al., 2010; Tolias et al., 2018b). The results obtained by (Feigenwinter et al., 1999) showed that the ratio between the vertical spectrum and the longitudinal spectrum (S_{ww}/S_{uu}) approaches the value 4/3 with increasing the height, where the ratio $S_{ww}/S_{uu} = 4/3$ represents the canonical result for isotropic turbulence (J. C. Kaimal & Finnigan, 1994). Note that the $-2/3$ or $-5/3$ slope is obtained in the inertial subrange for the normalized spectra or the spectra when represented in log-log scale, respectively. The normalized cross-spectra, $fS_{uw}/\overline{uw}$ approach $-4/3$ slope at high frequencies. The normalized vertical spectrum, in the mentioned studies showed that most of the energy is contained at high frequencies; this was also observed in the results obtained by (J. Wang, 1992). The energy contained in the inertial subrange for the lateral and the vertical spectra increases as the stratification becomes increasingly stable. The peak frequency, which is the frequency that corresponds to the highest value of the normalized spectra for the three velocity components, depends on the stability condition of the atmosphere and the height above the ground. As illustrated in Figure 2.10, the peak

of the normalized spectra is shifted to low frequencies as instability increases as shown by (J. C. Kaimal & Finnigan, 1994; Roth, 2000; Fortuniak & Pawlak, 2015). Furthermore, the peak of the normalized spectra for the three velocity components shifts to high frequencies with increasing height, as shown by (Feigenwinter et al., 1999; Roth, 2000; Ricciardelli & Polimeno, 2006). Some peaks can appear in the normalized spectra due to some features in the built environment. For instance, peaks appear in the normalized spectrum over a rooftop of a small building in a heterogeneous urban pattern due to vortex shedded from tall buildings. Also, peaks can appear in the normalized spectra depending on the location of the measurement over a rooftop, as (Vita et al., 2020) showed that, for an isolated building, the middle point in a flat rooftop is prone to vortex shedding, as shown in Figure 2.11.

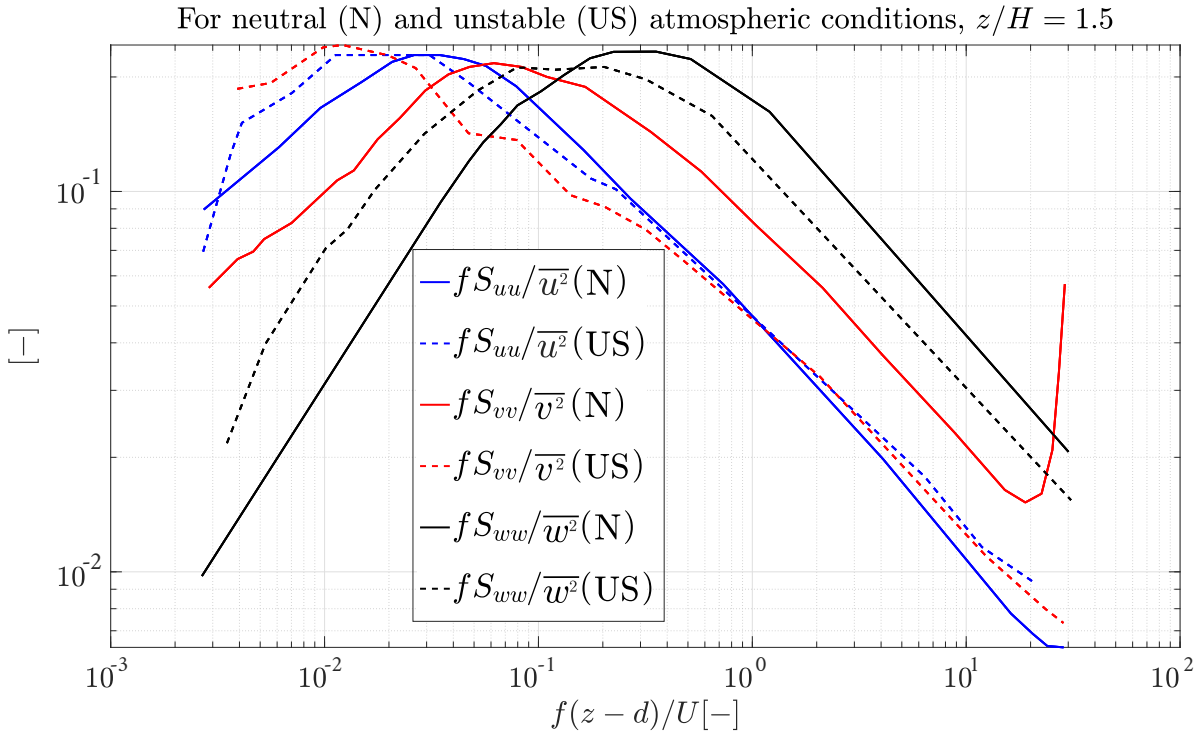

Figure 2.10: Normalized longitudinal, lateral and vertical spectra, $fS_{ii}/\overline{i^2}$, for $i = u, v, w$, obtained from field measurements at a rooftop of a building, at $z/H = 1.5$, for Neutral (N) and Unstable Stratification (US) conditions (d is the zero plane displacement height and U is the mean streamwise velocity component) (Figure adapted from (Feigenwinter et al., 1999)).

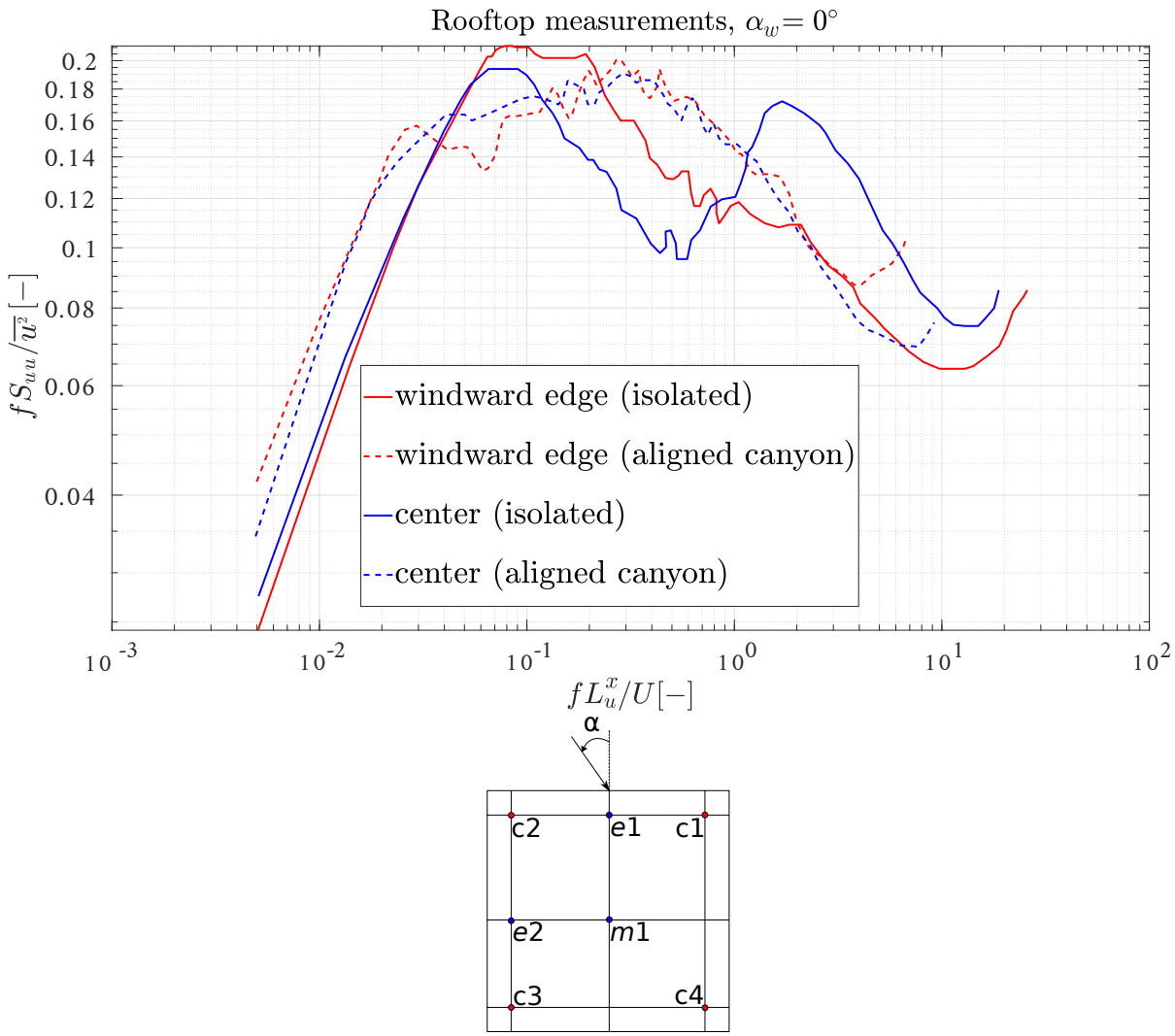

Figure 2.11: Normalized longitudinal spectrum, $fS_{uu}/\overline{u^2}$, obtained from wind tunnel measurements at a rooftop of an isolated building and atop of a building in an aligned canyon configuration, at a point close to the windward edge ($e1$) and a middle point over the roof ($m1$), for wind directions $\alpha_w = 0°, 45°$, note that the measured spectrum is smoothed in this figure (Figure adapted from (Vita et al., 2020)).

(Tabrizi et al., 2015) showed that the vK and Kaimal models underestimate the spectra for the three velocity components measured at the top of a warehouse. This is due to the fact the values of parameters suggested by the IEC standards (IEC 61400-2, 2019) to be used in these models are not suitable for the built environment. (Christen et al., 2007; Vita et al., 2020) showed that the integral length scales of the velocity components are affected by buildings. (Tabrizi et al., 2015) showed that by using the appropriate value for the integral length scale, the Kaimal model could be used for reproducing PSD in urban environments.

Parameters affecting the wind flow characteristics in urban areas

The influence of building height on the flow characteristics was examined by (Abohela et al., 2013), where three different building heights, $H, 2H$ and $4H$, where $H = 6$ m, were tested. The main flow features were the same for the three cases. The stagnation point on the windward facade was found at height $2/3H$ for all the cases. The standing vortex was formed at the same location in front of the windward side of the building for all cases. However, the reattachment length of the flow behind the building was increased with increasing building height. Also, due to the interference of a backflow area, the recirculation area did not reach the ground surface, although this behavior does not affect the characteristic of the flow on the roof as observed by (Abohela et al., 2013). The same I_u pattern was observed for the three height cases, as shown in Figure 2.12 and similarly for the mean $u-$velocity component. The location of the $I_{u,\max}$ and the $U_{\max}$ were the same for the three height cases, although their magnitudes increase with the building height.

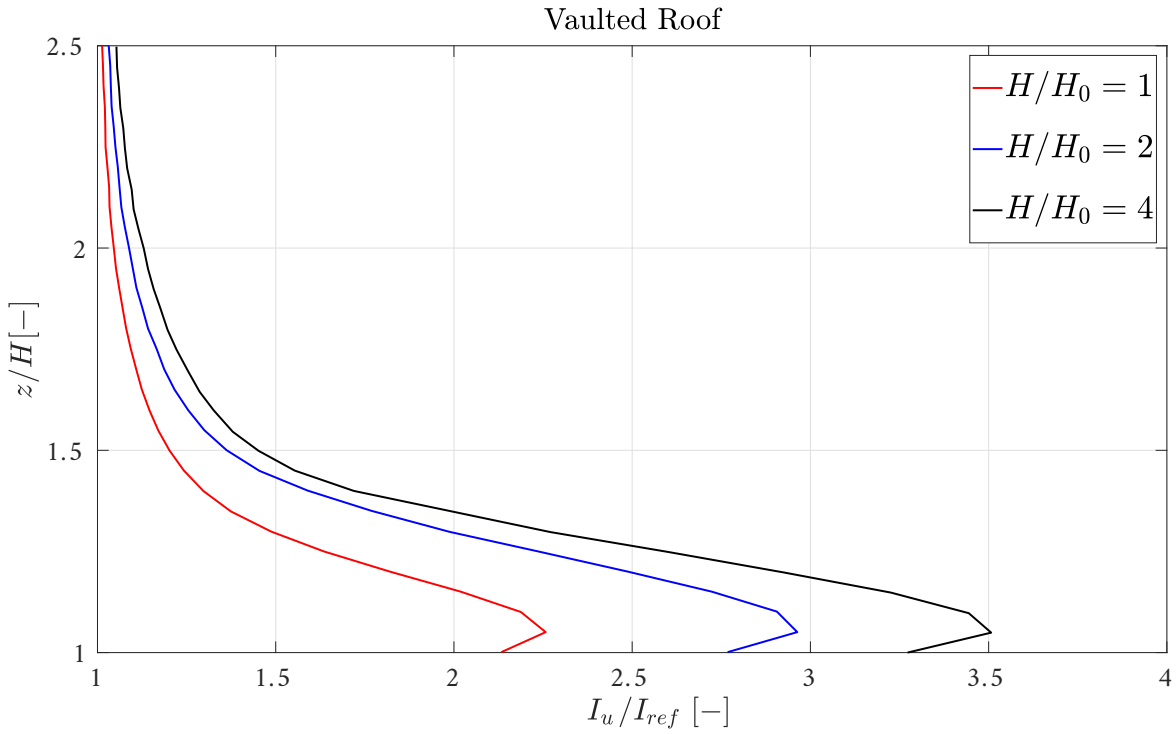

Figure 2.12: Normalized longitudinal intensity I_u/I_{ref}, where I_{ref} is the turbulence intensity at the same location in undisturbed flow, above a roof top of a building for three building heights: $H/H_0 = 1, H/H_0 = 2$ and $H/H_0 = 4$, where $H_0 = 6$ m (Figure adapted from (Abohela et al., 2013)).

The effect of the roof shape was examined by (Abohela et al., 2013; Toja-Silva et al., 2015). Six different roof profiles for an isolated building were tested by (Abohela et al., 2013). The shapes of the roof considered were flat, gabled, wedged, pyramid, barrel-vaulted and domed. It was observed that all the roofs lead to an acceleration effect on the wind flow; however, the

magnitude of acceleration was dependent on the profile of the roof. Moreover, the maximum turbulence intensity for all the roofs was obtained in the range $1 < z/H < 1.3$, which agrees with the recommendation of (WINEUR, 2007) and the results of Warwick Wind Trials Project (Encraft, 2009), which recommend that the hub of the wind turbine should be at $z/H \geq 1.3$. (Abohela et al., 2013) recommended that the wind turbine hub should be installed within the non-dimensional height ratio $1.35 < z/H < 1.5$. Furthermore, the location of $U_{\max}$ depends on the shape of the roof and wind direction (see Table 2 in (Abohela et al., 2013)). The results showed that both the barrel-vaulted roof and the domed roof cases presented the highest potential energy yield.

(Abohela et al., 2013) studied the effect of the specific urban configuration on the flow over a roof for aligned and staggered arrangements. Two cases were studied for each urban configuration. In the first case, the building has a height less or equal to the surrounding buildings. In the second case, the building has a height larger than the surrounding buildings. In the first group, the flow is dominated by the surface roughness. The turbulence intensity over the roof increases since the roughness of the surroundings increases. The acceleration effect on the longitudinal mean velocity U took place at $z/H > 1.5$ for height below the surrounding buildings and at $z/H > 1.4$ for height similar to the surrounding buildings. For both cases, the maximum streamwise velocity occurs at $z/H = 2.5$, as shown in Figure 2.13. It was observed that the acceleration effect for the staggered configuration is higher than for the aligned configuration. In the second group, where the building has a height higher than the surrounding buildings, the surface roughness has less effect. The turbulence intensity and mean velocity profiles are similar to the case corresponding to an isolated building. However, their magnitudes decrease due to the increase of the roughness of the surroundings. This decrease in their magnitude reduces with increasing the measured building height than the surrounding buildings. It was noticed that the aligned arrangement has a smaller effect than the staggered arrangement, which is contrary to what happened in the first case for height below or equal to the surrounding heights. Moreover, (Vita et al., 2020) showed that the normalized spectra of wind velocity components is affected by the urban environment. The normalized spectra obtained atop a building for isolated and urban environment cases were different, as shown in Figure 2.11.

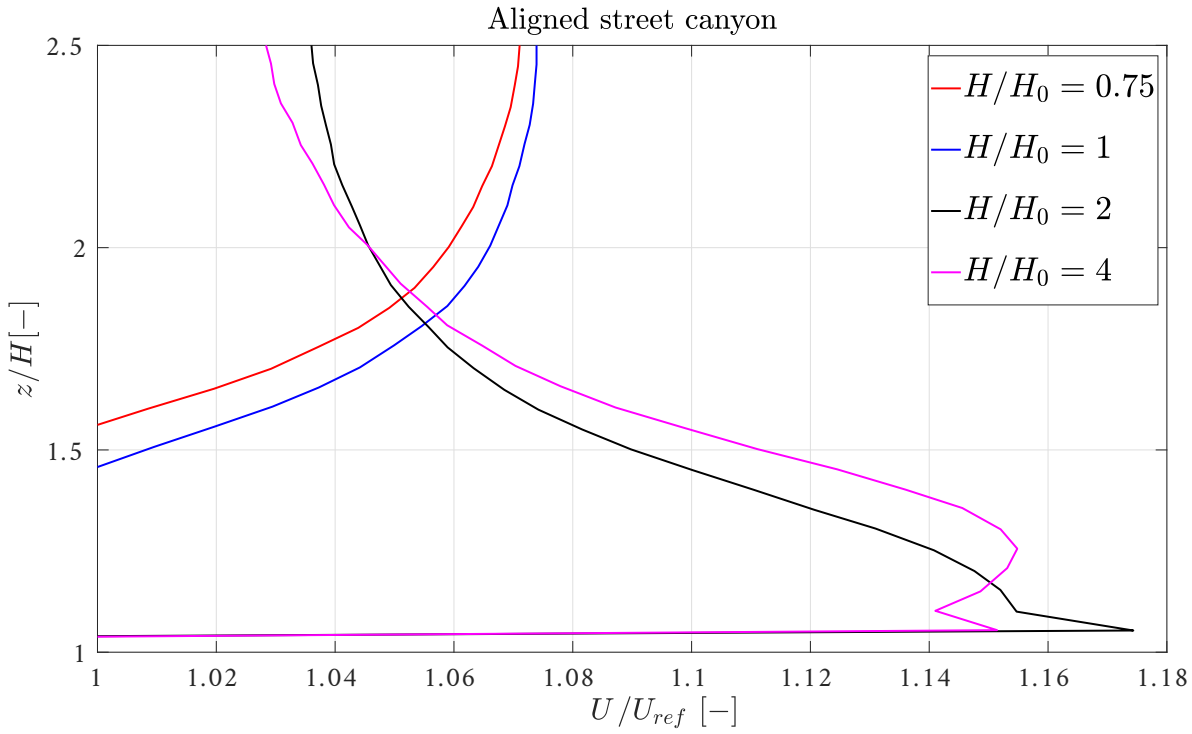

Figure 2.13: Normalized streamwise velocity U/U_{ref}, over a vaulted rooftop of buildings with various heights surrounded by buildings with height (H_0 = 6 m) in aligned canyon configuration (Figure adapted from (Abohela et al., 2013))

In homogeneous urban areas, the building's height is approximately similar, as shown in Figure 2.14. Whist, for heterogeneous urban patterns, the heights of the buildings that form the surrounding urban environment are different, as shown in Figure 2.15. The height difference enhances flow features such as downdrafts. The downdraft occurs due to the pressure difference between the windward side of a high building (high pressure) and the leeward side of a small building (low pressure), which leads to redirecting the flow with higher momentum down into lower level (Wise, 1971). Due to the downdraft effect, vortex shedding from tall buildings is downdrafted to lower surfaces. The vortex shedded from a tall building appeared as peaks at low frequencies in the spectra measured by (Nelson et al., 2007b) at the roof of a lower building. (Nelson et al., 2007b) observed that the value of the longitudinal, lateral and vertical spectra at low frequencies was dependent on the distance of the measuring point to the nearest surface. The closer the measuring point to the surface, the lower energy contained at low frequencies because the surrounding buildings to the lower building are restricting large-scale turbulent motions. In homogeneous urban patterns, (Eliasson et al., 2006) showed that eddies could penetrate the shear layer at the top of a building and affect the flow structure in the canyon. However, the effect of downdraft was not as strong as observed in heterogeneous urban patterns.

Figure 2.14: European urban style (Homogeneous)

Figure 2.15: American urban style (Heterogeneous).

A slight change in the wind direction can lead to different flow structures in the urban environment (Nelson et al., 2007a). Considering this, the dependence of the turbulent intensity on the wind direction has been observed in (Ledo et al., 2011). (Peng et al., 2020) showed the influence of changing the wind direction on the turbulence intensity over a flat roof through wind tunnel measurements. For 0° and slightly higher wind directions, higher turbulence intensity was observed on the leeward edge of the roof compared to the windward edge. For wind direction 45°, higher turbulence intensity was determined at the corners of the building as these regions are affected by the conical vortex pair (Ono et al., 2008) generated at the windward edges of the building. This increase of turbulence intensity, due to the conical vortex, was also described by (Vita et al., 2020; Peng et al., 2020), as shown in Figure 2.9.

(Abohela et al., 2013; Peng et al., 2020) showed that the location and the magnitude of the $U_{\max}$ in the vertical direction over rooftops are affected by changing wind direction. Moreover, the spectra for the three velocity components are affected by the wind direction, as shown in Figure 2.16. (Nelson et al., 2007b; Tabrizi et al., 2015; Vita et al., 2020) also showed the effect of changing wind direction on the spectra obtained from measurements in different urban densities and configurations.

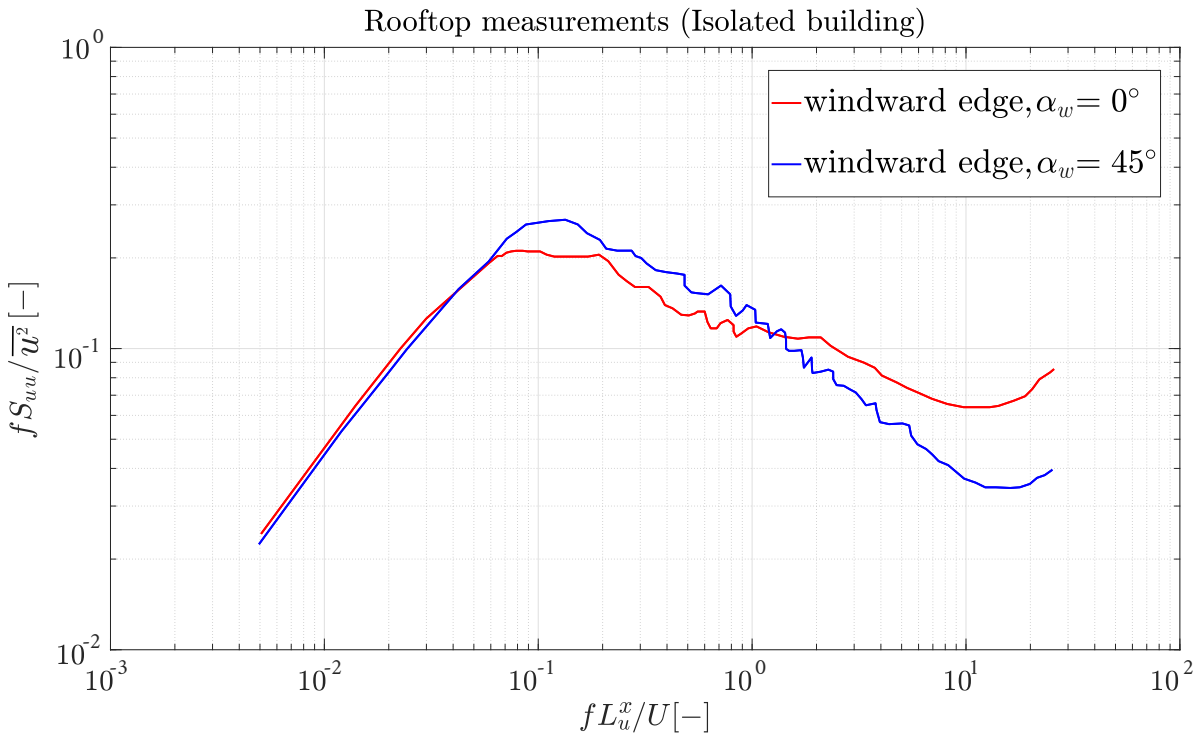

Figure 2.16: Normalized longitudinal spectrum, $fS_{uu}/\overline{u^2}$, obtained from wind tunnel measurements at the rooftop of an isolated building at a point close to the windward edge ($e1$), for wind direction $\alpha_w = 0°, 45°$, note that the measured spectrum is smoothed in this figure (Figure adapted from (Vita et al., 2020)).

In conclusion, this review highlights the requirement for more detailed studies about the flow characteristics in urban environments, providing statistical characteristics such as two-points second-order statistics (spatial correlations) and two-points two-times second-order statistics (spatial covariances, cross-spectra). There is a wide literature reflecting the effect of urban environment on first-order (mean velocity) and one-point second-order statistics (variance) of wind velocity components. However, few research has been performed to characterize the two-point second-order statistics (cross spectra, cross-correlations), even though this statistical information is very relevant for the aeroelastic simulations of wind turbines. There are various numerical and experimental studies focused on the analysis of wind fields in urban environments. Some of these studies are summarized in Table 2.1. The summary provides information about the available statistical characteristics of the analyzed wind field, as well as the urban configuration and the location of the measurements.

Field measurements			
Author	Availiable data	Configuration type	Measurements location
(Brook, 1972)	$I_{u,v,w}, S_{uu,vv,ww}$	Homogeneous config.	Rooftop
(Christen et al., 2003, 2007)	$U, \sigma_w, \mathrm{Sk}_w$, TKE, $L^x_{u,v,w}$	Homogeneous config.	Rooftop, street canyon
(Eliasson et al., 2006)	σ_w, u^*	Homogeneous config.	Rooftop, street canyon
(Evans et al., 2017)	S_{uu}	Homogeneous config.	Rooftop
(Feigenwinter et al., 1999)	$\sigma_{u,v,w}, S_{uu,vv,ww,uw}$	Homogeneous config.	Rooftop
(Fortuniak & Pawlak, 2015)	$S_{uu,vv,ww,uw}$	Homogeneous config.	Rooftop
(Nelson et al., 2007a, 2007b)	$U, V, W, I_{u,v,w}, S_{uu,vv,ww}$	Strong heterogeneous config.	Rooftop, street canyon
(Rotach, 1995)	$\sigma_{u,v,w}, S_{uu,ww}$	Homogeneous config.	Rooftop, street canyon
(Roth, 2000)	$U, V, W, I_{u,v,w}, S_{uu,vv,ww}$	-	Rooftop, street canyon
(Tabrizi et al., 2015)	$S_{uu,vv,ww}$	Homogeneous config.	Rooftop
(Vogel, 2009)	$S_{uu,ww}$	Homogeneous config.	Rooftop
(J. Wang, 1992)	$\sigma_{u,v,w}, S_{uu,vv,ww,uw}$	Homogeneous config.	

Wind tunnel measurements				
Author	Available data	Domain size [m] $(L \times W \times H)$	Configuration type	Measurements location
(Fischer et al., 2010)	U, L^x_u, S_{uu}, I_u	$18 \times 4 \times 2.75 - 3.25$ $11.5 \times 1.5 \times 1$	Homogeneous config.	Rooftop, street canyon
(Peng et al., 2020)	U, I_u	$24 \times 6 \times 3.6$	Isolated building	Rooftop
(Ricciardelli & Polimeno, 2006)	U, I_u, S_{uu}	$22 \times 2.4 \times 1.6$	Homogeneous config	street canyon, Higher than building
(Vita et al., 2020)	U, I_u, L^x_u, S_{uu}	$9.4 \times 1.8 \times 1.6$	Isolated building, Homogeneous config.	Rooftop

Computational fluid dynamics					
Author	Simulation type	Available data	Domain size [m] $(L \times W \times H)$	Configuration type	Measurements location
(Abohela et al., 2013)	3D steady RANS	U, I_u	$126 \times 36 \times 36$	Isolated building, homogeneous config.	Rooftop
(Kono et al., 2016)	LES	U, I_u	$1.776 \times 1.1 \times 0.9$	Isolated building	Rooftop
(Tolias et al., 2018b)	LES	U, V, S_{uu}	$1670 \times 900 \times 147$	Weak heterogeneous config.	Rooftop, street canyon
(Toja-Silva et al., 2015)	RANS	U, I_u	$940 \times 420 \times 400$	Isolated building	Rooftop

Table 2.1: Various numerical and experimental studies focused on urban wind fields in different urban configurations.

Chapter 3

Optimal calibration of the parameters of AR models (sequential method) applied to univariate cases

Some of the results shown in this chapter have been presented in the 17$^{\text{th}}$ European Academy of Wind Energy PhD seminar (Elagamy et al., 2021a) and published in the journal of stochastic environmental research and risk assessment (Gallego-Castillo et al., 2022).

As stated in the previous chapter, the most used methods in the NG of wind fields are the SRM and the SM. This chapter aims to provide an overview of the process of utilizing SM through an Autoregressive (AR) model to synthetically generate a single velocity component at a single point, since this simple case allows to present the characteristics of the different calibration strategies in the most pedagogical way. In this chapter, several calibration techniques (state-of-the-art) for the parameters of an AR from a predefined target ACF are analyzed. The merits and demerits of the state-of-the-art for the calibration of the parameters of an AR model from a target ACF are discussed. A methodology based on pole-placement is introduced to optimally calibrate the parameters of an AR model for reproducing a predefined target PSD. Both ACF and PSD-based approaches are compared, and the implications of reproducing a target ACF or a target PSD are presented.

3.1 Introduction to autoregressive (AR) models

In this section, basic concepts of AR models are introduced (P. D. Spanos & Mignolet, 1992; M. P. Mignolet & Spanos, 1992). The particular application to generate a synthetic time series for the $u-$velocity component is considered in what follows. In the AR(p) model (p is the AR model order), a RV at time t, u_t, is expressed as a weighted linear combination of past values, u_{t-l}, for $l > 0$, plus a random term, $\sigma\varepsilon_t$. Note that the 1V-1D discrete time RP $u(t;\alpha)$ is expressed as u_t to simplify the notation. The general formulation of an AR model

of order p, AR(p), is (Tsay, 2013):

$$u_t = \sum_{i=1}^{p} \varphi_i u_{t-i} + \sigma \varepsilon_t, \tag{3.1}$$

where φ_i, for $i = 1, \ldots, p$, are the regression coefficients, ε_t is a sequence of independent and identically distributed (iid) RVs with PDF $\mathcal{N}(0, 1)$ and σ is the noise coefficient. The noise coefficient, σ, is utilized to scale the variance of the random term ($\mathrm{E}\left[(\sigma\varepsilon_t)\,(\sigma\varepsilon_t)\right] = \sigma^2$). The regression and noise coefficients, which are deterministic terms, are referred to as the AR model parameters. Note that the formulation of the AR(p) model, represented in Equation (3.1), is called the unrestricted AR model since it includes the entire regression coefficients ($\varphi_1, \ldots, \varphi_p$) until the model order p.

Another formulation of the AR model, which includes only selected regression coefficients, is referred to as a restricted AR model (Giannini & Mosconi, 1987). The restricted AR model gives more flexibility while using the AR approach since it does not include all the regression terms (Krenk & Møller, 2019). The indexes of the selected regression terms are collected in a vector $\mathbf{j} = [j_1, j_2, \ldots, j_N]$, where N is the number of selected regression coefficients and $N \leq p$. The general formulation of a restricted AR model is defined as (Krenk & Møller, 2019; Gallego-Castillo et al., 2022):

$$u_t = \sum_{i=1}^{N} a_{j_i} u_{t-j_i} + b\varepsilon_t. \tag{3.2}$$

It is noteworthy that distinctive notations are employed for the restricted AR model parameters (a_{j_i} and b) in contrast to the notation used in the unrestricted AR model. This is done to differentiate between the two AR formulations (see Equations (3.1) and (3.2)). A restricted AR model can be considered as a special case of an unrestricted one, where the regression coefficients, φ_m, have a non-zero value just for the selected m terms and a zero value for the rest, this can be represented as follows:

$$\varphi_{j_n} = \begin{cases} a_{j_n}, & \text{for } j_n \in \mathbf{j}, \\ 0, & \text{for } j_n \notin \mathbf{j}. \end{cases} \tag{3.3}$$

Furthermore, an unrestricted AR model can be regarded as a special case of a restricted AR model with a vector $\mathbf{j} = [1, 2, 3, \ldots, p]$.

Both formulations of the AR model represented in Equations (3.1) and (3.2), can be employed for generating synthetic time series of one velocity component by combining past time series values with random values. However, the initial step in this process is to identify the AR model parameters. By appropriately selecting the AR model parameters, a large number of time series realizations, ideally infinite, could reproduce statistical features defined beforehand in the ensemble sense. In Sections 3.4 and 3.5, the computation of the AR model parameters from a predefined ACF or a predefined PSD is illustrated. Prior to explaining the calibration techniques of the AR model parameters, fundamental concepts, such as the theoretical ACF and PSD of the AR model, are explained in the proceeding sections.

3.2 Theoretical autocovariance function, ACF, of an AR model

For a stationary RP, the ACF, γ_l, of two RVs u_{t_1} and u_{t_2} at time t_1 and t_2, respectively, is a function of the lag $l = (t_2 - t_1)/\Delta t$ and it is defined as (Box et al., 2016):

$$\gamma_l = \mathrm{Cov}[u_t, u_{t-l}] = \mathrm{E}[u_t u_{t-l}]. \tag{3.4}$$

It is noteworthy that the order utilized for the multiplication of the RVs is u_t followed by u_{t-l}, as shown in Equation (3.4), where an alternate order may be found elsewhere. There are two relevant properties of the ACF to be addressed. Firstly, the ACF is symmetric. Thus, $\gamma_{-l} = \gamma_l$, which implies that the ACF is independent of the direction of the time lag. Additionally, the value of the ACF at time lag $l = 0$ is greater than the ACF for time lags $l > 0$ ($\gamma_0 \geq |\gamma_l|$). As previously stated, one of the advantages of the AR(p) model is that it has a theoretical ACF, which can be determined by substituting Equation (3.1) or (3.2) in Equation (3.4). The theoretical ACF for an unrestricted AR model is derived as follows:

$$\begin{aligned}
\gamma_l^{\mathrm{AR}} &= \mathrm{E}\left[\left(\sum_{i=1}^{p} \varphi_i u_{t-i} + \sigma\varepsilon_t\right) u_{t-l}\right] \\
&= \sum_{i=1}^{p} \varphi_i \mathrm{E}\left[u_{t-i} u_{t-l}\right] + \mathrm{E}\left[(\sigma\varepsilon_t)\, u_{t-l}\right] \\
&= \sum_{i=1}^{p} \varphi_i \gamma_{l-i} + \mathrm{E}\left[(\sigma\varepsilon_t)\, u_{t-l}\right],
\end{aligned} \tag{3.5}$$

where the superscript $(\cdot)^{\mathrm{AR}}$ indicates AR model. Since ε_t is a sequence of iid random variables, thus, $\mathrm{E}[\varepsilon_t \varepsilon_{t-l}] = 0$, for $l \neq 0$, whilst, for $l = 0$, $\mathrm{E}[\varepsilon_t \varepsilon_t] = 1$. The $\mathrm{E}[(\sigma\varepsilon_t) u_{t-l}]$ term shown in Equation (3.5) can be evaluated by substituting the expression of u_t given by in Equation (3.1) into Equation (3.5), to obtain the following:

$$\begin{aligned}
\mathrm{E}\left[(\sigma\varepsilon_t)\, u_{t-l}\right] &= \mathrm{E}\left[(\sigma\varepsilon_t)\left(\sum_{i=1}^{p} \varphi_i u_{t-i-l} + \sigma\varepsilon_{t-l}\right)\right] \\
&= \sum_{i=1}^{p} \underbrace{\varphi_i \mathrm{E}\left[(\sigma\varepsilon_t)\, u_{t-i-l}\right]}_{\text{initial term}} + \underbrace{\mathrm{E}\left[(\sigma\varepsilon_t)\,(\sigma\varepsilon_{t-l})\right]}_{\text{last term}}.
\end{aligned} \tag{3.6}$$

For the case $l \geq 0$, the value of the "initial term" in Equation (3.6) is zero as the infinite subsequent substitution of Equation (3.1) for the RV u_{t-i} yields to $\sum_{i=1}^{\infty} \mathrm{E}[(\sigma\varepsilon_t)(m_i \varepsilon_{t-i-l})]$ (where m_i is a coefficient), which amounts to zero due to the iid nature of ε_t. Whilst, for $l = 0$, the "last term" in Equation (3.6) attains a value σ^2, thus, $\mathrm{E}[(\sigma\varepsilon_t) u_{t-l}] = \sigma^2$. In the case $l > 0$, the "last term" equates to zero since $\mathrm{E}[(\sigma\varepsilon_t)(\sigma\varepsilon_{t-l})] = 0$, for $l > 0$. Therefore, the $\mathrm{E}[(\sigma\varepsilon_t) u_{t-l}]$ can be computed as (Madsen, 2007):

$$\mathrm{E}[(\sigma\varepsilon_t) u_{t-l}] = \begin{cases} \sigma^2, & \text{for } l = 0, \\ 0, & \text{for } l > 0. \end{cases} \tag{3.7}$$

By substituting Equation (3.7) in Equation (3.5), the general form of the theoretical ACF, γ_l, for an unrestricted AR(p) model can be written as:

$$\begin{aligned} \gamma_0^{\mathrm{AR}} &= \sum_{i=1}^{p} \varphi_i \gamma_{-i} + \sigma^2, && \text{for } l = 0, \\ \gamma_l^{\mathrm{AR}} &= \sum_{i=1}^{p} \varphi_i \gamma_{l-i}, && \text{for } l > 0. \end{aligned} \tag{3.8}$$

The theoretical ACF for the restricted AR model can be obtained by substituting Equation (3.2) in Equation (3.4) and applying the analogous procedures employed for the unrestricted AR model, to get the general form of the theoretical ACF, γ_l, for a restricted AR(p) model with vector $\mathbf{j} = [j_1, \ldots, j_N]$ as follows:

$$\begin{aligned} \gamma_0^{\mathrm{AR}} &= \sum_{i=1}^{N} a_{j_i} \gamma_{-j_i} + b^2, && \text{for } l = 0, \\ \gamma_l^{\mathrm{AR}} &= \sum_{i=1}^{N} a_{j_i} \gamma_{l-j_i}, && \text{for } l > 0. \end{aligned} \tag{3.9}$$

Note that the set of equations for calculating the theoretical AR ACF for different values of l, as presented in Equations (3.8) and (3.9), will be referred to as the "covariance equations."

The theoretical ACF represented in Equation (3.8) can be expressed in matrix form, which can be illustrated by considering computing the theoretical ACF up to time lag $l = N$ for an AR(2) model; thus the matrix form for the ACF of an AR(2) model is expressed as follows:

$$\begin{bmatrix} -\varphi_2 & -\varphi_1 & 1 & 0 & 0 & 0 & \ldots \\ 0 & -\varphi_2 & -\varphi_1 & 1 & 0 & 0 & \ldots \\ 0 & 0 & -\varphi_2 & -\varphi_1 & 1 & 0 & \ldots \\ 0 & 0 & 0 & -\varphi_2 & -\varphi_1 & 1 & \ldots \\ \vdots & & \vdots & & \vdots & & \ddots \end{bmatrix}_{(N+1)\times(N+3)} \begin{bmatrix} \gamma_{-2} \\ \gamma_{-1} \\ \gamma_0 \\ \vdots \\ \gamma_N \end{bmatrix}_{(N+3)\times 1} = \begin{bmatrix} \sigma^2 \\ 0 \\ 0 \\ \vdots \\ 0 \end{bmatrix}_{(N+1)\times 1} . \tag{3.10}$$

The system of equations by Expression (3.10) is under-determined due to the presence of $N + 1$ equations to solve for $N + 3$ unknowns; thus, the system can not be solved. The symmetry property of the ACF $\gamma_{-l} = \gamma_l$ is employed to address this issue. Therefore, the Equation (3.10) can be expressed as:

$$\begin{bmatrix} 1 & -\varphi_1 & -\varphi_2 & 0 & 0 & \ldots \\ -\varphi_1 & 1-\varphi_2 & 0 & 0 & 0 & \ldots \\ -\varphi_2 & -\varphi_1 & 1 & 0 & 0 & \ldots \\ 0 & -\varphi_2 & -\varphi_1 & 1 & 0 & \ldots \\ 0 & 0 & -\varphi_2 & -\varphi_1 & 1 & \ldots \\ & & \vdots & & & \ddots \end{bmatrix}_{(N+1)\times(N+1)} \begin{bmatrix} \gamma_0 \\ \gamma_1 \\ \gamma_2 \\ \gamma_3 \\ \vdots \\ \gamma_N \end{bmatrix}_{(N+1)\times 1} = \begin{bmatrix} \sigma^2 \\ 0 \\ 0 \\ 0 \\ \vdots \\ 0 \end{bmatrix}_{(N+1)\times 1} . \tag{3.11}$$

The ACF of the restricted AR model, represented in Equation (3.9), can also be expressed in a matrix format by employing the same procedures shown in Equations (3.10) and (3.11) and setting the non-selected terms to zero value, as shown in Equation (3.3).

In Figure 3.1, the ACF of a target obtained from the vK turbulence model (see Section 3.6) is shown. The ACF target is employed to acquire an AR(2) model using the general formulation detailed in Section 3.4. The theoretical AR ACF is computed using Equation (3.3) and is presented in Figure 3.1 together with the ACFs of 10 time series samples obtained from the AR(2) model.

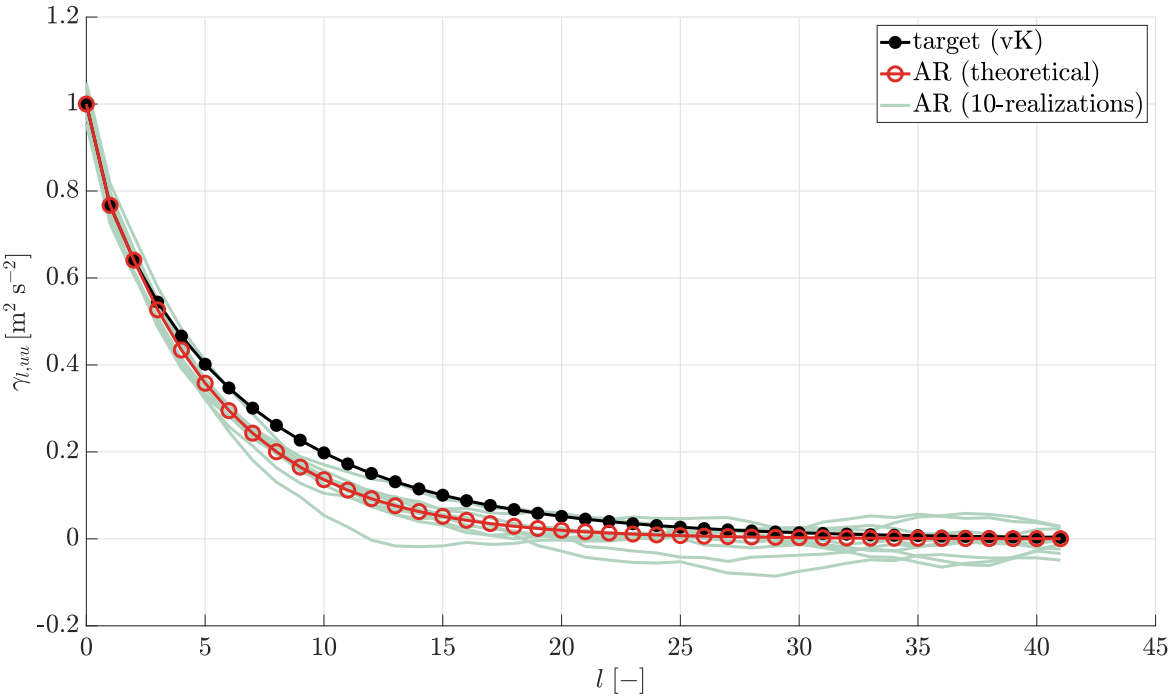

Figure 3.1: ACF, $\gamma_{l,uu}$, for a target computed from the vK turbulence model together with the corresponding theoretical ACF of an AR(2) model, obtained by employing the general formulation illustrated in Section 3.4, and the ACFs of 10 time series samples generated by the AR(2) model.

3.3 Theoretical auto-power spectral density, PSD, for an AR model

The PSD and the ACF are Fourier pairs, in accordance with the Wiener-Khintchine Theorem (Marple Jr & Carey, 2019). The PSD and the ACF share the same statistical information. The PSD represents the information in the frequency domain, while the ACF represents the information in the time domain. The PSD is, by definition, the power distribution of a signal as a function of frequency, f, or angular frequencies, ω. The PSD of a WSS-RP is a strictly real, positive function (Marple Jr & Carey, 2019). Additionally, the PSD of a real-valued WSS-RP presents Hermitian symmetry, thus $S(f) = S^*(-f)$. Furthermore, the variance of a RP can be determined from the one-sided PSD by utilizing the Fourier relation between the

ACF and the one-sided PSD as follows:

$$\gamma_l = F^{-1}[S(f)] = \int_0^\infty S(f)\exp(\mathrm{i}2\pi f l \Delta t)df, \tag{3.12}$$

by considering lag $l = 0$

$$\gamma_0 = \overline{u^2} = \int_0^\infty S(f)df. \tag{3.13}$$

The theoretical one-sided spectrum of the AR, $S^{\mathrm{AR}}(f)$, in terms of the frequency, f, is defined as (Marple Jr & Carey, 2019):

$$S^{\mathrm{AR}}(f) = \frac{1}{f_{\max}} \frac{\sigma^2}{|1 - \sum_{n=1}^{p} \varphi_n \exp(-\mathrm{i}n\frac{\pi f}{f_{\max}})|^2} \quad , \quad 0 \leq f \leq f_{\max}, \tag{3.14}$$

where the maximum frequency $f_{\max} = 1/\Delta t$. Note that the S^{AR} can be defined in various domains by applying the concept of changing an independent variable while preserving the integral of the function (see Appendix 1). The general form of the theoretical one-sided AR spectrum in terms of x-domain is defined as:

$$S^{\mathrm{AR}}(x) = C_{\mathrm{AR}} \frac{\sigma^2}{|1 - \sum_{n=1}^{p} \varphi_n \exp(-\mathrm{i}\, n\, g(x))|^2}, \quad x_a \leq x \leq x_b, \tag{3.15}$$

where x_a and x_b are the lower and upper limits of the independent variable range, respectively, the value of C_{AR} and $g(x)$ is defined in Table 3.1 for various domains (frequency, angular frequency or wavenumber magnitude).

$S^{\mathrm{AR}}(x)$	x	C_{AR}	$g(x)$	x_a	x_b
$S^{\mathrm{AR}}(f)$	f	$\frac{1}{f_{\max}}$	$\frac{\pi f}{f_{\max}}$	0	$f_{\max}$
$S^{\mathrm{AR}}(\omega)$	ω	$\frac{1}{\omega_{\max}}$	$\frac{\pi \omega}{\omega_{\max}}$	0	$\omega_{\max}$
$S^{\mathrm{AR}}(k)$	k	$\frac{1}{k_{\max}}$	$\frac{\pi k}{k_{\max}}$	0	$k_{\max}$

Table 3.1: Coefficients table for the general form of the AR spectrum equation (3.15), where f [Hz] is the frequency, ω [rad/s] is the angular frequency and k [rad/m] is the magnitude of the wavenumber.

3.4 Computation of AR model parameters from a target ACF

The general steps for computing the AR model parameters from a predefined ACF are illustrated in this section. Additionally, the state-of-the-art approaches are presented.

3.4.1 General steps for the evaluation of the AR model parameters from a predefined target ACF using the covariance equations

This section illustrates the computation of the parameters of unrestricted/restricted AR(p) model from a target ACF. The evaluation of the parameters of unrestricted/restricted an AR(p) model, through a predefined target ACF, is done by utilizing the relationship between the ACF and the parameters of the unrestricted/restricted AR(p) model, as shown in Equations (3.8) and (3.9). The evaluation of the parameters of an unrestricted/restricted AR(p) model, using given values of the predefined target ACF, can be described using a general formulation. The evaluation procedure can be divided into two steps as follows:

- The first step is to evaluate the N regression coefficients a_{j_i} of an AR(p) model with vector $\mathbf{j} = [j_1, j_2, \ldots, j_N]$. To compute the N regression coefficients a_{j_i}, N equations of the ACF are selected based on considering a set of selected lags identified in vector $\mathbf{l} = [l_1, \ldots, l_N]$, where $l_i > 0$ and $i = 1, \ldots, N$.
- After computing the regression coefficients, the second step is calculating the noise coefficient b, by employing the ACF equation for lag $l = 0$.

Each step is elaborated in detail in the subsequent sections for the restricted AR model case, where the general steps for the unrestricted model is a particular case of the restricted AR model where $\mathbf{j} = [1, \ldots, p]$.

First step: determination of the model coefficients a_{j_n}

The selected lags vector $\mathbf{l} = [l_1, l_2, \ldots, l_N]$ is used to obtain N equations for the ACF, as presented in Equation (3.9) to evaluate the N regression coefficient a_{j_i}. This set of equations can be presented in a matrix form as follows:

$$\begin{bmatrix} a_{j_1} \\ a_{j_2} \\ \vdots \\ a_{j_N} \end{bmatrix}^T_{1\times N} \begin{bmatrix} \gamma_{l_1-j_1} & \gamma_{l_2-j_1} & \cdots & \gamma_{l_N-j_1} \\ \gamma_{l_1-j_2} & \gamma_{l_2-j_2} & \cdots & \gamma_{l_N-j_2} \\ \vdots & \vdots & \ddots & \vdots \\ \gamma_{l_1-j_N} & \gamma_{l_2-j_N} & \cdots & \gamma_{l_N-j_N} \end{bmatrix}_{N\times N} = \begin{bmatrix} \gamma_{l_1} \\ \gamma_{l_2} \\ \vdots \\ \gamma_{l_N} \end{bmatrix}^T_{1\times N}, \tag{3.16}$$

or, in a more compact way:

$$\mathbf{a}\boldsymbol{\gamma}_{\mathbf{j},\mathbf{l}} = \boldsymbol{\gamma}_{\mathbf{l}}, \tag{3.17}$$

where $\mathbf{a}$ represents the AR model coefficients, and both $\boldsymbol{\gamma}_{\mathbf{l}}$ and $\boldsymbol{\gamma}_{\mathbf{j},\mathbf{l}}$ contains the values of the target ACF at specific lags. By utilizing Equation (3.17), the regression coefficients of an AR model can be evaluated as $\mathbf{a} = \boldsymbol{\gamma}_{\mathbf{l}}\boldsymbol{\gamma}_{\mathbf{j},\mathbf{l}}^{-1}$. It is worth mentioning that to guarantee a solution for determining the regression coefficients of the AR model, the inverse of $\boldsymbol{\gamma}_{\mathbf{j},\mathbf{l}}$ matrix is required to exist. Careful consideration should be taken with issues related to ill-conditioned matrices that may arise from some target ACF (Gallego-Castillo et al., 2022).

Second step: Determination of the noise coefficient b

The next step after calculating the regression coefficients of the AR(p) model is to evaluate the noise coefficient, b. The noise coefficient is computed using the ACF at lag $l = 0$ shown in Equation (3.9), which can be represented in a matrix form as follows:

$$\gamma_0 = \begin{bmatrix} a_{j_1} & a_{j_2} & \dots & a_{j_N} \end{bmatrix}_{1\times N} \begin{bmatrix} \gamma_{-j_1} \\ \gamma_{-j_2} \\ \dots \\ \gamma_{-j_N} \end{bmatrix}_{N\times 1} + b^2, \tag{3.18}$$

by applying the symmetry property of the ACF ($\gamma_{-l} = \gamma_l$), the noise coefficient is determined as:

$$b^2 = \gamma_0 - \begin{bmatrix} a_{j_1} & a_{j_2} & \dots & a_{j_N} \end{bmatrix} \begin{bmatrix} \gamma_{j_1} \\ \gamma_{j_2} \\ \dots \\ \gamma_{j_N} \end{bmatrix}, \tag{3.19}$$

or, in a more compact format:

$$b^2 = \gamma_0 - \mathbf{a}\boldsymbol{\gamma}_\mathbf{j}. \tag{3.20}$$

Similarly to $\boldsymbol{\gamma}_\mathbf{l}$ and $\boldsymbol{\gamma}_{\mathbf{j},\mathbf{l}}$, the values of the $\boldsymbol{\gamma}_\mathbf{j}$ vector are obtained from the target ACF at the lags defined by $\mathbf{j}$ vector.

3.4.2 State-of-the-art approaches for the evaluation of the AR model parameters from a target ACF

In the previous section 3.4.1, the general formulation for computing the parameters of an AR model was presented. As discussed there, the calculation of the parameters is dependent on the selected $\mathbf{j}$ and $\mathbf{l}$ vectors, as shown in Equations (3.17) and (3.20). This section illustrates the state-of-the-art approaches for selecting both $\mathbf{j}$ and $\mathbf{l}$ vectors. Moreover, the merits and drawbacks of each approach are discussed.

The vast majority of the works apply the Yule-Walker (Y-W) approach (P. D. Spanos & Hansen, 1981; Reed & Scanlan, 1983; P. D. Spanos, 1983; Samaras et al., 1985) to calibrate the parameters of an AR model. The Y-W approach includes the initial p regression coefficients of an AR(p) model (unrestricted AR model); thus, the selected $\mathbf{j} = [1, 2, \dots, p]$. Additionally, the Y-W approach utilizes the relationships between the parameters of the AR model and its ACF, shown in Equation (3.9), from lag $l = 0$ to lag $l = p$, to evaluate the parameters of the AR(p) model. This implies that the $\mathbf{l}$ vector equals the $\mathbf{j}$ vector. This approach leads to an exact match of the target ACF until lag $l = p$ (Gallego-Castillo et al., 2022). However, matching the target ACF at lags higher than p is uncontrollable. To match the values of the ACF for a sufficiently wide lag interval, the model order p must be increased, which leads to an increase in the computational cost of the calibration. Moreover, this will require more parameters to be stored, which will reduce the model parsimony[1] (Box et al., 2016).

[1]Model parsimony refers to the attainment of a specific level of model performance with the lowest number of model parameters.

A recent approach proposed by (Krenk & Møller, 2019) (K-M) suggests selecting regression coefficients only for lags equal to $2^n, n = 0, 1, 2, \ldots, N$ (exponential model scheme); therefore, $\mathbf{j} = [1, 2, 4 \ldots, 2^N]$. As for the Y-W approach, the K-M approach restricts $\mathbf{l}$ vector to be equal to the $\mathbf{j}$ vector. This approach improves the capability of an AR model to fit the theoretical ACF to the target ACF for a wide interval of lags, without requiring a high number of model parameters, which improves the model parsimony. Consequently, contrary to the Y-W approach, this leads to fewer model parameters being evaluated and stored.

Based on previous research, (Gallego-Castillo et al., 2022) (CG) analyzed in more depth the contribution of restricted AR models for reproducing a target ACF and introduced an optimal approach to determine the vectors $\mathbf{j}$ and $\mathbf{l}$, based on genetic algorithm. The methodology combines the general formulation described in Equations (3.17) and (3.20) with the use of genetic algorithms. The aim is to find, for a given number of regression coefficients N, optimal vectors $\mathbf{j} = [j_1, j_2, \ldots, j_N]$ and $\mathbf{l} = [l_1, l_2, \ldots, l_N]$. Thus, relaxing the assumption $\mathbf{j} = \mathbf{l}$, in this context, optimal means that the obtained AR model provides minimum Mean Square Error (MSE) between its theoretical ACF, γ_l^{AR}, and the target ACF, γ_l^{t} (the superscript $(\cdot)^{\mathrm{t}}$ refers to target). In this approach, the minimization problem, for M lags in the γ_l^{t}, is defined as:

$$\min\left[\mathrm{MSE}\right] = \min\left[\frac{1}{M}\sum_{l=0}^{M}\left(\gamma_l^{\mathrm{t}} - \gamma_l^{\mathrm{AR}}\right)^2\right], \tag{3.21}$$

which subject to the inequality constraints $0 < j_1 < j_2 < \ldots < j_N$, with $j_i \in \mathbb{N}$, for $i = 1, \ldots, N$ and $0 < l_1 < l_2 < \ldots < l_N$, with $l_i \in \mathbb{N}$, for $i = 1, \ldots, N$. This approach leads to better fits to the target ACF than the Y-W and K-M approaches since it searches for the optimal $\mathbf{j}$ and $\mathbf{l}$ vectors. Additionally, this approach relaxes the constraint $\mathbf{j} = \mathbf{l}$, thus exploring the potential improvements arising from this constraint. However, a higher computational cost is required for this approach due to the optimization process.

3.5 Computation of AR model parameters from a target PSD

This section illustrates the evaluation of the AR model parameters from a target spectrum. All the previously cited approaches are based on fitting a predefined ACF (see Section 3.4); thus, a better fit is obtained between the theoretical ACF and the target ACF, compared to the theoretical PSD and the target PSD (the Fourier pair of the ACF). These approaches require previous discretization of such target ACF, which could introduce aliasing in the reproduced AR PSD (see Appendix 2) if the discretization is not fine enough, as discussed by (Gallego-Castillo et al., 2022). Furthermore, pre-processing would be needed as a previous step, when advanced turbulence models originally described in the frequency domain are utilized to obtain the target ACF. To avoid the issues of using the information in the time domain as a target, (M. Mignolet & Spanos, 1987) proposed an approach to directly fit information in the frequency domain through an optimization process by directly controlling the AR model parameters. However, this approach may lead to obtaining non-stationary AR models. This section presents an approach for calibrating the parameters of an AR model

directly from a predefined target PSD. A methodology is proposed utilizing the relation between the poles of the AR model and the AR spectrum to fit a target spectrum, where the stationarity of the model is ensured by constraining the location of the poles. This approach is referred to as Pole-Placement Approach (PPA) (Lyons, 2010; Phillips et al., 2015).

3.5.1 Reproducing a target PSD through the pole-placement approach

The time series $\{u_t\}$ can be seen as the output to a linear filter with white noise ε_t as the input (Takalo et al., 2005), as shown in Figure 3.2. The transfer function $H(\mathrm{z})$ is the ratio between the z−transform of the output sequence $Y(\mathrm{z})$ and the z−transform of the input sequence $X(\mathrm{z})$. The transfer function $H(\mathrm{z})$ is obtained by applying the z−transform to Equation (3.1) to get the following:

$$A(\mathrm{z})Y(\mathrm{z}) = B(\mathrm{z})X(\mathrm{z}),$$

where $A(\mathrm{z}) = 1 - \varphi_1 \mathrm{z}^{-1} - \cdots - \varphi_p \mathrm{z}^{-p}$ and $B(\mathrm{z}) = 1$. Thus, for an AR process, the transfer function $H(\mathrm{z})$ is defined as follows (Marple Jr & Carey, 2019):

$$H(\mathrm{z}) = \frac{Y(\mathrm{z})}{X(\mathrm{z})} = \frac{B(\mathrm{z})}{A(\mathrm{z})} = \frac{1}{1 - \varphi_1 \mathrm{z}^{-1} - \cdots - \varphi_p \mathrm{z}^{-p}}. \tag{3.22}$$

The transfer function $H(\mathrm{z})$ can be presented on a complex plane, as shown in Figure 3.3, where the vertical axis is the imaginary axis and the horizontal axis is the real axis. This representation is useful because the location of poles and zeros to a unit circle, $\mathrm{z} = e^{i\theta}$, in z−domain, define some relevant features in the PSD, such as the local maxima. The poles are the roots of the denominator of the transfer function, $A(\mathrm{z})$, and the zeros are the roots of the numerator of the transfer function, $B(\mathrm{z})$. Considering Equation (3.22) is evident that the AR model is an all-pole model with no zeros. The characteristic equation, $A(\mathrm{z}) = 0$, is

$$1 - \varphi_1 \mathrm{z}^{-1} - \cdots - \varphi_p \mathrm{z}^{-p} = 0, \tag{3.23}$$

which can be factorized as follows:

$$(1 - G_1 \mathrm{z}^{-1})(1 - G_2 \mathrm{z}^{-1}) \ldots (1 - G_p \mathrm{z}^{-1}) = 0, \tag{3.24}$$

where $G_1, \ldots, G_p$ are the poles of the AR model, and the roots of the characteristic equation are $G_1^{-1}, \ldots, G_p^{-1}$. Equations (3.23) and (3.24) represent the relationship between the regression coefficients of the AR model, φ_j, and the poles of the AR model, G_j. Thus, the regression coefficients can be obtained by placing the poles. For a stationary AR model, the modulus of every pole of the AR model has to be less than 1 ($|G_j| < 1, j = 1, \ldots, p$) or the roots of the characteristic equation have to be greater than one ($|G_j^{-1}| > 1, j = 1, \ldots, p$). The poles of an AR process can be real poles P^r or/and complex conjugate poles P^c. The real poles are located on the real axis in the interval [-1,1] and the complex poles P^c are defined by a radial location $r_{_P}$ within the interval $[0, 1]$ and a phase angle θ_P within the interval $[0, \pm\pi]$, where $P^c = r_{_P} e^{i\theta_P}$. Moreover, the locations of the poles of the AR model to the unit circle affect the shape of the peaks of the AR spectrum (Chao, 1984).

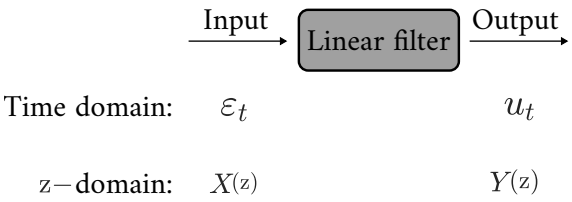

Figure 3.2: Representation of the time series u_t as the output of a linear filter when the input is the white noise ε_t.

From Table 3.1 and Equation (3.15), the one-sided AR spectrum $S^{\mathrm{AR}}(k)$ in terms of wavenumber k (Box et al., 2016) is written as:

$$S^{\mathrm{AR}}(k) = \frac{1}{k_{\max}} \frac{\sigma^2}{\left|1 - \sum_{j=1}^{p} \varphi_j \exp(-\mathrm{i}j\pi \frac{k}{k_{\max}})\right|^2}, \quad 0 \le k \le k_{\max}, \tag{3.25}$$

where $k_{\max}$ is the maximum wavenumber, $k_{\max} = \pi/(U\Delta t) = \pi/\Delta x$, U is the mean velocity and Δx is the spatial step. Note that the TFTH is assumed to relate the wavenumber to the frequency as $k = 2\pi f/U$ (see Section 2.1.3). The definition of non-dimensional one-sided AR spectrum $\mathring{S}^{\mathrm{AR}}(\mathring{k}) = S^{\mathrm{AR}}(k)/(L\sigma_c^2)$, where L is a length scale, in terms of non-dimensional wavenumber $\mathring{k} = kL$ is:

$$\mathring{S}^{\mathrm{AR}}(\mathring{k}) = \frac{1}{\mathring{k}_{\max}} \frac{\sigma^2/\sigma_c^2}{\left|1 - \sum_{j=1}^{p} \varphi_j \exp(-ij\pi \frac{\mathring{k}}{\mathring{k}_{\max}})\right|^2}, \quad 0 \le \mathring{k} \le \mathring{k}_{\max}, \tag{3.26}$$

where $\mathring{k}_{\max}$ is the non-dimensional maximum wavenumber and σ_c^2 is a characteristic variance, which is selected to be equal to the ACF of the AR model for time lag $l = 0$, γ_0^{AR}, that is the variance of the process. Subsequently, $\int_0^\infty \mathring{S}^{AR}(\mathring{k})d\mathring{k} = 1$ and since γ_0^{AR} is proportional to σ^2 (Box et al., 2016), therefore, in Equation (3.26), the parameters which are required to be determined are only the regression coefficients φ_j.

The effect of changing the phase angle θ_P of the complex poles on the theoretical spectrum of an AR(2) model is shown in Figure 3.3 as an example. Three cases, with different complex conjugate poles P_1^c, P_2^c and P_3^c for each case, were considered. The complex conjugate poles P_1^c, P_2^c and P_3^c have values $0.8e^{\pm i\pi/9}, 0.8e^{\pm i2\pi/9}$ and $0.8e^{\pm i\pi/3}$ respectively. The regression coefficients φ_j obtained for each case, are evaluated using equations (3.23) and (3.24). Finally, the regression coefficients φ_j obtained from each case are utilized to evaluate the AR spectra $\mathring{S}_1^{\mathrm{AR}}, \mathring{S}_2^{\mathrm{AR}}$ and $\mathring{S}_3^{\mathrm{AR}}$ using Equation (3.26). As shown in Figure 3.3, by increasing the phase angle, the peak of the AR spectrum $\mathring{S}^{\mathrm{AR}}$ is shifted from low to higher frequencies. Moreover, the effect of the changing radial location on the theoretical spectrum of the AR(2) model was considered. AR spectra, $\mathring{S}_4^{\mathrm{AR}}, \mathring{S}_5^{\mathrm{AR}}$ and $\mathring{S}_6^{\mathrm{AR}}$ were obtained from three different complex poles P_4^c, P_5^c and P_6^c with values $0.7e^{\pm i\pi/4}, 0.8e^{\pm i\pi/4}$and $0.9e^{\pm i\pi/4}$ respectively. As shown in Figure 3.4, changing the radial location of the poles changes the amplitude of the peak obtained in the AR spectrum. As the pole gets closer to the unit circle, it will lead to a rise and sharpening of the peak in the AR spectrum. Ultimately, increasing the number of poles N

leads to increasing the number of peaks of the AR spectrum $\mathring{S}_7^{\mathrm{AR}}$. For a AR(3) model, with one real pole $P_7^r = -0.8$ and two complex conjugate poles $P_7^c = 0.8e^{\pm i\pi/3}$, two peaks were obtained, as depicted in Figure 3.5. Due to the complex conjugate poles, the first peak is at $\mathring{k} \approx 8$. The second peak is at $\mathring{k}_{\max}$ due to the negative real pole, as a positive real pole leads to a peak in the AR spectrum at $\mathring{k} = 0$ and a negative real pole leads to a peak in the AR spectrum at $\mathring{k}_{\max}$.

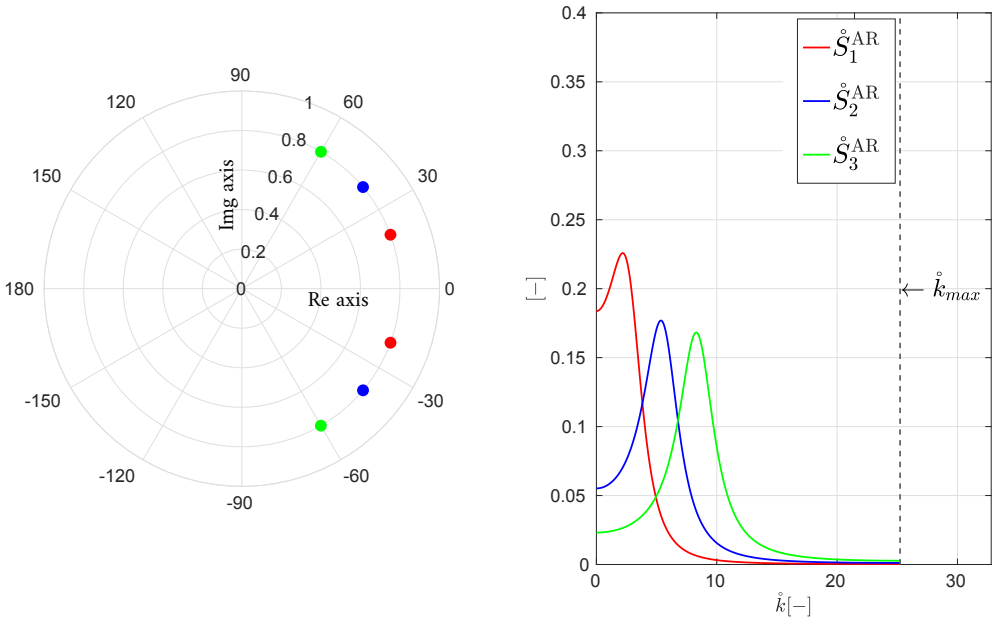

Figure 3.3: Non-dimensional one-sided AR spectrum of the AR(2) models, $\mathring{S}_i^{\mathrm{AR}}(\mathring{k})$ for $i = 1, 2, 3$, obtained from three different poles, P_i^c, with a fixed radial location $r_{_P}$.

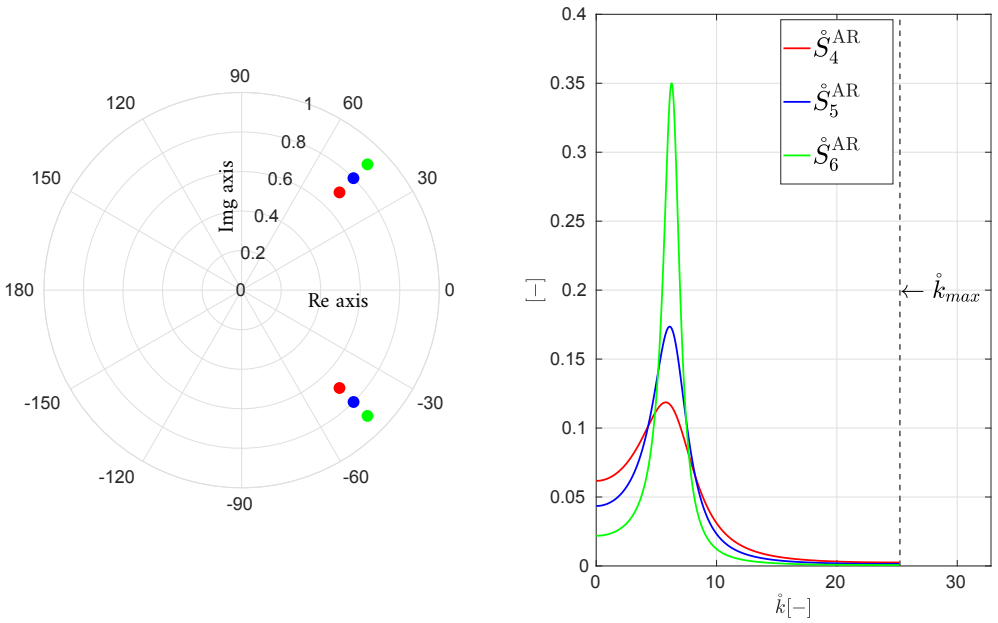

Figure 3.4: Non-dimensional one-sided AR spectrum of the AR(2) models, $\mathring{S}_i^{\mathrm{AR}}(\mathring{k})$ for $i = 4, 5, 6$, obtained from three different poles, P_i^c with a fixed phase angle θ_P.

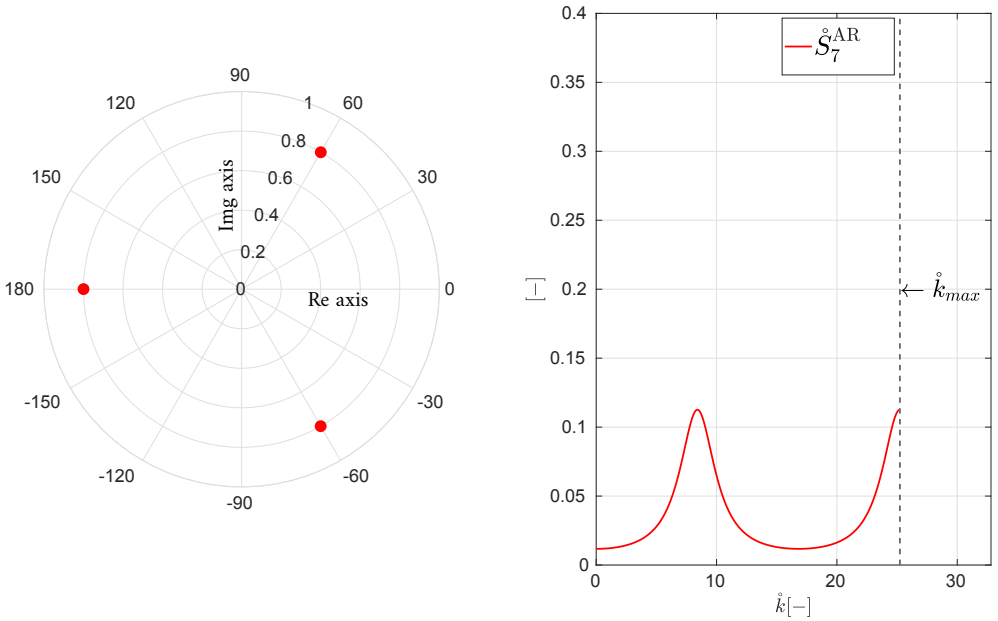

Figure 3.5: Non-dimensional one-sided AR spectrum of the AR(3) model $\mathring{S}_7^{\mathrm{AR}}(\mathring{k})$ with a real pole P_7^r and complex conjugate poles P_7^c.

3.5.2 Problem definition

The proposed approach uses PPA to optimally fit the AR spectrum to a predefined target spectrum. The relationship between the poles and the regression coefficients is employed to compute the regression coefficients, as represented in Equations (3.23) and (3.24). The poles of the AR model are obtained through an optimization process to get the optimal poles for the AR(p) model, where optimal poles mean that the obtained AR spectrum from the poles provides minimum error. The error criterion employed is based on MSE, as in (Gallego-Castillo et al., 2022), and it is defined as follows:

$$\text{MSE} = \frac{1}{M}\sum_{n=0}^{M} e_n^2, \tag{3.27}$$

where the score function $e_n = \mathring{k}_n \mathring{S}^{\text{t}}(\mathring{k}_n) - \mathring{k}_n \mathring{S}^{\text{AR}}(\mathring{k}_n)$. The MSE between the target and AR spectrum was evaluated at M points in the interval $\mathring{k} = [0, \mathring{k}_{\text{max}}]$. The inequality constraints $-1 \leq P^r \leq 1$, $0 \leq \theta_P \leq \pi$ and $0 \leq r_{_P} \leq 1$, were defined in the optimization problem, where these constraints are required to ensure the stationarity of the AR model. The optimization is performed by using the interior-point method. It is worth mentioning that when fitting a predefined target spectrum in the dimensional form instead of the non-dimensional form, an additional step is required to compute the noise coefficient σ for the AR model.

3.6 Case study: application to von Karman turbulence model

The stationary-homogeneous-isotropic vK turbulence model was employed to obtain the target spectrum (Von Karman, 1948) and its Fourier pair, the target ACF (Krenk & Møller, 2019). The acquired target spectrum was used for the proposed approach, whilst the obtained target ACF was utilized for the ACF-based approaches described in Section 3.4.2.

The ACF of a longitudinal wind velocity, which is statistically stationary, homogeneous and isotropic, between two spatial points separated by a longitudinal distance r [m] is defined as (Wyngaard, 2010):

$$\gamma(r) = \text{E}[u(x+r)u(x)] = \overline{u^2} f(r), \tag{3.28}$$

where $\overline{u^2}$ [m^2 s^{-2}] is the isotropic variance (which is the same for the three velocity components) and the non-dimensional longitudinal correlation function, $f(r)$, is evaluated through the Fourier transform of the one-dimensional spectrum of the longitudinal velocity component, defined in term of the wavenumber, $F(k)$,

$$\overline{u^2} f(r) = \int_{-\infty}^{\infty} F(k)\exp(\text{i}kr)dk. \tag{3.29}$$

By utilizing the generalized form of the vK one-dimensional spectrum, F^{vK}, defined as (Krenk, 1996)

$$F^{\text{vK}}(k) = \frac{1}{\sqrt{\pi}}\frac{\Gamma(\gamma)}{\Gamma(\gamma - 1/2)}\frac{\overline{u^2}L}{[1+(kL)^2]^{\gamma}}, \tag{3.30}$$

in Equation (3.29), therefore, the analytical expression of the non-dimensional longitudinal correlation function $f(r)$ is defined as (Krenk & Møller, 2019):

$$f(r) = \frac{2}{\Gamma(\gamma - 1/2)} \left(\frac{r}{2L}\right)^{\gamma-1/2} K_{\gamma-1/2}\left(\frac{r}{L}\right), \tag{3.31}$$

where L [m] is the length scale of the vK spectral velocity tensor, $\Gamma(\cdot)$ is the Gamma function, $K_n(\cdot)$ is the modified Bessel function of the second kind of order n and $\gamma = 5/6$ as utilized in the F^{vK} (Von Karman, 1948). The non-dimensional vK ACF, $\mathring{\gamma}^{\text{vK}}(\mathring{r})$, for the longitudinal wind velocity components in terms of the non-dimensional separation $\mathring{r} = r/L$ is expressed as:

$$\mathring{\gamma}^{\text{vK}}(\mathring{r}) = \overline{u^2}^{-1}\gamma(r = \mathring{r}L) = \frac{2}{\Gamma(\gamma - 1/2)} \left(\frac{\mathring{r}}{2}\right)^{\gamma-1/2} K_{\gamma-1/2}(\mathring{r}), \tag{3.32}$$

The target ACF, γ_l^{t}, in terms of the time lag l is evaluated by utilizing the discrete values from $\mathring{\gamma}^{\text{vK}}(\mathring{r})$ for a given $\Delta\mathring{r}$ (note that the TFTH is assumed):

$$\gamma_l^{\text{t}} = \mathring{\gamma}^{\text{vK}}(l\Delta\mathring{r}), \text{ where } l = 0, 1, \ldots, \tag{3.33}$$

where the considered value for $\Delta\mathring{r}$, in the presented case study, is equal to 0.1245.

The non-dimensional one-sided vK spectrum $\mathring{S}^{\text{vK}}(\mathring{k})$ in terms of non-dimensional wavenumber $\mathring{k}$ (Wyngaard, 2010) is given by:

$$\mathring{S}^{\text{vK}}(\mathring{k}) = C_1 \frac{1}{[(\mathring{k})^2 + 1]^{m-2}}, \quad \mathring{k} \in [0, \infty), \tag{3.34}$$

where $C_1 = 3C_{\text{vK}}/2(m-2)(m-1)$ and $C_{\text{vK}} = \Gamma(m)/\Gamma(5/2)\Gamma(m-5/2)$. The parameter m takes the value $17/6$, and $\gamma = m - 2$. For the sake of comparison to (Gallego-Castillo et al., 2022), $\mathring{k}_{\text{max}}$ is selected to be $\pi/0.1245$. The MSE is evaluated at $M = 1000$ points over the non-dimensional wavenumber interval $[0, \mathring{k}_{max}]$. Based on the discussion presented in (Elagamy et al., 2021b), the area of the AR spectrum is imposed to be smaller than one, in particular, equal to the area of the target spectrum corresponding to the interval $[0, k_{max}]$ to prevent the appearance of spurious peaks at high wavenumbers. In this case, this means imposing the AR variance $\sigma^2 = 0.9171$. Moreover, different combinations of real and complex conjugate poles are tested to obtain the combination of poles, that gives the least MSE for each N case.

3.7 Results and discussion

In Figure 3.6, the *MSE* is plotted for the ACF and the PSD, referred to as E_γ and E_S, respectively, obtained for cases $N = 1, 2, \ldots, 10$ for Y-W, PPA, K-M and CG approaches. As expected, the E_γ value for ACF-based approaches decreases with increasing N. However, for the K-M approach, the E_γ is almost constant for $N \geq 5$. This is due to the fact that including a regression term for lag $l = 2^5 = 32$ yields minimal enhancement in the AR model's

fitting to a target ACF that closely approximates zero for such lag values. For $N > 2$, the CG approach exhibits a lower value of the E_γ error compared to the ACF-based (Y-W and K-M) approaches and the PPA. This demonstrates that searching for optimal AR models that fit a predefined ACF leads to better matching to the target ACF. Whereas the PPA shows the least E_S error value, which decreases further with increasing N in comparison with the other approaches.

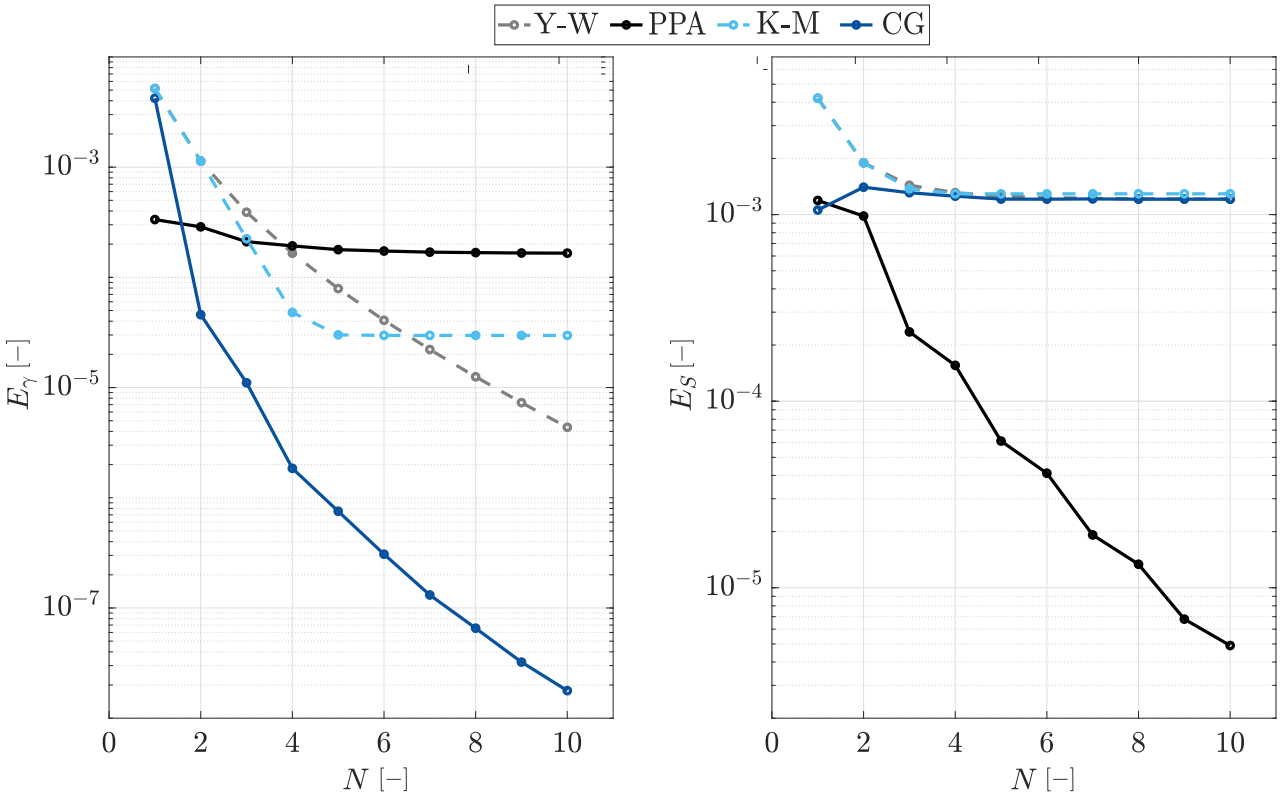

Figure 3.6: ACF error E_γ (left) and PSD error E_S (right), as a function of the number of regression terms of the AR model, N, for the introduced methods (see text for details).

The $\mathbf{j}$ and $\mathbf{l}$ vectors, selected through the CG approach, are shown in Figure 3.7 together with the corresponding $\mathbf{j}$ and $\mathbf{l}$ vectors from the Y-W and K-M approaches. It was observed that the optimal $\mathbf{j}$ and $\mathbf{l}$ vectors exhibit a form consistent with a power function, a^n. However, the observed form did not conform to the power function 2^n, for $n = 0, \ldots, N-1$, as proposed by the K-M approach (Krenk & Møller, 2019). Additionally, it was observed that $\mathbf{j} \neq \mathbf{l}$ for the optimal models, since relaxing $\mathbf{j} = \mathbf{l}$ assumption allows the optimization process to explore additional improvements related to the optimal selection of the covariance equations utilized in the computation of the AR model parameters.

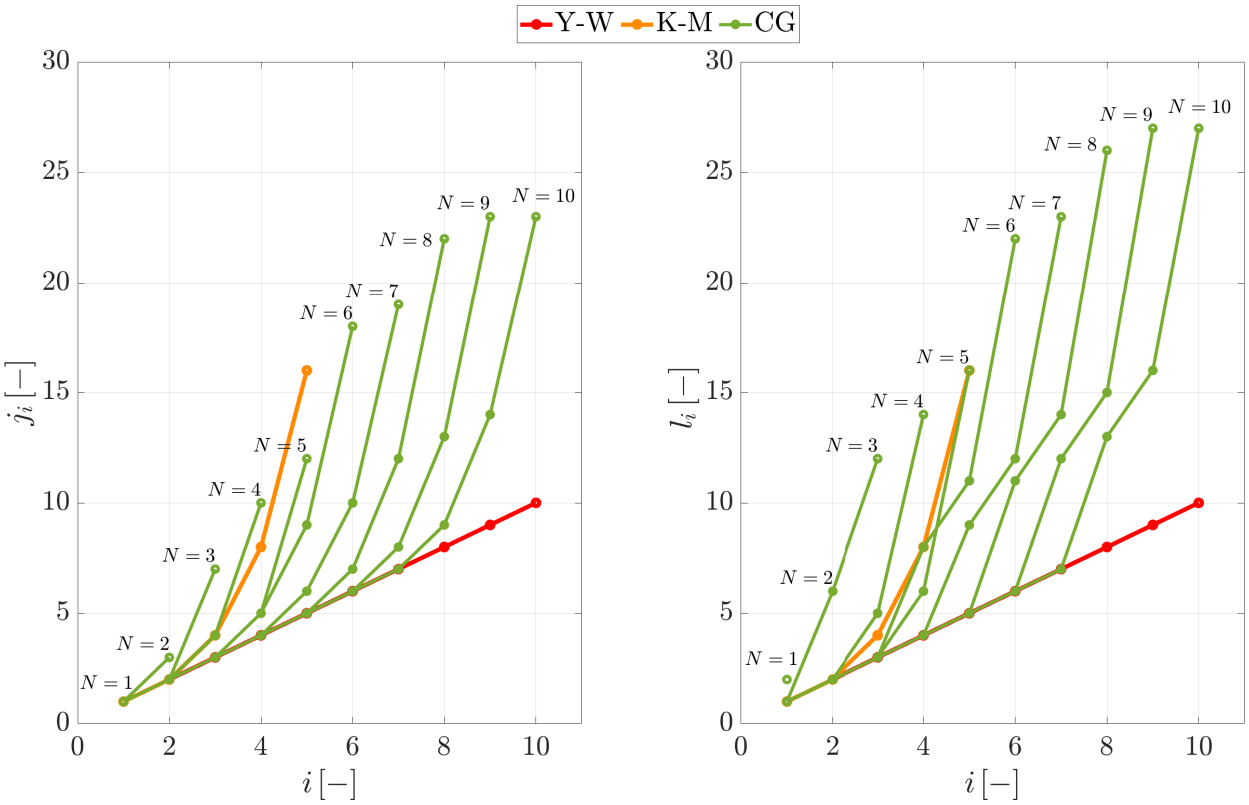

Figure 3.7: **j** and **l** vectors for the Y-W, K-M and CG approaches as a function of the number of regression terms of the AR model, N.

The combination of the real and complex conjugates poles, which gave the least MSE for each N case, is shown in Figure 3.8. It was observed that for even N case, the number of real poles N_{Pr} is 2, and the real poles take positive and negative values. For the odd N case, the number of real poles N_{Pr} is 1 and the real pole takes a positive value, and the number of complex poles $N_{Pc} = N - N_{Pr}$.

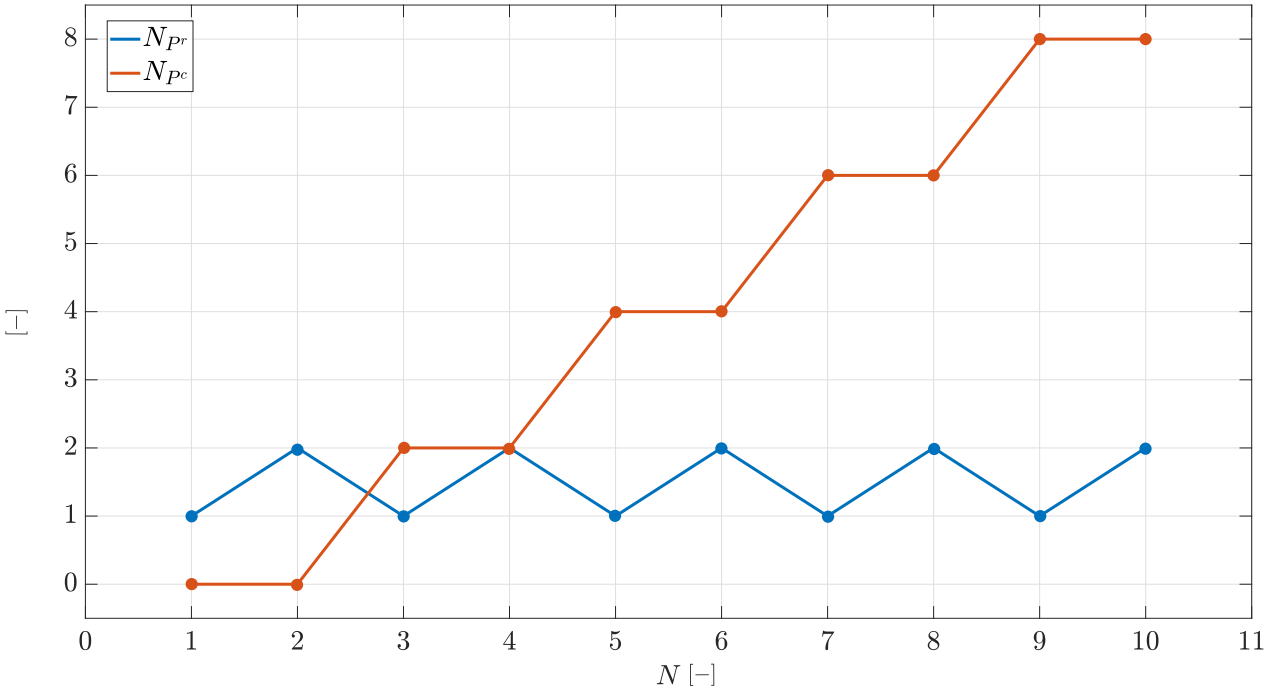

Figure 3.8: Optimal poles combination for different N cases.

The normalized AR spectrum obtained by using PPA, for case $N = 6$, is shown in Figure 3.9 together with the AR spectrum obtained by utilizing the CG approach (Gallego-Castillo et al., 2022) and the target spectrum. The AR spectrum from PPA shows a good fit to the target spectrum within the wavenumber interval $\mathring{k} = [\mathring{0}, \mathring{k}_{\max}]$, while the AR spectrum from the CG approach shows the aliasing effect due to discretization of the target ACF (Gallego-Castillo et al., 2022) (see Appendix 2). The non-dimensional ACF from the PPA does not match the target ACF at lag $l = 0$, due to the aforementioned constraint on the AR spectrum area (Elagamy et al., 2021b), as shown in Figure 3.10. Conversely, the non-dimensional ACF from the CG approach shows a perfect match to the non-dimensional target ACF.

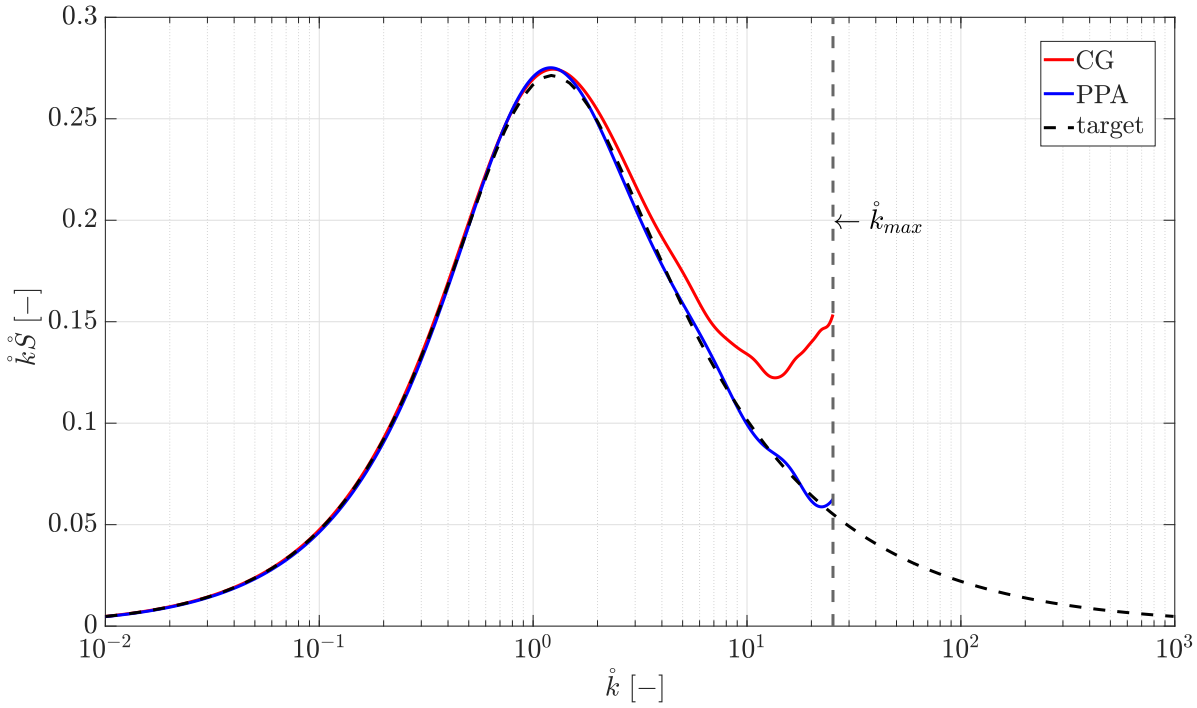

Figure 3.9: Normalized one-sided target spectrum, $\mathring{k}\mathring{S}^{\mathrm{t}}(\mathring{k})$, together with the corresponding theoretical spectrum of the AR models obtained by using the PPA, for reduced variance (0.9171) and by using the CG approach (Gallego-Castillo et al., 2022). Case $N = 6$.

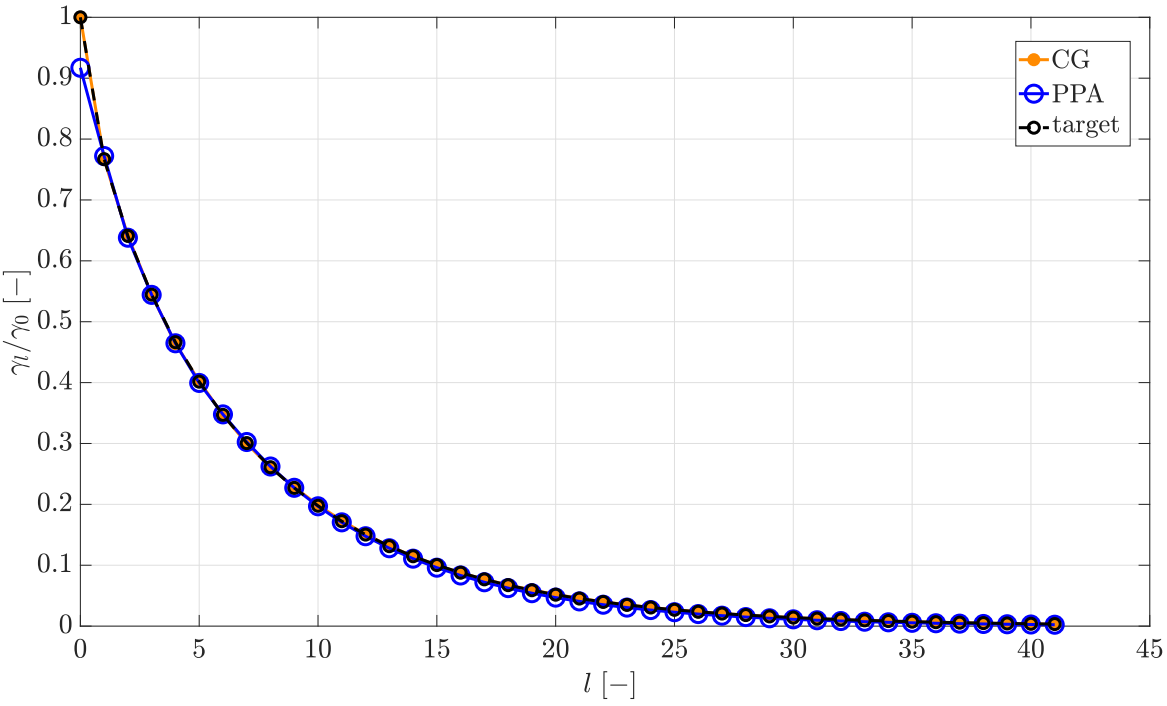

Figure 3.10: Non-dimensional target ACF, γ_l/γ_0, together with the theoretical ACF of the AR models obtained by using the PPA, for reduced variance (0.9171) and by using the CG approach (Gallego-Castillo et al., 2022). Case $N = 6$.

3.8 Conclusions

A comparison between two approaches related to the determination of the coefficients of AR models for the synthetic generation of turbulence has been presented. One approach consists of fitting a target PSD, for which a pole-placement based method was analyzed. The other approach consists of fitting a target ACF, for which a methodology presented by the author and his colleagues in previous research was employed. As a case study, the vK turbulence model was used to obtain the target ACF and the target PSD for each approach. While the ACF and the PSD function represent the same underlying statistical information in either time or frequency domains (they are Fourier pairs), it was found that the choice of the target function (PSD or ACF) to be reproduced by an AR model has implications in the reproduced statistical features. In particular, on the one hand, fitting a target ACF with an AR model requires previous discretization of such target function, which could introduce aliasing in the spectrum reproduced by the obtained AR model if the discretization is not fine enough, as shown in previous research (Gallego-Castillo et al., 2022). On the other hand, fitting a target PSD function with an AR model can only be done in a range of frequencies, in this work defined by the wavenumber interval $\mathring{k} \in [0, \mathring{k}_{\max}]$. This means that the contribution of the PSD to the target variance corresponding to frequencies $\mathring{k} > \mathring{k}_{\max}$ cannot be accounted for by the AR model while optimally fitting the PSD in the range $\mathring{k} \in [0, \mathring{k}_{\max}]$. Consequently, the

AR model only reproduces a fraction of the target variance. The described limitations of both approaches decrease as the sampling time decreases (i.e., the maximum frequency increases), making both approaches virtually similar in terms of reproduced statistical features. However, this parameter is usually constrained in practice due to measurement equipment resolution or computational simulation cost. Thus, the implications described in this work provide a basis for discussing which approach would be more convenient to employ, depending on the application of the generated wind field.

The comparison shows that the choice of fitting either the ACF or the PSD has diverse implications that need to be considered when selecting the approach. These implications are summarized in Table 3.2.

Approach	Advantages	Disadvantages
ACF-based	• The fitting of the target ACF can be asymptotically improved (by increasing the number of model parameters). • In particular, the variance of the process is properly reproduced.	• Discretization of target ACF leads to the aliasing effect in target PSD, which is reproduced in the AR PSD. • Pre-processing to obtain the target ACF will be required when turbulence models are described in the frequency-wavenumber domain (e.g. Mann uniform shear model).
PSD-based	• The fitting of the target PSD can be asymptotically improved (by increasing the number of model parameters). • In particular, no aliasing effect decreases the fitting quality.	• Only a fraction of the target variance (corresponding to the range $[0, \mathring{k}_{\max}]$) is properly reproduced.

Table 3.2: A comparison between the implications of fitting ACF and fitting PSD.

Chapter 4

Optimal calibration of the parameters of VAR models (sequential method) applied to multivariate cases

The results presented in this chapter have been published by the author in the Journal of Wind Engineering and Industrial Aerodynamics (Elagamy et al., 2023).

The previous chapter introduced the AR model to generate a synthetic single velocity component at a spatial point. This chapter deals with the use of the VAR model to generate synthetic wind fields (3−velocity components) at multiple spatial points. Basic concepts of the VAR model are illustrated. In this chapter, an extension of the PPA to the multivariate case is presented. This approach is based on a VAR eigenvalues analysis implemented to obtain an optimal VAR model from a predefined CPSDM, where both the real and imaginary parts of the target CPSDM are considered. This extension requires new research involving the eigenanalysis of the VAR model to understand not only the role of the VAR eigenvalues (poles) on the auto-spectra of the different wind components but also the role of the eigenvectors on the cross spectra.

4.1 Introduction to the VAR(p) models

In a VAR model, the fluctuations of the atmospheric turbulent wind field velocity on a plane perpendicular to the mean wind velocity at time t, $\boldsymbol{u}_t$, are expressed as a weighted linear combination of past values at selected time lags, $\boldsymbol{u}_{t-l}$, for $l > 0$, plus a random term $\boldsymbol{\varepsilon}_t$ (Hytti et al., 2006). Note that for simplicity, the hV-1D RP $\boldsymbol{u}(t;\alpha)$ is written as $\boldsymbol{u}_t$ in the following sections. The general formulation of a zero-mean h-variate VAR model of order p, VAR(p), is defined as (Tsay, 2013):

$$\boldsymbol{u}_t = \sum_{m=1}^{p} \boldsymbol{\Phi}_m \boldsymbol{u}_{t-m} + \boldsymbol{\Sigma}\boldsymbol{\varepsilon}_t, \tag{4.1}$$

where $\boldsymbol{u} = [u_1, v_1, w_1 \ldots, u_{N_p}, v_{N_p}, w_{N_p}]^T$, u_i, v_i and w_i are the three velocity components at point i, N_p is the number of grid points, $\boldsymbol{\Phi}_m$ are the regression coefficient matrices with dimensions $h \times h$, $\boldsymbol{\Sigma}$ is the noise coefficient matrix with dimensions $h \times h$ and $\boldsymbol{\varepsilon}_t$ is a sequence of independent and identically distributed RVs with $\mathcal{N}(0, \boldsymbol{I})$ PDF. Note that the two-points two-times second-order statistics such as the CMF and the CPSDM, which are described by the VAR(p) model (Equation (4.1)), are fully determined from the VAR(p) model parameters, $\boldsymbol{\Phi}_m$ and $\boldsymbol{\Sigma}$ (Tsay, 2013; Gallego-Castillo et al., 2022).

The restricted VAR model (Krenk & Møller, 2019) gives more flexibility while using the VAR scheme, since it does not include all the regression terms, but it includes selected ones, which here are defined by the set of indexes corresponding to the lags of the regression terms included in the vector $\mathbf{j} = [j_1, j_2, \ldots, j_N]$. The general formulation of a restricted VAR model of order p, VAR(p), is:

$$\boldsymbol{u}_t = \sum_{i=1}^{N} \mathbf{A}_{j_i} \boldsymbol{u}_{t-i} + \mathbf{B}\boldsymbol{\varepsilon}_t, \tag{4.2}$$

where N is the number of selected regression terms ($N \leq p$). Note that the relationships between the restricted and the unrestriced versions of a VAR model follows similar rules as those for the univariate case (see Section 3.1).

4.2 VAR(1) representation of a VAR(p) model

A VAR(p) model, shown in Equation (4.1), can be expressed in the form of a VAR(1) model by using an expanded time series to form an extended VAR(1) with ph-dimension. The VAR(1) representation of the VAR(p) model is given by (Tsay, 2013):

$$\boldsymbol{u}_{*_t} = \boldsymbol{\Phi}_* \boldsymbol{u}_{*_{t-1}} + \boldsymbol{\Sigma}_* \boldsymbol{\varepsilon}_{*_t}, \tag{4.3}$$

where $\boldsymbol{u}_{*_t} = [\boldsymbol{u}_t, \ldots, \boldsymbol{u}_{t-(p-1)}]^T$ and $\boldsymbol{\Phi}_*$ is usually referred to as the companion matrix (Tsay, 2013), has $ph \times ph$ dimension and is expressed as

$$\boldsymbol{\Phi}_* = \begin{bmatrix} \boldsymbol{\Phi}_1 & \boldsymbol{\Phi}_2 & \ldots & \boldsymbol{\Phi}_{p-1} & \boldsymbol{\Phi}_p \\ \boldsymbol{I} & \mathbf{0} & \ldots & \mathbf{0} & \mathbf{0} \\ \mathbf{0} & \boldsymbol{I} & \ldots & \mathbf{0} & \mathbf{0} \\ \vdots & & \vdots & & \vdots \\ \mathbf{0} & \mathbf{0} & \ldots & \boldsymbol{I} & \mathbf{0} \end{bmatrix}_{ph \times ph}, \tag{4.4}$$

where $\boldsymbol{\Sigma}_*$ and $\boldsymbol{\varepsilon}_{*_t}$ are:

$$\boldsymbol{\Sigma}_* = \begin{bmatrix} \boldsymbol{\Sigma} & \mathbf{0} & \ldots & \mathbf{0} \\ \mathbf{0} & \mathbf{0} & \ldots & \mathbf{0} \\ \vdots & & \vdots & \vdots \\ \mathbf{0} & \mathbf{0} & \ldots & \mathbf{0} \end{bmatrix}_{ph \times ph}, \quad \boldsymbol{\varepsilon}_{*_t} = \begin{bmatrix} \boldsymbol{\varepsilon}_t \\ \mathbf{0} \\ \vdots \\ \mathbf{0} \end{bmatrix}_{ph \times 1}. \tag{4.5}$$

The VAR(1) form is convenient for calculating the theoretical CMF of the VAR(p). Additionally, the companion matrix in Equation (4.4) is analyzed in Section 4.5 by using eigenanalysis

to derive the relationships of the eigenvalues and eigenvectors of the VAR model with the CPSDM.

4.3 Theoretical covariance matrix function (CMF) of a VAR model

In Section 3.2, the theoretical ACF of an AR model was introduced. This section illustrates the expansion of the ACF for a vector RP $\boldsymbol{u}_t$, with h-variates. For a stationary process, the CMF, $\boldsymbol{\Gamma}_l$, of a vector RP $\boldsymbol{u}_t$ with h components, depends only on the time lag l, and it is defined as (Tsay, 2013):

$$\boldsymbol{\Gamma}_l = \mathrm{E}\left[\boldsymbol{u}_t \boldsymbol{u}_{t-l}^T\right] = \begin{bmatrix} \gamma_{l,11} & \gamma_{l,12} & \cdots & \gamma_{l,1h} \\ \vdots & \vdots & \ddots & \vdots \\ \gamma_{l,h1} & \gamma_{l,h2} & \cdots & \gamma_{l,hh} \end{bmatrix}, \tag{4.6}$$

where $\gamma_{l,mn}$, for $m, n = 1, \ldots, h$, is the covariance function between m and n univariate random processes at lag l. Note that the CMF, for $l < 0$, can be evaluated from the transposed the CMF at the equivalent positive time lag as $\boldsymbol{\Gamma}_{-l} = \boldsymbol{\Gamma}_l^T$. By following the same procedures illustrated in Equation (3.5) to obtain the AR theoretical ACF, the CMF of a VAR(p) is determined by substituting Equation (4.1) in Equation (4.6) as follows:

$$\begin{aligned} \boldsymbol{\Gamma}_l &= \mathrm{E}\left[\left(\sum_{m=1}^{p} \boldsymbol{\Phi}_m \boldsymbol{u}_{t-m} + \boldsymbol{\Sigma}\boldsymbol{\varepsilon}_t\right) \boldsymbol{u}_{t-l}^T\right] \\ &= \sum_{m=1}^{p} \boldsymbol{\Phi}_m \mathrm{E}\left[\boldsymbol{u}_{t-m} \boldsymbol{u}_{t-l}^T\right] + \mathrm{E}\left[\left(\boldsymbol{\Sigma}\boldsymbol{\varepsilon}_t\right) \boldsymbol{u}_{t-l}^T\right], \end{aligned} \tag{4.7}$$

where the covariance function $\mathrm{E}\left[\left(\boldsymbol{\Sigma}\boldsymbol{\varepsilon}_t\right) \boldsymbol{u}_{t-l}^T\right]$ is evaluated as follows:

$$\mathbf{E}\left[\left(\boldsymbol{\Sigma}\boldsymbol{\varepsilon}_t\right) \boldsymbol{u}_{t-l}^T\right] = \begin{cases} \boldsymbol{\Sigma}\boldsymbol{\Sigma}^T, & \text{for } l = 0, \\ \mathbf{0}_h, & \text{for } l > 0. \end{cases} \tag{4.8}$$

From Equations (4.7) and (4.6), the analytical expressions that relate the CMF for different time lags and the unrestricted VAR(p) model parameters are as follows (Tsay, 2013; Gallego-Castillo et al., 2022):

$$\begin{aligned} \boldsymbol{\Gamma}_0 &= \sum_{m=1}^{p} \boldsymbol{\Phi}_m \boldsymbol{\Gamma}_{-m} + \boldsymbol{\Sigma}\boldsymbol{\Sigma}^T, && \text{for } l = 0, \\ \boldsymbol{\Gamma}_l &= \sum_{m=1}^{p} \boldsymbol{\Phi}_m \boldsymbol{\Gamma}_{l-m}, && \text{for } l > 0. \end{aligned} \tag{4.9}$$

Similarly as for the CMF of the unrestricted VAR model, the CMF of the restricted VAR model is evaluated by employing Equation (4.2) in Equation (4.6) and by utilizing Equation

(4.8) to ultimately obtain the CMF of the restricted VAR for different lags, defined as follows:

$$\begin{aligned} \boldsymbol{\Gamma}_0 &= \sum_{i=1}^{N} \mathbf{A}_{j_i} \boldsymbol{\Gamma}_{-j_i} + \boldsymbol{B}\boldsymbol{B}^T, \qquad \text{for } l = 0, \\ \boldsymbol{\Gamma}_l &= \sum_{i=1}^{N} \mathbf{A}_{j_i} \boldsymbol{\Gamma}_{l-j_i}, \qquad \text{for } l > 0. \end{aligned} \tag{4.10}$$

The direct solution of Equations (4.9) and (4.10), by employing the symmetry assumption as previously done for the AR ACF (see Section 3.2), is unfeasible, since for the VAR, the CMF at negative lags is equal to the transpose of the CMF at positive lags. To address this issue, the VAR(1) representation and VMA representation of the VAR model can be used to evaluate the VAR CMF (Tsay, 2013), as illustrated in the following sections.

4.3.1 CMF of a VAR(p) model through VAR(1) representation

As discussed in Section 4.2, a VAR(p) model can be represented in a VAR(1) format as shown in Equation (4.3). The CMF of the extended VAR(1) representation is computed as follows (Tsay, 2013):

$$\boldsymbol{\Gamma}_{*,0} = \boldsymbol{\Phi}_* \boldsymbol{\Gamma}_{*,0} \boldsymbol{\Phi}_*^T + \boldsymbol{\Sigma}_* \boldsymbol{\Sigma}_*^T, \tag{4.11}$$

where

$$\boldsymbol{\Gamma}_{*,0} = \begin{bmatrix} \boldsymbol{\Gamma}_0 & \boldsymbol{\Gamma}_1 & \dots & \boldsymbol{\Gamma}_{p-2} & \boldsymbol{\Gamma}_{p-1} \\ \boldsymbol{\Gamma}_{-1} & \boldsymbol{\Gamma}_0 & \dots & \boldsymbol{\Gamma}_{p-3} & \boldsymbol{\Gamma}_{p-2} \\ \vdots & & \ddots & & \vdots \\ \boldsymbol{\Gamma}_{-(p-2)} & \boldsymbol{\Gamma}_{-(p-3)} & \dots & \boldsymbol{\Gamma}_0 & \boldsymbol{\Gamma}_1 \\ \boldsymbol{\Gamma}_{-(p-1)} & \boldsymbol{\Gamma}_{-(p-2)} & \dots & \boldsymbol{\Gamma}_{-1} & \boldsymbol{\Gamma}_0 \end{bmatrix}_{ph \times ph}. \tag{4.12}$$

To solve Equation (4.11), a vectorization process is applied to the $\boldsymbol{\Gamma}_{*,0}$ matrix into a column vector, to acquire the solution for Equation (4.11) as follows (Tsay, 2013):

$$\text{vec}\left(\boldsymbol{\Gamma}_{*,0}\right) = \text{vec}\left(\boldsymbol{\Sigma}_* \boldsymbol{\Sigma}_*^T\right) \left(\mathbf{I}_{(ph)^2 \times (ph)^2} - \boldsymbol{\Phi}_* \otimes \boldsymbol{\Phi}_*\right)^{-1}, \tag{4.13}$$

where $\otimes$ is the Kronecker product. By computing $\boldsymbol{\Gamma}_{*,0}$, the value of $\boldsymbol{\Gamma}_l$ at time lags $l = -p, \dots, p$ is obtained through the relationship expressed in Equation (4.12). For lags exceeding p, the $\boldsymbol{\Gamma}_l$ can be evaluated using Equations (4.9) and (4.10). Note that this approach provides the exact CMF for a VAR(p) model. However, it is computationally costly, as it involves the formulation of matrices with dimensions $(ph)^2 \times (ph)^2$. Hence, alternative methods, such as the VMA(q) representation of a VAR(p) model (see Section 4.3.2), are required to decrease the computational burden associated with computing the VAR CMF.

4.3.2 CMF of a VAR(p) model through VMA(q) representation

A VAR(p) model can be expressed as a VMA though the recursive substitutions of $\boldsymbol{u}_{t-m}$ in Equation (4.1) with $\sum_m^p \Phi_m \boldsymbol{u}_{t-m-1} + \boldsymbol{\Sigma}\boldsymbol{\varepsilon}_{t-m}$, to attain the following representation (Tsay,

2013):

$$\boldsymbol{u}_t = \boldsymbol{\Sigma\varepsilon}_t + \sum_{i=1}^{\infty} \boldsymbol{\Psi}_i \left(\boldsymbol{\Sigma\varepsilon}_{t-i}\right), \tag{4.14}$$

where $\boldsymbol{\Psi}_i$ is the regression coefficient matrix of the VMA model, and it is computed as follows:

$$\boldsymbol{\Psi}_i = \sum_{j=1}^{\min(i,p)} \boldsymbol{\Phi}_j \boldsymbol{\Psi}_{i-j} \qquad \text{for } i \geq 1, \tag{4.15}$$

and $\boldsymbol{\Psi}_0 = \boldsymbol{I}$.

The theoretical CMF of a VMA process, $\boldsymbol{\Gamma}_l^{\text{VMA}}$, in terms of the lag l is computed as follows (Tsay, 2013):

$$\begin{aligned}
\boldsymbol{\Gamma}_l^{\text{VMA}} &= \text{Cov}\left[\boldsymbol{u}_t, \boldsymbol{u}_{t-l}\right] = \text{E}\left[\boldsymbol{u}_t \boldsymbol{u}_{t-l}^T\right] \\
&= \mathbf{E}\left\{\left[\boldsymbol{\Sigma\epsilon}_t + \sum_{i=1}^{\infty} \boldsymbol{\Psi}_i \left(\boldsymbol{\Sigma\epsilon}_{t-i}\right)\right]\left[\boldsymbol{\Sigma\epsilon}_{t-l} + \sum_{i=1}^{\infty} \boldsymbol{\Psi}_i \left(\boldsymbol{\Sigma\epsilon}_{t-l-i}\right)\right]^T\right\} \\
&= \mathbf{E}\left\{\left[\sum_{i=0}^{\infty} \boldsymbol{\Psi}_i \left(\boldsymbol{\Sigma\epsilon}_{t-i}\right)\right]\left[\sum_{i=0}^{\infty} \left(\boldsymbol{\epsilon}_{t-l-i}^T \boldsymbol{\Sigma}^T\right) \boldsymbol{\Psi}_i^T\right]\right\} \\
&= \sum_{i=1}^{\infty} \boldsymbol{\Psi}_i \boldsymbol{\Sigma\Sigma}^T \boldsymbol{\Psi}_{i-l}^T,
\end{aligned} \tag{4.16}$$

where, by considering infinite terms, the $\boldsymbol{\Gamma}_l^{\text{VMA}}$ achieves an exact match of the $\boldsymbol{\Gamma}_l^{\text{VAR}}$ $\left(\boldsymbol{\Gamma}_l^{\text{VMA}} \to \boldsymbol{\Gamma}_l^{\text{VAR}} \text{ as } i \to \infty\right)$. Due to practical considerations, the VMA representation, shown in Equation(4.14), is truncated up to the first q terms to express the VMA(q) model as follows:

$$\boldsymbol{u}_t = \boldsymbol{\Sigma\varepsilon}_t + \sum_{i=1}^{q} \boldsymbol{\Psi}_i \left(\boldsymbol{\Sigma\varepsilon}_{t-i}\right). \tag{4.17}$$

Additionally, the theoretical CMF of the VMA(q) model is defined as (Tsay, 2013):

$$\boldsymbol{\Gamma}_l^{\text{VMA}(q)} = \text{Cov}\left[\boldsymbol{u}_t, \boldsymbol{u}_{t-l}\right] = \begin{cases} \sum_{i=l}^{q} \boldsymbol{\Psi}_i \boldsymbol{\Sigma\Sigma}^T \boldsymbol{\Psi}_{i-l}^T, & \text{for } 0 \leq l \leq q, \\ \mathbf{0}_h, & \text{for } l > q. \end{cases} \tag{4.18}$$

Note that a suitable selection for the VMA model order q would be the lag l at which the $\boldsymbol{\Gamma}_l^{\text{VAR}}$ components are nearly equal to zero, given that the $\boldsymbol{\Gamma}_l^{\text{VMA}(q)}$ is equal to a null $h \times h$ matrix for lags exceeding q. To gain a better understanding of the selection of VMA model order q, a VAR(2) model is considered with the following parameters value:

$$\boldsymbol{\Phi}_1 = \begin{bmatrix} 1.1 & -0.2 \\ -0.3 & -0.1 \end{bmatrix}, \boldsymbol{\Phi}_2 = \begin{bmatrix} -0.1 & 0.7 \\ 0.2 & 0.1 \end{bmatrix}, \boldsymbol{\Sigma} = \begin{bmatrix} 0.3 & 0 \\ 0.1 & 0.2 \end{bmatrix}. \tag{4.19}$$

The CMF of the VAR(2) model and its VMA(q) representation for $q = 10, 30$ is depicted in Figure 4.1. The parameters of the VMA model are computed utilizing Equation (4.15) and the parameters value of the VAR(2) model is given in Equation (4.19). Following that, the

CMF of the VMA(q) model is evaluated by using Equation (4.18). As shown in Figure 4.1, for $l > 30$, the VAR CMF exhibits values close to zero. Consequently, selecting $q = 30$ gave an improved representation of the VAR CMF compared to $q = 10$.

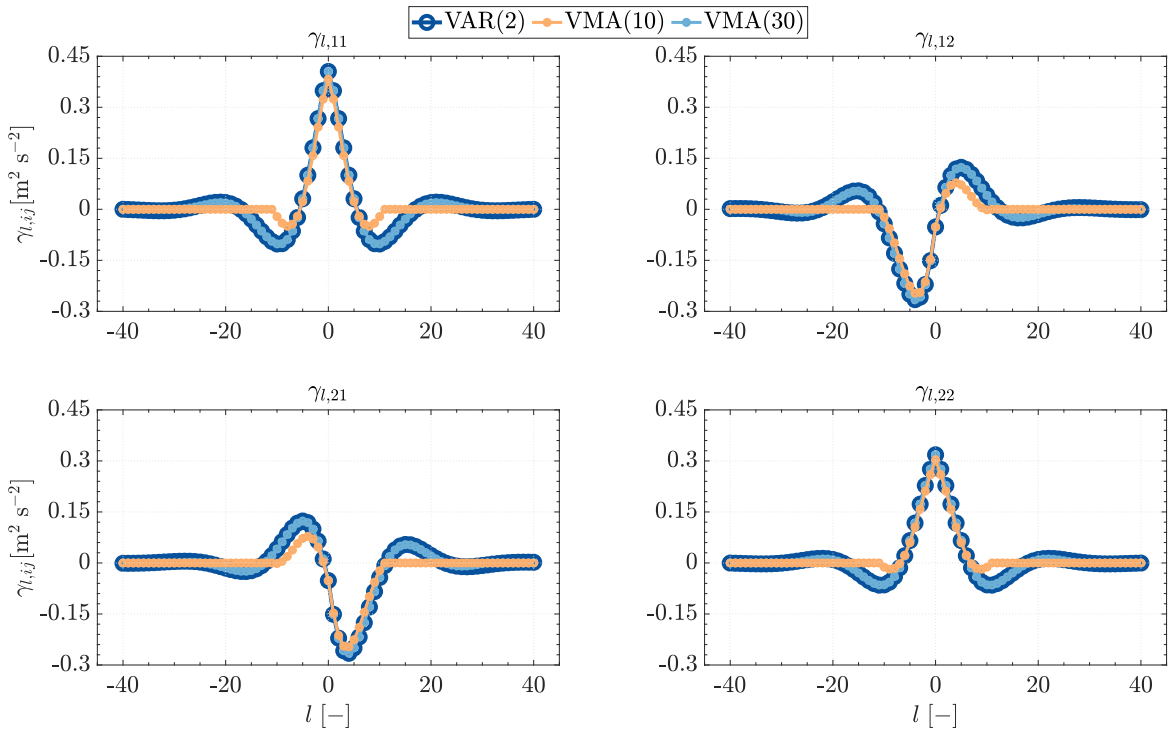

Figure 4.1: The CMF, $\gamma_{l,ij}$, evaluated for VAR(2) model and its VMA(q) representation for $q = 10, 30$. The values of the parameters of the VAR(2) model, $\mathbf{\Phi}_i$ and $\mathbf{\Sigma}$, can be found in Equation (4.19).

4.4 Theoretical cross-power density matrix, CPSDM, of a VAR model

The theoretical one-sided CPSDM of the VAR model, $\boldsymbol{S}(f)$, (the Fourier pair of the corresponding CMF) in terms of frequency f (Marple Jr & Carey, 2019) is written as:

$$\boldsymbol{S}(f) = \frac{1}{f_{max}} \left[\boldsymbol{W}_1 \boldsymbol{W}_2(f)\right]^{-1} \mathbf{\Sigma}\mathbf{\Sigma}^H \left[\boldsymbol{W}_1 \boldsymbol{W}_2(f)\right]^{-H}, \quad 0 \leq f \leq f_{\max}, \tag{4.20}$$

where the superscript $(\cdot)^{-H}$ indicates the inverse of the Hermitian transpose, $\boldsymbol{W}_1 = [\boldsymbol{I}, \mathbf{\Phi}_1, \ldots, \mathbf{\Phi}_p]$ and $\boldsymbol{W}_2 = [\boldsymbol{I}, -\exp(-\mathrm{i}(2\pi f/f_{\max}))\boldsymbol{I}, \ldots, -\exp(-\mathrm{i}p(2\pi f/f_{\max}))\boldsymbol{I}]^T$. Note that stationary conditions and real-value RPs, $S_{ii}(f)$, for $i = 1, \ldots, h$, are non-negative real-valued even functions of f, where $f \in [0, f_{\max}]$ (Bendat & Piersol, 2011). Additionally, S_{ij}, for $i, j = 1, \ldots, h$ and $i \neq j$, is a complex-valued function of f and is Hermitian $\left(S^*_{ij}(f) = S_{ji}(f)\right)$.

4.5 Optimal VAR model for reproducing a target CPSDM

This section presents the extension of the PPA (Section 3.5.1) to the multivariate case. The aim is to comprehend the connection between the structure of a VAR model (from the eigenanalysis perspective) and its theoretical CPSDM to set an optimization problem to determine a VAR model whose theoretical CPSDM optimally fits a target CPSDM.

4.5.1 Eigenanalysis of the companion matrix of VAR(1) representation

For a stationary VAR(p) process, the roots of its characteristic equation, given by (Lütkepohl, 2013) as

$$\det(\boldsymbol{I} - \boldsymbol{\Phi}_1 B - \cdots - \boldsymbol{\Phi}_p B^p) = 0, \tag{4.21}$$

have to be outside of the complex unit circle (have a modulus greater than one) (Lütkepohl, 2013; Tsay, 2013), B is the back-shift operator ($Bu_t = u_{t-1}$). This is equivalent to the eigenvalues modulus $|\lambda_i|$, for $i = 1, \ldots, ph$, of the companion matrix $\boldsymbol{\Phi}_*$ to be less than 1 (Zivot & Wang, 2006; Tsay, 2013). The companion matrix $\boldsymbol{\Phi}_*$ can be decomposed as follows:

$$\boldsymbol{\Phi}_* \boldsymbol{V} = \boldsymbol{V}\boldsymbol{D}, \tag{4.22}$$

where $\boldsymbol{D}$ is a diagonal matrix, with $\text{diag}(\boldsymbol{D}) = [\lambda_1, \lambda_2, \ldots, \lambda_{ph}]$ and $\boldsymbol{V}$ is the right-eigenvectors matrix, whose columns are the eigenvectors of the companion matrix $\boldsymbol{V} = [\boldsymbol{v}_1, \boldsymbol{v}_2, \ldots, \boldsymbol{v}_{ph}]$. The eigenvalues of the companion matrix represent the poles of AR/VAR models, as elaborated in Appendix 3. Similarly, as for the poles (Section 3.5.1), the eigenvalues can be real, λ^r, and/or complex conjugate, λ^c. The eigenvector associated with a real eigenvalue is real. Whereas, in case λ_i and λ_{i+1} are complex conjugate eigenvalues ($\lambda_i = \lambda_{i+1}^*$), the associated eigenvectors are complex conjugate eigenvectors ($\boldsymbol{v}_i = \boldsymbol{v}_{i+1}^*$).

The objective of the presented work is to use the smooth relationship between the eigenvalues and the eigenvectors, and the VAR CPSDM to define some features in the VAR CPSDM, rather than directly controlling the VAR parameters to define the VAR CPSDM as in (M. Mignolet & Spanos, 1987). Using the eigenvalues and the eigenvectors facilitates the search for the optimal VAR model compared to considering the VAR coefficients as the variables of the problem directly. In addition, using the eigenvalues and eigenvectors as control variables allows readily constraint of the search of the VAR model to stationary VAR models by forcing the eigenvalues modulus to $|\lambda_i| < 1$. To illustrate the influence of the eigenvectors on the $\boldsymbol{S}^{\text{VAR}}$, a VAR(1) model is considered with h-variates and the noise coefficient matrix $\boldsymbol{\Sigma} = \boldsymbol{I}$ (note that values different from $\boldsymbol{I}$ for the noise coefficient function act as scaling factors on the generated spectrum). By applying the eigen-decomposition, defined in Expression (4.22), to the companion matrix of this VAR model, $\boldsymbol{\Phi}_*$, the eigenvalues matrix $\boldsymbol{D} = [\lambda_1, 0; 0, \lambda_2]$ and the eigenvectors matrix, $\boldsymbol{V}$, are obtained. As an example, the following particular cases concerning the eigenvectors are considered:

1. First case: the eigenvectors matrix is $\boldsymbol{V} = \boldsymbol{I}$. By substituting $\boldsymbol{V}$ in Equation (4.22) and using Equations (4.20) and (4.4), thus, the $\boldsymbol{S}^{\text{VAR}}$, for $f = 0$, is as follows:

$$\boldsymbol{S}^{\text{VAR}}(f=0) = \frac{1}{f_{\max}} \begin{bmatrix} (\lambda_1 - 1)^{-2} & 0 \\ 0 & (\lambda_2 - 1)^{-2} \end{bmatrix}.$$

2. Second case: the eigenvectors matrix is $\boldsymbol{V} = \boldsymbol{J}$ (where $\boldsymbol{J}$ is the backward identity matrix), therefore, the $\boldsymbol{S}^{\text{VAR}}$, for $f = 0$, is as follows:

$$\boldsymbol{S}^{\text{VAR}}(f=0) = \frac{1}{f_{\max}} \begin{bmatrix} (\lambda_2 - 1)^{-2} & 0 \\ 0 & (\lambda_1 - 1)^{-2} \end{bmatrix}.$$

It is derived from both, the first case and the second case, that changing the direction of the eigenvectors changes the assigned eigenvalue for each spectrum. For the first case, the eigenvalue λ_1 is assigned to spectrum S_{11} and λ_2 is assigned to spectrum S_{22}. Whereas, for the second case, the eigenvalue λ_2 is assigned to spectrum S_{11} and λ_1 is assigned to spectrum S_{22}. Thus, it can be noted that the eigenvectors are in charge of sharing the spectral content of the eigenvalues between the spectra of the VAR components. It should be noted that only the direction of the eigenvectors and the angle between the eigenvectors affect the $\boldsymbol{S}^{\text{VAR}}$, whereas the modulus of the eigenvectors do not influence the $\boldsymbol{S}^{\text{VAR}}$. In Figure 4.2, the effect of changing the direction of the eigenvectors on the $\boldsymbol{S}^{\text{VAR}}$, for VAR(1) model with $2-$variates, is shown. The companion matrix is obtained for $\boldsymbol{D} = [0.5, 0; 0, 0.2]$ and the eigenvector matrix $\boldsymbol{V}$ contains two perpendicular eigenvectors. The $\boldsymbol{S}^{\text{VAR}}$ was calculated for different rotating perpendicular eigenvectors, where the first eigenvector is considered to form angles $= 0°, 30°$ and $60°$ with the $x-$axis. Whereas in Figure 4.3, the effect of changing the angle between the eigenvectors on the $\boldsymbol{S}^{\text{VAR}}$ is shown. It was observed that for perpendicular eigenvectors, the imaginary part of the VAR cross-spectrum S_{12} is zero; however, for angles other than $90°$ between the eigenvectors, the imaginary part is nonzero. Similarly, as discussed in Section 3.5.1 and in (Takalo et al., 2005; Elagamy et al., 2021a), the locations of the eigenvalues on the unit circle affect the shape of the peaks of the $\boldsymbol{S}^{\text{VAR}}$. Therefore, the radial location of the real and complex eigenvalues affects the amplitude of the peak of the spectra and cross-spectra, and the values of the phase angle of the eigenvalues affect the location of the peak of the spectra and cross-spectra, as shown in Figure 4.4.

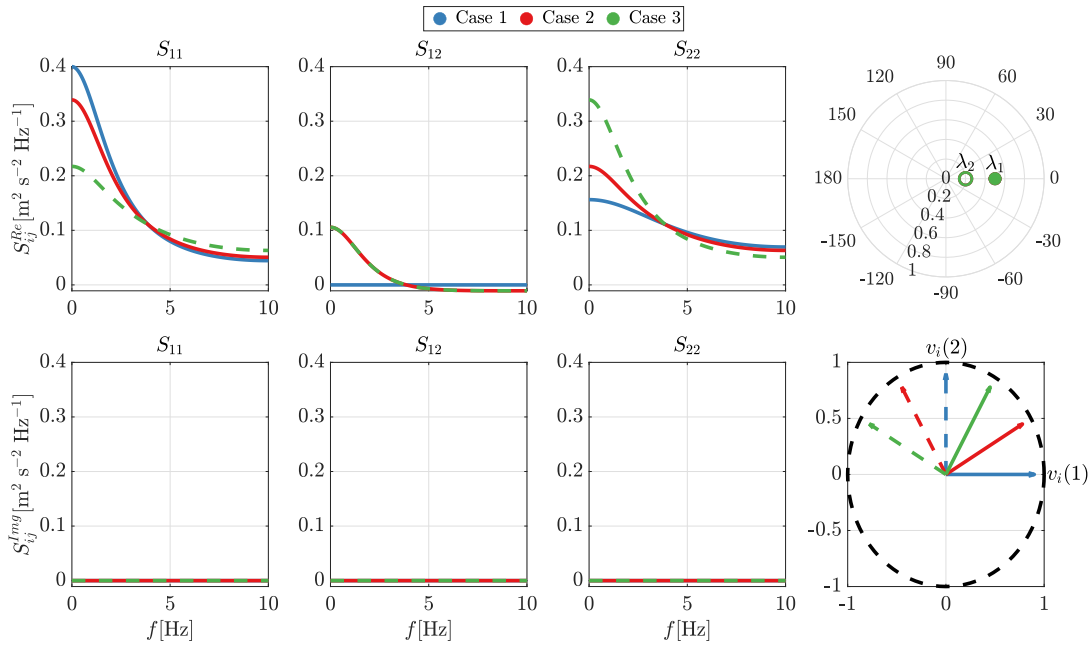

Figure 4.2: Real and imaginary parts of one-sided VAR CPSDM, S_{ij}^{VAR}, of the 2-variates VAR(1) models, obtained from different perpendicular eigenvectors, $\boldsymbol{v}_{\lambda_1}$ (solid line) and $\boldsymbol{v}_{\lambda_2}$ (dashed line), where $\boldsymbol{v}_{\lambda_1}$ forms angles $= 0°$ (Case 1), $30°$ (Case 2) and $60°$ (Case 3) with the x-axis. The case presented corresponds to fixed real eigenvalues $\lambda_1 = 0.5$ (solid dot) and $\lambda_2 = 0.2$ (empty dot).

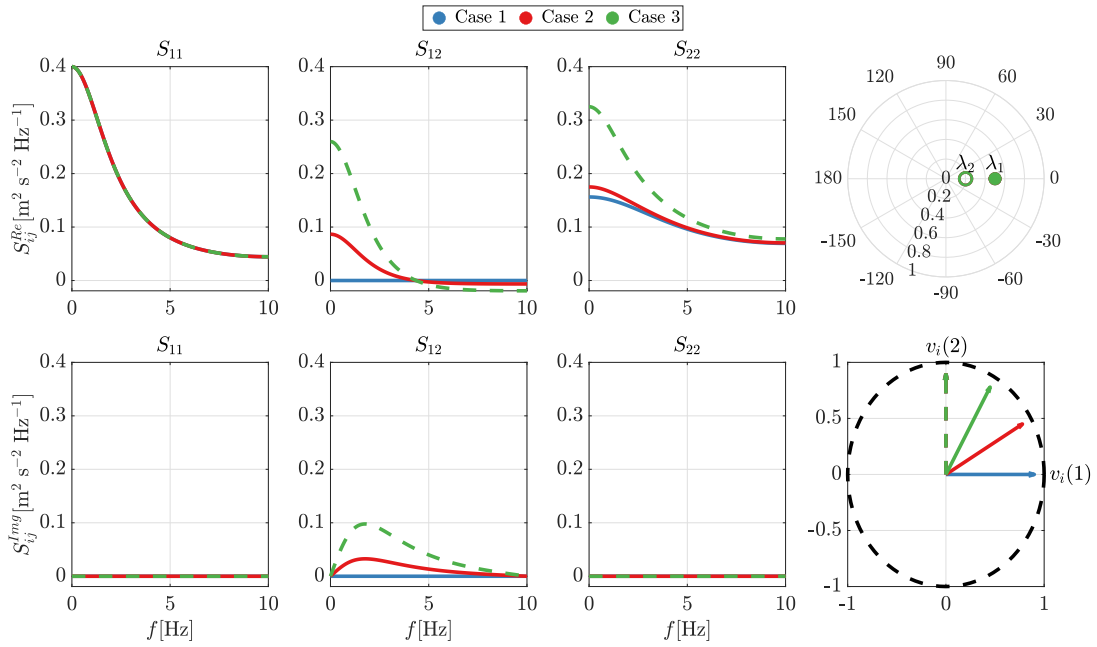

Figure 4.3: Real and imaginary parts of one-sided VAR CPSDM, S_{ij}^{VAR}, of the 2-variates VAR(1) models, obtained for different angles between the eigenvectors, $\boldsymbol{v}_{\lambda_1}$ (solid line) and $\boldsymbol{v}_{\lambda_2}$ (dashed line), for angle = 90° (Case 1), angle = 60° (Case 2) and angle = 30° (Case 3), with fixed real eigenvalues $\lambda_1 = 0.5$ (solid dot) and $\lambda_2 = 0.2$ (empty dot).

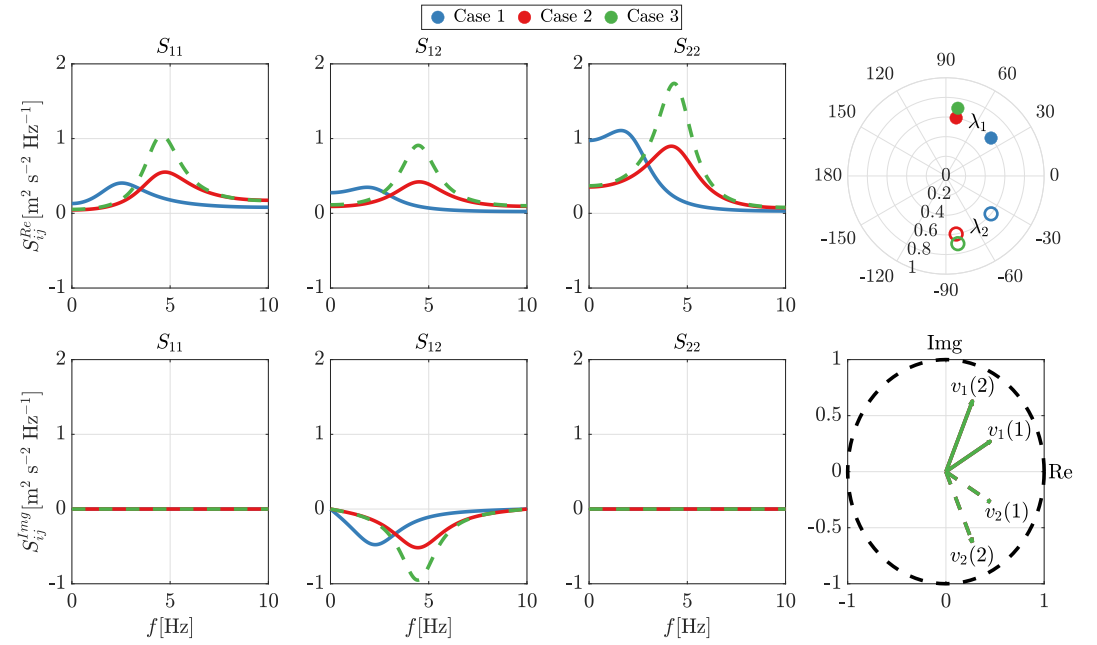

Figure 4.4: Real and imaginary parts of one-sided VAR CPSDM, S_{ij}^{VAR}, of the 2-variates VAR(1) models, obtained for different complex eigenvalues with $r_\lambda = 0.6$ and $\theta_\lambda = 40°$ (Case 1), $r_\lambda = 0.6$ and $\theta_\lambda = 80°$ (Case 2) and $r_\lambda = 0.7$ and $\theta_\lambda = 80°$ (Case 3) with fixed complex conjugate eigenvectors $\boldsymbol{v}_{\lambda_{1,2}} = [0.5 \pm \mathrm{i}0.3, 0.3 \pm \mathrm{i}0.7]^T$.

It is worth mentioning that, due to the special form of the companion matrix $\boldsymbol{\Phi}_*$, as shown in Equation (4.4), the eigenvector matrix $\boldsymbol{V}$ of the companion matrix, for VAR(p) model with h-variates, has the following form (see Appendix 4):

$$\boldsymbol{V} = \begin{bmatrix} (\lambda_1^0)^{-1}v_{11} & (\lambda_2^0)^{-1}v_{21} & \dots & (\lambda_{ph}^0)^{-1}v_{(ph)1} \\ \vdots & \vdots & \ddots & \vdots \\ (\lambda_1^0)^{-1}v_{1h} & (\lambda_2^0)^{-1}v_{2h} & \dots & (\lambda_{ph}^0)^{-1}v_{(ph)h} \\ \vdots & \vdots & & \vdots \\ (\lambda_1^{p-1})^{-1}v_{11} & (\lambda_2^{p-1})^{-1}v_{21} & \dots & (\lambda_{ph}^{p-1})^{-1}v_{(ph)1} \\ \vdots & \vdots & \ddots & \vdots \\ (\lambda_1^{p-1})^{-1}v_{1h} & (\lambda_2^{p-1})^{-1}v_{2h} & \dots & (\lambda_{ph}^{p-1})^{-1}v_{(ph)h} \end{bmatrix}_{ph\times ph} . \tag{4.23}$$

From Equation (4.23), it can be noted that the first h-rows in eigenvector matrix $\boldsymbol{V}$ (components related to the random vector at time t) are independent variables and the rest of the elements in the eigenvector matrix $\boldsymbol{V}$ (components related to the random vector at times $t-1,\dots,t-p$) can be obtained by knowing its first h-rows and the eigenvalues of the companion matrix.

The previous analysis envisages smooth and meaningful relationships between eigenvalues and eigenvectors of the companion matrices with the CPSD of the corresponding VAR model. The proposed approach uses the previous analyses to define an optimization problem to obtain a VAR model, where an optimal VAR model provides a minimum error between the theoretical VAR CPSDM and the target CPSDM. The proposed approach is identified as Optimal CPSDM fitting through Eigen ANalysis (OCEAN) in the following sections. In general, the CPSDM has real and imaginary parts, and both parts are considered in the error definition of the optimization problem. This is one of the advantages of the proposed approach, as some works neglect the imaginary part of the cross-spectra (Veers, 1988; Di Paola & Gullo, 2001; Melaku & Bitsuamlak, 2021), which is inaccurate as the non-symmetry in the CMF is represented in the frequency domain, by the non-zero imaginary part of the spectra. The optimal VAR model is obtained by choosing the location of the eigenvalues and the direction of eigenvectors; then, the companion matrix is evaluated by using Equation (4.22) for the selected $\boldsymbol{D}$ and $\boldsymbol{V}$ matrices. Therefore, the regression coefficients matrices can be obtained from the companion matrix (Equation (4.4)), to be used to evaluate the $\boldsymbol{S}^{\text{VAR}}$ from Equation (4.20).

4.5.2 Problem definition

In this section, the problem statement for the proposed approach is defined. The independent variables defined in the optimization problem are the noise coefficient matrix, $\boldsymbol{\Sigma}$, the diagonal matrix of eigenvalues, $\boldsymbol{D}$, and the first $h-$rows of the right eigenvectors matrix $\boldsymbol{V}$. Note that the noise coefficient matrix is considered as a lower triangular matrix, resulting from the Cholesky decomposition of matrix $\boldsymbol{\Sigma}\boldsymbol{\Sigma}^T$, which represents the variance of the noise term of the VAR model (Gallego-Castillo et al., 2022). The number of terms to be optimized in each independent variable is summarized in Table 4.1. The minimization problem for the approach

proposed is defined as

$$
\begin{aligned}
\min_{\boldsymbol{\Sigma},\boldsymbol{V},\boldsymbol{D}} \quad & \left\{ \sum_{m=1}^{M} \sum_{r=1}^{h} \sum_{q=1}^{h} \left| \left[S_{rq}^{\mathrm{t}}\left(f_m\right) - S_{rq}^{\mathrm{VAR}}\left(\boldsymbol{\Sigma},\boldsymbol{V},\boldsymbol{D},f_m\right) \right]^2 W_{rq}(f_m) \right| \right\}^{1/2}, \\
\text{subject to} \quad & 0 \leq \sigma_{ij} \leq 1, && \text{for } i,j = 1,\ldots,h \text{ and } i \geq j, \\
& -1 \leq v_{ij}^{r} \leq 1, && \text{for } i = 1,\ldots,h \text{ and } j = 1,\ldots,N_{\lambda^r}, \\
& -1 \leq \mathrm{Re}\{v_{ij}^{c}\} \leq 1, && \text{for } i = 1,\ldots,h \text{ and } j = 1,\ldots,,N_{\lambda^c}, \\
& -1 \leq \mathrm{Img}\{v_{ij}^{c}\} \leq 1, && \text{for } i = 1,\ldots,h \text{ and } j = 1,\ldots,,N_{\lambda^c}, \\
& -1 < \lambda_i^{r} < 1, && \text{for } i = 1,\ldots,N_{\lambda^r}, \\
& 0 < |\lambda_i^{c}| < 1, && \text{for } m = 1,\ldots,N_{\lambda^c}, \\
& 0 < \arg\{\lambda_i^{c}\} < \pi, && \text{for } m = 1,\ldots,N_{\lambda^c},
\end{aligned}
\tag{4.24}
$$

where the superscripts $(\cdot)^r$ and $(\cdot)^c$ indicate real and complex, respectively, W_{rq} is a defined error weight, and M is the number of equally spaced frequencies within the interval $[0,f_{\max}]$ for each component of the CPSDM during the error evaluation, S_{rq}^{t} is the CPSDM target to be fitted. Finally, f_m is the discrete frequency values and σ_{ij} are the components of the noise coefficient matrix $\boldsymbol{\Sigma}$.

Independent variables	Number of terms to optimize
1 - **Noise coefficient matrix ($\boldsymbol{\Sigma}$)**	$h + h(h-1)/2$
2- **The first h rows of the Right eigenvector matrix ($\boldsymbol{V}$)**:	
i- Real eigenvector ($\boldsymbol{v}^r$)	$h \times 2N_{\lambda^r}$
ii- Complex eigenvectors ($\boldsymbol{v}^c$)	$h \times 2N_{\lambda^c}$
3- **Diagonal eigenvalue matrix ($\boldsymbol{D}$)**:	
i- Real eigenvalues (λ^r)	N_{λ^r}
ii- Complex eigenvalues (λ^c)	$2N_{\lambda^c}$
Total number of terms	$p \times h(h+1) + h + h \times (h-1)/2$

Table 4.1: Independent variables defined in the optimization problem. Note that, $ph = N_{\lambda^r} + 2N_{\lambda^c}$, where N_{λ^r} is the number of real eigenvalues and N_{λ^c} is the number of complex conjugate eigenvalues, defined beforehand.

The optimization process was done using the Enhanced Gradient-Based Optimization method (EGBO) (Ahmadianfar et al., 2021). This optimization method combines the population-based optimizer concept with the gradient-based optimizer concept. This combination is needed for complex optimization processes to prevent obtaining local minimum solutions instead of the desired global minimum solution. Moreover, simulations for different combinations of the companion matrix's real and complex conjugate eigenvalues were done to obtain the least error, which can be obtained for a specific VAR model of order p.

4.6 Case study: application to Mann's turbulence model

This section briefly describes the turbulence model employed for generating target CMF and CPSDM for a particular case of a turbulence model based on a given form of the SVT. Both the proposed OCEAN and CG optimization approaches are applied to find a VAR model whose CMF and CPSDM optimally fit the target CMF and CPSDM derived from the Mann Uniform-Shear SVT (US-SVT), $\Phi_{ij}(\boldsymbol{k}, \tau_e(k))$, (Mann, 1994a, 1998), which reproduces the two-points second order statistics of a stationary-homogeneous-anisotropic turbulence velocity field, where anisotropy is introduced by a constant mean shear of the mean longitudinal velocity component along the vertical direction, $\partial U/\partial z = cons \neq 0$. $\boldsymbol{k}$ is the vector wavenumber and k is its magnitude. $\tau_e(k)$ is the eddy lifetime which represents the order of magnitude of the time over which the eddies of dimension k^{-1} are stretched by shear. In the present analysis, the basic dependence $\tau_e(k) = (\partial U/\partial z)^{-1}\Gamma k^{-2/3}$ analyzed in (Mann, 1994a, 1994b), is used instead of its final proposal $\tau_e(k) = (\partial U/\partial z)^{-1}\Gamma k^{-2/3}{}_2\mathrm{F}_1\,(1/2, 17/6; 4/3; (kL)^{-2})$ (${}_2\mathrm{F}_1$ is the hypergeometric function, Γ is the anisotropy parameter, $\Gamma = 0$ means isotropy, and L is the length scale of the energy spectrum) due to its cheaper calculation cost.

The Mann's US-SVT model depends on three parameters, the already defined Γ and L, and the isotropic variance $\overline{u_{iso}^2}$ which is defined as

$$\overline{u_{iso}^2} = \iiint_{\boldsymbol{k}} \Phi_{ij}(\boldsymbol{k})|_{\Gamma=0}\, d\boldsymbol{k}.$$

The Mann's US-SVT model $\Phi_{ij}(\mathbf{k}, \tau_e(k))$ is utilized to evaluate the CPSDM of the velocity components fluctuations determined at two points of a plane normal to the mean wind speed, separated by a vector $\boldsymbol{r} = [r_2, r_3]^T$, by using the following relation (Kristensen & Jensen, 1979):

$$S_{ij}(\omega, r_2, r_3) = \frac{1}{U}\int\int_{-\infty}^{\infty} \Phi_{ij}(\mathbf{k})\exp\left[\mathrm{i}(k_2 r_2 + k_3 r_3)\right] dk_2 dk_3|_{k_1=\omega U^{-1}}, \tag{4.25}$$

where the TFTH has been applied to relate the longitudinal component of the vector wavenumber, k_1, with the angular frequency, ω, using the mean wind speed, U, and $i, j = 1, 2, 3$, represent the velocity components. Moreover, by assuming stationarity, the CMF $\gamma_{ij}(\tau, r_2, r_3)$, for the velocity components i and j at two points with spatial distance $\boldsymbol{r}$, and two times $t_2 - t_1 = \tau$ can be obtained using the expression of the well-known Wiener-Khintchine Theorem as:

$$\gamma_{ij}(\tau, r_2, r_3) = \int_{-\infty}^{\infty} S_{ij}(\omega, r_2, r_3)\exp(\mathrm{i}\tau\omega)d\omega. \tag{4.26}$$

In the present analysis, the target CPSDM and CMF, obtained from Mann's US-SVT model, are generated for three cases (see Table 4.2) by numerically integrating Equation (4.25) and by applying Fast Fourier Transform (FFT) techniques to represent expression (4.26), respectively.

Parameters	First case	Second case	Third case
U $[\mathrm{m\,s^{-1}}]$	10	10	10
L [m]	30	42	42
$\overline{u_{iso}^2}$ $[\mathrm{m^2\,s^{-2}}]$	1	0.79	0.79
Γ $[-]$	3.9	2.6	0
Velocity components	u, v, w	u, w	u
Number of grid points	1	2	4

Table 4.2: Parameters used in Mann's US-SVT model to generate the target CPSDM.

4.7 Results and discussion

The OCEAN approach was applied to three test cases to check its applicability to fit the CPSDM of different turbulence velocity fields. The parameters selected for the Mann's US-SVT model are shown in Table 4.2. In this table, the considered test cases are the following:

1. First test case: the three velocity components u, v, and w, at a single point, are considered. The aim is to check the capability of the proposed approach to fit the CPSDM generated for the three velocity components.
2. Second test case: the velocity components u and w are considered at two points. The objective is to assess the performance of the proposed method in reproducing two-points statistics.
3. Third test case: the target CPSDM was generated for the longitudinal velocity components u, at four grid points at the same height while applying zero shear, $\partial U/\partial z = 0$, along the vertical direction, to obtain two-points second order statistics of a stationary-homogeneous-isotropic turbulence velocity field (von Karman isotropic).

In the following sections, each test case is illustrated in detail. Note that the OCEAN approach is compared to the CMF-based approaches (Y-W,K-M, and CG) only for the first case.

4.7.1 Application to stationary, homogenous and anisotropic wind field at a single point (3 velocity components)

As discussed in Section 4.6, the Fourier pairs, the CMF and the CPSDM, are generated by utilizing the Mann's turbulence model, and they are used as targets for the proposed approach (OCEAN) and the presented state-of-the-art (Y-W, K-M, and CG) in this section. The generated CMF is utilized as a target for Y-W, K-M, and CG approaches. Whereas, for the OCEAN approach, the evaluated CPSDM is provided as a target (see Section 4.5.2). To measure the performance of each approach for reproducing the target CMF, the CMF error, E_Γ, is evaluated from the equivalent form of the Equation (4.24) for CMF. Whilst, to compare their performance for reproducing the CPSDM target, the CPSDM error, E_S, is computed from Equation (4.24). For this case study, the selected number of points is $M = 206$ along the lag interval of $[0, l_{\max}]$, where $l_{\max} = 205$, for the CMF case, as the target CMF is nearly equal zero at $l_{\max} = 205$. For the CPSDM case, the selected number of points is $M = 200$, for both the real and imaginary parts of the spectra, along the interval $[0, f_{\max}]$, where the time step $\Delta t = 0.25$ s and $f_{\max} = 2$ Hz. To avoid double-counting of the error corresponding to the cross spectra S_{ij} $(i \neq j)$, since $S^*_{ij}(f) = S_{ji}(f)$ as discussed in Section 4.4, only the upper triangle of the error matrix $S^t_{rq} - S^{\text{VAR}}_{rq}$ is considered. This is done by defining the error weight W_{rq} equal to 1, for $r \geq q$, and equal to zero, for $r < q$. Whereas, for the CMF, the error weight matrix is considered to be equal to $W_{rq} = 1$, since in general $\gamma_{ij,l} \neq \gamma_{ji,l}$, for $i \neq j$. However, only the positive lags are considered to avoid double-counting. Due to the computational burden associated with calculating the theoretical CMF, $\mathbf{\Gamma}^{\text{VAR}}$, the theoretical CMF for the VMA representation of the VAR model is evaluated instead for the minimization process.

In Figure 4.5, the E_Γ is represented for different values of the number of regression terms N for both OCEAN and CG approaches, together with the error E_Γ for the Y-W and K-M approaches. The CG approach shows lower values of the error E_Γ compared to the Y-W and K-M ones, which show the out-performance of searching for optimal models rather than assuming a predefined model structure. As expected, the E_Γ value for Y-W and K-M approaches decreases with increasing N. However, for $N \geq 7$, the E_Γ is almost constant for the K-M approach. This can be explained by the fact that including an additional regression term for lag $l = 2^8 = 256$ does not significantly improve the fitting of a target CMF that becomes very close to zero for such lag values. For $N \geq 4$, the highest E_Γ values were obtained for the OCEAN approach. This is due to the fact that the OCEAN approach is based on fitting the target CPSDM (that is directly reproducing spectral features).

Compared to all other approaches, the OCEAN approach shows the lowest E_S value. The error E_S decreases by increasing the model order $p = N$. Note that the computational burden of the optimization process is very high, and more computational resources would eventually lead to improved results for the proposed OCEAN approach. Figure 4.5 indicates that the VAR models determined from Y-W, K-M, and CG approaches, which are CMF-based approaches, are better for reproducing a predefined CMF. While the VAR model obtained from the proposed OCEAN approach, which is a CPSDM-based approach, is better for reproducing a predefined CPSDM. Thus, depending on the application, wind field synthesis

should be based on one or another approach, as discussed in Table 3.2.

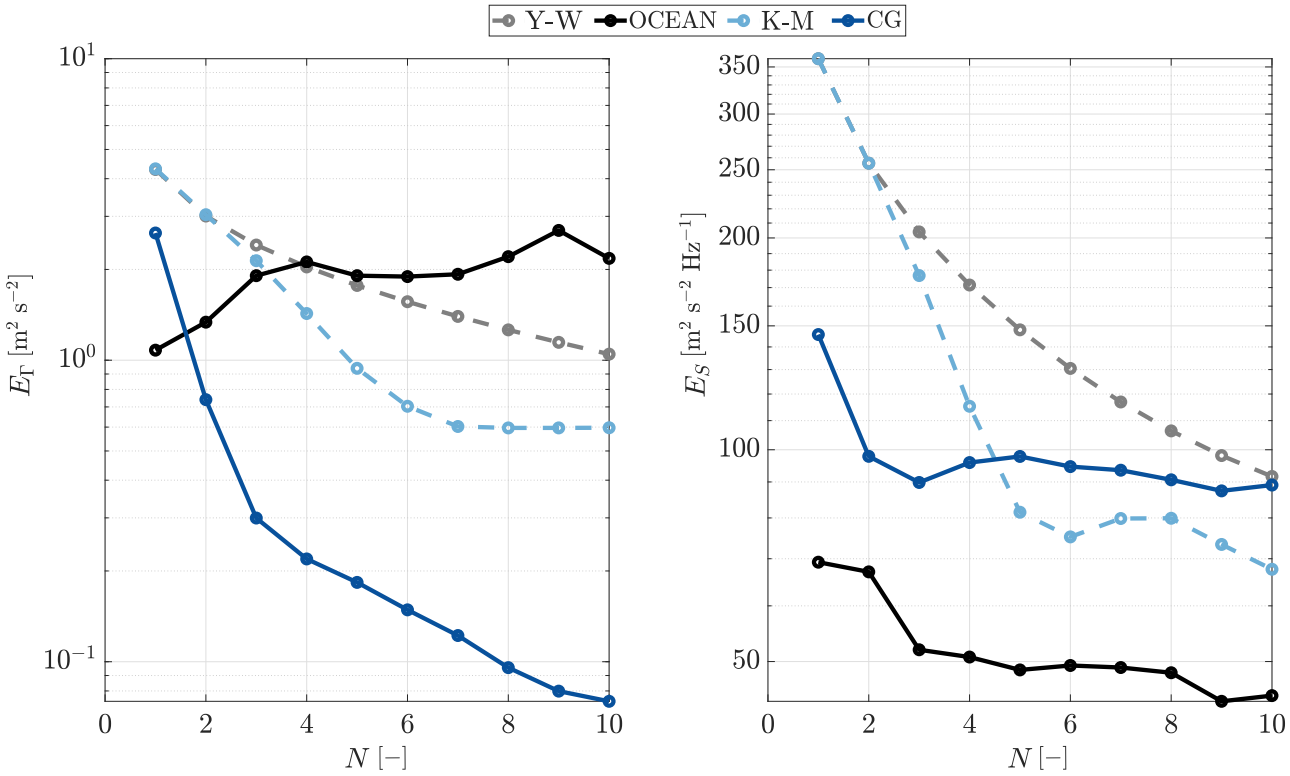

Figure 4.5: CMF error E_Γ (left) and CPSDM error E_S (right), as a function of the number of regression terms of the VAR model, N.

The performance of the optimal VAR($N = 10$) models, evaluated by OCEAN and CG approaches to reproduce the target CMF and the target CPSDM, is checked. The **j** and **l** vectors of the acquired optimal VAR through the CG approach are shown in Figure 4.6 against various values of the number of regression terms included. The optimal **j** and **l** vectors exhibit the same patterns as for the univariate case (see Section 3.7).

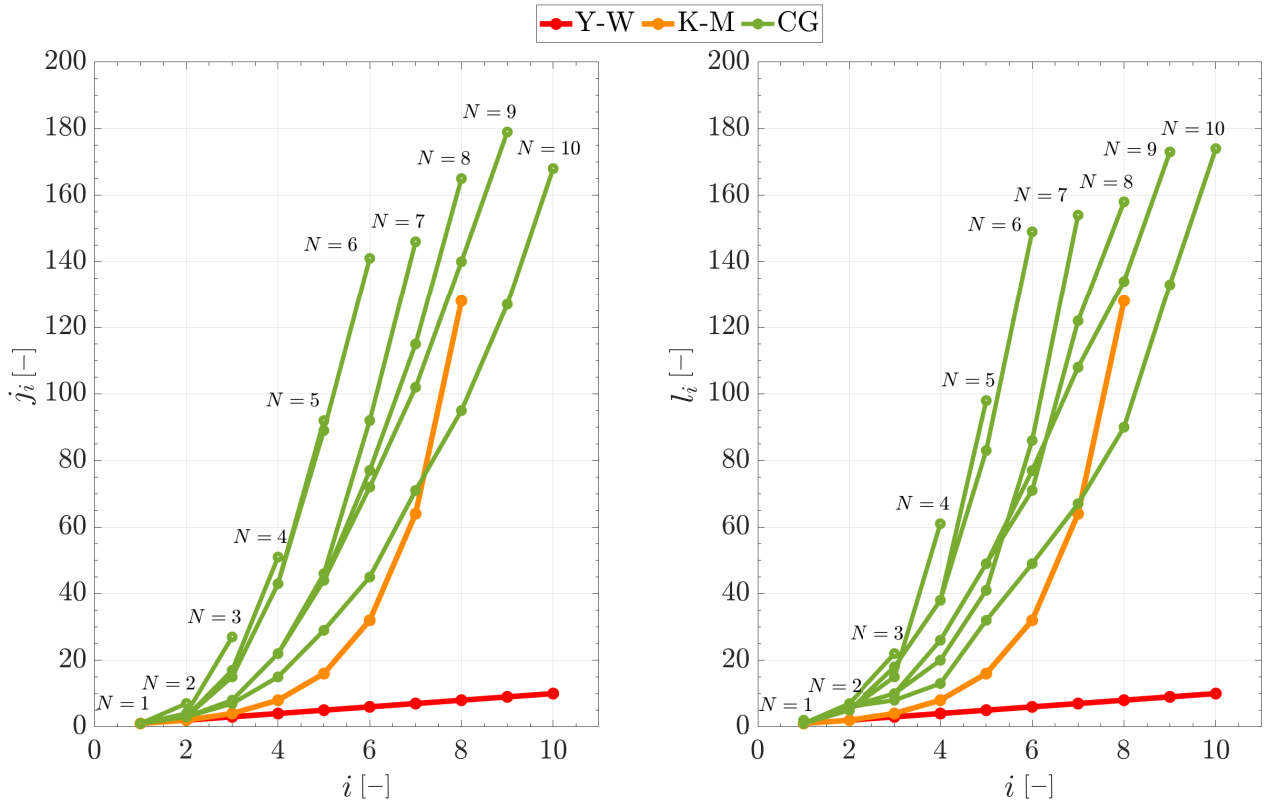

Figure 4.6: **j** and **l** vectors for the Y-W, K-M and CG approaches as a function of the number of regression terms of the VAR model, N.

The eigenvalues combination of the optimal VAR($N = 10$) model, obtained from OCEAN approach, is $N_{\lambda^r} = 4$ and $N_{\lambda^c} = 13$. Figure 4.7 depicts the obtained eigenvalues combination on the complex plane. The eigenvectors obtained for the optimal VAR($N = 10$) model, acquired from the OCEAN approach, are not shown due to the complexity of visualizing such high dimensional eigenvectors.

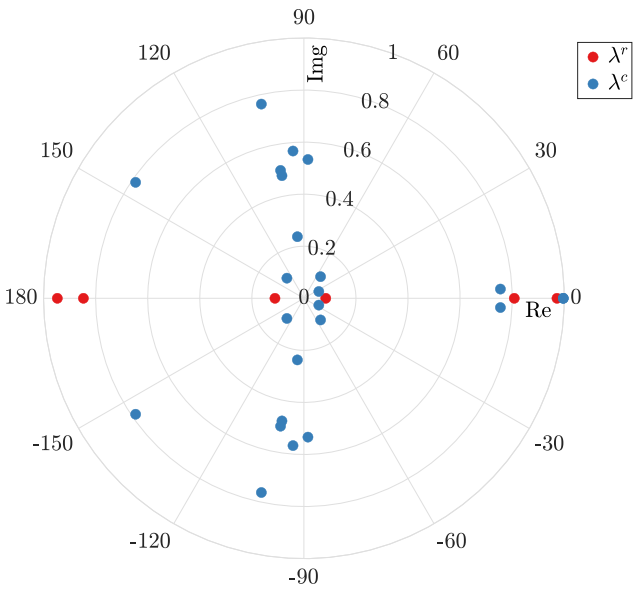

Figure 4.7: Real, λ^r, (red) and complex conjugate, λ^c, (blue) eigenvalues of the optimal VAR(10) model, obtained from OCEAN approach, presented on the complex plane.

Figures 4.8 and 4.9 show the real and imaginary parts of the theoretical one-sided spectra of the VAR, S_{ij}^{VAR}, obtained from CG and OCEAN approaches, for $N = 10$, together with the target CPSDM, S_{ij}^{t}. The OCEAN approach better fits the target CPSDM compared to other approaches. For the OCEAN approach, a good match to the target CPSDM was obtained at lower frequencies within the interval $f \in [10^{-3}, 10^{-2}]$ Hz for the components S_{11} and $\text{Re}\{S_{13}\}$. Whereas, for the spectrum of the vertical velocity component, S_{33}, a better fitting by the CG approach was obtained within the interval $f \in [10^{-3}, 10^{-1}]$ Hz. Note that the spectrum S_{33} might convey the impression that the CG approach is outperforming the OCEAN approach; however, the magnitude of the error obtained for the spectrum S_{33}, is lower compared to other spectra. In Figure 4.10, the theoretical CMF for the VMA model, γ_{ij}^{VMA}, obtained from CG and OCEAN approaches, together with the target CMF, γ_{ij}^{t}, are shown. The fitting of the CMF based on the CG approach is better than the one based on the OCEAN approach. The OCEAN approach underestimates the variance for the u and w velocity components and overestimates the variance for the v velocity component. Since the target CMF is provided for the CG approach until $l_{\text{max}} = 205$, the obtained spectra from the CG approach do not match the decrease in the spectra at low frequencies (See Appendix 6). Figures 4.8 and 4.9 show that the OCEAN approach is capable of fitting the predefined CPSDM over a wider range of frequencies than the other approaches, where the weights defined in the minimization function (see Equation (4.24)) can be employed to improve the fitting in any frequency range of interest, i.e., high frequency or more interestingly, the frequency range associated with the WT dynamics (Elagamy et al., 2021a). However, underestimation or overestimation of the variances of the wind velocity components could occur since the target CPSDM is fitted instead of the target CMF. Since the variance is the integral of the spectrum along the frequency interval ($\overline{i^2} = \int_0^\infty S_{ii}(f)df$, for $i = u, v, w$). Therefore, a good fit for the auto-spectra over the whole frequency interval is required to match the target variances. Whilst the variance of a velocity component is equal to the value

of the CMF at lag $l = 0$ ($\overline{i^2} = \gamma_{0,ii}$, for $i = u, v, w$). Thus, the CMF approach can readily match the target variances by matching only one point (lag $l = 0$).

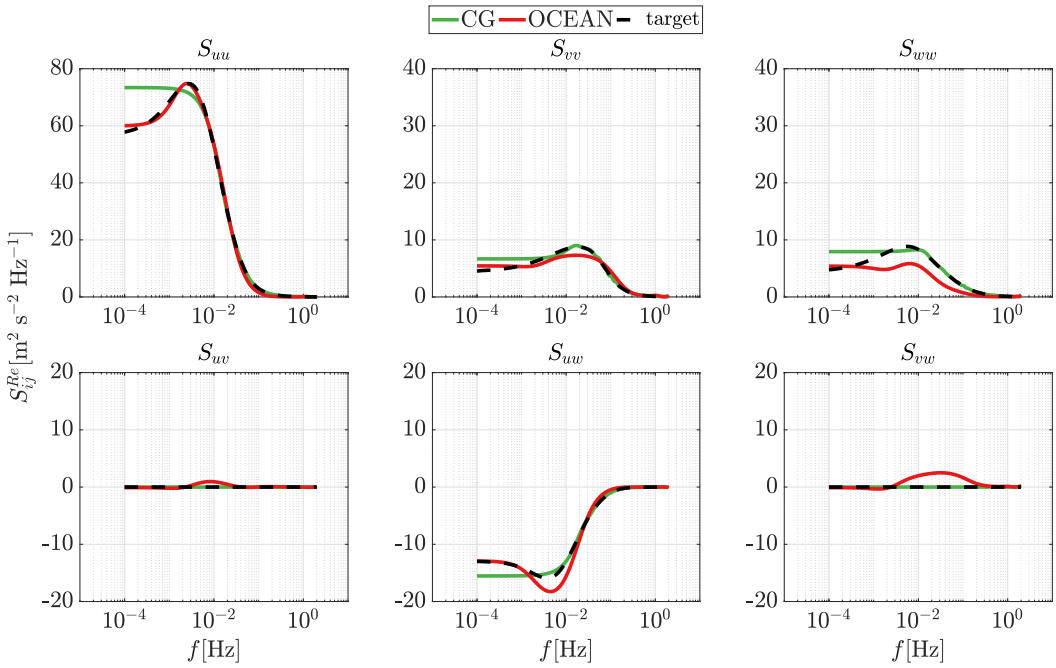

Figure 4.8: Real part of one-sided CPSDM of the VAR model, S_{ij}^{VAR}, for $N = 10$, in terms of frequency f, obtained from CG (green) and OCEAN (red) approaches, together with the target CPSDM, S_{ij}^{t} (black).

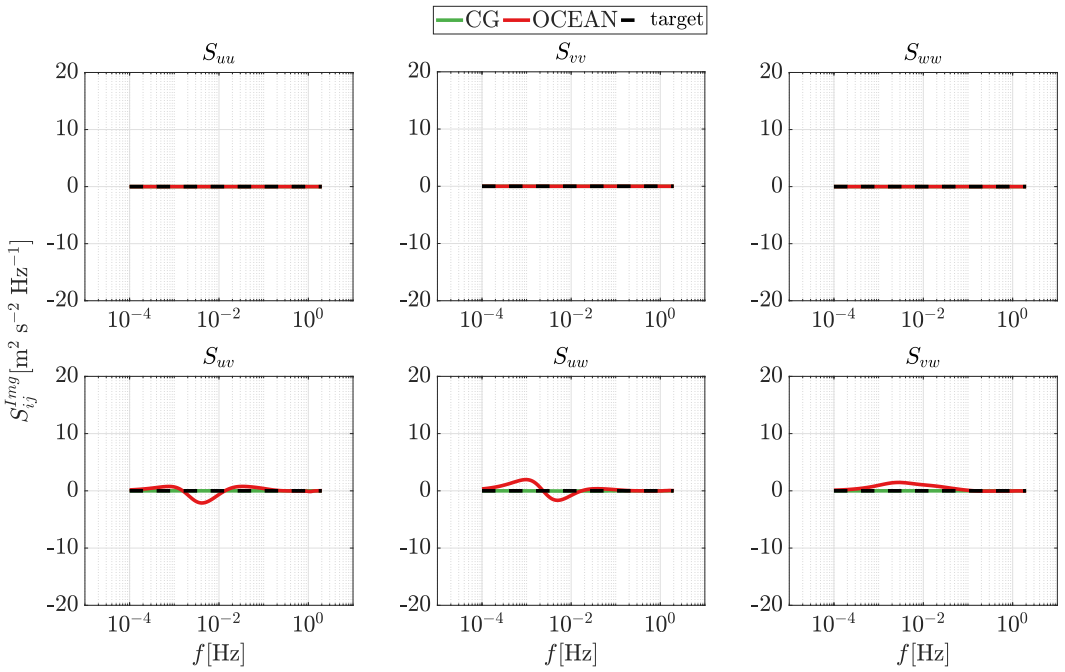

Figure 4.9: Imaginary part of one-sided CPSDM of the VAR model, S_{ij}^{VAR}, for $N = 10$, in terms of frequency f, obtained from CG (green) and OCEAN (red) approaches, together with the target CPSDM, S_{ij}^{t} (black).

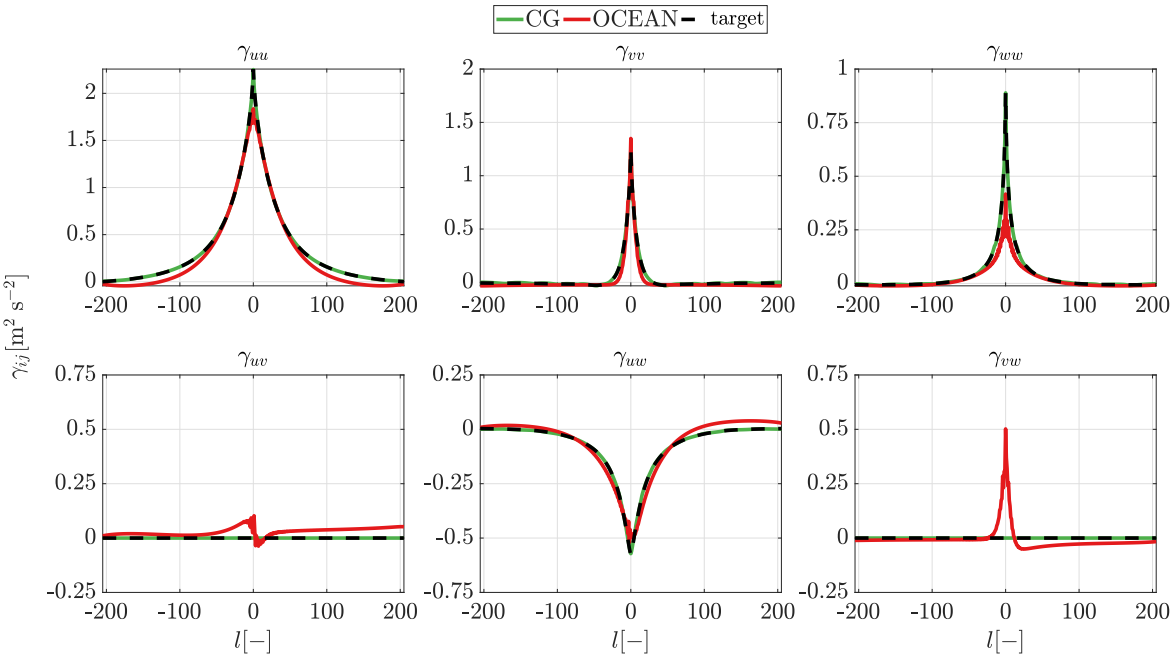

Figure 4.10: Theoretical CMF for the VAR model, $\gamma_{ij}^{\mathrm{VAR}}$, (obtained for VAR(10) model), obtained from CG (green) and OCEAN (red) approaches, versus the lag l together with target CMF, γ_{ij}^{t} (black).

Time series samples (realizations) of the longitudinal, lateral and vertical wind velocity components fluctuation, u, v and w, have been simulated for a time period $T = 3600$ s and with time step $\Delta t = 0.25$ s, by applying Equation (4.1) and using the VAR(10) model parameters obtained from the OCEAN approach. One of the synthesized sample time series is shown in Figure 4.11. The sample(s) variances for the three velocity components and the uw covariance are compared to the target values and the theoretical values in Table 4.3. The variances of the longitudinal and vertical velocity components, u and w, are underestimated (this behavior can also be observed in Figure 4.10). On the other hand, the variance of the lateral velocity component is overestimated. However, the covariance $\overline{uw}$ is well captured by the time series generated by the VAR(10) model. In Figures 4.12 and 4.13, the ensemble mean of the one-sided CPSDM of 10 samples, in terms of frequency f, together with the theoretical CPSDM VAR($N = 10$) model and the target CPSDM, is shown.

	$\overline{u^2}$ [m^2 s^{-2}]	$\overline{v^2}$ [m^2 s^{-2}]	$\overline{w^2}$ [m^2 s^{-2}]	$\overline{uw}$ [m^2 s^{-2}]
Target	2.25	1.25	0.88	-0.57
One sample	1.9	1.4	0.43	-0.53
10 samples	1.86 ± 0.14	1.36 ± 0.03	0.42 ± 0.02	-0.51 ± 0.05
VAR model	1.84	1.35	0.42	-0.5

Table 4.3: Variances of the longitudinal, lateral and vertical wind velocity components, $\overline{u^2}, \overline{v^2}$ and $\overline{w^2}$, and covariance, $\overline{uw}$, of the single sample of the time series generated from the VAR(10) model obtained by OCEAN approach, compared to the target variances and covariance.

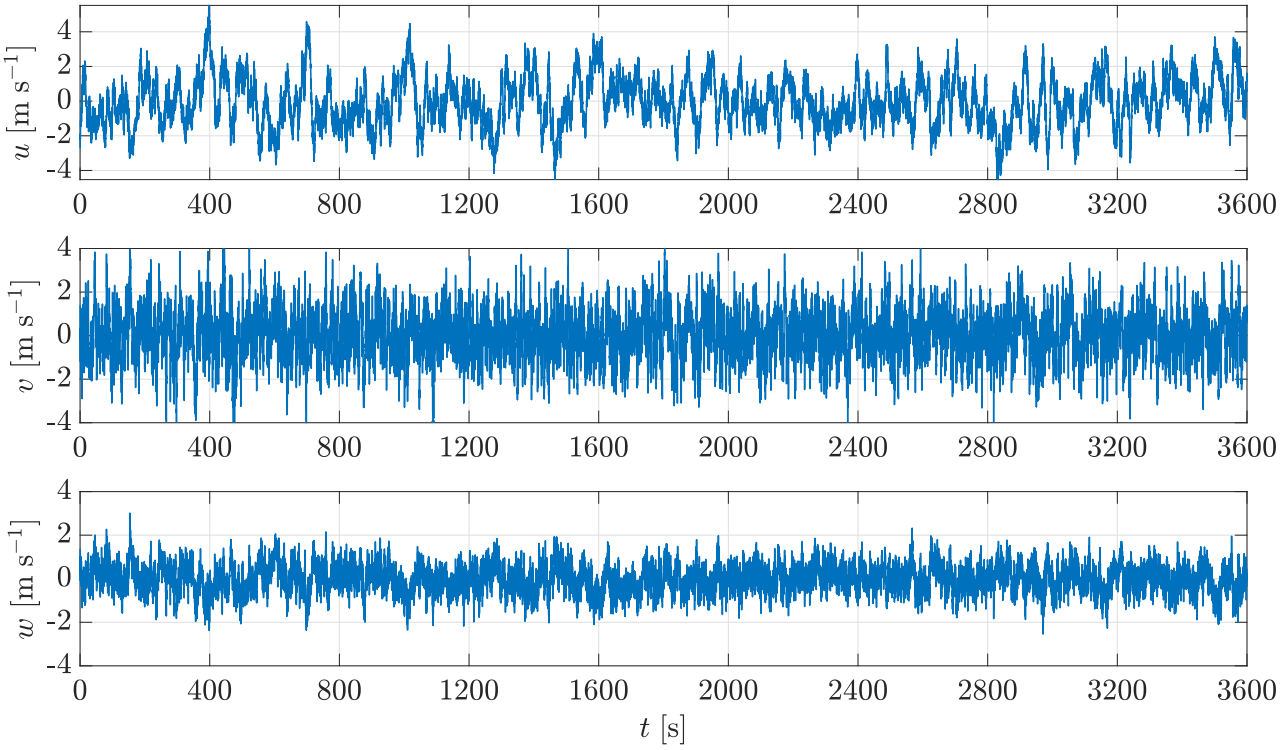

Figure 4.11: One sample (realization) of time series of the longitudinal, lateral and vertical wind velocity components fluctuation, u, v and w, generated by the VAR(10) model, obtained from OCEAN approach.

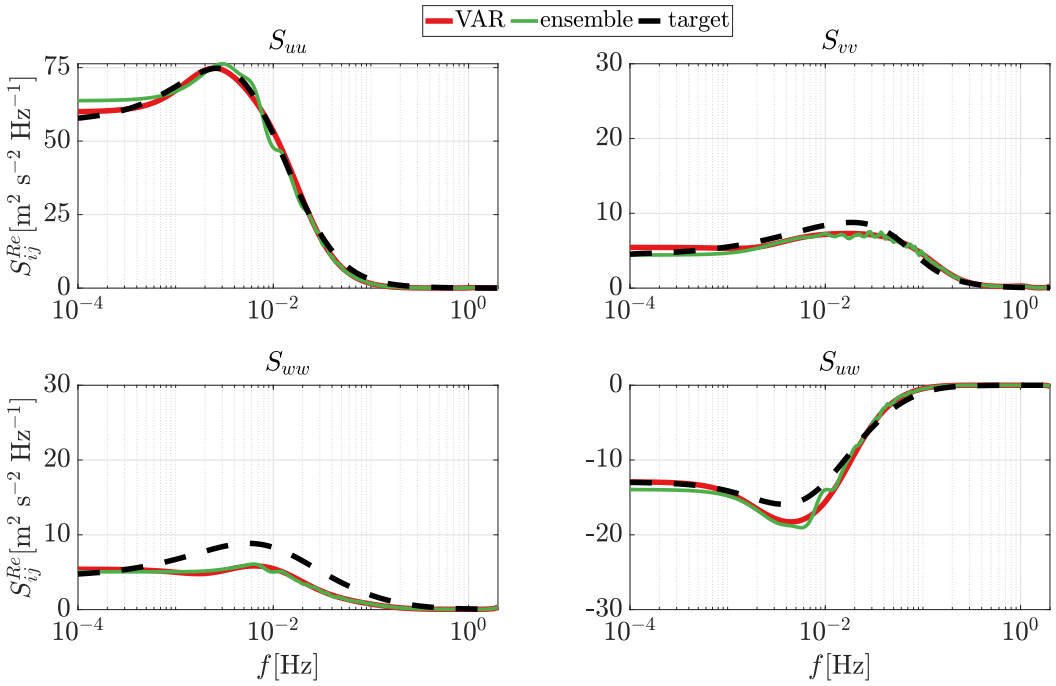

Figure 4.12: Real part of the one-sided CPSDM, S_{ij}^{Re}, in terms of frequency f, for: (a) theoretical CPSDM VAR($N = 10$) (red) obtained from OCEAN approach, (b) ensemble mean of the CPSDM evaluated for 10 samples (green) generated from VAR($N = 10$) obtained from OCEAN approach, and (c) target CPSDM (black).

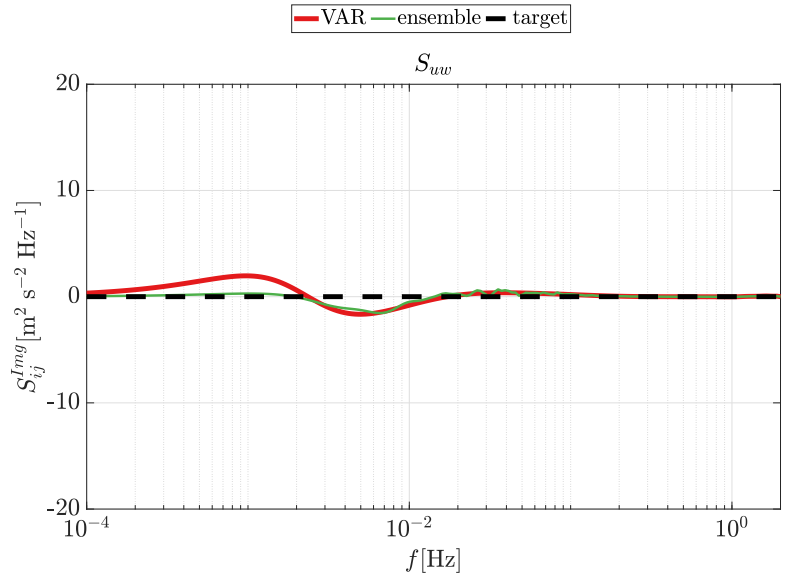

Figure 4.13: Imaginary part of the one-sided CPSDM, S_{13}^{Img}, in terms of frequency f, for: (a) theoretical CPSDM VAR($N = 10$) (red) obtained from OCEAN approach, (b) ensemble mean of the CPSDM evaluated for 10 samples (green) generated from VAR($N = 10$) obtained from OCEAN approach, and (c) target CPSDM (black).

4.7.2 Application to stationary, homogeneous and anisotropic wind field at two points (2 velocity components)

In this test case, the OCEAN approach is utilized to fit predefined CPSDM terms generated by Mann's US-SVT turbulence model for the u and w velocity components at two grid points. The aim of this test case is to check the applicability of the OCEAN approach to fit two-points spectra for different wind velocity components with different wind parameters. Since, as shown in the previous test case (Section 4.7.1), increasing the model order will lead to better fitting of the spectra; only the VAR(4) model was used in this test case. Similarly, as in the previous case, the selected number of points is $M = 200$, for both the real and imaginary parts of the spectra along the interval $[0, f_{\max}]$, where $f_{\max} = 10$ Hz (the selected time step $\Delta t = 0.05$ s). In Figure 4.14, the eigenvalues combination of the optimal VAR($N = 4$), is shown, where the optimal VAR(4) model has $N_{\lambda^r} = 12$ and $N_{\lambda^c} = 1$. In Figures 4.15 and 4.16, the theoretical VAR spectra and cross-spectral are shown against the target counterparts. As in the previous example, the obtained VAR spectra fit the peak generated within the frequency interval $[10^{-4}, 10^{-2}]$ Hz (see Appendix 6), where utilizing a higher VAR model order will result in a better match to the target spectra.

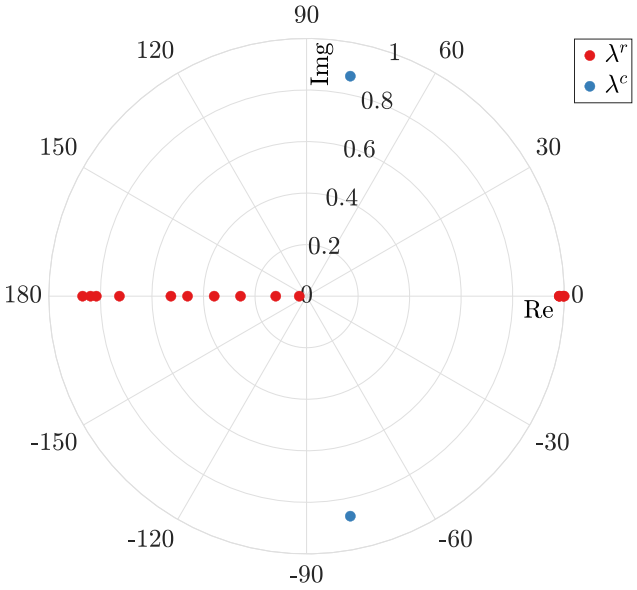

Figure 4.14: Real, λ^r, (red) and complex conjugate, λ^c, (blue) eigenvalues of the optimal VAR(4), obtained from OCEAN approach, presented on a complex plane. Results for the second test case.

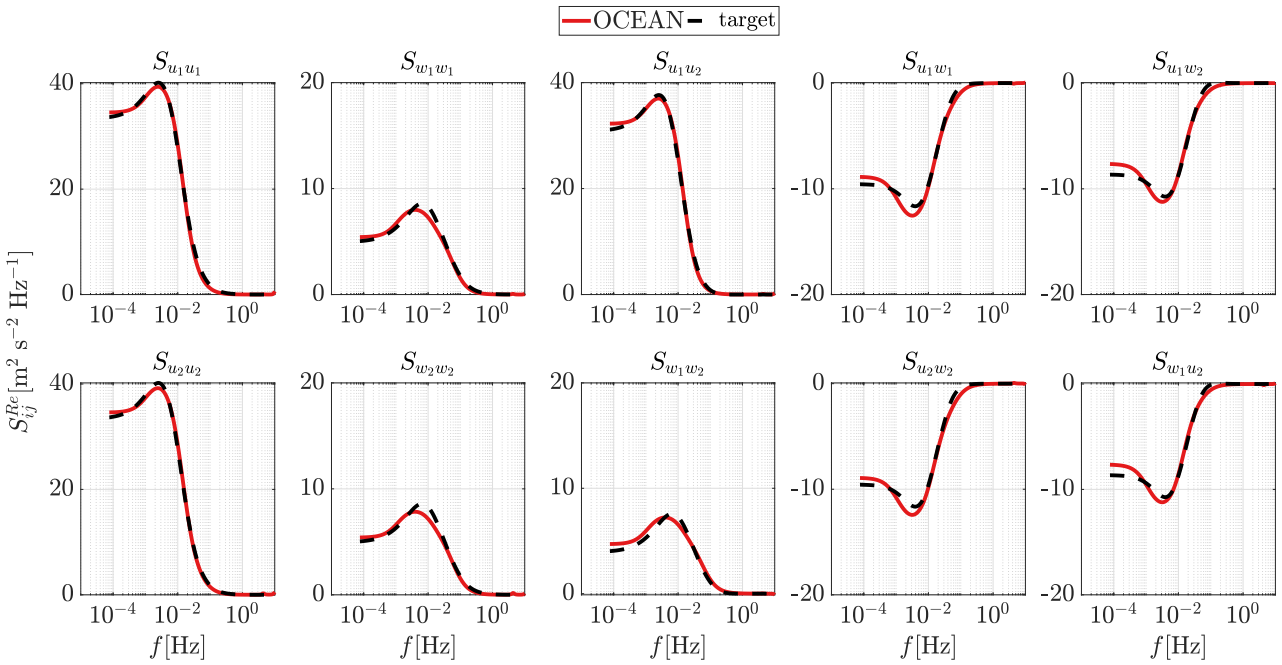

Figure 4.15: Real part of the one-sided CPSDM, S_{ij}^{Re}, in terms of frequency f, for: (a) theoretical CPSDM VAR($N = 4$) (red) obtained from OCEAN approach, and (b) target CPSDM (black). Results for the second case (see Table 4.2).

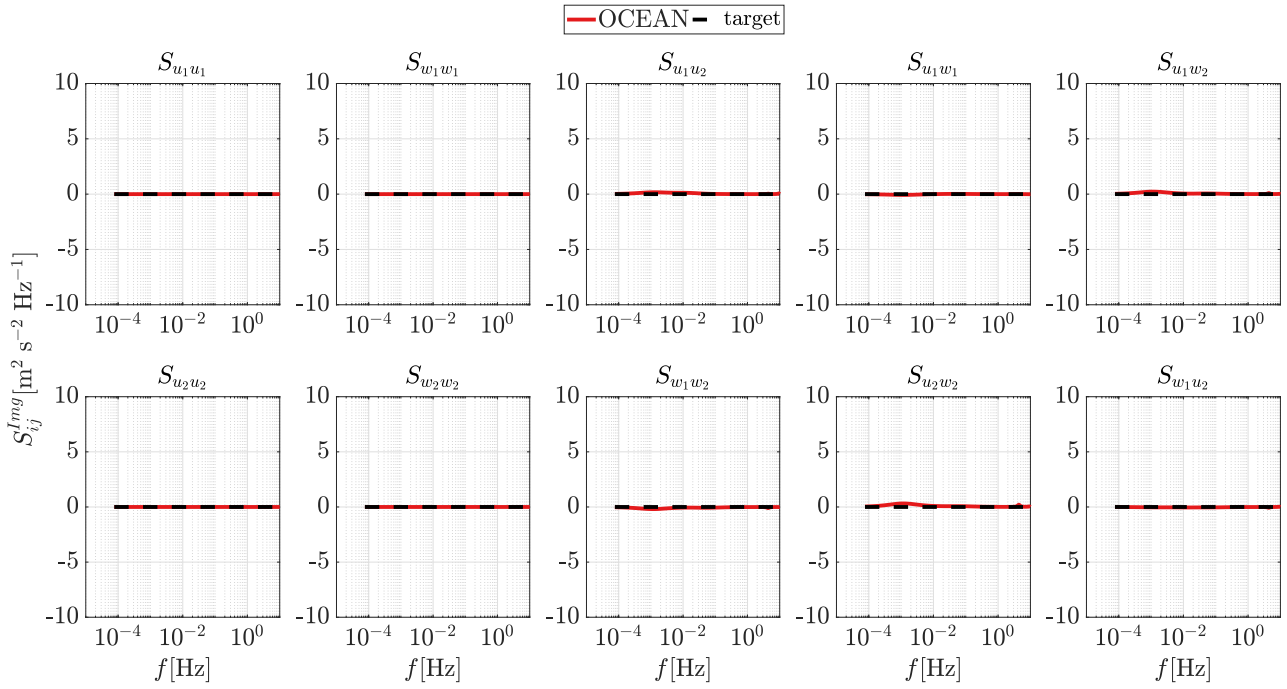

Figure 4.16: Imaginary part of the one-sided CPSDM, S_{ij}^{Img}, in terms of frequency f, for: (a) theoretical CPSDM VAR($N = 4$) (red) obtained from OCEAN approach, and (b) target CPSDM (black). Results for the second case (see Table 4.2).

As an example, a synthetic synthesized sample was generated with the optimal VAR(4) model for the u and w velocity components at the two considered grid points, and shown in Figure 4.17. The variances and covariance of the synthesized sample of the considered velocity components are shown in Table 4.4 against the theoretical VAR values and the target values. The VAR model overestimates the variances and the covariance; however, these overestimations can be reduced by increasing the VAR model order, p, since it will improve the fitting to the target spectra.

	$\overline{u_1^2}$ \ $\overline{u_2^2}$ [m^2 s^{-2}]	$\overline{w_1^2}$ \ $\overline{w_2^2}$ [m^2 s^{-2}]	$\overline{u_1w_1}$ \ $\overline{u_2w_2}$ [m^2 s^{-2}]	$\overline{u_1u_2}$ [m^2 s^{-2}]	$\overline{w_1w_2}$ [m^2 s^{-2}]
Target	1.25	0.76	-0.35	0.84	0.42
One sample	1.6 \2	0.77 \1	-0.57 \-0.47	1.3	0.49
VAR model	1.4 \1.9	0.73 \0.94	-0.48 \-0.4	1.1	0.45

Table 4.4: Variances and covariances of the longitudinal and vertical velocity components, of the single sample of the time series generated from the VAR(4) model obtained by OCEAN approach for the second test case, compared to the target variances.

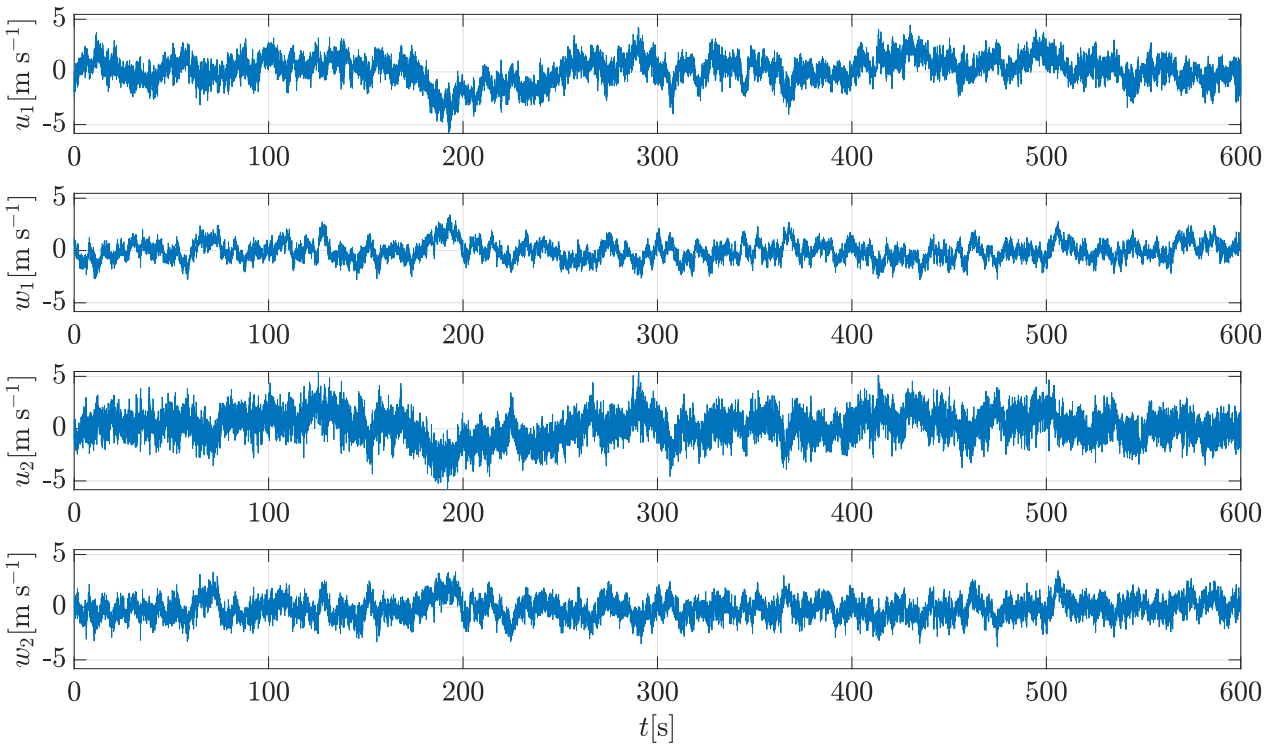

Figure 4.17: One sample (realization) of time series of the longitudinal and vertical wind velocity components fluctuation, u, w, generated with the VAR(4) model, obtained from OCEAN approach, for the second case (see Table 4.2).

4.7.3 Application to stationary, homogeneous and isotropic wind field at four points (one velocity component)

Another test case was applied to the OCEAN approach, where predefined spectra for a stationary-homogeneous-isotropic for the longitudinal velocity component are utilized as target CPSDM. The target CPSDM were obtained from the Mann's US-SVT model, utilizing the parameters outlined in Table 4.2. Similarly, as in the second test case, VAR($N = 4$) was considered to fit the target CPSDM. In this test case, the optimization parameters employed are similar to those utilized in the previous test cases. The eigenvalues combination of the optimal VAR($N = 4$), obtained for this test case, is $N_{\lambda^r} = 8$ and $N_{\lambda^c} = 4$ is shown in Figure 4.18. In Figure 4.19, the VAR CPSDM components and the target CPSDM components are shown. The obtained imaginary part of the VAR spectra and cross-spectra is nearly zero; thus, it was not included. As shown in Figure 4.19, a good fit to the target spectra was obtained by the VAR spectra. In Figure 4.20, the normalized spectrum, $fS^{Re}_{u_2u_2}/\overline{u_2u_2}$, for the longitudinal velocity component u_2, is shown together with the normalized theoretical VAR counterpart, the ensemble of the normalized spectra of 10 realizations and the target spectrum. There is a mismatch between the VAR spectrum and the target spectrum at high frequency, as shown in Figure 4.20. It should be noted that the mismatch observed is not a result of aliasing.

However, it is due to the low order of error magnitude at the high frequencies range compared to the low frequencies range, which leads the optimization process to prioritize fitting of the low-frequency interval over the high-frequency interval. This issue can be addressed by increasing the VAR model order p and/or using dissimilar error weights (W_{rq} in Equation (4.24)) for each frequency, which will force the optimization process to fit the frequency range of interest.

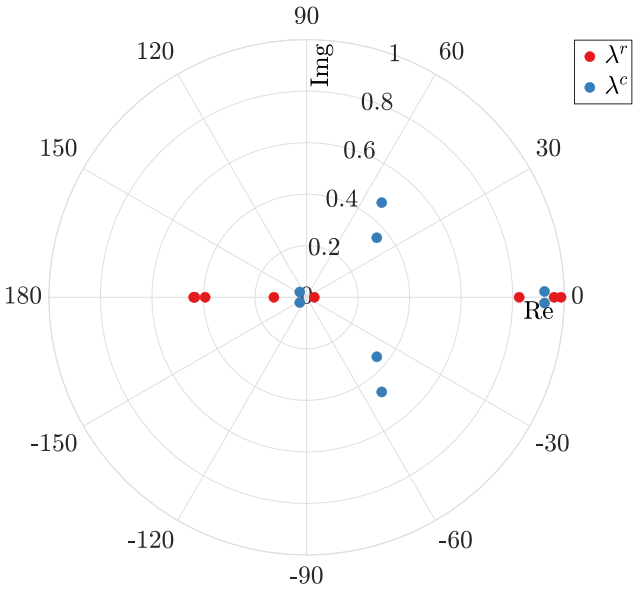

Figure 4.18: Real, λ^r, (red) and complex conjugate, λ^c, (blue) eigenvalues of the optimal VAR(4), obtained from OCEAN approach, presented on a complex plane. Results for the third test case.

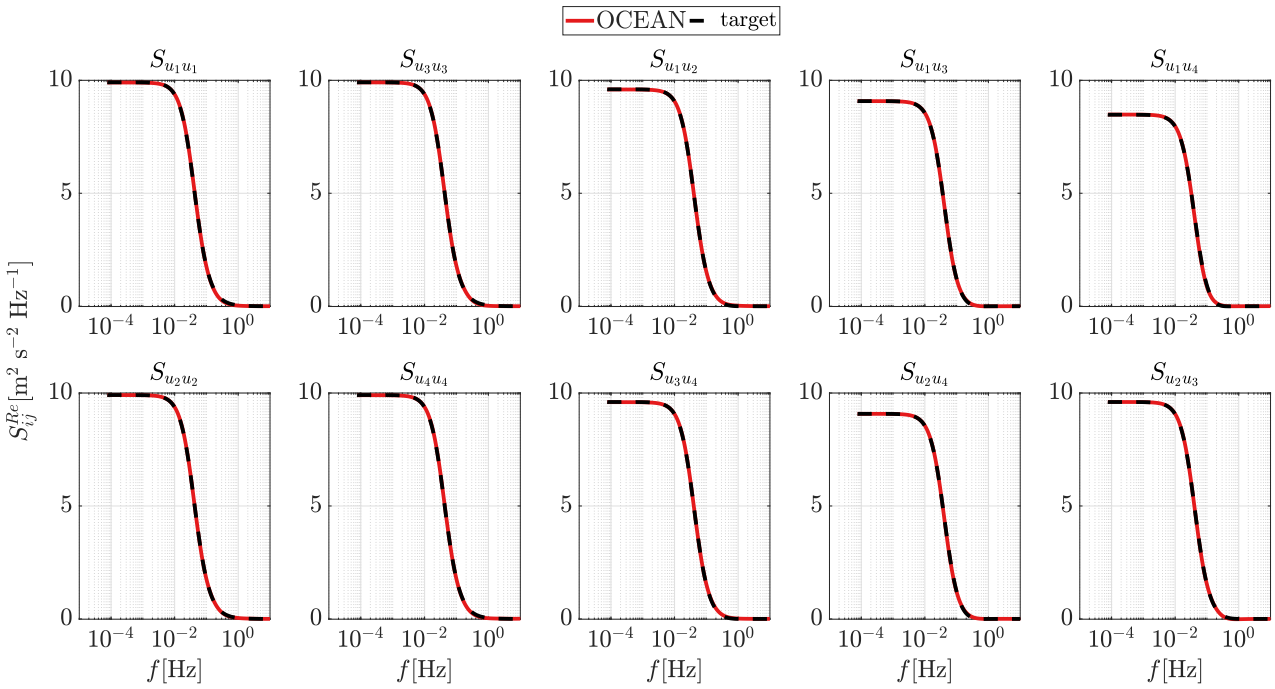

Figure 4.19: Real part of the one-sided CPSDM, S_{ij}^{Re}, in terms of frequency f, for: (a) theoretical CPSDM VAR($N = 4$) (red) obtained from OCEAN approach, and (b) target CPSDM (black). Results for the third case (see Table 4.2).

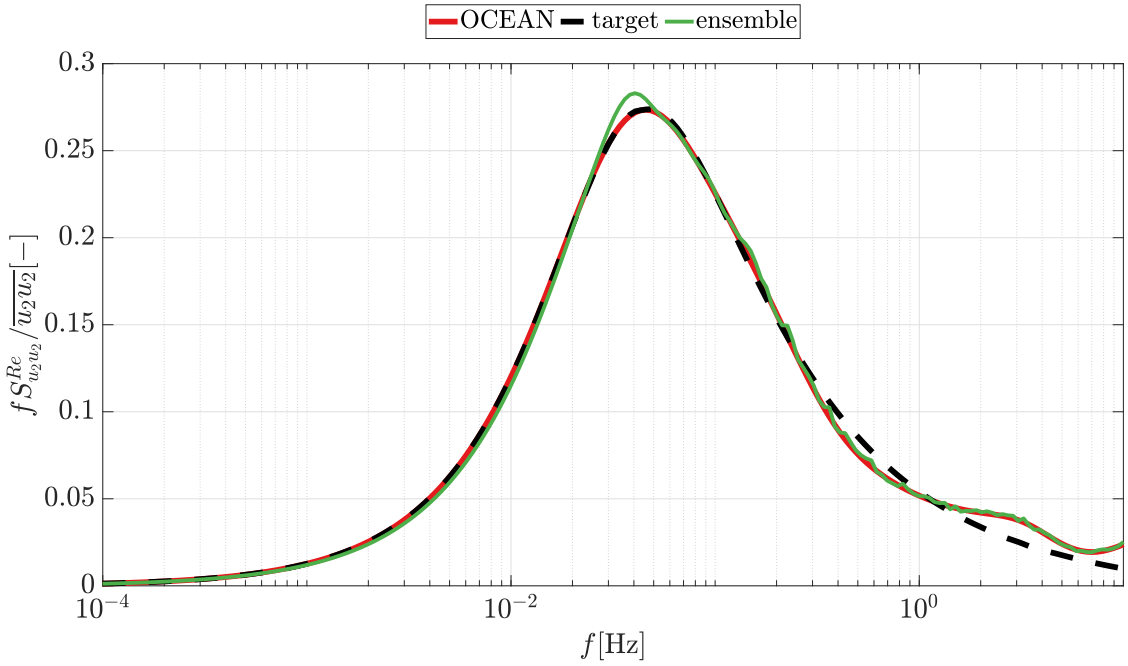

Figure 4.20: Real part of the one-sided normalized spectrum, $fS^{Re}_{u_2u_2}/\overline{u_2u_2}$, at the second grid point, in terms of frequency f, for: (a) the ensemble of 10 samples (b) theoretical CPSDM VAR($N = 4$) (red) obtained from OCEAN approach, and (c) target CPSDM (black). Results for the third case (see Table 4.2).

Figure 4.21 shows one synthesized sample time series for the longitudinal velocity component, u, for the four grid points. The variances of the synthesized sample for the four longitudinal velocity components are shown in Table 4.5, together with the theoretical value of the variances and the target values. As shown in Table 4.5, the variances of the target are well captured by the VAR(4) model.

	$\overline{u_1^2}$ \ $\overline{u_2^2}$ [m^2 s^{-2}]	$\overline{u_3^2}$ \ $\overline{u_4^2}$ [m^2 s^{-2}]	$\overline{u_1u_2}$ \ $\overline{u_3u_4}$ [m^2 s^{-2}]	$\overline{u_1u_3}$ \ $\overline{u_2w_4}$ [m^2 s^{-2}]	$\overline{u_1u_4}$ [m^2 s^{-2}]
Target	0.78	0.78	0.61	0.51	0.43
One sample	0.74 \0.8	0.75 \0.83	0.68 \0.69	0.53 \0.58	0.48
VAR model	0.73 \0.78	0.72 \0.79	0.66	0.51 \0.54	0.45

Table 4.5: Variances and covariances of the longitudinal velocity component, at 4 grid points, of the single sample of the time series generated from the VAR(4) model obtained by OCEAN approach for the third test case, compared to the target variances.

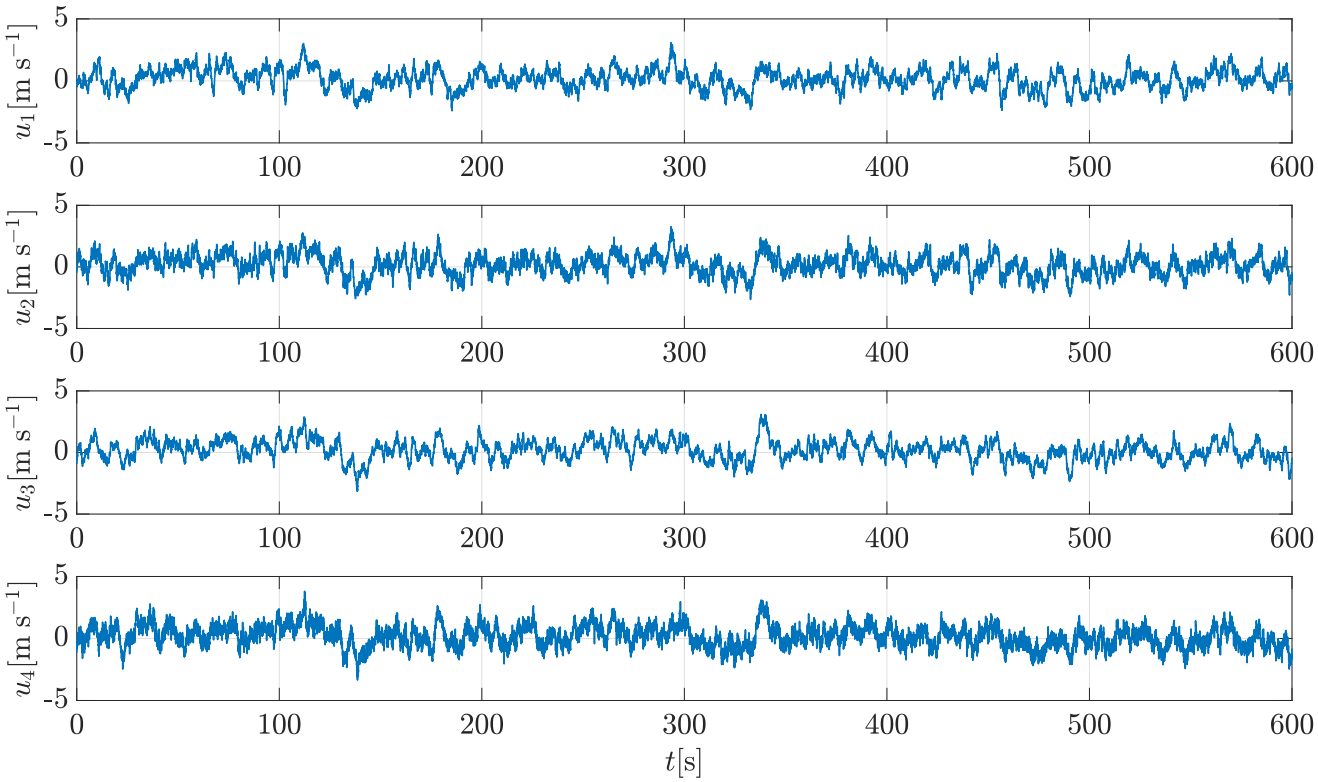

Figure 4.21: One sample (realization) of time series of the longitudinal wind velocity component fluctuation, u_i, generated by VAR(4) model, obtained from OCEAN approach, for the third case (see Table 4.2).

4.8 Conclusions

This study presents an approach to obtain an optimal VAR model from fitting second-order statistics of turbulent wind field described in the frequency domain (predefined CPSDM), where both real and imaginary parts of the CPSDM are considered. Fitting the CPSDM is crucial as the CPSDM of the simulated turbulent wind field is a turbulence property driver of the fatigue loads experienced by the wind turbine. The proposed approach, referred to as "OCEAN" approach, can be used for the synthetic generation of stationary, homogeneous/non-homogeneous, and isotropic/anisotropic turbulent wind fields since the fitting process of the proposed approach to the target CPSDM is independent of the statistical information represented in the predefined CPSDM. The proposed approach is based on the eigenanalysis of the companion matrix of VAR(1) representation of a VAR(p) model. The proposed approach is applied to a predefined target CPSDM generated from Mann's turbulence model.

A comparison between the proposed CPSDM and CMF-based approaches (state-of-the-art) was made to fit a target CPSDM and a target CMF. The proposed approach better matches the CPSDM than the approaches based on fitting target CMF. However, a better fit to the

target CMF is obtained by the CMF-based approaches than by the OCEAN approach. The CG approach proved to be the most effective in fitting the target CMF, as it involves the search for optimal combinations of the **j** and **l** vectors that result in the closest match between the VAR CMF and the target CMF. The optimal **j** and **l** vectors displayed a pattern resembling a power function a^n with $a \neq 2$, which is the case explored in (Krenk & Møller, 2019). The present approach does not require extra pre-processing to obtain the CMF from advanced turbulence models described in the spectral domain as for the CMF-based approaches.

The main challenge of the OCEAN and CG approaches is the required computational cost due to the optimization process, and additional work is required to reduce it. In the same line, fitting the CPSDM and CMF for multiple points on the rotor plane on the wind turbine needs to be investigated to reduce the computational cost. Moreover, applying the OCEAN and CG approaches to match the CPSDM and CMF acquired from the turbulence model, LES, and experiments for different flow conditions (i.e., complex terrain, urban environment) is to be studied.

Chapter 5

Investigation of the impact of a high-rise building on the statistical characteristics of turbulent wind fields in a characteristicsurban environment

The results shown in this chapter have been included in a submitted article, which is under review (Elagamy et al., n.d.).

This chapter investigates the statistical characteristics of urban wind fields, particularly over a single High-Rise Building (HRB). The methodologies represented can be readily reproduced on more complex urban environments. A LES study builds upon the previous research done by (Šarkić Glumac et al., 2018a; Hemida et al., 2020; Vita et al., 2020) is presented in the following sections. The contribution of this work can be divided into two parts. Firstly, two possible locations for the SWT were further investigated by analyzing the two-points two-times second-order statistics of the velocity field, such as the spectra and the covariance at different height levels along a vertical line at the rooftop, as well as providing the coherence of the wind field. Additionally, the characteristics of the wind field on a vertical plane rather than just a vertical line at the possible WT locations are analyzed. Secondly, the impact of the HRB on the wind field characteristics was investigated. The results of the isolated building were compared to a LES simulation conducted without including the isolated building to analyze its influence on the wind field characteristics. The obtained second-order statistics of the wind field at the HRB rooftop from the conducted LES study are used as inputs for the synthetic approaches to generate synthetic urban wind fields (see Chapter 6).

5.1 Preliminary definitions employed to compute wind field characteristics

This section introduces preliminary definitions of the statistical characteristics of wind fields.

5.1.1 Transformation from the LES reference system to the streamlines coordinates reference system

The wind velocity components expressed in the LES coordinates system are identified by subindex "s" and are transformed to the streamwise coordinates system as follows (J. C. Kaimal & Finnigan, 1994):

$$\begin{bmatrix} \tilde{u} \\ \tilde{v} \\ \tilde{w} \end{bmatrix} = \begin{bmatrix} \cos(\gamma_s) & 0 & \sin(\gamma_s) \\ 0 & 1 & 0 \\ -\sin(\gamma_s) & 0 & \cos(\gamma_s) \end{bmatrix} \begin{bmatrix} \cos(\varphi_s) & \sin(\varphi_s) & 0 \\ -\sin(\varphi_s) & \cos(\varphi_s) & 0 \\ 0 & 0 & 1 \end{bmatrix} \begin{bmatrix} \tilde{u}_s \\ \tilde{v}_s \\ \tilde{w}_s \end{bmatrix}, \tag{5.1}$$

where the velocity components $\tilde{u}, \tilde{v}$ and $\tilde{w}$, with no subscript, indicate that the velocity time series are expressed in the streamwise coordinates system, φ_s is the mean wind direction during the evaluated period and γ_s is the mean inclination angle during the analyzed period. φ_s leads to a rotation around the z-axis and γ_s to rotate around the y-axis. The $\varphi_s[^\circ]$ and $\gamma_s[^\circ]$ angles are calculated as follows:

$$\varphi_s = \frac{180}{\pi} \tan^{-1}_{\pi,-\pi}(V_s, U_s) \quad \text{and} \quad \gamma_s = \frac{180}{\pi} \tan^{-1}_{\frac{\pi}{2},-\frac{\pi}{2}}(W_s, U_h). \tag{5.2}$$

where U_h is the horizontal wind velocity ($U_h = \sqrt{U_s^2 + V_s^2}$), U_s, V_s and W_s are the mean values of the $\tilde{u}_s$, $\tilde{v}_s$ and $\tilde{w}_s$ velocity components, respectively. Note that Equation (5.2) corresponds to MATLAB notation $(180/\pi)\text{atan2}(x, y)$.

5.1.2 Mean velocity and turbulence intensities

The wind velocity vector $[\tilde{u}, \tilde{v}, \tilde{w}]^T$ is expressed by Reynolds's decomposition (Pope, 2000):

$$\begin{bmatrix} \tilde{u} \\ \tilde{v} \\ \tilde{w} \end{bmatrix} = \begin{bmatrix} U \\ V \\ W \end{bmatrix} + \begin{bmatrix} u \\ v \\ w \end{bmatrix}, \tag{5.3}$$

where $[U, V, W]^T$ is the mean value (here considered as time average, i.e., statistical stationarity is considered) of the wind velocity vector, and $[u, v, w]^T$ is its fluctuation.

Additionally, the turbulence intensity of each velocity component, $I_i = \sqrt{\overline{i^2}}/S$, for $i = u, v, w$, is evaluated by dividing its variance, $\overline{i^2}$ (where the overline $\overline{(\cdot)}$ refers to time average), of the $i-$velocity component by the local mean wind speed defined as $S = \sqrt{U^2 + V^2 + W^2}$.

5.1.3 Autocovariance functions and integral length scales

The integral length scales in the $x-$direction, $L_i^x = ST_i$, are calculated from the corresponding integral time scales T_i and the application of the TFTH (Panofsky & Dutton, 1984; J. C. Kaimal & Finnigan, 1994). The integral time scale is defined as $T_i = \int_0^{\tau^*} \gamma_{ii}(\tau)/\overline{i^2} d\tau$, where τ is the time lag, τ^* is the upper limit of the integration and $\gamma_{ii}(\tau)$ is the ACF of the $i-$velocity

component fluctuation. The first zero-cross approach is considered to define τ^*, where τ^* is set to the time lag at which the ACF reaches its first zero value (Panofsky & Dutton, 1984; Emes et al., 2016).

5.1.4 Spectra, cross-spectra and spatial coherence functions

The spatial coherence, $coh_i(f, \Delta z)$, for $i = u, v, w$, as a function of frequency f and a vertical separation distance Δz, is defined as (Burton et al., 2011):

$$coh_i(f, \Delta z) = \frac{|S_{i_A i_B}(f)|^2}{S_{i_A i_A}(f) S_{i_B i_B}(f)}, \tag{5.4}$$

where $S_{i_A i_A}$ and $S_{i_B i_B}$ are the PSD, $S_{i_A i_B}$ is the PSD, the sub-index $(\cdot)_A$ and $(\cdot)_B$ refer to the grid points at (x, y, z) and $(x, y, z + \Delta z)$, respectively.

5.2 Description of the reference LES analysis and the experimental database

This section briefly describes the setup of the reference wind tunnel experiment, which was carried out by (Hemida & Šarkić, 2014; Šarkić Glumac et al., 2018a; Hemida et al., 2020; Vita et al., 2020). Additionally, it illustrates the setup of the reference LES simulations done by (Vita, 2020; Vranešević et al., 2022), which were used as part of the validation for the LES study done in the present work.

5.2.1 Wind tunnel experiments database

Wind tunnel experiments were conducted at the atmospheric boundary layer Wind Tunnel Lab of Ruhr-Universität Bochum (RUB), Germany, to investigate the wind flow over the rooftop of HRBs (Hemida & Šarkić, 2014; Šarkić Glumac et al., 2018a; Hemida et al., 2020; Vita et al., 2020). In the present work, only the wind direction perpendicular to the windward face of the building is considered. The experimental data may be accessed as Mendelay Data in (Šarkić Glumac et al., 2018b, 2020). Figure 5.1a shows the model of the single HRB along with the Hot-Wire Anemometer (HWA) and the traverse system, which is used to take measurements above the rooftop. The HWA is utilized to measure the u and w velocity components in the x and $z-$directions, respectively. Notably, the probe could not account for reverse flow (Vita et al., 2020; Vita, 2020). The building model has a height $H = 0.4$ [m] and a width $D = H/3 \approx 0.13$ [m]. In Figure 5.1b, the measurement locations at the rooftop are depicted. The six considered locations are the middle of the rooftop (m_1), the windward and leeward corners (c_1, c_2, c_3), and the edges of the windward and leeward (e_1, e_2).

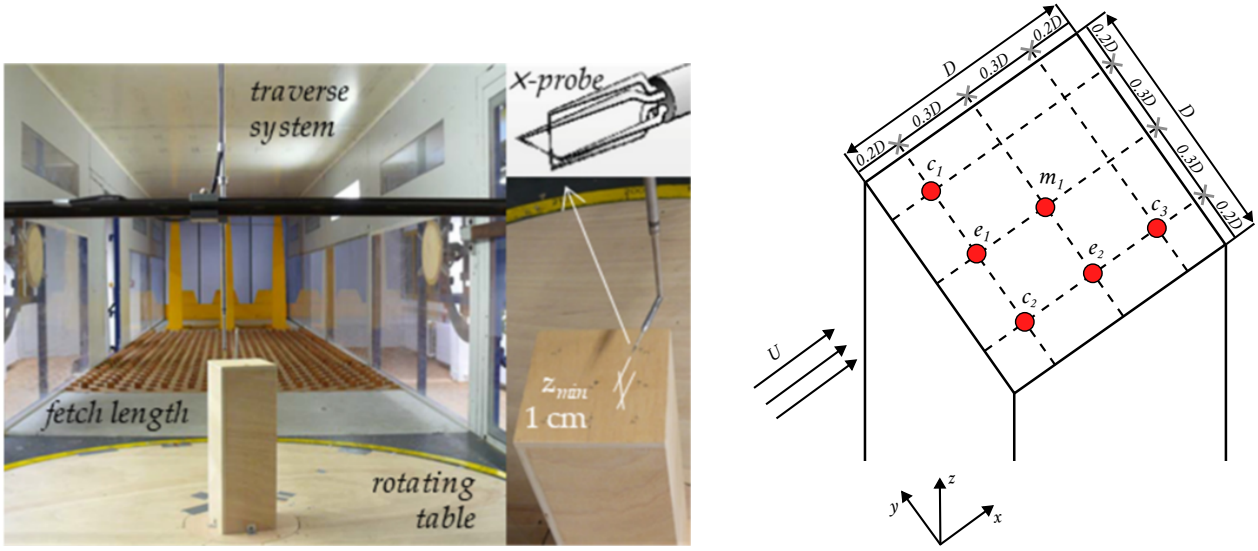

(a) (b)

Figure 5.1: (a) Wind tunnel in RUB with the building model (Vita, 2020) (Figure adapted from (Vita et al., 2020)) and (b) the locations of the measurements of the HWA on the rooftop.

The turbulent inflow was generated in the wind tunnel by a long fetch equipped with wood blocks (see Figure 5.1b) and fits the power law profile:

$$U(z) = U_{ref}\left(\frac{z}{z_{ref}}\right)^{\alpha_e}, \tag{5.5}$$

with exponent $\alpha_e = 0.2$ and a reference velocity $U_{ref} = 16$ [m s^{-1}] at the reference height $z_{ref} = H$. The turbulent inflow generated is representative of a terrain category II defined in the Eurocode (Eurocode, 2005; Vita et al., 2020). Figure 5.2 shows the non-dimensional mean wind longitudinal velocity profile, U/U_{ref} of the conducted LES simulation and the corresponding from the reference experiment and the power law profile. The longitudinal and vertical turbulence intensities, I_u and I_w, are also shown with their corresponding experimental values. Further information about the wind tunnel experiment can be found in (Hemida & Šarkić, 2014; Šarkić Glumac et al., 2018a; Hemida et al., 2020; Vita et al., 2020). The Reynolds number based on the building width D is equal to

$$\mathrm{Re} = DU_{ref}/\nu_{air} = 1.4 \times 10^5.$$

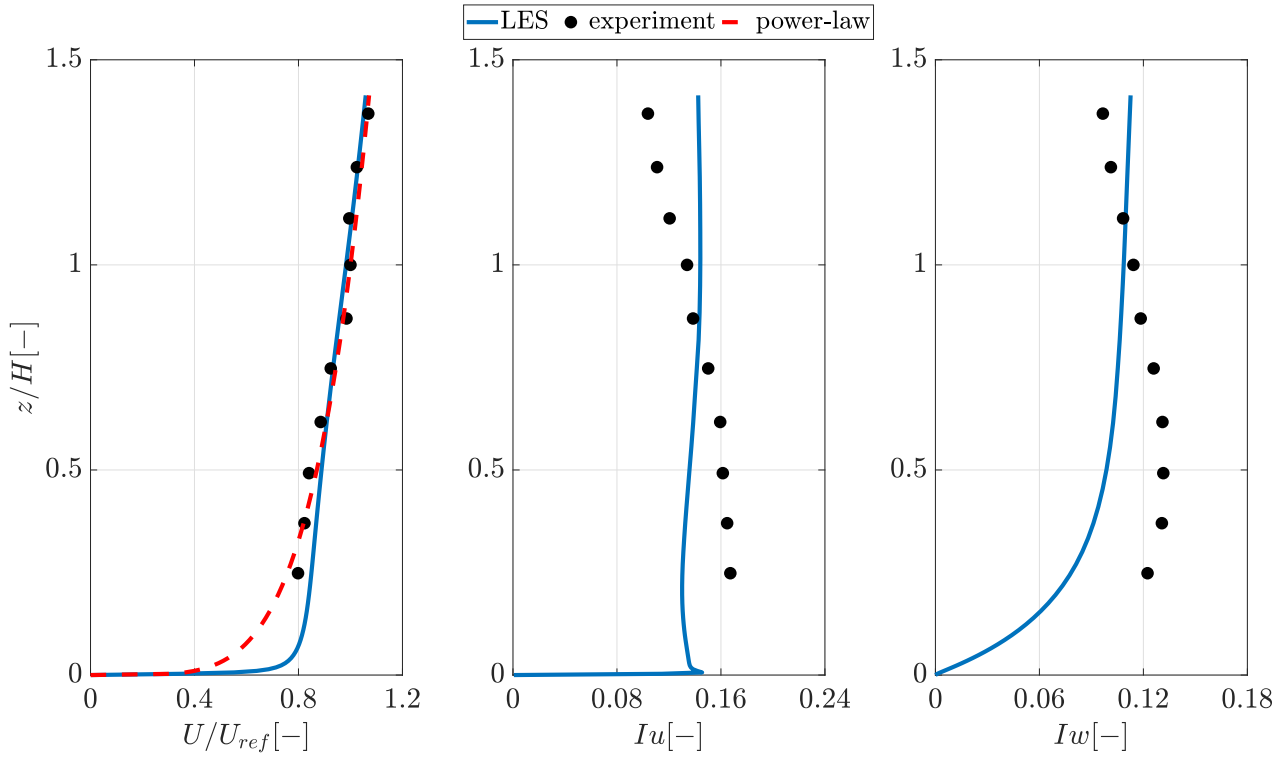

Figure 5.2: Comparison of the LES turbulent inflow, the experiment turbulent inflow and the power law. [left] Non-dimensional mean speed profile, U/U_{ref}, [middle] longitudinal turbulence intensity, I_u, and [right] vertical turbulence intensity, I_w.

5.2.2 LES analysis database

In addition to the wind tunnel experiments, LES simulations were conducted in OpenFOAM by (Vita, 2020) and (Vranešević et al., 2022), modeling a virtual wind tunnel similar to the wind tunnel of RUB. The turbulent inlet in the LES simulations was generated with roughness cubes and barriers at the inlet of the computational domain. (Vita, 2020) used the Smagornisky-Lilly model (Smagorinsky, 1963; Lilly, 1962) as the Sub-Grid Scale (SGS) model in the LES simulation, whereas, (Vranešević et al., 2022) used the Wall-Adapting Local Eddy-viscosity (WALE) model (Nicoud & Ducros, 1999). In the following sections, these reference LES simulations will be referred to as LES-Vita and LES-Vranešević. The results from both reference LES simulations for the e_1 and m_1 locations at the rooftop were used to assess the LES study done in the present work.

5.3 Numerical methodologies

This section provides an overview of the governing equations and the simulation setup employed in the LES study. Moreover, it introduces the SRM utilized for generating turbulent inflow in the LES study. Additionally, it covers the parametric investigation conducted to

determine the values of the parameters applied in the Mann turbulence model.

5.3.1 Governing equations

The governing equations for LES are obtained by spatial filtering of the incompressible NS equations as follows (Pope, 2000; Wyngaard, 2010):

$$\begin{aligned} \frac{\partial \tilde{u}_i^r}{\partial x_i} &= 0, \\ \frac{\partial}{\partial t}\left(\tilde{u}_i^r\right) + \frac{\partial}{\partial x_j}\left(\tilde{u}_i^r \tilde{u}_j^r\right) &= \nu \frac{\partial^2 \tilde{u}_i^r}{\partial x_j \partial x_j} - \frac{1}{\rho}\frac{\partial \tilde{p}^r}{\partial x_i} - \frac{\partial \tau_{ij}}{\partial x_j}, \end{aligned} \tag{5.6}$$

where $\tilde{u}_i^r$ is the filtered velocity component in the direction x_i (for $i = 1, 2, 3$), t is the time coordinate, $\tilde{p}^r$ is the filtered pressure, ρ and ν are the air density and kinematic viscosity, respectively and the superscript $(\cdot)^r$ refers to the resolved-scale quantity after spatial filtering. Compared with the classic N-S equations, a term with the SGS stress tensor (τ_{ij}) is added to Equation (5.6) as a result of the applied filtering. In the present work, the WALE model (Nicoud & Ducros, 1999) has been used to evaluate the SGS tensor instead of the well-known Smagorinsky model (Smagorinsky, 1963) due to its capability to more accurately capture the near-wall behavior of turbulent flows. Furthermore, the PIMPLE algorithm, which is a combination of the PISO (Pressure Implicit with Splitting of Operators) algorithm (Issa, 1986) and SIMPLE (Semi-Implicit Method for Pressure-Linked Equations) algorithm (Patankar & Spalding, 1972), is used for the pressure-velocity coupling.

5.3.2 Simulation setup

Figure 5.3 shows the computational domain utilized in the presented LES simulation. The domain was selected according to the guidelines provided by the European Cooperation in Science and Technology (Franke et al., 2007) and the AIJ (Tominaga et al., 2008). The inlet boundary is selected to be $4.5H$ upstream of the building, and the outlet boundary is set to be $10H$ downstream of the building. The lateral boundaries are set to be $5H$ away from the building and the top boundary is set at a height of $4H$. The Blockage Ratio (BR) of the selected computational domain is

$$\text{BR } (\%) = \frac{H \times D}{\text{domain cross section}} = 0.81\%,$$

which is in agreement with the guidelines provided in (Tominaga et al., 2008).

A numerically generated synthetic wind field, generated by Mann's approach (described in Section 5.3.3 and 5.3.4), is prescribed at the inlet boundary. No-slip boundary conditions are imposed on the ground and all the surfaces of the building. Zero-gradient conditions are prescribed at the top boundary. Moreover, periodic boundary conditions are set on boundaries in the spanwise directions. The boundary condition used at the outlet is inletOulet, which sets the patch value to the fixed value in case of the reversed flow and treats the patch as the zero gradient condition in case of outflow.

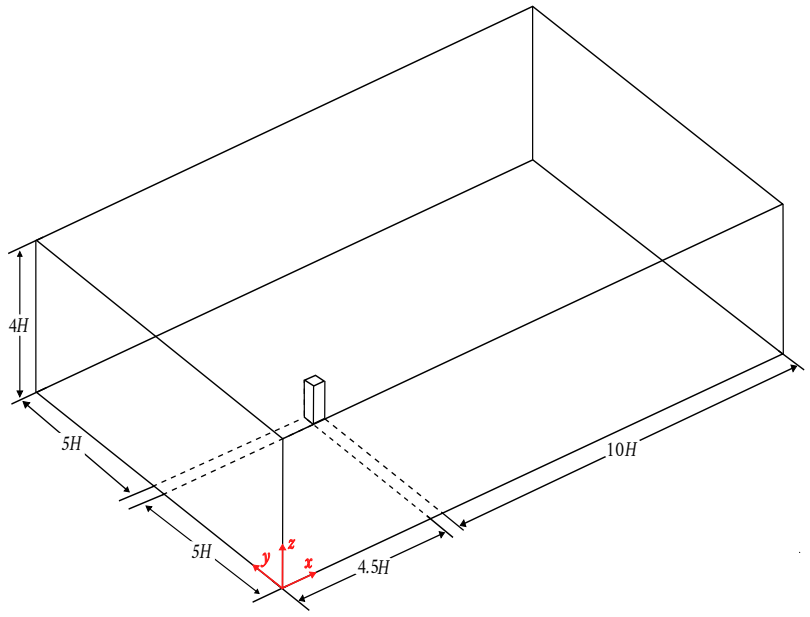

Figure 5.3: Scheme of the computational domain with a representation of the HRB of height H and width D.

The objective of this study is to examine the statistical characteristics of wind flow over the rooftop, both with and without the presence of the building. This is accomplished in two distinct cases: case I (without the building) and case II (with the building). The hexahedral unstructured mesh is generated using the Numeca Hexpress tool. The computational domain was discretized using embedded subdomains of hexahedral cells that maintain a constant ratio of two between successive subdomains. The finer mesh near the building was created using block refinement, followed by a refinement diffusion, which is less dissipating and is required for the transport of turbulent flow. A scheme of the subdomains's mesh for the fine grid, is depicted in Figure 5.4. The size of the smallest and the largest cells for the fine grid is $\Delta x_{\min}/D = 3.75 \times 10^{-2}$ and $\Delta x_{\max}/D = 0.6$ for both cases I and II. Moreover, the number of cells for the fine grid is ~ 6 million and ~ 6.7 million for case I and case II, respectively. A value $y^+ \sim 2$ is obtained for the fine grid simulation. The mesh grid parameters are summarized in Table 5.1. Furthermore, Appendix 7 shows the mesh dependence study. The simulation time (T) is 65 s.

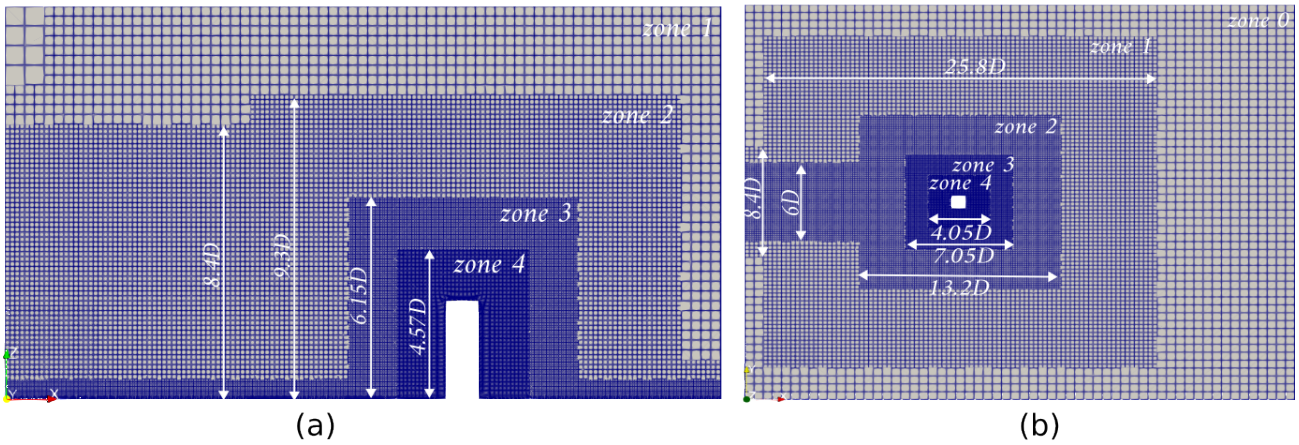

Figure 5.4: View of the mesh domain close to the HRB showing (a) the side view of the mesh domain, and (b) the top view of the mesh domain.

	Case I (fine)	Case II (coarse)	Case II (intermediate)	Case II (fine)
Refinement levels	3	3	3	4
Δt [s]	2.5×10^{-5}	2.5×10^{-5}	2.5×10^{-5}	2.5×10^{-5}
$\Delta x_{\min}/D$ [–]	3.75×10^{-2}	6.25×10^{-2}	4.69×10^{-2}	3.75×10^{-2}
$\Delta x_{\max}/D$ [–]	0.6	0.6	0.6	0.6
Δ_0/D [–]	1.9×10^{-3}	3×10^{-3}	1.5×10^{-3}	7.5×10^{-4}
Number of cells	6, 018, 108	2, 468, 718	4, 058, 145	6, 718, 696

Table 5.1: Main parameters of the numerical setup. Δ_0 is the thickness of the first mesh layer on the building surface.

5.3.3 Spectral representation method for inlet turbulence synthetic generation

The approach proposed by (Mann, 1998) was applied to generate synthetic turbulent fluctuations for the $\tilde{u}, \tilde{v}$ and $\tilde{w}$ velocity components to be used as turbulent velocity field at the inlet of the domain. The synthetic wind field was generated by utilizing the MATLAB code "MannTurb4D_v1 (Version v1.0)" developed by (Guo & Mann, 2022). In Mann's approach, a stochastic process representing the fluctuation of the wind velocity vector field, $u_i(\mathbf{x}_\perp, t; \alpha)$, for each velocity component $i = 1, 2, 3$, is obtained from a purely spatial RP defined on a grid with dimension $L_x \times L_y \times L_z$. The L_x is discretized into N_x spatial intervals. The fluctuation field $u_i(\mathbf{x}_\perp, t; \alpha)$ of each realization, α, is obtained by applying the TFTH as follows:

$$u_i(\mathbf{x}_\perp, t; \alpha) = u_i(\mathbf{x}_\perp - tU\mathbf{i}, 0; \alpha), \tag{5.7}$$

and the spatial-discrete RP $u_i(\mathbf{x}_\perp, 0; \alpha)$ is expressed as:

$$u_i(\mathbf{x}_\perp, 0; \alpha) = \sum_{k_1} \sum_{k_2} \sum_{k_3} U_{ij}(\boldsymbol{k}) n_j(\boldsymbol{k}, \alpha) \exp(\mathrm{i}\boldsymbol{k}^T \mathbf{x}), \tag{5.8}$$

where $j = 1, 2, 3$ and $n_j(\boldsymbol{k}; \alpha)$ are the independent Gaussian stochastic complex variables with unit variance. The deterministic coefficient matrix $U_{ij}(\boldsymbol{k})$, in expression (5.8), can be related to the SVT, $\Phi_{ij}(\boldsymbol{k})$ as (Mann, 1998):

$$U^*_{ik}(\boldsymbol{k}) U_{jk}(\boldsymbol{k}) = \frac{2\pi}{L_x L_y L_z} \Phi_{ij}(\boldsymbol{k}). \tag{5.9}$$

The SVT, used in Equation (5.9), is evaluated from the Mann US-SVT, $\Phi_{ij}(\boldsymbol{k}, \tau_e(k))$, (Mann, 1994b, 1998), which reproduces the second order statistics of a stationary-homogeneous-anisotropic turbulence velocity field (see Section 4.6).

5.3.4 Parametric study for synthetic generation of turbulent inflow at the inlet for LES simulation

To replicate the inlet flow for the HRB simulation, a parametric study was conducted by changing the values of (L, Γ and $\overline{u^2_{iso}}$) of the Mann turbulence model, to generate a synthetic wind field fluctuation, by using Mann's approach (Mann, 1994b, 1998). Subsequently, the mean value of the longitudinal velocity component represented by the power law profile, shown in Equation (5.5), is added to the generated synthetic wind velocity vector fluctuation field. The generated synthetic wind field is prescribed as turbulent inflow for a LES study for an empty domain, utilizing the same boundary conditions as those employed in the main simulation. Additionally, the dimensions of the empty domain are similar to the dimensions of the main simulation. Furthermore, a mesh with a number of cells ~ 2 million was used for simulating the empty domain. The mean velocity profile and the turbulence intensities of the velocity components resolved for from the LES at the mid-plane of the empty domain were analyzed and compared to the provided experimental results. Four combinations of the

Mann's model parameters, presented in Table 5.2, have been considered. To investigate the impact of Mann's parameters, a reference case (Case 1) is established to compare the other cases.

Figures 5.5 and 5.6 show the vertical profiles of the mean wind longitudinal velocity component, turbulence intensities, and integral length scales of the simulated wind field at the mid-plane of the empty domain, for the mentioned four combinations of Mann's model parameters. From Figure 5.5, it is evident that the four combinations of Mann's parameters do not have a relevant impact on the mean velocity vertical profiles resolved by the LES. In contrast, the turbulence intensities and integral length scales are clearly dependent on the considered combination of parameters. For cases 1 and 2, a variation in the length scale of the three dimensional energy spectrum, L, was introduced while maintaining the other parameters constant. For the integral length scale profiles, a decrease in the L parameter causes an expected reduction in the integral length scale profiles for all three directions, as depicted in Figure 5.6a. While, for the turbulence intensities profiles, it was observed that a decrease in the L value leads to a reduction in the I_u and I_v profiles, with only a minor reduction observed in the I_w profile at high heights, as shown in Figure 5.6b.

To investigate the influence of the anisotropy parameter, Γ, for case 1 and case 3, the Γ value was changed while keeping all other parameters constant. It was observed that increasing the value of Γ has a noticeable effect on the I_u profile, which increases with an increase in Γ, as shown in Figure 5.6b. However, the I_v experiences only a slight change, and the I_w profile is almost the same. With regards to the integral length scale, both the L_u^x and L_v^x show a noticeable increase in their profiles, while the L_w^x displays a slight change only at high levels.

The impact of the $\overline{u_{iso}^2}$ on statistical characteristics of the resolved wind field was investigated by varying its value while keeping the other parameters the same for case 1 and case 4. As shown in Figure 5.6b, a reduction in the $\overline{u_{iso}^2}$ results in an expected decrease in the turbulence intensity profile for all three directions. Whereas the integral length scales display a slight change with changing $\overline{u_{iso}^2}$, as depicted in Figure 5.6b.

It can be concluded from the previous analysis that to replicate the turbulence intensity, especially I_w, of the desired turbulent inflow provided by the experiments (shown in Figure 5.2), a high value of $\overline{u_{iso}^2}$ (to some extend, unrealistic) is required. A numerical predictor model has been developed to facilitate the process of identifying the Mann parameters. This predictor utilizes quadratic polynomials to predict the change of the turbulence intensity profiles at different heights by changing the Mann's parameters. These polynomials are obtained by fitting the turbulence intensity profiles obtained for the considered LES results considered the synthetic inlets in Table 5.2. Finally, an optimization process was conducted to search for the Mann parameters, leading to better replicating the turbulence intensities I_u and I_w, of the turbulent undisturbed inflow provided by the experiments. The optimization process uses the predictor to forecast the turbulence intensity profiles and compare them to the desired profiles. Note that only the turbulence intensity profiles were considered since, from the previous analysis, it was observed that Mann's parameters have a negligible effect on the mean speed profile resolved by the LES. Notably, the increased number of turbulence profiles generated by more LES runs has led to a more precise and reliable prediction of the turbulence intensity since the polynomials become more representative of the change of the

turbulence intensity profiles with the change of the Mann's parameters.

Cases	L [m]	$\overline{u_{iso}^2}$ [m^2 s^{-2}]	Γ [–]
Case 1 (Ref)	0.5	2	2
Case 2	0.2	2	2
Case 3	0.5	2	3
Case 4	0.5	1	2

Table 5.2: The four synthetic inlets prescribed in the empty domain inlet, considered in the parametric study to analyze the effect of the Mann's parameter on the generated wind field in the middle of the empty domain.

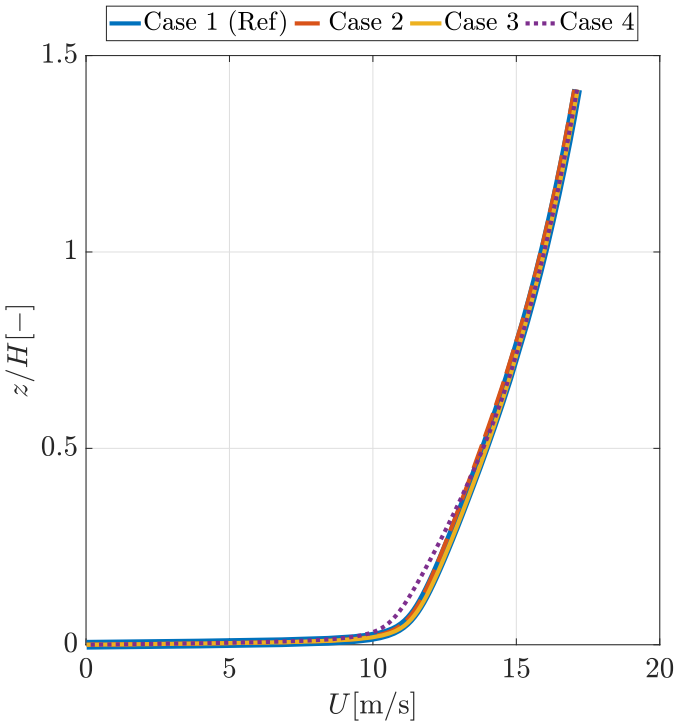

Figure 5.5: Mean wind longitudinal velocity profile of the simulated wind field at the mid-plane of the empty domain, for the considered cases (see Table 5.2).

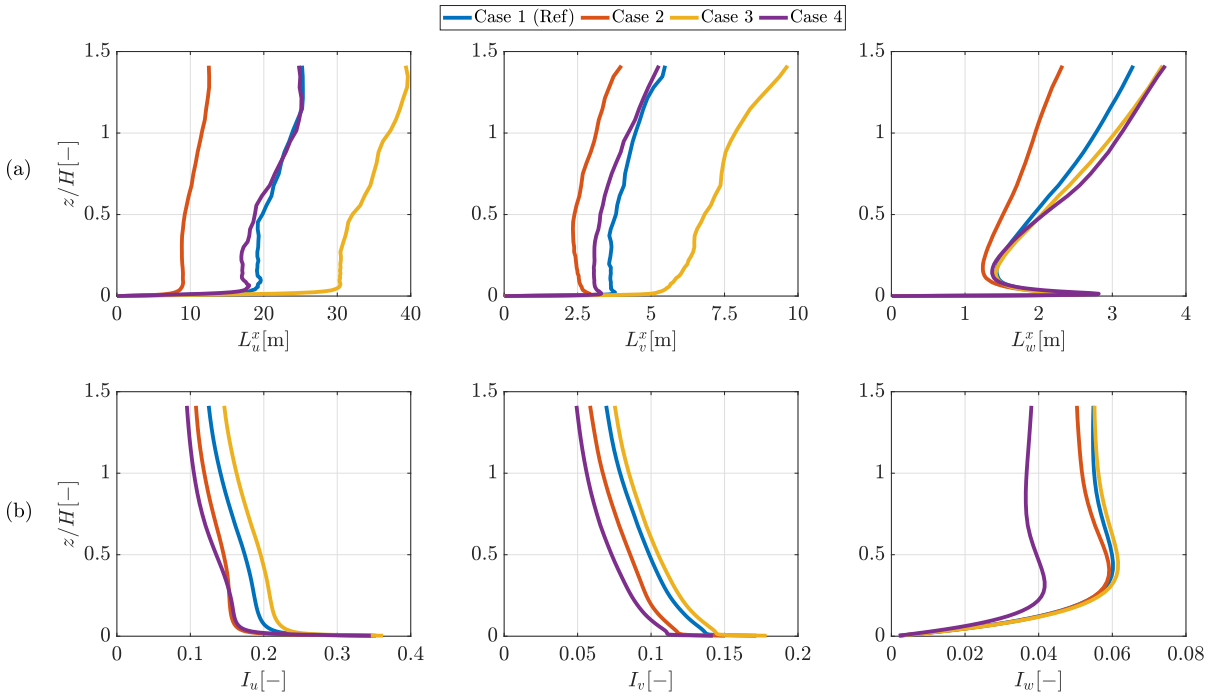

Figure 5.6: Vertical profiles of (a) Intregral length scales along the $x-$direction and (b) the turbulence intensity, for the u, v and w velocity components at the mid-plane of the empty domain, for the four considered synthetic inlets (see Table 5.2).

The application of the predictor tool described above yielded to the following values for the Mann's model parameters: $\Gamma = 0$ [$-$], $L = 0.25$ [m] and $\overline{u_{iso}^2} = 11$ [m^{2}s^{-2}]. It must be noted that these parameters correspond to an unphysical flow, as the value of isotropic variance is excessively high. However, utilizing the generated synthetic wind field as a turbulent inflow at the inlet for the empty domain resulted in the obtainment of a realistic wind field at the middle of the domain, which is in good agreement with the desired turbulent inflow as shown in Figure 5.2. Realistic inflow conditions are crucial for acquiring realistic wind fields at WT locations, thereby ensuring the accuracy of loading predictions. Subsequently, the wind field shown in Figure 5.2 is used as the turbulent inflow to the main case, which includes the HRB.

5.4 Assessment of the numerical approach

This section deals the validation of the LES results defined in Section 5.3.2 by comparing with the reference cases (Vita et al., 2020; Vita, 2020; Vranešević et al., 2022) discussed in Section 5.2. The statistical characteristics of the wind velocity field at the rooftop locations shown in Figure 5.1b, are used for the comparison. Note that, although, the Δt used in the LES simulation is 2.5×10^{-5} s (see Table 5.1), the wind velocity field was saved every $\Delta t = 5 \times 10^{-4}$ s ($f_{\max} = 1000$ Hz) to decrease the memory requirement. The first second of the LES simulation was truncated to eliminate the initial transient part in the statistical calculations. In Figure 5.7, the non-dimensional mean longitudinal velocity component,

U/U_{ref}, along the non-dimensional height above the HRB rooftop, z^*/D (where $z^* = z - H$), is shown at various locations atop of the building. The results from the LES analysis are in an agreement with the experimental data and LES-Vranešević results at high elevations. It is worth noting that the HWA is insensitive to reversed flow conditions; thus, the experimental results from the HWA are unreliable in the region close to the rooftop surface where flow recirculation is present due to the detachment bubble (Šarkić Glumac et al., 2018a; Vita, 2020). The LES simulation well captures the reversed flow close to the surface. This reversed flow exhibits a level of agreement with the LES-Vita and LES-Vranešević for the rooftop locations e_1 and m_1.

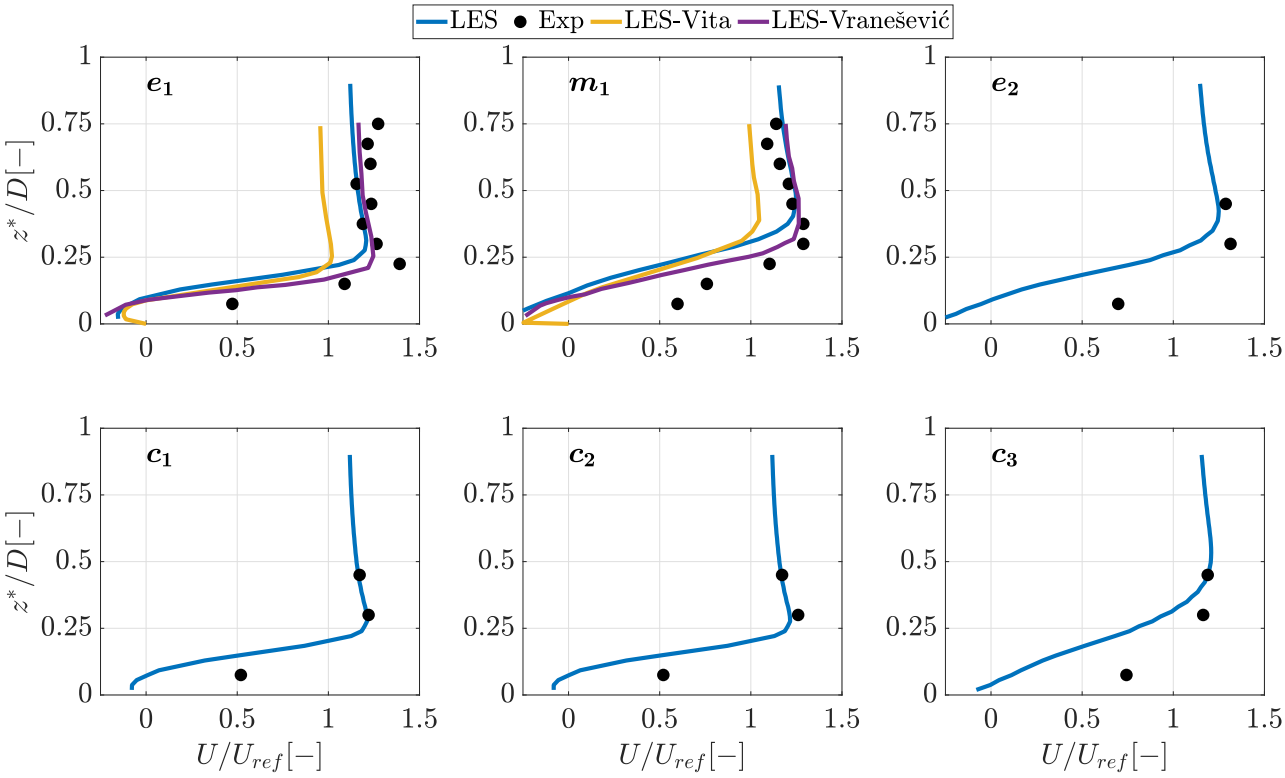

Figure 5.7: Non-dimensional mean longitudinal velocity component, U/U_{ref}, along the non-dimensional height z^*/D, at different vertical lines over the rooftop locations shown in Figure 5.1b. In the figure, the results from the present LES analysis are represented as well as the results from the experimental data, LES-Vita and LES-Vranešević.

In Figures 5.8 and 5.9, the longitudinal and vertical turbulence intensities I_u and I_w are shown at the validation locations. The I_u and I_w from the LES results show good agreement with the experimental data, particularly at high levels. However, some differences between the LES and the experimental results were observed over the leeward side of the rooftop. This might be due to the increase in the thickness of the reverse flow region at the leeward side, and also to the fact that most of the HWA measuring points are in the high turbulence intensity region, which might lead to inaccurate measurements from the HWA. Moreover, it is expected that the thickness of the high turbulence intensity region is higher at the leeward edge of the building compared to the windward edge, which was observed in the DNS results

from (Yakhot et al., 2006). At the region closer to the surface, LES results for the e_1 and m_1 locations show an agreement with the LES-Vranešević analysis. However, the LES results show a slightly thicker high turbulence intensity region, particularly for m_1, compared to LES-Vranešević. For the I_u and I_w, the thickness of the high intensity region depends on the location at the rooftop of the building. For the e_1, c_1 and c_2 locations, this region is up to $z^*/D \sim 0.18$. Whilst for e_2 and m_1, it is up to $z^*/D \sim 0.24, 0.28$, respectively. For the c_3 location, the thickness reaches $z^*/D \sim 0.25$. This evidences the high non-homogeneity of the flow velocity field in the $x-$direction close to the rooftop. In the undisturbed region (above the boundary layer), both the I_u and I_w reach a constant value for the turbulence intensity $I_i \sim 12 - 14\%$ (for $i = u, w$), at all the locations evaluated over the rooftop.

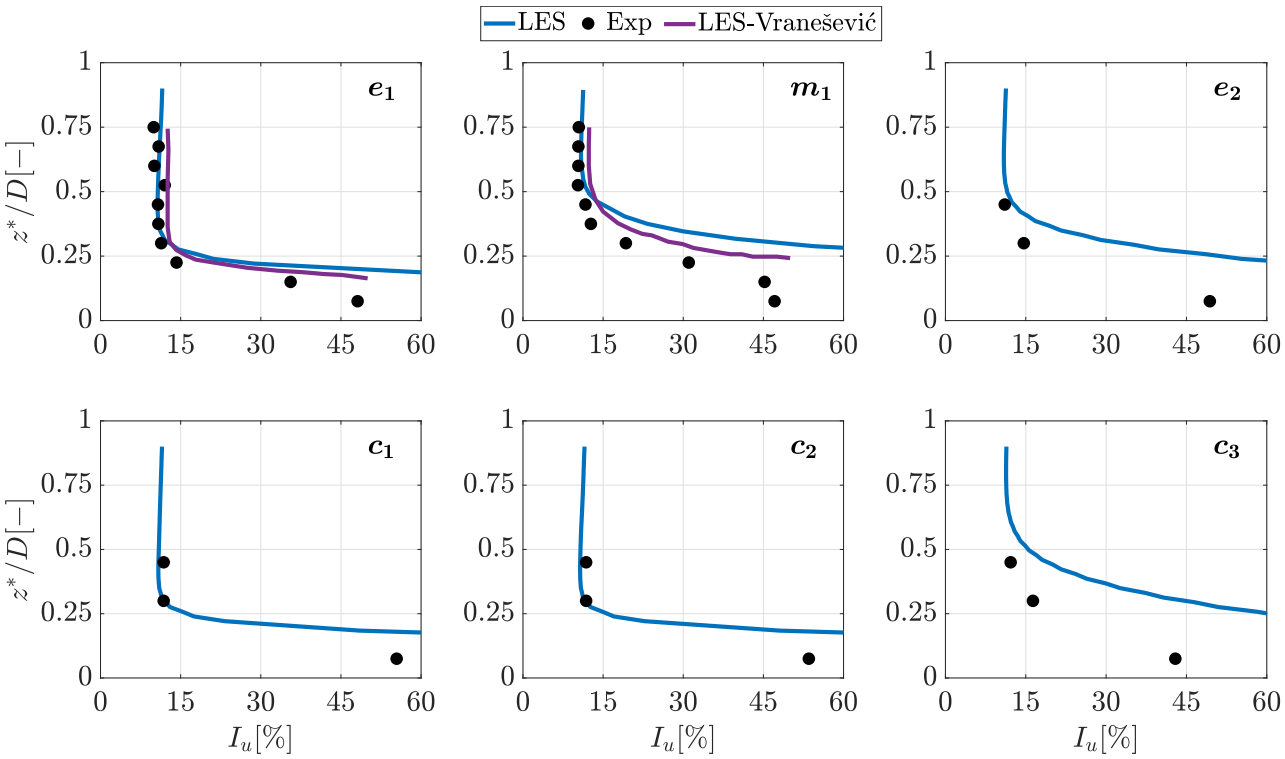

Figure 5.8: Longitudinal turbulence intensity, I_u, along the non-dimensional height z^*/D, at different vertical lines over the rooftop locations shown in Figure 5.1b. In the figure, the results from the present LES analysis are represented as well as the results from the experimental data and LES-Vranešević.

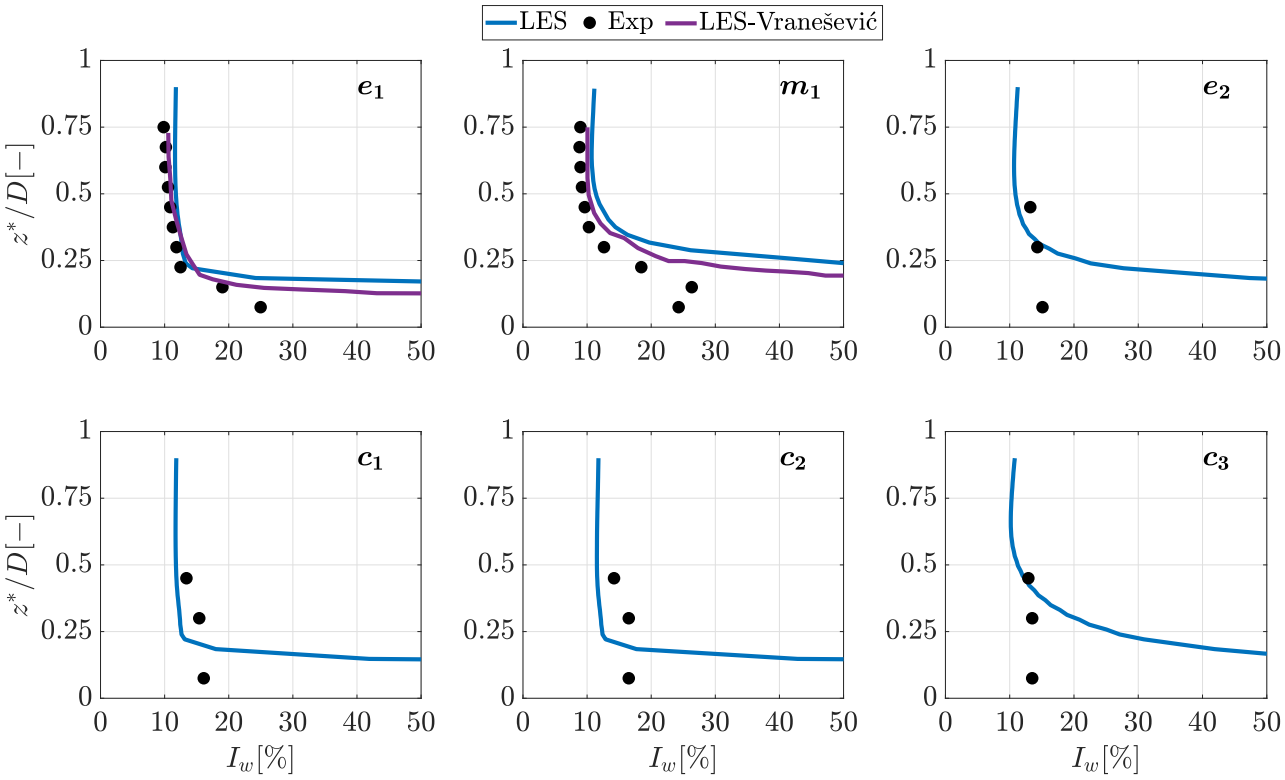

Figure 5.9: Vertical turbulence intensity, I_w, along the non-dimensional height z^*/D, at different vertical lines over the rooftop locations shown in Figure 5.1b. In the figure, the results from the present LES analysis are represented as well as the results from the experimental data and LES-Vranešević.

The longitudinal integral length scale in the $x-$direction, L_u^x, normalized by the building width D is shown in Figure 5.10, along the non-dimensional height z^*/D, at various locations over the roof. The strong spatial variation of the integral length scale values, evidenced by the experiment, is well captured by the LES. The integral length scales resolved from the LES show the same order of magnitude and similar spatial patterns compared to the reference values. In some locations the obtained integral length scales are lower than those of the reference studies.

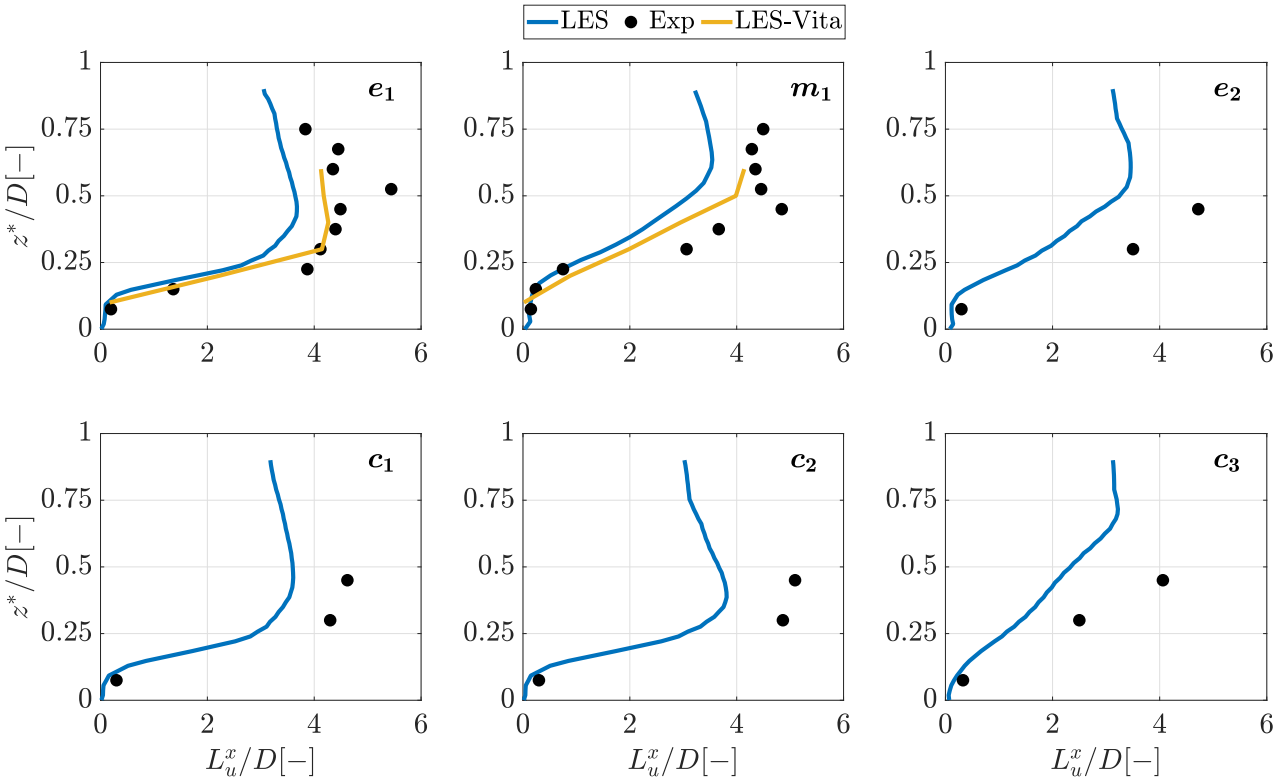

Figure 5.10: Non-dimensional longitudinal integral length scale, L_u^x/D, along the non-dimensional height z^*/D, at different vertical lines over the rooftop locations shown in Figure 5.1b. In the figure, the results from the present LES analysis are represented as well as the results from the experimental data and LES-Vita.

In Figure 5.11, the normalized spectrum for the $u-$velocity component, $fS_{uu}/\overline{u^2}$, against the non-dimensional frequency fD/U_{ref}, is shown at the locations e_1 and m_1, and at the non-dimensional heights $z^*/D = 0.1, 0.3, 0.6$. Note that the value of the minimum frequency of the estimated spectra from the simulated LES case is $f_{\text{min}} = 1/64$ Hz (equivalent to the non-dimensional frequency $fD/U_{ref} = 1.3 \times 10^{-4}$), however, the normalized spectra in Figure 5.11 are shown starting from the non-dimensional frequency $fD/U_{ref} = 10^{-3}$. This is done to improve the visualization of the normalized spectra within the frequency region of the available normalized spectra of the reference experiment and LES simulation. It is worth mentioning that the spectra in Figure 5.11 are computed using Blackman and Tukey spectrum estimator (Marple Jr & Carey, 2019). The normalized spectra obtained from the LES analysis agree with the experimental results and LES-Vita. The normalized spectra from the LES simulation exhibit a sharp decline at $fD/U_{ref} > 1$ due to the LES grid cut-off. The $fS_{uu}/\overline{u^2}$ shows a shift in its peak to high frequencies closer to the surface of the building, which was also observed in the field measurements done by (Rotach, 1991). The subsequent Section 5.5.1 presents a more comprehensive analysis of this shift.

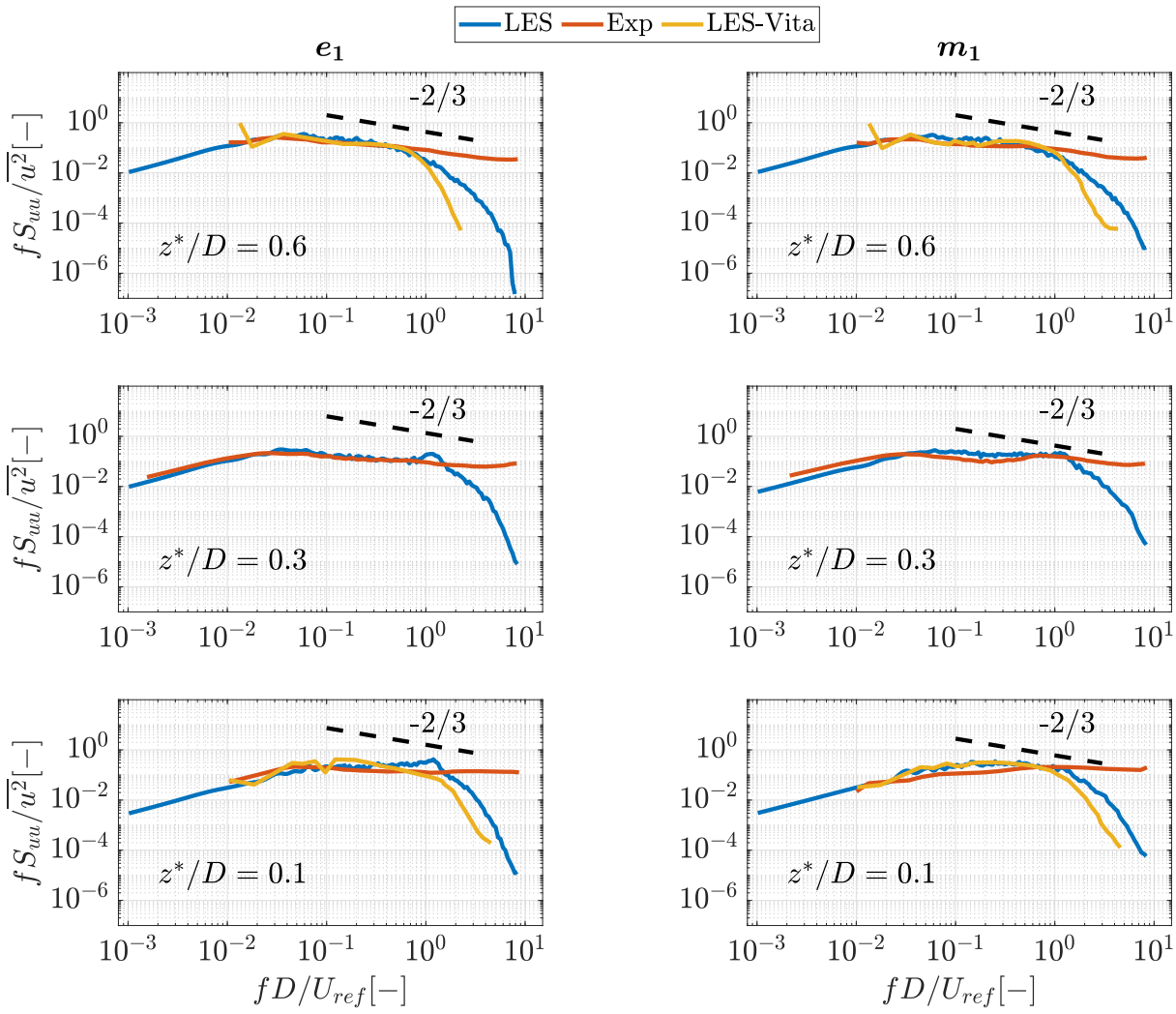

Figure 5.11: Normalized spectrum for the u velocity component, $fS_{uu}/\overline{u^2}$, at the rooftop locations e_1 and m_1 and at a non-dimensional height $z^*/D = 0.1, 0.3, 0.6$, with the $-2/3$ slope line. In the figure, the results from the present LES analysis are shown as well as the results from the experimental data and LES-Vita. Note that the normalized spectra from the experimental data and the LES-Vita are smoothed.

5.5 Impact of the high-rise building on the wind field statistical characteristics

In this section, different statistics of the wind velocity field along vertical lines located at positions e_1 and m_1 are compared for Case I (empty domain) and Case II (HRB in the domain). Additionally, statistical characteristics were analyzed at vertical planes perpendicular to the mean wind direction centered at e_1 and m_1 (e_1-plane and m_1-plane). Also, a vertical plane parallel to the mean wind direction centered at m_1 was considered ($p-$plane).

In Figure 5.12, the modulus of the non-dimensional mean longitudinal velocity component distribution, $|U|/U_{ref}$, is depicted with the mean streamlines corresponding to the $[U, W]$ vector on the $p-$plane over the roof. Recirculation patterns are resolved in the mean velocity field over the rooftop. The center of the primary recirculation pattern (point A) is located at $(x^*, z^*) \sim (0.56D, 0.11D)$ m from the windward edge and the HRB rooftop. The maximum thickness of the primary recirculation bubble is $\sim 0.23D$ m from the roof surface. A thin recirculation structure (point B) was observed at $x^* \sim 0.15D$ m close to the windward edge, which was also noticed in the LES analysis done by (Vranešević et al., 2022).

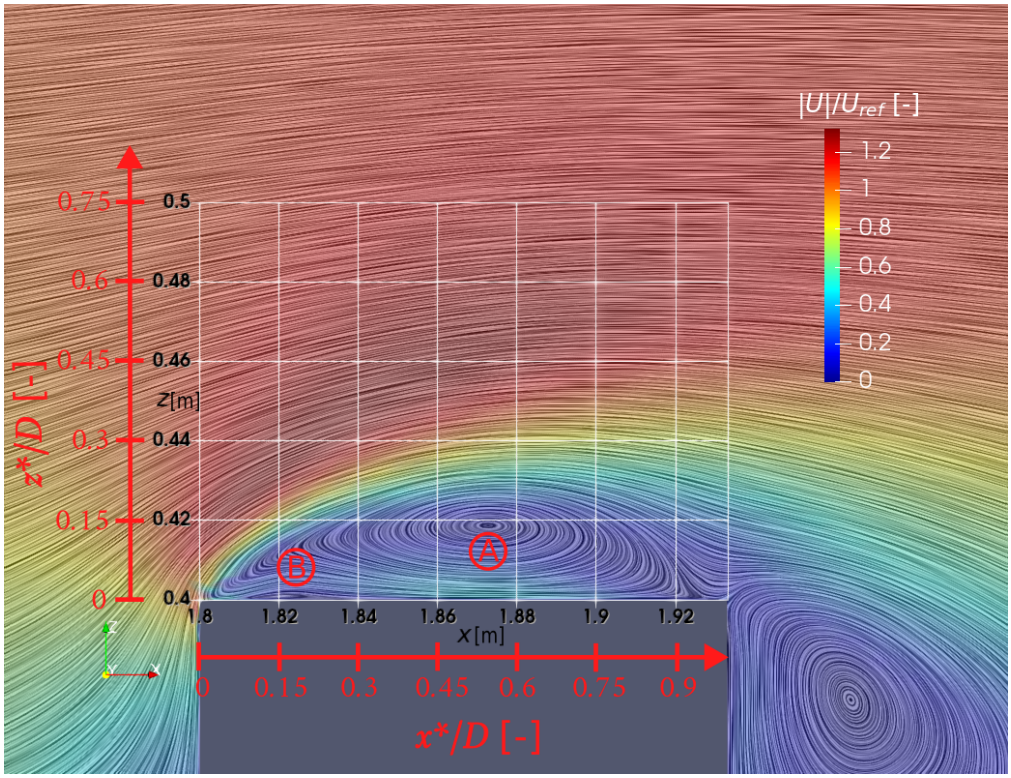

Figure 5.12: Modulus of the non-dimensional mean longitudinal velocity component distribution, $|U|/U_{ref}$, with the streamlines in the middle plane of the building. The points A and B indicate the cross-sections of the recirculation regions over the rooftop.

5.5.1 Wind velocity characteristics along vertical lines

Figure 5.13 shows the vertical profiles of the mean velocity components U and W. The results show the well-known variation of the velocity component U over the building, with respect to its values in the unperturbed case I. This known pattern consists on a relative decrease in velocity near the rooftop and an increase in higher positions, which is compatible with the existence of the recirculation bubble. This pattern of the wind velocity above the building has been documented in previous works. For instance, it was also observed in the RANS simulations of the wind flow over a flat rooftop done by (Abohela et al., 2013; Toja-Silva et al., 2015). The vertical profiles of the mean velocity component W over the rooftop (Case

II) also exhibit the expected variations relative to the undisturbed values (Case I), hence significantly positive and negative values on the windward side, respectively, which is evidence of the expected detachment bubble pattern.

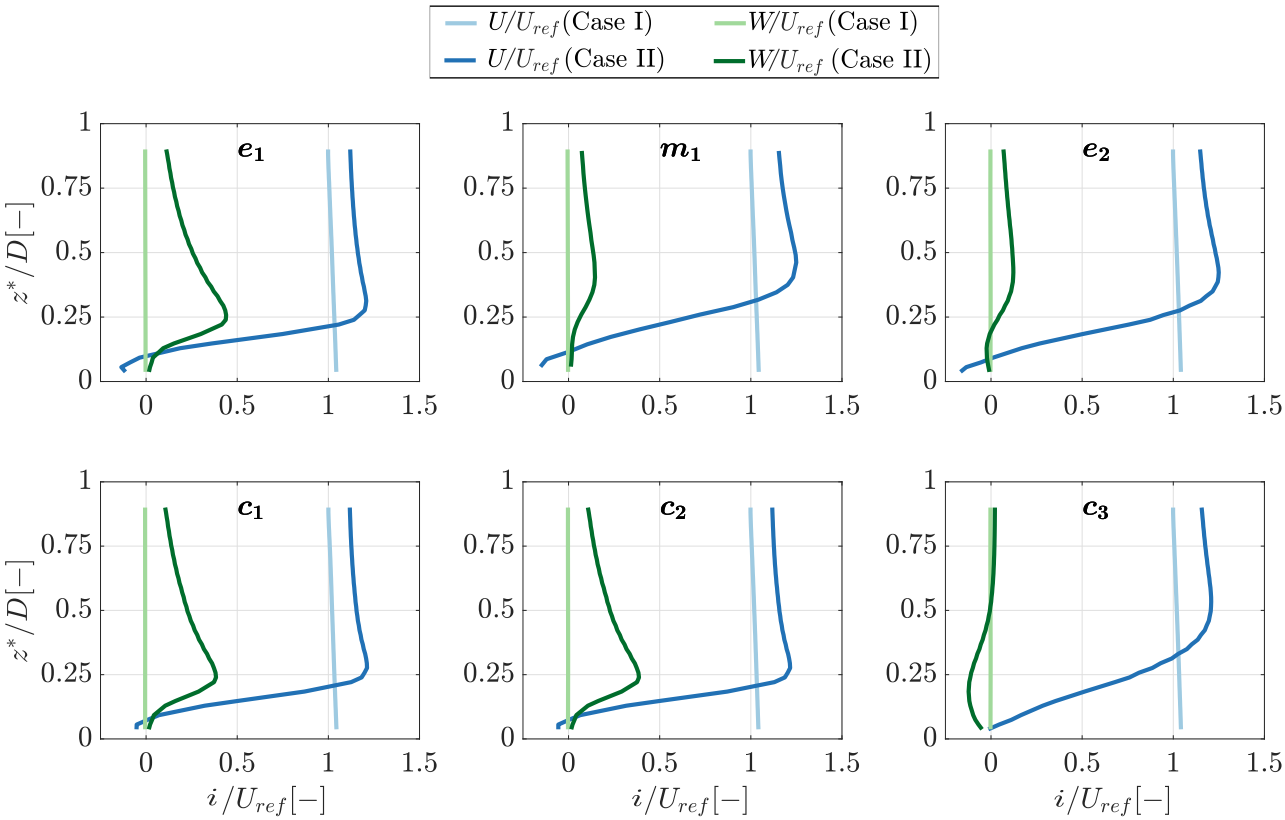

Figure 5.13: Vertical profiles of the non-dimensional mean wind velocity components, i/U_{ref} (for $i = U, W$), evaluated from the LES, at the rooftop locations shown in Figure 5.1b, for Case I (empty domain) and Case II (HRB in the domain).

The turbulence intensity for the longitudinal, lateral, and vertical velocity components I_u, I_v and I_w, is shown in Figure 5.14. For Case I, the absence of the building leads to nearly constant values of the turbulence intensities for the three velocity components $I_i \sim 13\%$. In the presence of the HRB, the three turbulence intensities exhibit high values close to the rooftop surface. Far from the rooftop, the turbulence intensities are nearly constant and similar to the undisturbed value at all the rooftop locations.

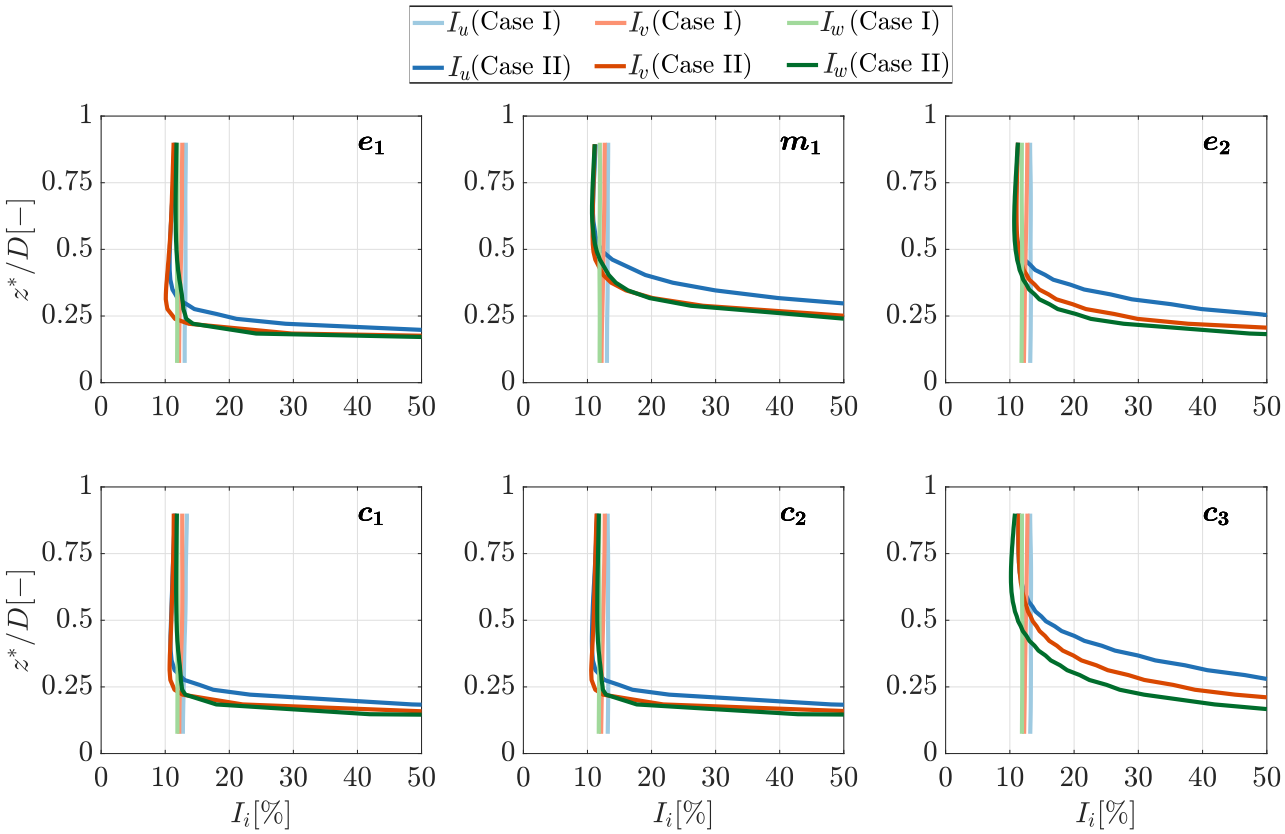

Figure 5.14: Vertical profiles of the turbulence intensities, I_i, for $i = u, v, w$, evaluated from the LES, at the rooftop locations shown in Figure 5.1b, for Case I (empty domain) and Case II (HRB in the domain).

The non-dimensional longitudinal integral length scale for the three wind velocity components, L_i^x/D, for $i = u, v, w$, are shown in Figure 5.15. In the absence of the building, the L_i^x/D exhibits low variation with height for the three velocity components. L_v^x/D and L_w^x/D have nearly the same value ~ 1.2, and L_u^x/D is ~ 2.7 for all rooftop locations. While the HRB introduces a strong spatial dependence with the distance to the rooftop for the L_i^x/D.

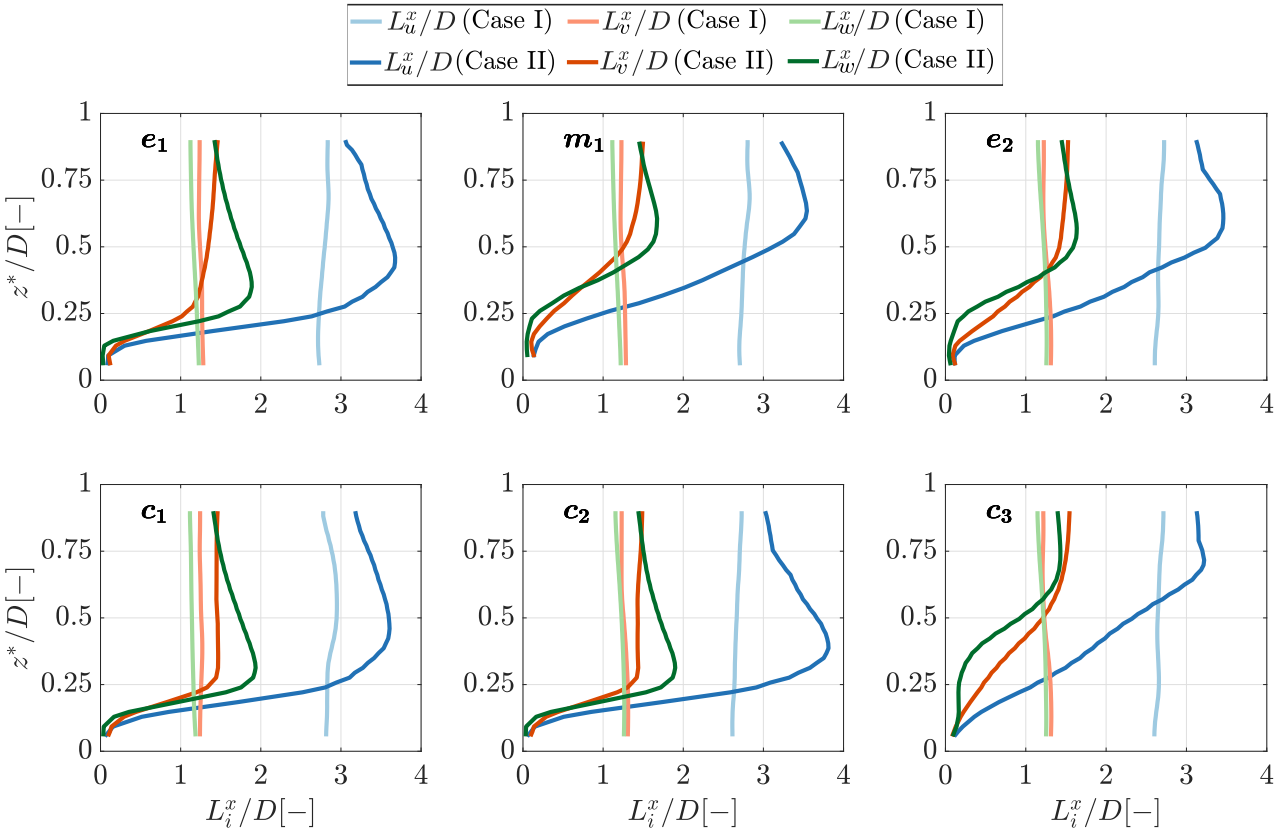

Figure 5.15: Vertical profiles of the non-dimensional longitudinal integral length scales, L_i^x/D for $i = u, v, w$, evaluated from the LES, at the rooftop locations shown in Figure 5.1b, for Case I (empty domain) and Case II (HRB in the domain).

The normalized PSD for the u, v, w velocity components, $fS_{ii}/\overline{i^2}$, at non-dimensional heights $z^*/D = 0.1, 0.3, 0.6$, is shown in Figures 5.16 (at location e_1) and 5.17 (at location m_1) against the non-dimensional frequency fD/U_{ref} together with a $-2/3$ slope line. The peak frequency, which is the frequency that corresponds to the highest value of the normalized spectra, depends on the distance to the surface of the rooftop for Case II. The peak frequency of normalized spectra, at both e_1 and m_1, shifts to high frequencies as the distance to the building rooftop decreases. To further analyze the mentioned frequency shift, the normalized spectra are plotted in Figure 5.18 (at location m_1) as colormap dependent on the non-dimensional z^*/D and non-dimensional frequency fD/U_{ref}. The dependency of the peak shift with the height is clearly observed in the colormap plots.

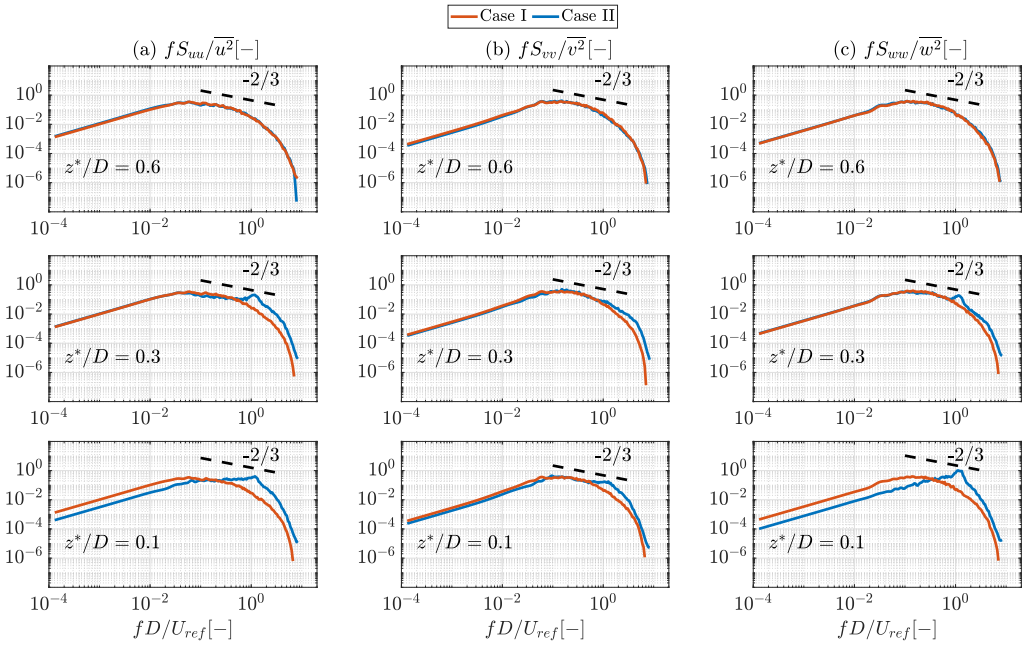

Figure 5.16: Normalized PSD, $fS_{ii}/\overline{i^2}$ for $i = u, v, w$, against the non-dimensional frequency, fD/U_{ref}, at the rooftop locations e_1 and at a non-dimensional height $z^*/D = 0.1, 0.3, 0.6$, evaluated from the LES simulation, for Case I and Case II .

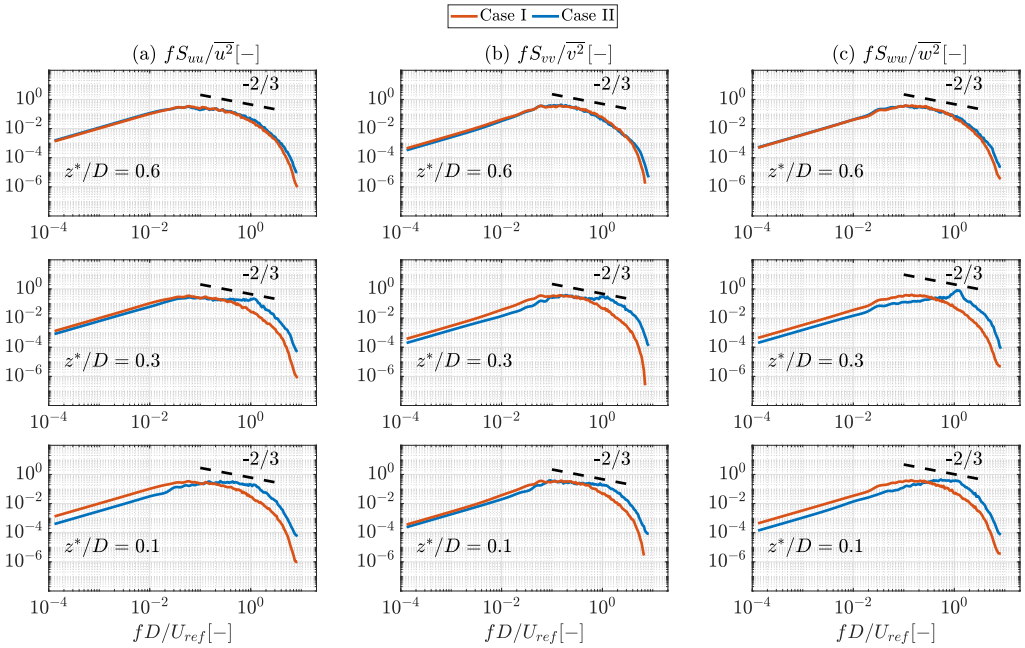

Figure 5.17: Normalized PSD, $fS_{ii}/\overline{i^2}$ for $i = u, v, w$, against the non-dimensional frequency, fD/U_{ref}, at the rooftop locations m_1 and at a non-dimensional height $z^*/D = 0.1, 0.3, 0.6$, evaluated from the LES simulation, for Case I and Case II.

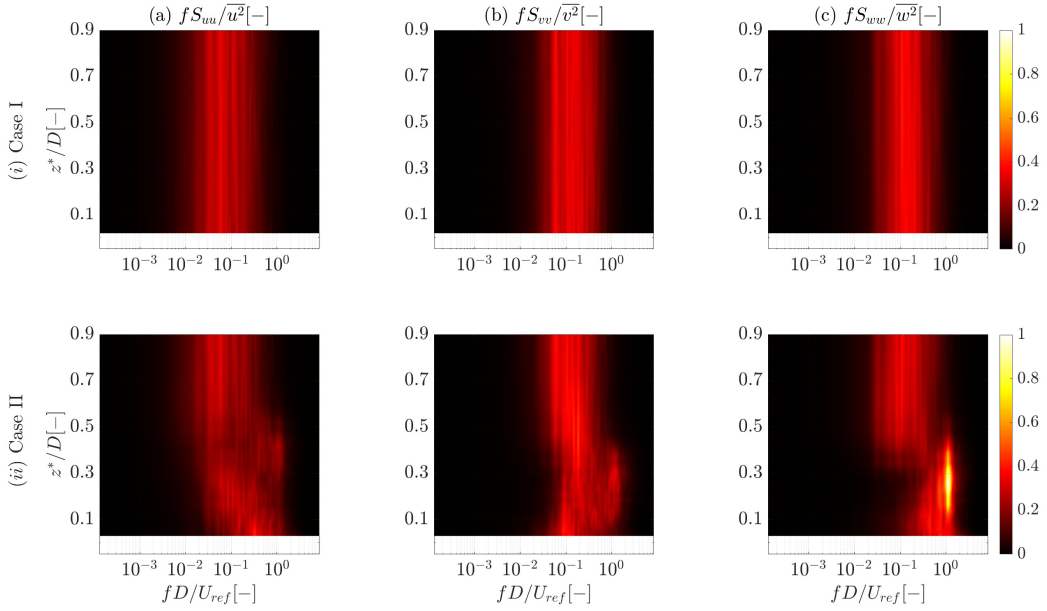

Figure 5.18: Normalized PSD, $fS_{ii}/\overline{i^2}$, for i = (a) u, (b) v, and (c) w, velocity components, against the non-dimensional frequency, fD/U_{ref}, and the non-dimensional vertical direction, z^*/D, for Case I and Case II at the rooftop location m_1.

The coherence function is evaluated for two non-dimensional vertical separation distances $\Delta z/D = 3.6 - 3.3 = 0.3$ (where $\Delta z = z_2 - z_1$) and $\Delta z/D = 3.6 - 3.1 = 0.5$. In Figure 5.19, the coherence function is plotted against the non-dimensional frequency fD/U_{ref}. Generally, for all cases analyzed, coherence functions exhibit the expected decay when the normalized frequency increases. This decay presents an asymptote at a value of 0.15 and not towards 0, and this could be since the coherence function defined in Equation (5.4) is a biased estimator (Kristensen & Kirkegaard, 1986) and/or attributed to the numerical noise as reported in the work done by (Shaler et al., 2019). Additionally, as expected, increasing the vertical separation leads to a faster decay in the coherence function for both Case I and II. The decay rate for the coherence function of the u-velocity component is faster than the v and w velocity components at the two rooftop locations analyzed. It was noticed that the decay rate for Case I is generally lower than for Case II at both e_1 and m_1 locations. Moreover, the decay rate of the coherence functions at location e_1 was observed to be lower compared to the decay rate at the m_1 location, which is coherent with the fact that location m_1 is deep immersed in the recirculation region where coherence is rapidly lost. To have a better visualization of the decay rate of the coherence functions with the vertical separation, the coherence functions are plotted against the non-dimensional frequency fD/U_{ref} and the non-dimensional vertical separation $\Delta z/D$ in Figure 5.20 for location m_1. The value of z_2/D is fixed to be 4.125, and the value of z_1 is changed along the vertical line at location m_1. As shown in the results, increasing the non-dimensional vertical separation leads to a faster decay rate of the coherence functions, although the decay rate of the coherence functions for Case II is more intense than for Case I.

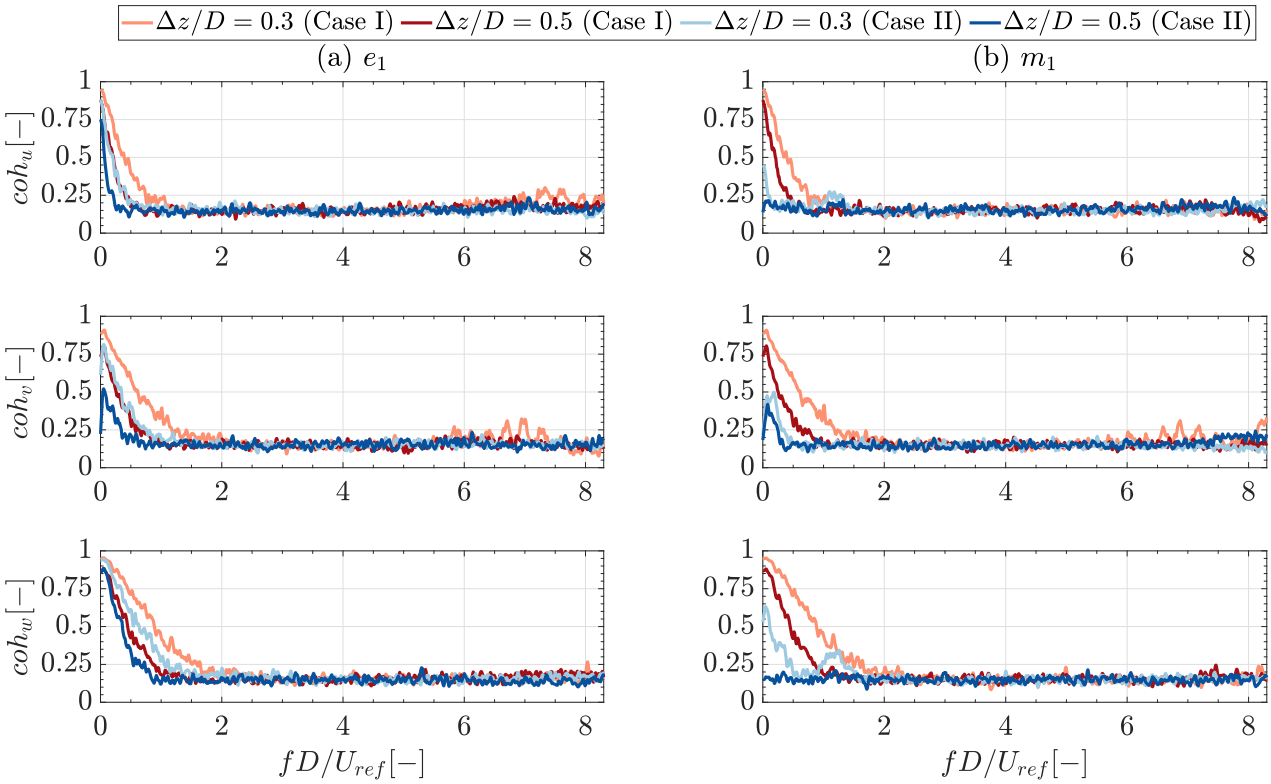

Figure 5.19: Coherence, coh_i for $i = u, v, w$, as a function of the non-dimensional frequency fD/U_{ref}, for non-dimensional vertical separation, $\Delta z/D = 0.3$ and 0.5, at the rooftop location e_1 evaluated from the LES results, for Case I and Case II.

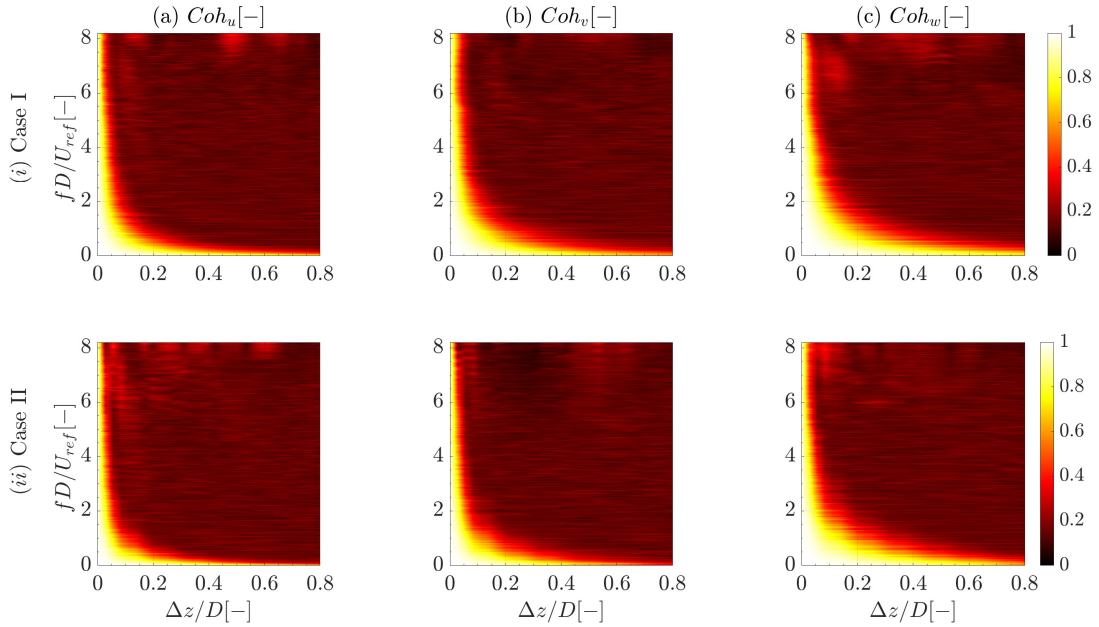

Figure 5.20: Coherence, coh_i for $i = u, v, w$, as a function of the non-dimensional frequency fD/U_{ref} and the non-dimensional vertical separation, $\Delta z/D$, at the rooftop location m_1 evaluated from the LES results, for Case I and Case II.

The normalized ACF, $\gamma_{ii}(\tau)/\gamma_{ii}(0)$ (for $i = u, v, w$), is shown against the time lag, τ, and the non-dimensional height z^*/D in Figure 5.21 for location m_1. It is worth mentioning that the ACF was calculated by using the biased ACF estimator, as recommended in (Marple Jr & Carey, 2019). For Case I, the decay rate of the ACF is constant with the non-dimensional height z^*/D for the three velocity components, and the decay rate of the ACF of the longitudinal velocity components is slower than for the lateral and vertical velocity components. For Case II, the decay rate depends on the distance to the rooftop since it decays faster in the vicinity of the rooftop, as expected from the previous analysis on the integral length scales. A damped sinusoidal oscillation in the normalized ACF for the vertical velocity was observed inside the recirculation region at m_1 location.

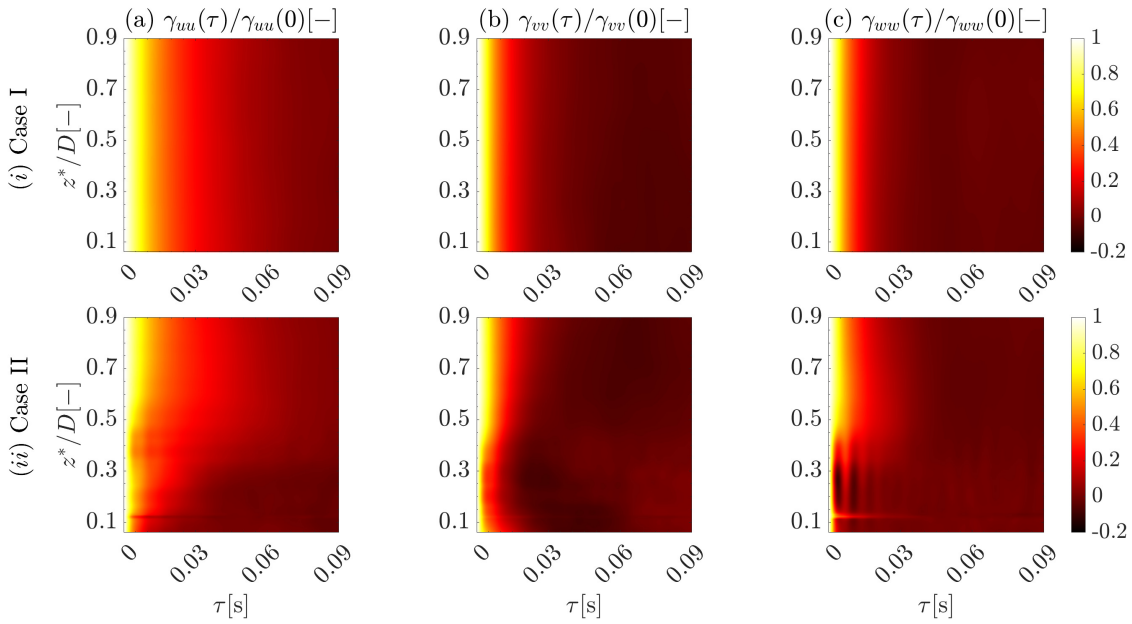

Figure 5.21: Normalized ACF, $\gamma_{ij}(\tau)/\gamma_{ij}(0)$, for i = (a) u, (b) v, and (c) w, velocity components, against the time lag, τ, and the non-dimensional vertical direction, z^*/D, for Case I and Case II at the rooftop location m_1.

5.5.2 Analysis of wind velocity field characteristics on cross-flow and along-wise vertical planes

The statistics of the wind velocity field have been resolved on three vertical planes. Note that cross-statistics are shown in Chapter 6 and compared with reproduced cross-statistics by the statistical methods. Two planes are perpendicular to the mean wind direction, and one is parallel to the mean wind direction over the HRB. The two perpendicular planes are located at $x^* = 0.2D$ (centered at the windward point e_1) and $x^* = 0.5D$ (centered at the middle point m_1), where $x^* = x - 4.5H$. In the rest of this section, note that the perpendicular planes will be referred to as the e_1- plane and m_1-plane. The parallel plane ($p-$plane) is located in the middle of the roof. The considered planes are shown in Figure 5.22.

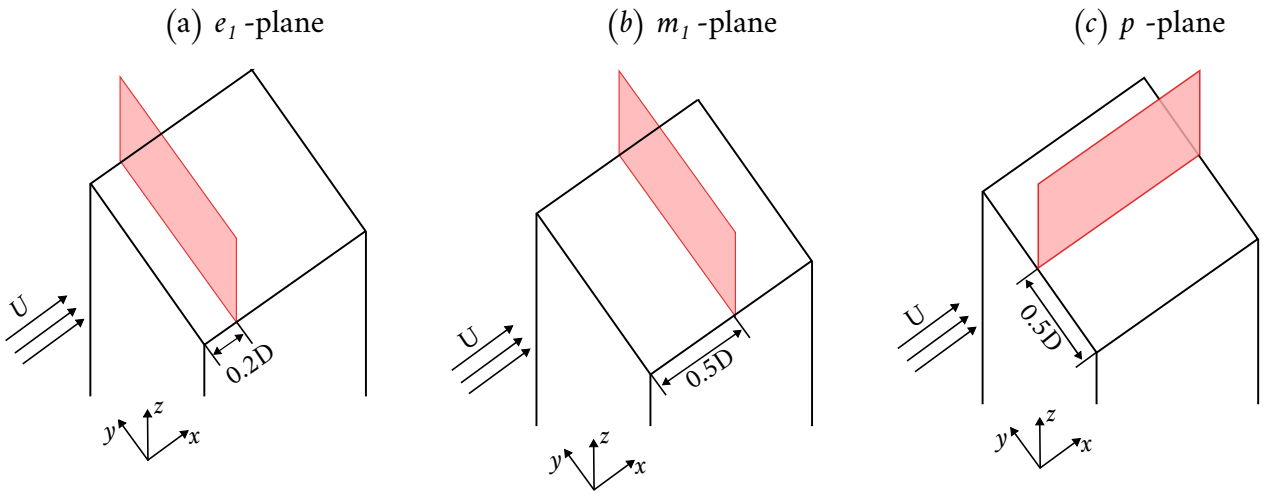

Figure 5.22: Scheme of the considered perpendicular and parallel planes in the statistical analysis.

Figure 5.23 shows the non-dimensional mean wind velocity components on the $p-$plane. As shown in Figure 5.23a, a flow detachment pattern is observed in the mean velocity field, begin to develop from the windward edge of the rooftop. The lateral component, V/U_{ref}, exhibits very low values as expected. The component V/U_{ref} shows very small positive values near the windward edge and very small negative values close to the leeward edge; similar behavior was observed in the experiment done by (Meng & Hibi, 1998) on the flow around a HRB. The behavior of mean velocity component W/U_{ref} corroborates the results documented in the literature. Hence, high values near the windward edge are obtained since the flow is deflected vertically at that region (Oke et al., 2017). Also, the W/U_{ref} presents negative values near the leeward edge since the low-pressure region behind the high-rise building causes downdraft of the wind flow (Nelson et al., 2007a; Oke et al., 2017). This pattern of W/U_{ref} has also been predicted by RANS simulations of the flow around HRBs (Xiong et al., 2022).

Figure 5.24 shows the longitudinal integral length scale for the three velocity components on the $p-$plane. The integral length scale exhibits its lowest values inside the separation bubble, increasing outside the separation region, which denotes that ACF decays faster, as the time lag increases, inside the bubble, as was shown before. The longitudinal integral length scale for the u-velocity component presents higher maximum values ($L^x_{u,\max}/D \sim 4$) compared to the maximum values obtained for the v and w velocity components ($L^x_{v,\max}/D, L^x_{w,\max}/D \sim 2.3$). Moreover, its maximum value is located close to the windward edge for all the velocity components.

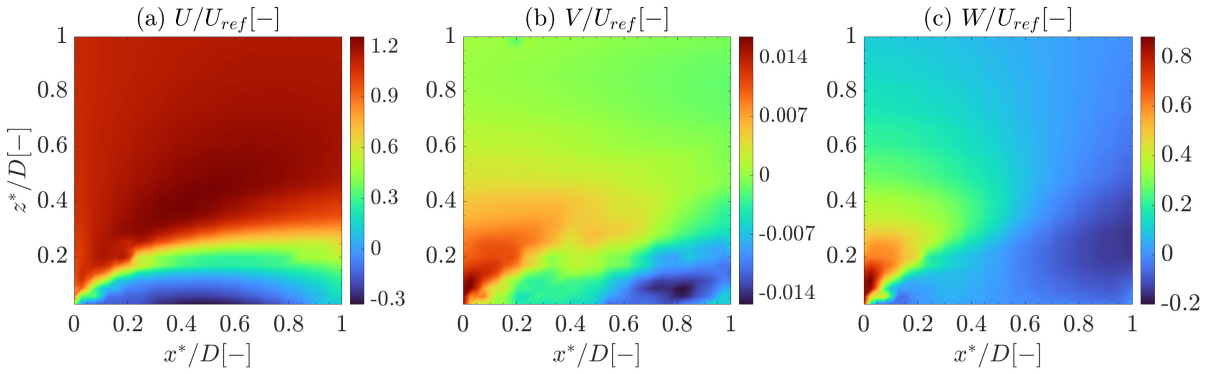

Figure 5.23: Non-dimensional mean velocity distribution for the (a) longitudinal, U/U_{ref}, (b) lateral, V/U_{ref}, and (c) vertical, W/U_{ref}, velocity components, against the non-dimensional longitudinal direction, x^*/D, and the non-dimensional vertical direction, z^*/D, for Case II on $p-$plane.

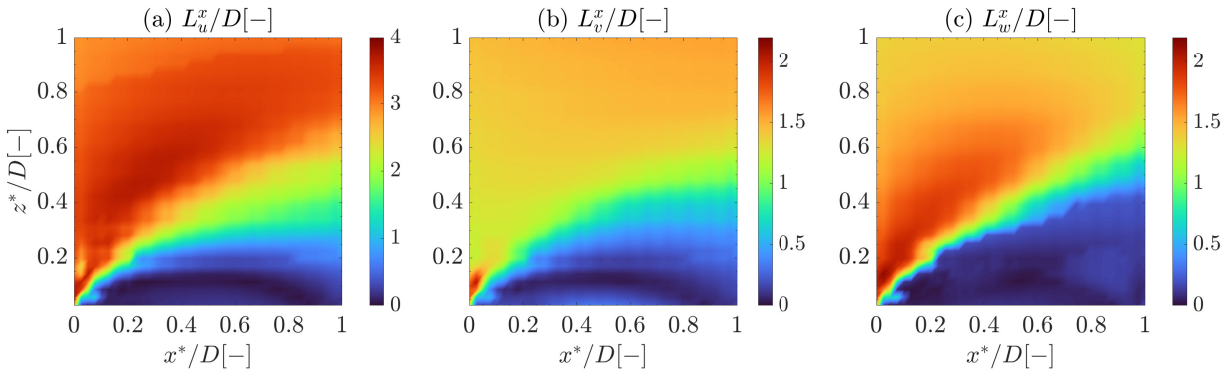

Figure 5.24: Non-dimensional longitudinal integral length scale distribution for the (a) longitudinal, L_u^x/D, (b) lateral, L_v^x/D, and (c) vertical, L_w^x/D, velocity components, versus the non-dimensional longitudinal and vertical directions, x^*/D and z^*/D, for Case II on $p-$plane.

The non-dimensional standard deviation, σ_i/U_{ref} (for $i = u, v, w$), on the $p-$plane is shown in Figure 5.25. The anisotropy of the velocity field is evident close to the rooftop. The regions of high values of the σ_i/U_{ref} are close to the surface of the building. On the other hand, as the distance from the surface increases above the recirculation region ($z^*/D > 0.6$), σ_i/U_{ref} for the three velocity components tends to similar values, which is an indicator of near-isotropy. This observation indicates the isotropic and homogeneity (for x and z directions) of the wind velocity field at elevated levels.

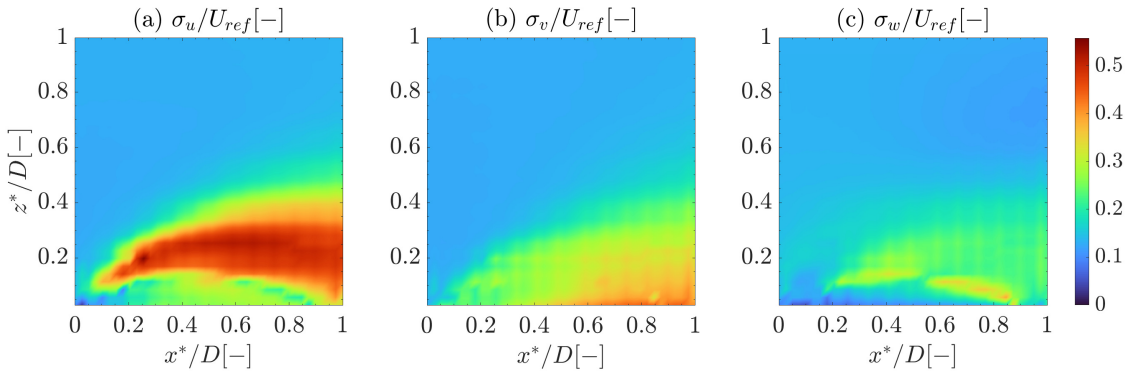

Figure 5.25: Non-dimensional standard deviation distribution for the (a) longitudinal, σ_u/U_{ref}, (b) lateral, σ_v/U_{ref}, and (c) vertical, σ_w/U_{ref}, velocity components, against the non-dimensional longitudinal direction, x^*/D, and the non-dimensional vertical direction, z^*/D, for Case II on $p-$plane.

The normalized mean wind velocity components are shown in Figure 5.26 on the e_1-plane and m_1-plane. The thickness of the recirculation region depends on the longitudinal direction as it changes from e_1-plane to m_1-plane.

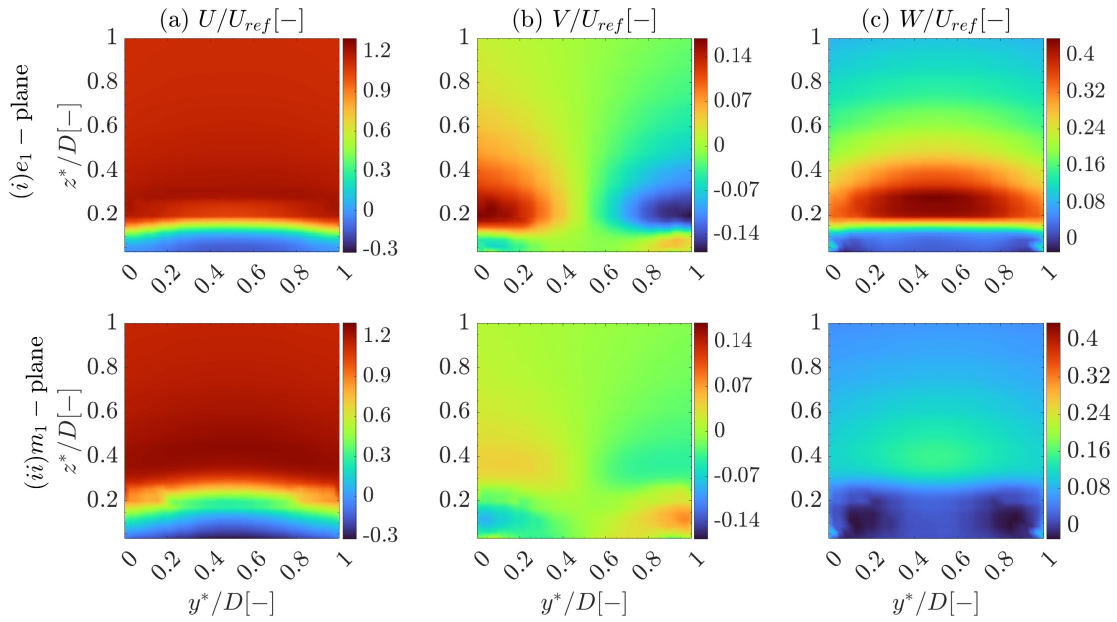

Figure 5.26: Non-dimensional mean velocity distribution for the (a) longitudinal, U/U_{ref}, (b) lateral, V/U_{ref}, and (c) vertical, W/U_{ref}, velocity components, against the non-dimensional lateral direction, y^*/D, and the non-dimensional vertical direction, z^*/D, for Case II (i) e_1-plane and (ii) m_1-plane.

The spatial distribution of longitudinal integral length scales of the three velocity components on e_1-plane and m_1-plane is shown in Figure 5.27. The integral length scale distribution presents the expected lateral symmetry for both planes. Both the L_v^x and L_w^x converge to almost similar constant values at $z^*/D > 0.7$.

Similarly as for the integral length scales, the non-dimensional standard deviation for the wind velocity components, σ_i/U_{ref}, shows a level of homogeneity in the $y-$direction at all height levels ($z^*/D > 0.3$ and 0.4, for e_1 and m_1 planes, respectively), as depicted in Figure 5.28. Moreover, the σ_i/U_{ref} values for the three velocity components tend to a constant value at the homogeneous regions, which is an indication of higher degree of isotropy of the wind velocity field in these regions.

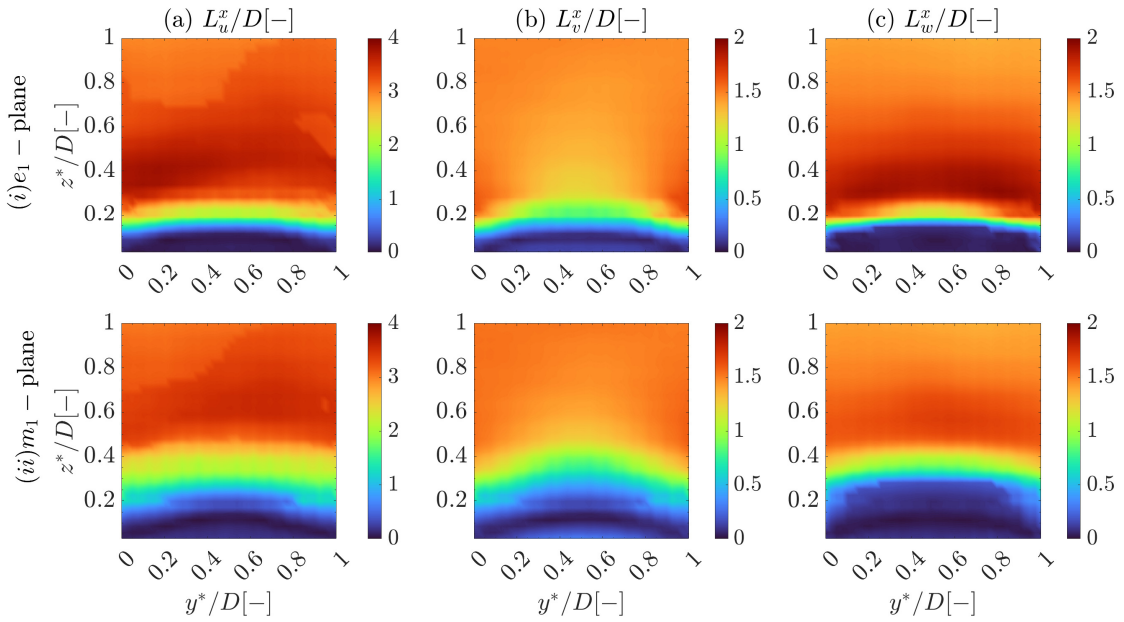

Figure 5.27: Non-dimensional longitudinal integral length scales distribution for the (a) longitudinal, L_u^x/D, (b) lateral, L_v^x/D, and (c) vertical, L_w^x/D, velocity components, against the non-dimensional lateral direction, y^*/D, and the non-dimensional vertical direction, z^*/D, for Case II (i)e_1-plane and (ii) m_1-plane.

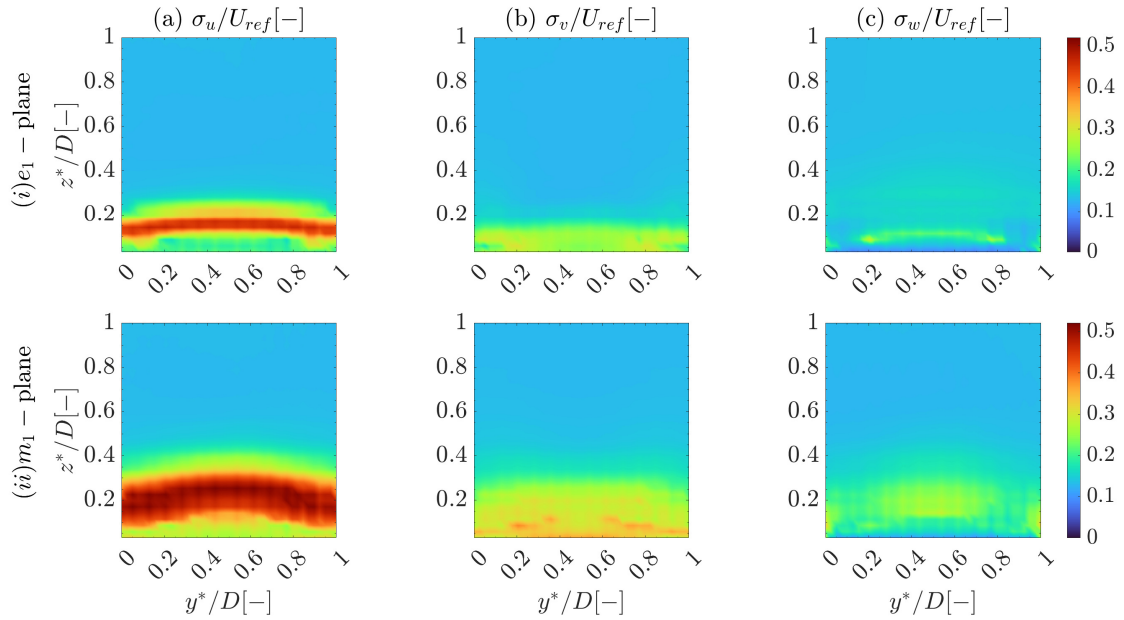

Figure 5.28: Non-dimensional standard deviation distribution for the (a) longitudinal, σ_u/U_{ref}, (b) lateral, σ_v/U_{ref}, and (c) vertical, σ_w/U_{ref}, velocity components, against the non-dimensional lateral direction, y^*/D, and the non-dimensional vertical direction, z^*/D, for Case II (i) e_1-plane and (ii) m_1-plane.

5.6 Conclusions

In the presented work, a LES was employed to replicate a reference experimental study and references LES analysis for a high-rise building. The main objective of this study is to gain a deeper understanding of the statistical characteristics of the wind field over a high-rise building with a turbulent inflow compatible with the Eurocode Terrain Type II. The secondary goal is to understand the impact of the HRB on the statistical characteristics of wind fields. The generated second-order statistics from the LES (such as the spectra and the ACF) of the urban wind field at the rooftop of a high-rise building will be used in the next chapter as deterministic inputs of NG methods to obtain synthetic realizations of turbulent velocity fields representative of the urban environment. This is crucial since having a synthetic wind field, which accurately replicates the second-order statistics of urban wind fields, will improve the predictions of the power performance and the loading state during the aeroelastic design process of WTs to be used in the built environment.

The turbulent inflow at the inlet BC of the LES domain was generated using the SRM, particularly using Mann's approach for the synthetic generation of the turbulent wind velocity fields. A sensitivity study was conducted to identify the value of the parameters of Mann's model for the synthetic generation of the wind field at the inlet of the domain, to acquire the desired turbulent inflow observed in the experimental study. The results of the conducted LES analysis in the present study were validated against the data collected from a reference experimental study and reference LES studies conducted by other researchers investigating the same building setup.

To compare the effect of the building on the wind field characteristics, two configurations were analyzed: an empty domain and the same domain, including the high-rise building. The longitudinal mean wind velocity exhibits acceleration outside the boundary layer, and the height of the maximum longitudinal mean wind velocity is dependent on the thickness of the boundary layer. In the proximity to the building's surface rooftop, elevated levels of turbulence intensities were observed to be dependent on the thickness of the boundary layer. Moreover, the values of turbulence intensities decrease as the distance from the surface increases. In general, the spectra and its Fourier pair (the ACF) exhibit similar characteristics for the two considered cases in the region far away from the building rooftop surface, although a noticeable difference arises in the region close to the building rooftop surface. A shift in the peak of the normalized spectra towards high frequencies was observed closer to the building rooftop surface. The ACF exhibits faster decay in the region inside the boundary layer compared to the region outside the boundary layer. A faster decay in the coherence function was noticed in the presence of the building compared to the values corresponding ot the empty domain.

Chapter 6

Synthetic generation of urban wind fields by using SRM and SM methods

In the previous chapters, the SM has been presented to synthesize wind fields from predefined target CMF and CPSDM. The target CMF and CPSDM were obtained from turbulence models such as vK and Mann ones, which propose a parameterization of the two-points, two-times second-order statistics for stationary, Gaussian, homogeneous, and isotropic/anisotropic wind fields, respectively. However, as described in Chapters 2 and 5, the wind field in urban environments is characterized to be highly non-homogeneous, non-Gaussian and anisotropic. In this chapter, the capabilities of the SRM and the SM to generate synthetic urban wind field are analyzed for a set of particular case studies. The second-order statistics of the wind field developed over the HRB's rooftop of the conducted LES (see Chapter 5) are provided as the statistical inputs to the SRM and SM approaches. Several case studies were conducted to analyze the capability of each approach.

6.1 Eigen-decomposition of the CPSDM with Veers-Shinozuka approach

As discussed in Section 2.2, the SRM was formally proposed by (Shinozuka, 1971) and it typically relies on inverse FFT (Shinozuka & Deodatis, 1991, 1996). The two implementations mainly used in SRM are the Mann approach (Mann, 1998) and Veer-Shinozuka approach (Shinozuka, 1971; Veers, 1988). Both approaches are used to generate the three velocity components of wind fields on M $\boldsymbol{x}_{\perp}$ points on the rotor plane. The rotor plane is considered to be perpendicular to the mean flow velocity. The points $M = N_y \times N_z$, where N_y and N_z are the number of points in y and z directions of the plane, respectively. The Mann's approach was briefly illustrated in Section 5.3.3. In this section, the Veers-Shinozuka approach is explained to generate synthetic wind fields ($3M$V-1D RP).

In Veers-Shinozuka approach, a $3M$V-1D vector RP $\boldsymbol{u}_t = \boldsymbol{u}(t;\alpha)$ representing the three velocity components in M points on a perpendicular plane to the mean wind speed, where

$\boldsymbol{u}_t = [u(\boldsymbol{x}_1, t; \alpha), v(\boldsymbol{x}_1, t; \alpha), w(\boldsymbol{x}_1, t; \alpha), ..., u(\boldsymbol{x}_M, t; \alpha), v(\boldsymbol{x}_M, t; \alpha), w(\boldsymbol{x}_M, t; \alpha)]^T$ is computed as:

$$\boldsymbol{u}_t = \sum_{d=-\infty}^{d=\infty} \boldsymbol{V}\left(\omega_d\right) \exp\left(\mathrm{i}\omega_d t\right) \exp\left[\mathrm{i}\theta\left(\omega_d; \alpha\right)\right], \tag{6.1}$$

where $\boldsymbol{V}(\omega)$ is a deterministic matrix which is related to the CPSDM $\boldsymbol{S}(\omega)$ as:

$$\boldsymbol{V}^*(\omega)\boldsymbol{V}(\omega) = \Delta\omega \boldsymbol{S}_{\boldsymbol{u}}(\omega). \tag{6.2}$$

The deterministic matrix $\boldsymbol{V}(\omega)$ is evaluated from Equation (6.2) by means of Cholesky decomposition. The CPSDM is computed through Equation (2.13), where the wind field is usually determined from LES or measurements. The CPSDM by definition is Hermitian positive-definite matrix ($\boldsymbol{x}^T \boldsymbol{S}_{\boldsymbol{u}} \boldsymbol{x} > 0 \; \forall \, \boldsymbol{x} \in \mathbb{R}^{3M} \backslash \{\boldsymbol{0}\}$). However, numerical issues may arise during the CPSDM computation from Equation (2.13), which can result in having eigenvalues that are in close proximity to zero but exhibit negative values. This situation makes it infeasible to apply Cholesky decomposition to evaluate the deterministic matrix $\boldsymbol{V}(\omega)$.

To avoid the issues associated with Cholesky decomposition, the $3M$V-1D process $\boldsymbol{u}_t$ can be decomposed to the summation of $3M$ $3M$V-1D RP $\boldsymbol{y}^j(t; \alpha)$ (Di Paola & Gullo, 2001)as:

$$\boldsymbol{u} = \sum_{j=1}^{3M} \boldsymbol{y}^j(t; \alpha). \tag{6.3}$$

The RP $\boldsymbol{u}_t$ has a CPSDM, $\boldsymbol{S}_{\boldsymbol{u}}(\omega)$, with dimension $3M \times 3M$. By applying eigen decomposition to the CPSDM of the $3M$V-1D RP $\boldsymbol{u}(t; \alpha)$, the $\boldsymbol{S}_{\boldsymbol{u}}(\omega)$ is expressed as:

$$\boldsymbol{\Psi}(\omega)\boldsymbol{S}_{\boldsymbol{u}}(\omega)\boldsymbol{\Psi}^T(\omega) = \boldsymbol{\Lambda}(\omega), \tag{6.4}$$

where $\boldsymbol{\Psi}(\omega)$ is the eigenvector matrix with dimension $3M \times 3M$ whose columns are the $\boldsymbol{S}_{\boldsymbol{u}}(\omega)$ eigenvectors and $\boldsymbol{\Lambda}(\omega)$ is the diagonal eigenvalues matrix with dimension $3M \times 3M$, whose diagonal elements $\lambda_j(\omega)$ are the $\boldsymbol{S}_{\boldsymbol{u}}(\omega)$ eigenvalues with $\lambda_1(\omega) > \ldots > \lambda_{3M}(\omega)$. It is worth mentioning that the components of both $\boldsymbol{\Psi}(\omega)$ and $\boldsymbol{\Lambda}(\omega)$ matrices are real, since, $\boldsymbol{S}_{\boldsymbol{u}}(\omega)$ is a Hermitian positive-definite matrix $\forall\, \omega$. Similarly as the RP $\boldsymbol{u}_t$, the $\boldsymbol{S}_{\boldsymbol{u}}(\omega)$ is decomposed into the summation of the CPSDM of each RP $\boldsymbol{y}^j(t; \alpha)$, $\boldsymbol{S}_{\boldsymbol{y}^j}$, to be defined as:

$$\boldsymbol{S}_{\boldsymbol{u}}(\omega) = \sum_{j=1}^{3M} \boldsymbol{S}_{\boldsymbol{y}^j} = \boldsymbol{\Psi}(\omega)\boldsymbol{\Lambda}(\omega)\boldsymbol{\Psi}^T(\omega). \tag{6.5}$$

Note that $\boldsymbol{\Psi}^T(\omega)\boldsymbol{\Psi}(\omega) = \boldsymbol{I}$. The CPSDM of each RP $\boldsymbol{y}^j(t, \alpha), j = 1, \ldots, 3M$ is computed as follows:

$$\boldsymbol{S}_{\boldsymbol{y}^j}(\omega) = \boldsymbol{\psi}_j(\omega)\boldsymbol{\psi}_j^T(\omega)\lambda_j(\omega), \tag{6.6}$$

where the vector $\boldsymbol{\psi}_j$ is the j^{th} column of the eigenvector matrix $\boldsymbol{\Psi}$ (i.e. it is the j^{th} eigenvector of $\boldsymbol{S}_{\boldsymbol{u}}$. The $3M$V-1D RP $\boldsymbol{y}^j(t; \alpha)$ is evaluated as follows:

$$\boldsymbol{y}^j(t; \alpha) = \sum_{d=-\infty}^{d=\infty} \exp\left(\mathrm{i}\omega_d t\right) \hat{\boldsymbol{Y}}^j\left(\omega_d\right) \exp\left[\mathrm{i}\theta\left(\omega_d; \alpha\right)\right], \tag{6.7}$$

where $\hat{\boldsymbol{Y}}^j(\omega_d) = \boldsymbol{\psi}_j(\omega_d)\sqrt{\Delta\omega\lambda_j(\omega_d)}$. Observe that, in this approach, the vector Fourier coefficient $\hat{\boldsymbol{Y}}^j(\omega_d)$ is computed from the j^{th} eigenvalue and eigenvector of the CPSDM and it does not involve applying the Cholesky decomposition. Hence, it avoids the challenges associated with Cholesky decomposition to compute the deterministic matrix. It is noteworthy that the modes with eigenvalues in close proximity to zero, can be neglected to reduce the summation in Equation (6.3) to N_m, where $N_m < 3M$, to synthesize the $3M$V-1D RP $\boldsymbol{u}_t$ considering,

$$\boldsymbol{u} = \sum_{j=1}^{N_m} \boldsymbol{y}^j(t;\alpha), \tag{6.8}$$

which subsequently leads to a reduction of the required computational cost to synthesize the $3M$V-1D RP $\boldsymbol{u}_t$. Note that the Veers-Shinozuka approach combined with the eigendecomposition of the CPSDM will be referred to as the VSED approach.

6.2 Practical considerisations for synthesis of wind fields through NG

This section introduces a computationally efficient optimization approach for calibrating the VAR model parameters based on a predefined CMF (Gallego-Castillo et al., 2024), aimed at reducing the computational cost associated with the CG approach (Gallego-Castillo et al., 2022). Furthermore, it demonstrates the process of obtaining non-Gaussian wind velocity fields by combining the quantile-to-quantile transformation (Grigoriu, 1984; Lebrun & Dutfoy, 2009) with the NG methods discussed previously.

6.2.1 A computationally efficient optimization approach for VAR model calibration with a predefined target CMF

In Section 3.4.2, the CG approach was presented. This approach optimally calibrates a restricted AR/VAR model from a target CMF, employing GA for the optimization process. The main limitation of this approach is the high computational cost required by the optimization process. This is due to the need to explore different combinations of **j** and **l** vectors to identify an optimal VAR model with N regression coefficients. In this section, a computationally efficient approach to calibrate the structure of a restricted AR/VAR model parameters by assuming an exponential scheme is illustrated.

The **j** and **l** vectors, obtained through the CG approach for the case study detailed in Chapter 4, are shown in Figure 4.6 together with the corresponding **j** and **l** vectors from the Y-W and K-M approaches. It was observed that the optimal **j** and **l** vectors exhibit a form consistent with a power function, a^n, with $n = 0, \ldots, N-1$. However, the observed form did not conform to the base value $a = 2$, as proposed in the K-M approach (Krenk & Møller, 2019). Thus, the computational cost required by the CG approach can be reduced by optimizing the base of the power function, a, rather than all the components within the **j** vector. Further simplification

to reduce the associated computational cost can be achieved by assuming $\mathbf{j} = \mathbf{l}$. Consequently, the number of variables to be optimized is reduced from $2N$ to a single variable, namely, a. The base a is constrained within the range $]1, m]$, with m as a selected upper limit for the possible values of a. This approach was presented by (Gallego-Castillo et al., 2024) and it is denoted as "CG-Computationally Efficient Optimization" (CG-CEO) in the subsequent sections.

6.2.2 Application of quantile-to-quantile transformation for non-Gaussian synthetic wind fields in the NG

The synthetic wind velocity time series generated by the previously described statistical methods follows a Gaussian distribution. Nevertheless, it is important to note that the urban wind field is typically characterized by high non-Gaussianity. Recent studies have presented conflicting findings regarding the impact of Gaussian and non-Gaussian wind fields on wind turbine dynamic responses. Some studies, such as (Schottler et al., 2017), have reported differences, while others, like (Berg et al., 2016), have not observed such distinctions. A combination between the statistical methods (SRMS and SMs) and the quantile-to-quantile transformation (Grigoriu, 1984; Lebrun & Dutfoy, 2009) is proposed to reproduce non-Gaussianity of actual velocity fields in this research. The findings have been accepted to be presented in the TORQUE Conference 2024 (Gallego-Castillo et al., 2024). This combination aims to capture by the proposed NG methods the unique features of non-Gaussian PDFs of velocity components in wind fields generated through LES. To generate a non-Gaussian synthetic wind field, the utilization of a quantile-to-quantile transformation can be employed. The process of generating non-Gaussian synthetic wind velocity time series using the quantile-to-quantile transformation can be illustrated through the following steps:

- Employing the quantile-to-quantitle transformation to obtain Gaussian fluctuation wind field, $u_{\mathcal{N},i} = \Phi^{-1}(G_i(u_i))$ for $i = 1, \ldots, h$, where h is the number of variates, $\Phi^{-1}(\cdot)$ is the inverse Cumulative Distribution Function (CDF) of a $\mathcal{N}(0, 1)$ RV, and $G_i(\cdot)$ is the marginal CDF.
- Computing the necessary input (CMF or CPSDM) for the statistical method, utilizing the resolved Gaussian fluctuation wind field, $u_{\mathcal{N},i}$. Subsequently, generating synthetic Gaussian wind field following the calibration of the necessary coefficients from the defined target CMF or CPSDM.
- Transforming the generated synthetic Guassian velocity field to non-Gaussian wind field by employing $G_i^{-1}(\Phi(\cdot))$.

The previous step to obtain non-Gaussian wind fields using the quantile-to-quantile transformation are illustrated in a diagram shown in Figure 6.1. Note that Gaussian wind fields are denoted with subscript $(\cdot)_{\mathcal{N}}$.

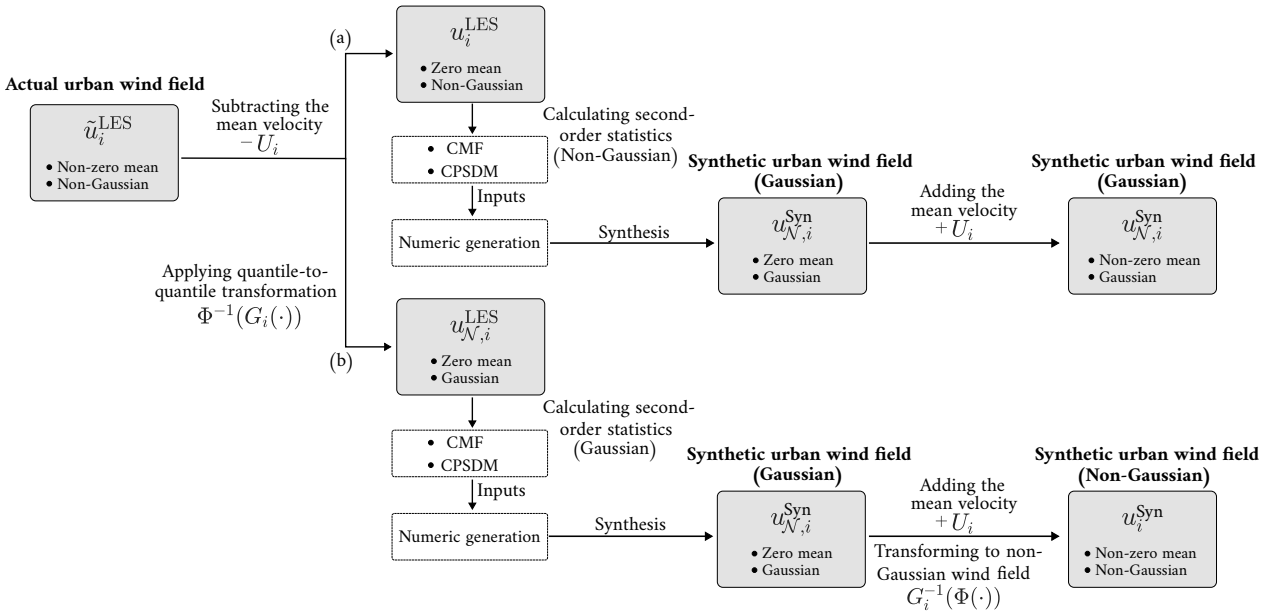

Figure 6.1: Diagram illustrating the procedural scheme for obtaining (a) Gaussian wind fields, and (b) non-Gaussian wind fields by combining statistical methods with the quantile-to-quantile transformation.

6.3 Results and discussion

The synthesis of the generated wind field from the target CMF and CPSDM resolved from the conducted LES study on the HRB rooftop (See Chapter 5) is discussed in this section. The CPSDM of the resolved LES wind field is evaluated, using the Blackman and Tukey estimator (Marple Jr & Carey, 2019). This CPSDM is used as the input to the OCEAN approach and to the VSED approach (Di Paola & Gullo, 2001), discussed in Sections 4.5 and 6.1, respectively. Whilst, the CMF of the resolved LES wind field is computed, utilizing the biased estimator (Marple Jr & Carey, 2019), to be provided to the VAR CMF based approaches illustrated in Sections 3.4.2 and 6.2.1.

Three case studies are analyzed: synthesization along a vertical line, synthesization on perpendicular and parallel planes to the mean wind speed as shown in Figure 6.2. In the first case study, the OCEAN approach is used to synthesize the longitudinal velocity component along a vertical line with $M = 10$ points. In the second case, the longitudinal and vertical velocity components were synthesized on a parallel plane with 25×25 grid points, utilizing the SM approach. Finally, the lateral and vertical velocity components were synthesized on a perpendicular plane with 28×16 grid points in the third case study, using the VSED approach. Note that the quantile-to-quantile transformation was employed only in the second case to reproduce the non-Gaussian characteristics of the LES wind field.

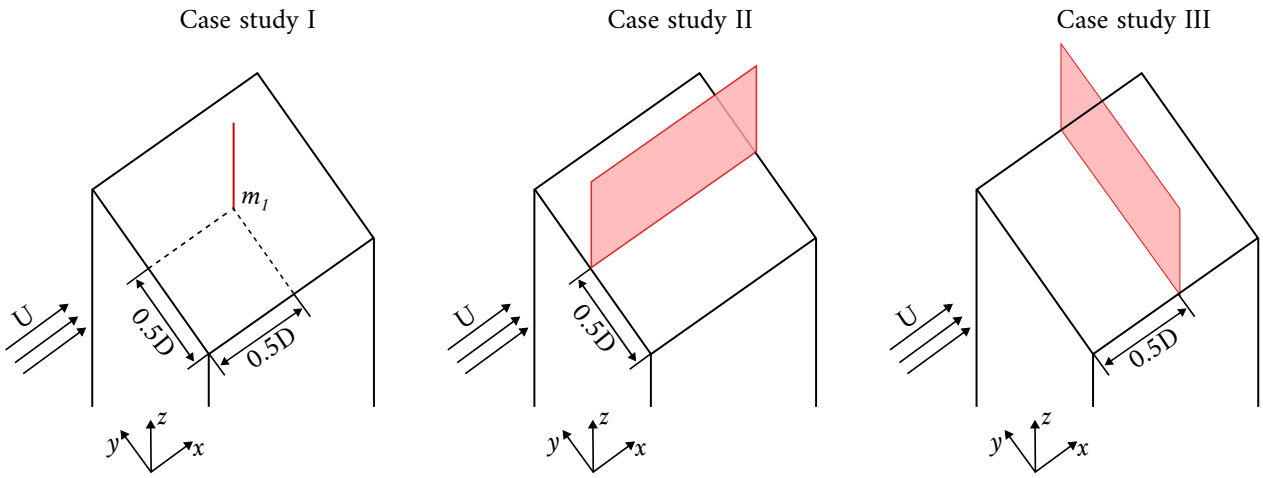

Figure 6.2: Considered case studies for the synthesization of urban wind fields.

6.3.1 Synthesis of the longitudinal wind velocity component along a vertical line using a VAR model (spectra-based approach)

In this case study, the OCEAN approach (see Section 4.5) is used to synthesize the longitudinal velocity component fluctuation, u along a vertical line at the center of the HRB's rooftop as shown in Figure 6.2. The mean $u-$velocity profile resolved from the conducted LES is subsequently added to the synthetic u to obtain the longitudinal velocity field, $\tilde{u}$, along the vertical line. To reduce the required computational cost by the OCEAN approach, only 10 grid points along the vertical line, within the range of heights $z^*/D \in [0.029, 0.663]$, are considered. Additionally, the chosen order for the VAR model is 5. This VAR model order was selected to reduce the number of eigenvalues and eigenvectors to be optimized. In this particular case, the quantile-to-quantile transformation was not employed to demonstrate the PDF of the generated synthetic wind field and compare it with the proceeding case, where the quantile-to-quantile transformation was utilized. The CPSDM characterizing the longitudinal velocity components for the 10 grid points is computed utilizing the Blackman and Tukey CPSDM estimator (Marple Jr & Carey, 2019). This estimator is selected to provide a smooth CPSDM to facilitate the fitting of the VAR CPSDM to the target CPSDM. The spectra error, E_S is computed from Equation (4.24) at $M_f = 200$ points, for both the real and imaginary parts of the spectra, along the interval $[f_{\min}, f_{\max}]$, where $f_{\min} = 1/64$ Hz, the time step $\Delta t = 5 \times 10^{-4}$ s and $f_{\max} = 1000$ Hz. It is worth mentioning that the error weight matrix, W_{rq}, is considered to be equal to 1 in Equation (4.24). The eigenvalues combination of the optimal VAR(5), obtained for this test case, is $N_{\lambda^r} = 0$ and $N_{\lambda^c} = 25$. This eigenvalues combination is depicted in Figure 6.3.

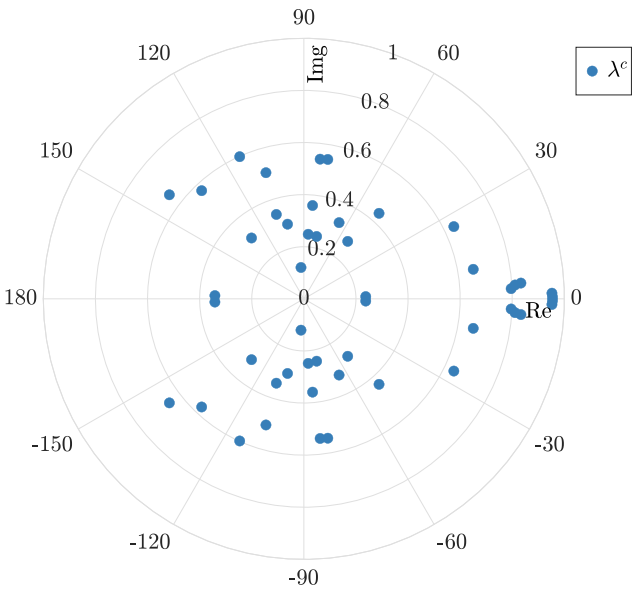

Figure 6.3: Complex conjugate, λ^c, eigenvalues of the optimal VAR(5), obtained from OCEAN approach, presented on a complex plane.

Figures 6.4 and 6.5 show the real and imaginary parts of the theoretical one-sided cross-spectra of the VAR, $S^{\text{VAR}}_{u_i u_j}$, obtained OCEAN approach together with the target CPSDM (LES) components at three grid points $z^*/D \approx 0.029, 0.49, 0.663$. The OCEAN approach shows a good match to the target CPSDM over a wide range of frequencies. The PSD for the $u-$velocity component, $S_{u_i u_i}$, is depicted in Figure 6.6 as a contour plot dependent on the non-dimensional z^*/D and non-dimensional frequency fD/U_{ref} for the target PSD and PSD of one sample generated by the optimal VAR(5) model. Figure 6.6a reveals an increase in the $S_{u_i u_i}$ value at the transition region between the undistributed flow and the recirculation bubble, indicating an increase in the energy contained within this region. The estimated PSD for the one sample reproduces very well this energy increase in the transition region.

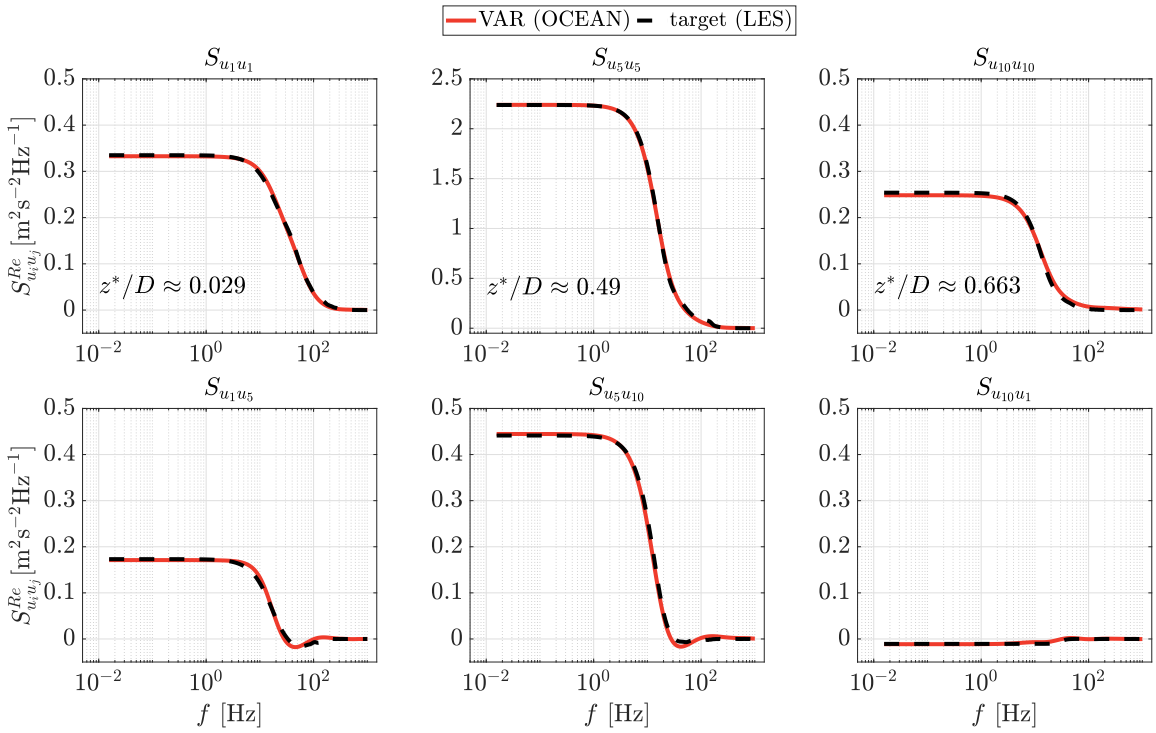

Figure 6.4: Real part of the one-sided CPSDM, $S^{Re}_{u_iu_j}$, in terms of frequency f, for: (a) theoretical CPSDM VAR(5) (red) obtained from OCEAN approach, and (b) target CPSDM (black) at heights $z^*/D \approx 0.029, 0.49, 0.663$.

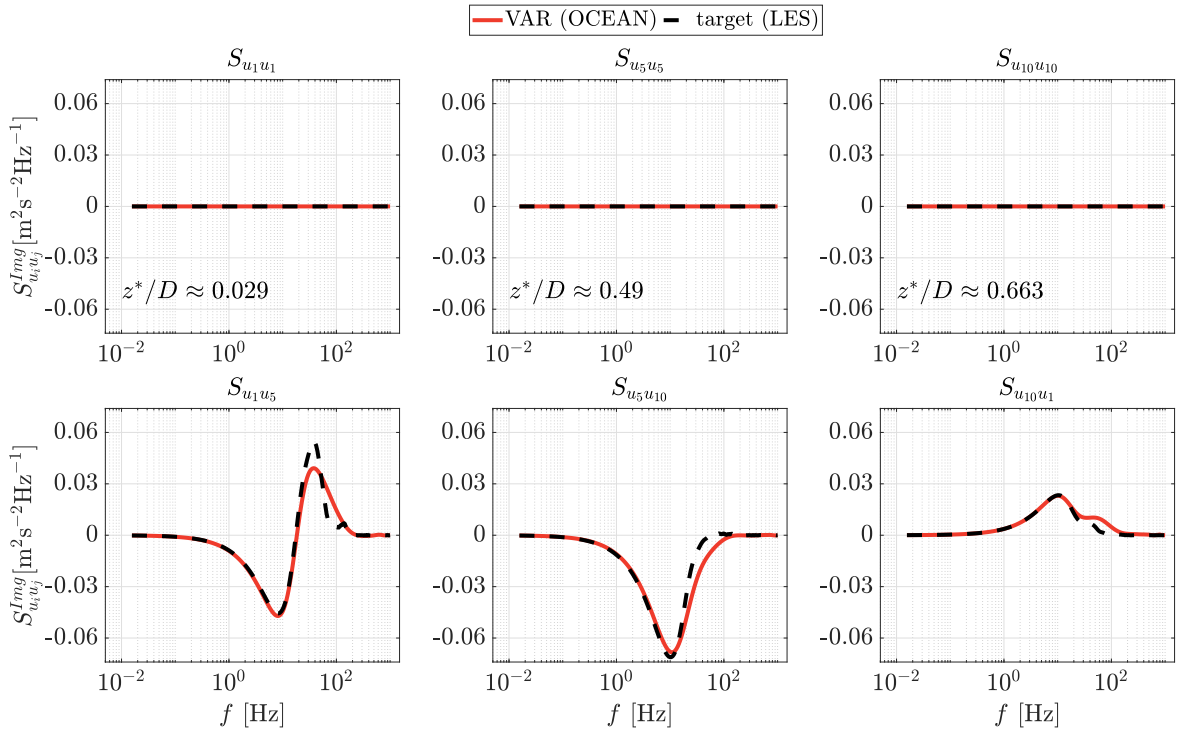

Figure 6.5: Imaginary part of the one-sided CPSDM, $S^{Re}_{u_iu_j}$, in terms of frequency f, for: (a) theoretical CPSDM VAR(5) (red) obtained from OCEAN approach, and (b) target CPSDM (black) at heights $z^*/D \approx 0.029, 0.49, 0.663$.

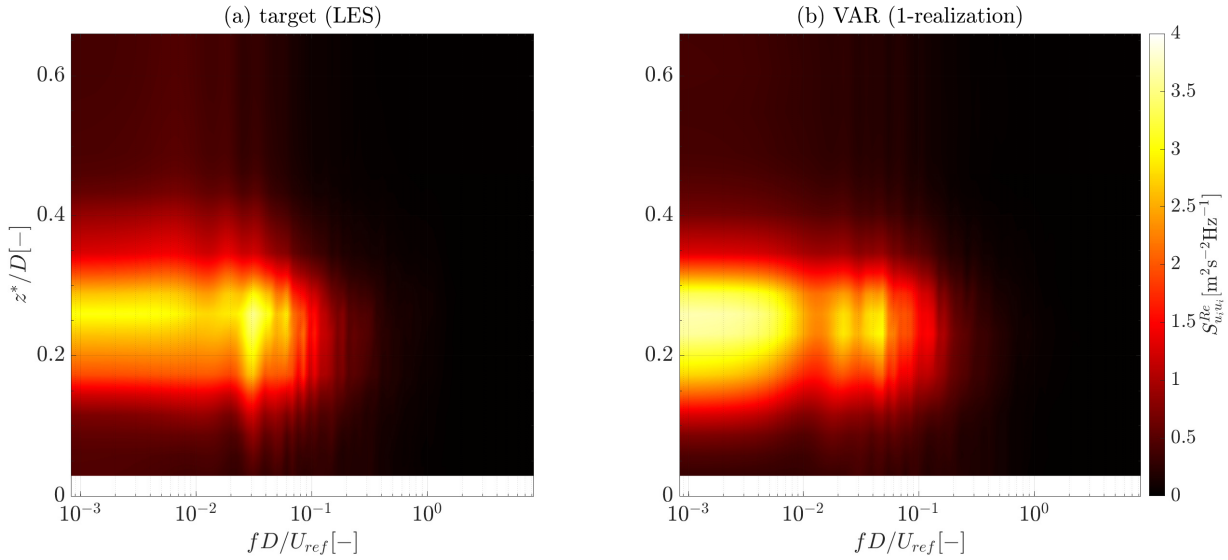

Figure 6.6: Colormap of the PSD of the longitudinal velocity component, $S_{u_iu_i}$, against the non-dimensional frequency, fD/U_{ref}, and the non-dimensional vertical direction, z^*/D for the longitudinal wind field (a) obtained from the LES and (b) from a synthesized sample generated by the optimal VAR(5).

In Figure 6.7a, the non-dimensional mean longitudinal velocity vertical profile is shown for the wind field generated from the conducted LES, one sample generated from the optimal VAR(5) model, and the ensemble of 10 samples generated from the optimal VAR(5) model. The vertical profile of the non-dimensional standard deviation for the $u-$velocity component, σ_u/U_{ref}, is shown in Figure 6.7b for the target profile obtained from the LES, one sample and ensemble of 10 samples generated from the optimal VAR(5) model. The variation of the standard deviation within the height range $0.029 < z^*/D < 0.46$ is well captured by the VAR model, however, a slight overestimation of the standard deviation is observed within the range $0.46 < z^*/D < 0.663$. This overestimation can be mitigated by increasing the VAR model order. A higher model order leads to a better fit of the VAR CPSDM to the target CPSDM, consequently resulting in a better capture of the variance.

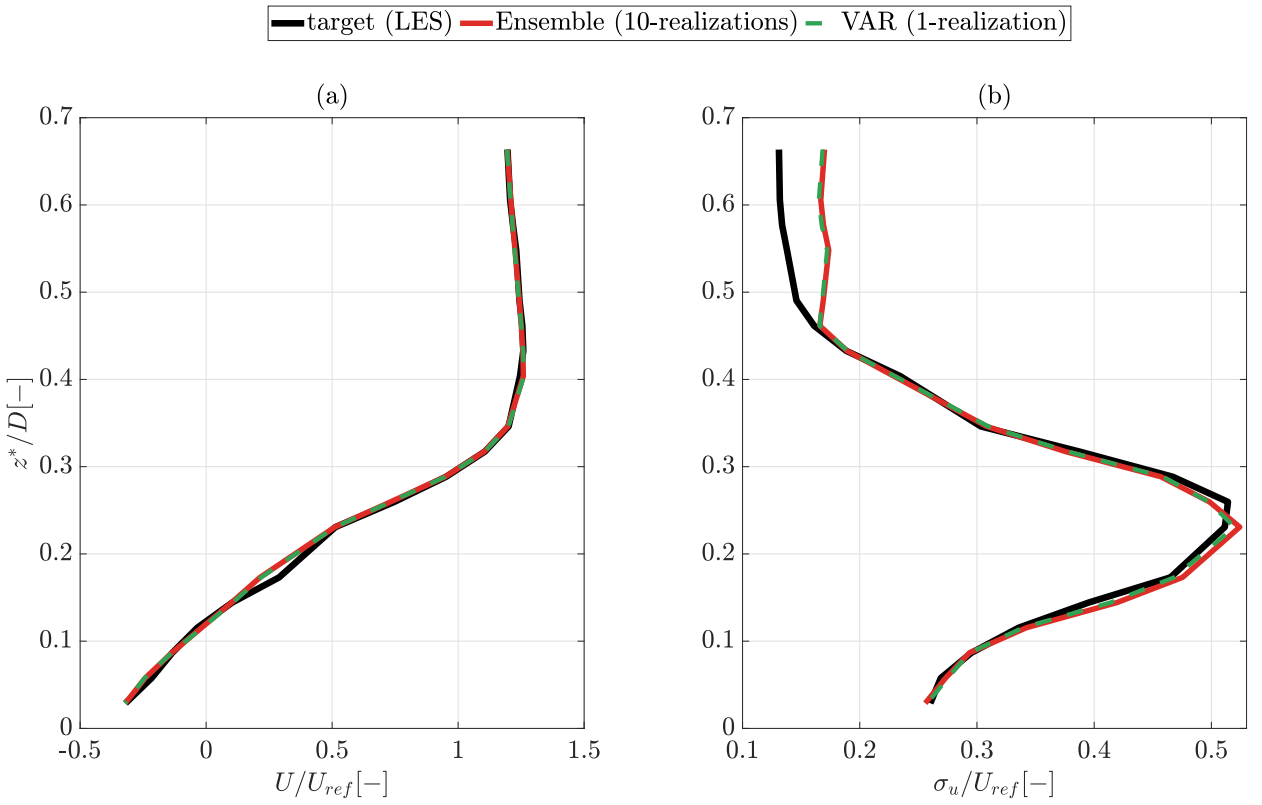

Figure 6.7: Vertical profile of (a) the non-dimensional mean longitudinal velocity U/U_{ref} and (b) the non-dimensional longitudinal standard deviation σ_u/U_{ref} for the wind field generated by the conducted LES, ensemble of 10 synthesized samples generated by the optimal VAR(5) model and one synthesized sample.

Figure 6.8 shows the time series of the non-dimensional longitudinal wind velocity, $\tilde{u}/U_{ref}$, obtained from the LES simulation and from one synthesized sample generated by the optimal VAR(5), along a vertical line until the non-dimensional time $t/T = 0.1$, where $T = 64$ seconds. The pattern of the single synthesized sample time series generated by the optimal VAR(5) allows to identify very well the signature of the recirculation bubble region near the rooftop surface. The reduction in the longitudinal wind velocity value inside the recirculation bubble is well-represented by the synthesized sample time series.

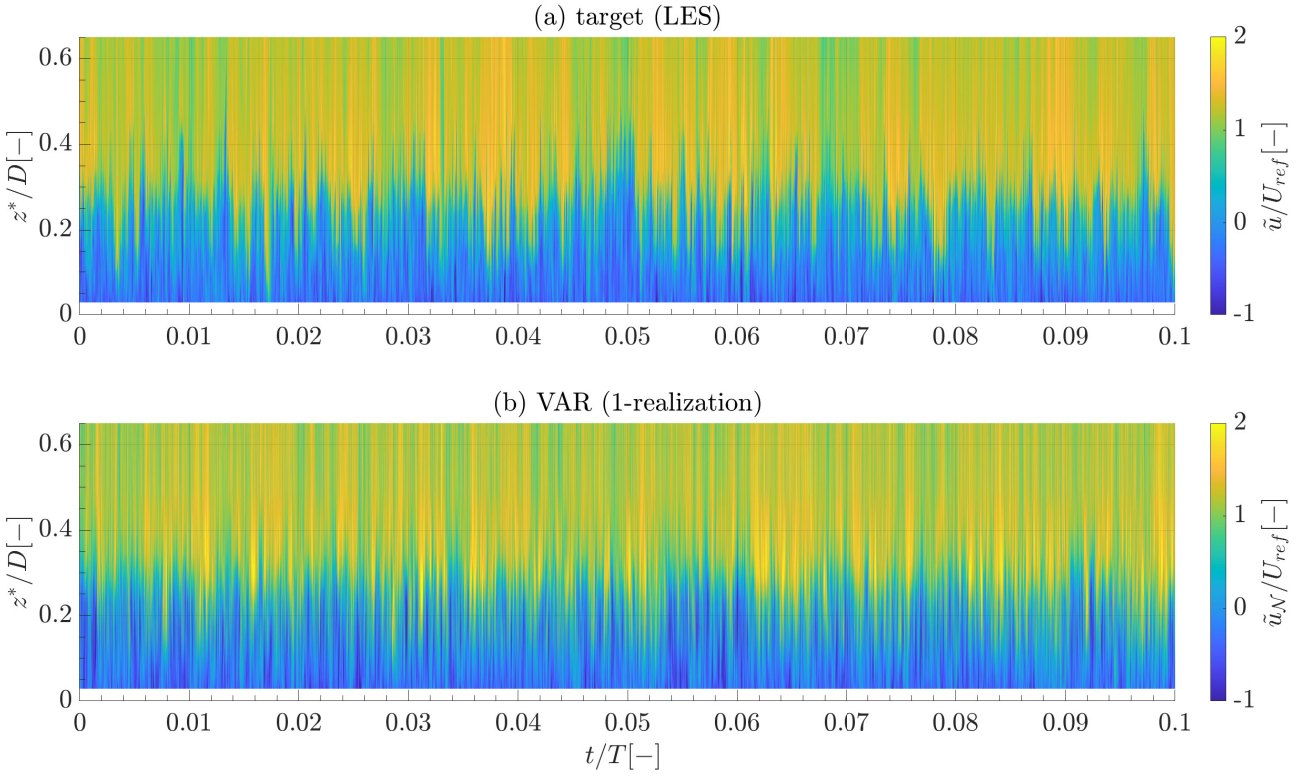

Figure 6.8: Non-dimensional longitudinal wind velocity, $\tilde{u}/U_{ref}$ and $\tilde{u}_{\mathcal{N}}/U_{ref}$ for the LES and the synthesis, respectively, against the non-dimensional height z^*/D and non-dimensional time t/T, obtained from (a) the conducted LES and (b) one sample of Gaussian time series generated by optimal VAR(5) model, obtained from OCEAN approach.

In Figure 6.9, PDFs of the longitudinal velocity component of the wind field generated by the conducted LES and a sample generated by the OCEAN approach are shown. PDFs are presented for various heights. Variations in the PDFs distribution for the wind field obtained from the LES were observed. The PDFs for the regions outside the shear layer display, with some degree of variability, Gaussian distribution. Whilst, in the region of the shear layer, a highly non-Gaussian PDF distribution was observed. However, the generated synthetic wind field through the OCEAN approach displays Gaussian distributions across all flow regions. This observation shows the necessity of applying the quantile-to-quantile transformation (see Section 6.2.2), to match the velocity PDF distribution of the target wind fields.

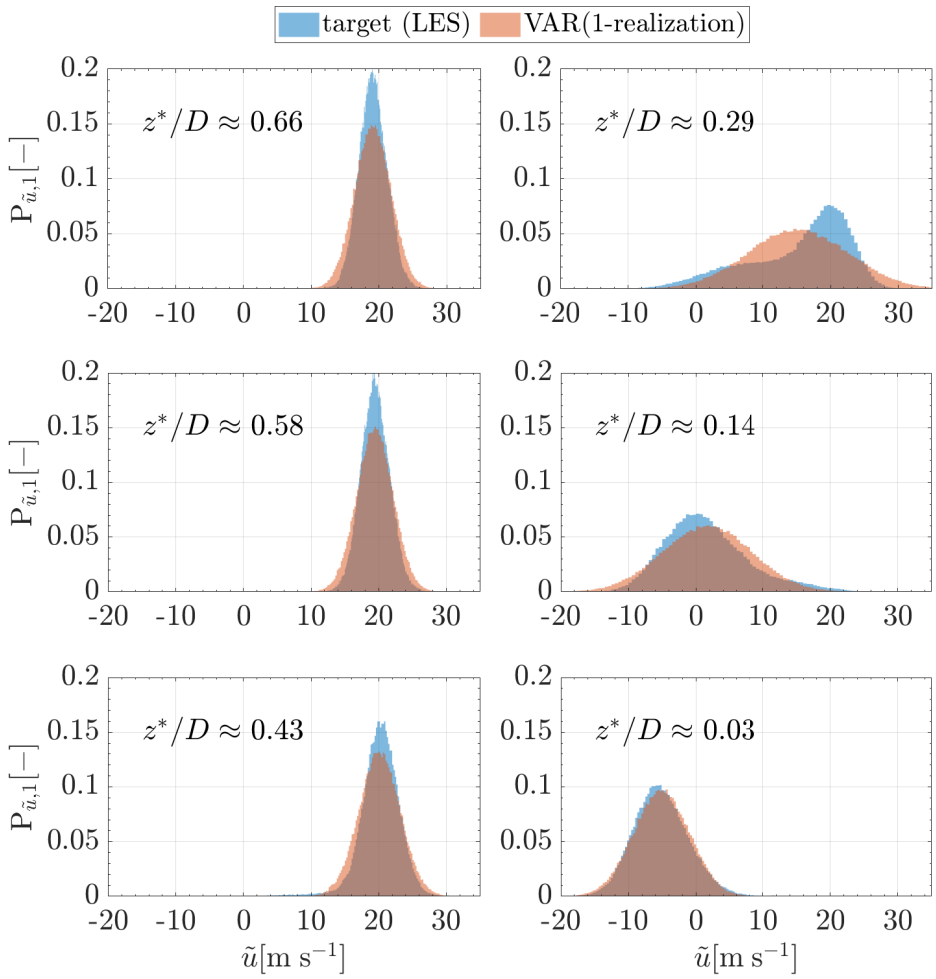

Figure 6.9: First-order PDF of the longitudinal velocity component of the wind field, $P_{\tilde{u},1}$, from the conducted LES (target) and a Gaussian sample generated by the OCEAN approach located at $z^*/D \approx 0.03, 0.14, 0.29, 0.43, 0.58, 0.66$.

6.3.2 Synthesis of the longitudinal and vertical velocity components on the $p-$plane using a VAR model (covariance-based approach)

The CG-CEO approach is employed in this study case to synthesize u and $w-$velocity components on the $p-$plane. A 25×25 spatial grid was considered for the synthesis. The wind field resolved from the conducted LES was utilized to obtain a target CMF, using the "biased" method for the CMF computation (Marple Jr & Carey, 2019). By utilizing the target CMF, an optimal VAR model with $N = 5$ regression terms was obtained using the CG-CEO (see Section 6.2.1). For this case study, M_τ (= 201 points) is selected along the lag interval of $[0, l_{\max}]$, where $l_{\max} = 200$ to evaluate the MSE. The considered interval for the power function base, a, is $]1, 4]$. Under the assumption $\mathbf{j} = \mathbf{l}$, the obtained optimal VAR

model has $\mathbf{j} = [1, 2, 6, 15, 37]$, acquired from a base value $a^n = 2.46^n$, for $n = 0, 1, \ldots, N-1$. The quantile-to-quantile transformation was employed to obtain non-Gaussian PDFs for the synthesized longitudinal and vertical velocity components. In Figure 6.10, the PDF of the $u-$velocity component, $\mathrm{P}_{\tilde{u},1}$, is presented for both the wind field generated by the LES and a sample of synthetic wind field generated by the VAR model at four distinct points along a vertical line. The $\mathrm{P}_{\tilde{u},1}$ of the synthetic $u-$velocity component captures the variations in the $\mathrm{P}_{\tilde{u},1}$ along the vertical line, reproducing the non-Gaussianity of the target wind field.

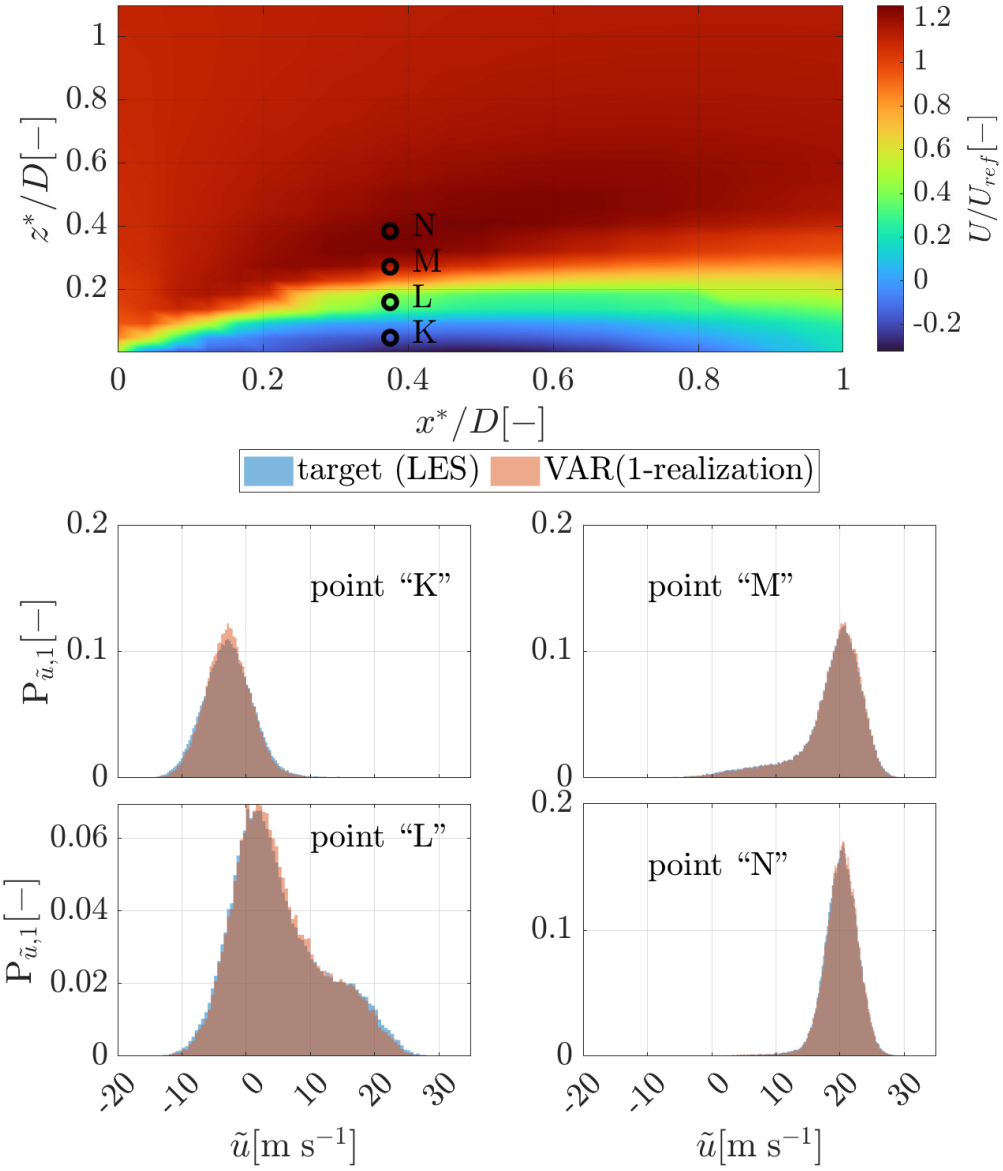

Figure 6.10: [top] Non-dimensional mean velocity distribution for the longitudinal velocity component, U/U_{ref}, on the $p-$plane, and [bottom] the PDF of the longitudinal velocity component of the wind field, $\mathrm{P}_{\tilde{u},1}$, resolved from the conducted LES (target) and a sample generated by the VAR model, at the highlighted points "K, L, M, N".

The correlations for the u and $w-$velocity components between three selected points along a vertical line at $x^*/D = 0.3$ are shown in Figures 6.11 and 6.12. These figures illustrate the correlations for the target data, the synthetic wind field both before and after the application of quantile-to-quantile transformation. It was observed that the employment of the quantile-to-quantile transformation induces changes in the correlation, however, these changes are minimal. The correlation of the non-Gaussian synthetic u and $w-$ velocity components exhibit a good match to the target correlation. Faster decay was observed in the correlation $\gamma_{l,u_3u_3}/\sigma_{u_3}\sigma_{u_3}$ compared to the other two points, since this point is located inside the recirculation bubble. Additionally, the correlation $\gamma_{l,u_3u_1}/\sigma_{u_3}\sigma_{u_1}$ exhibit lower values compared to $\gamma_{l,u_1u_2}/\sigma_{u_1}\sigma_{u_2}$. This distinction may be attributed to the fact that point 1 is situated outside the recirculation bubble and point 2 is in the shear region.

The spatial correlation is represented by the correlation function on the $p-$plane for a specific lag l for the u and $w-$velocity components, $\gamma_{l,u_iu_j}/\sigma_{u_i}\sigma_{u_j}$ and $\gamma_{l,w_iw_j}/\sigma_{w_i}\sigma_{w_j}$, respectively. It was computed between the acquired wind fields on the $p-$plane and three grid points located at different heights. In Figures 6.13 - 6.18, the spatial correlation distributions are shown for both the LES wind field and one sample of a synthetic wind field obtained from the optimal VAR model, at lags $l = 0, 5, 10, 15$, to assess the reliability of the VAR model to reproduce accurately the target CMF. The three points considered for the spatial correlation computation are located: inside the circulation bubble, at the shear layer region, and outside the circulation bubble, respectively. The spatial correlations of the synthetic longitudinal and vertical wind fields reproduce very well the variation in the spatial correlations distribution for the three selected points, accurately representing the strong correlation in the vicinity of the selected points. Capturing spatial correlations with enough accuracy is crucial as they distinctly indicate expected structures within the velocity field, such as the presence of the recirculation bubble (mainly in the longitudinal component plots) and the occurrence of vortex shedding (mainly in the vertical component plots).

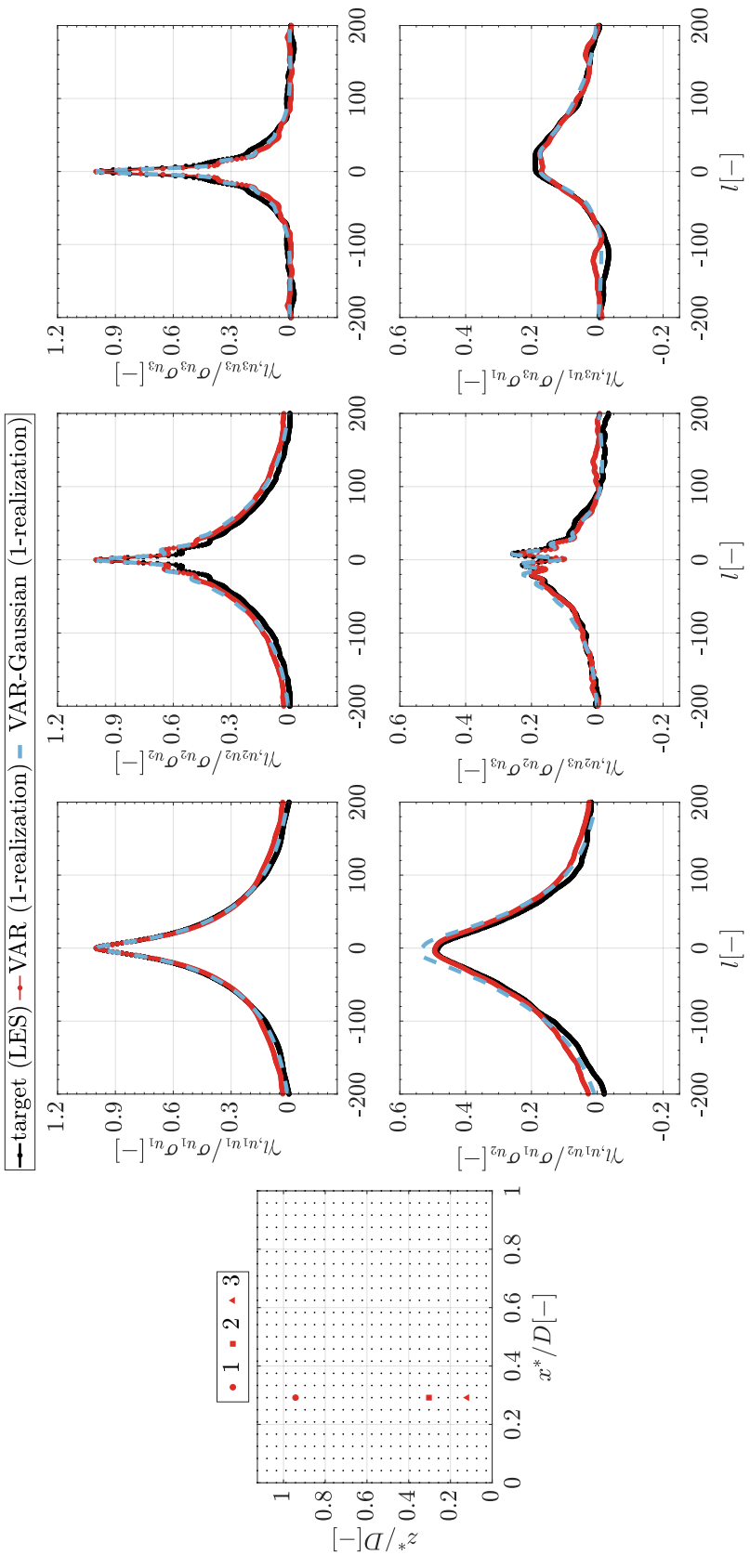

Figure 6.11: [left] Scheme of the $N_x \times N_z = 25 \times 25$ grid points distributed across the $p-$plane, highlighting specific grid points (circle, square and triangle) located at $x^*/D \approx 0.29$ and $z^*/D \approx 0.12, 0.30, 0.94$, which are considered for the correlation calculation, and [right] the correlation for the $u-$velocity component, $\gamma_{l,u_iu_j}/\sigma_{u_i}\sigma_{u_j}$, computed for both the target data and a single sample generated by the VAR model (for Gaussian and non-Gaussian wind fields), at the highlighted three grid points.

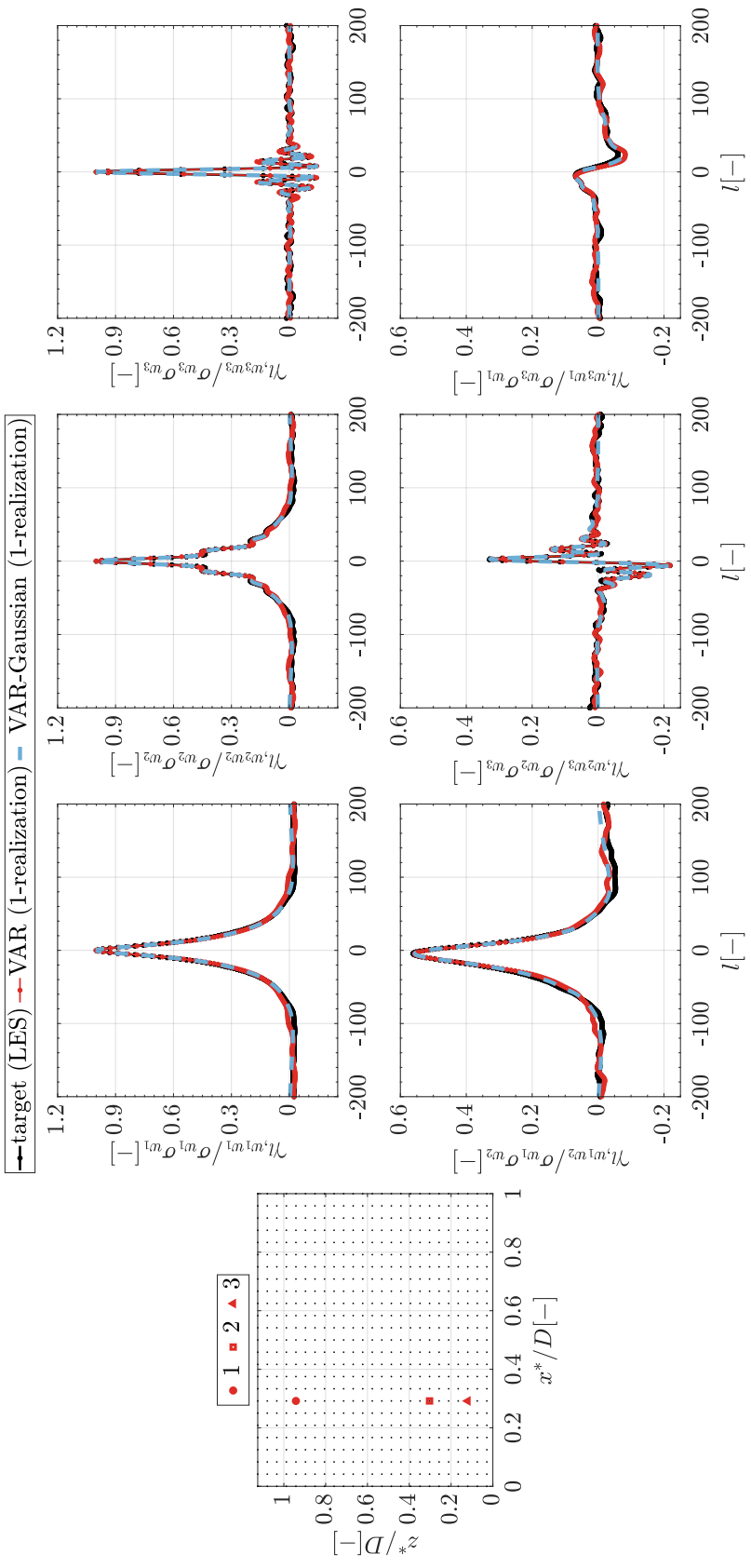

Figure 6.12: [left] Scheme of the $N_x \times N_z = 25 \times 25$ grid points distributed across the $p-$plane, highlighting specific grid points (circle, square and triangle) located at $x^*/D \approx 0.29$ and $z^*/D \approx 0.12, 0.30, 0.94$, which are considered for the correlation calculation, and [right] the correlation for the $w-$velocity component, $\gamma_{l,w_iw_j}/\sigma_{w_i}\sigma_{w_j}$, computed for both the target data and a single sample generated by the VAR model (for Gaussian and non-Gaussian wind fields), at the highlighted three grid points.

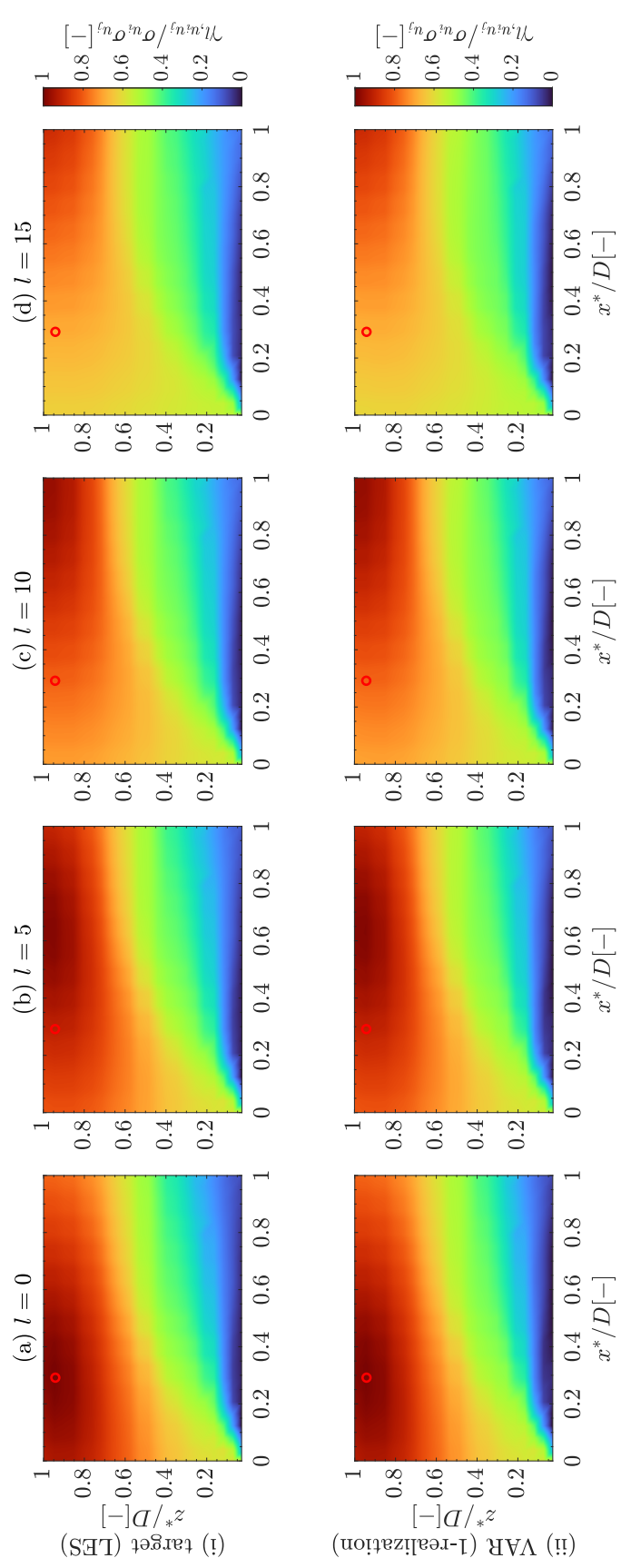

Figure 6.13: Correlation of the $u-$velocity component, $\gamma_{l,u_iu_j}/\sigma_{u_i}\sigma_{u_j}$ distribution on the $p-$plane with respect to the highlighted point (red circle) located at $(x^*/D, z^*/D) \approx (0.29, 0.94)$ (outside the circulation bubble) at time lags $l = 0, 5, 10, 15$, computed for both the target data (top row) and a single sample generated by the VAR model (bottom row).

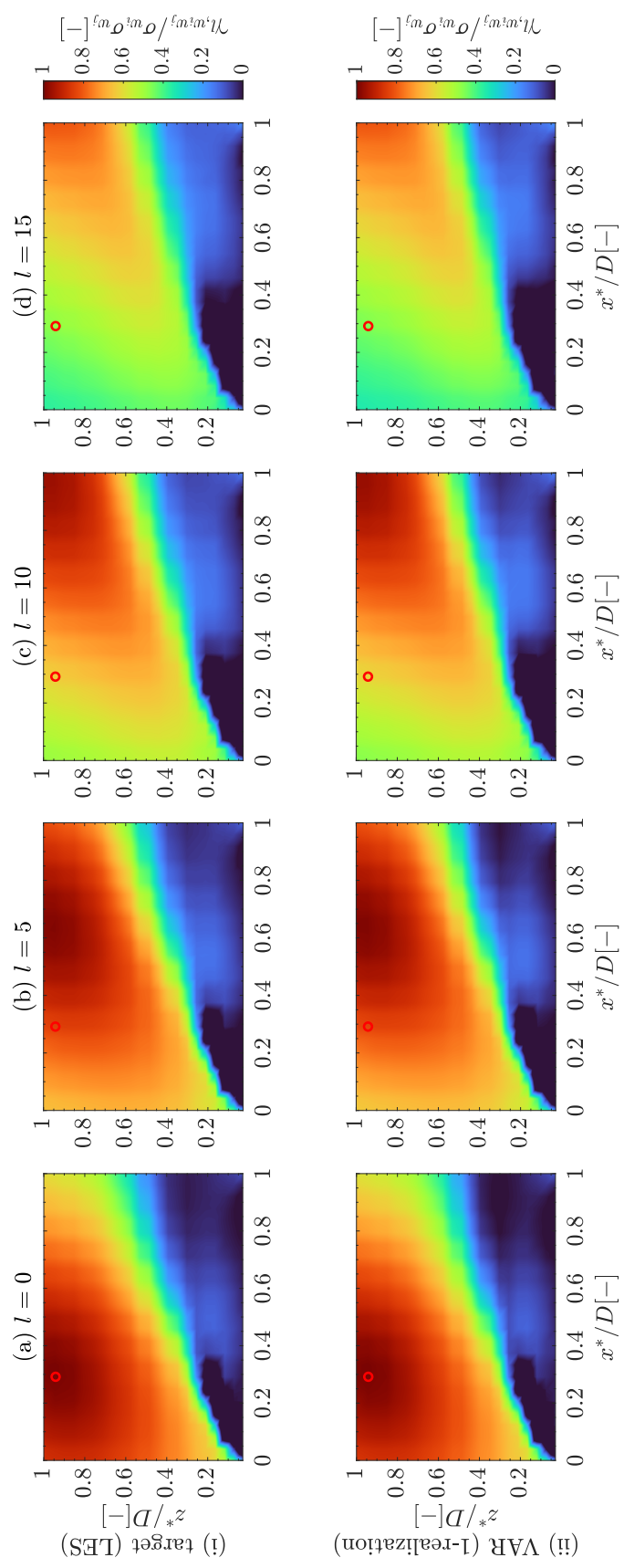

Figure 6.14: Correlation of the $w-$velocity component, $\gamma_{l,w_i w_j}/\sigma_{w_i}\sigma_{w_j}$ distribution on the $p-$plane with respect to the highlighted point (red circle) located at $(x^*/D, z^*/D) \approx (0.29, 0.94)$ (outside the circulation bubble), at time lags $l = 0, 5, 10, 15$, computed for both the target data (top row) and a single sample generated by the VAR model (bottom row).

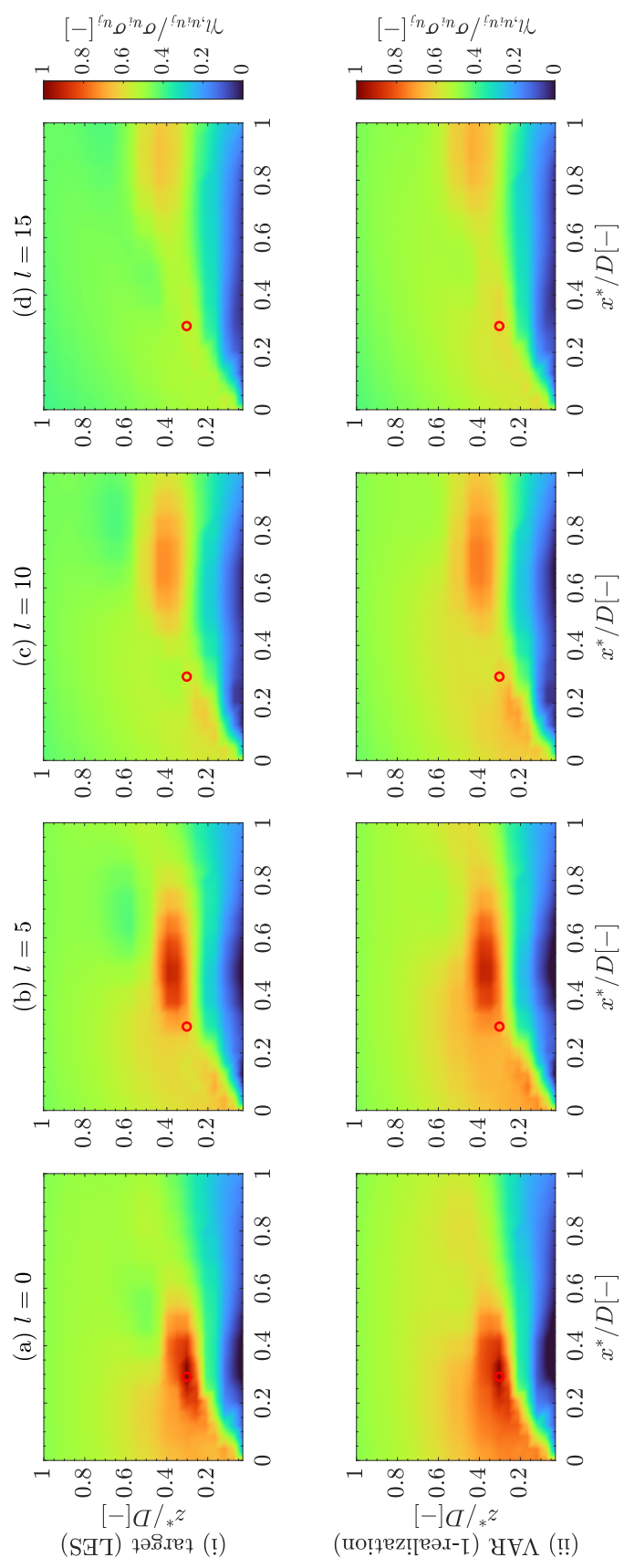

Figure 6.15: Correlation of the $u-$velocity component, $\gamma_{l,u_iu_j}/\sigma_{u_i}\sigma_{u_j}$ distribution on the $p-$plane with respect to the highlighted point (red circle) located at $(x^*/D, z^*/D) \approx (0.29, 0.30)$ (at the shear layer region) at time lags $l = 0, 5, 10, 15$, computed for both the target data (top row) and a single sample generated by the VAR model (bottom row).

Figure 6.16: Correlation of the $w-$velocity component, $\gamma_{l,w_iw_j}/\sigma_{w_i}\sigma_{w_j}$ distribution on the $p-$plane with respect to the highlighted point (red circle) located at $(x^*/D, z^*/D) \approx (0.29, 0.30)$ (at the shear layer region) at time lags $l = 0, 5, 10, 15$, computed for both the target data (top row) and a single sample generated by the VAR model (bottom row).

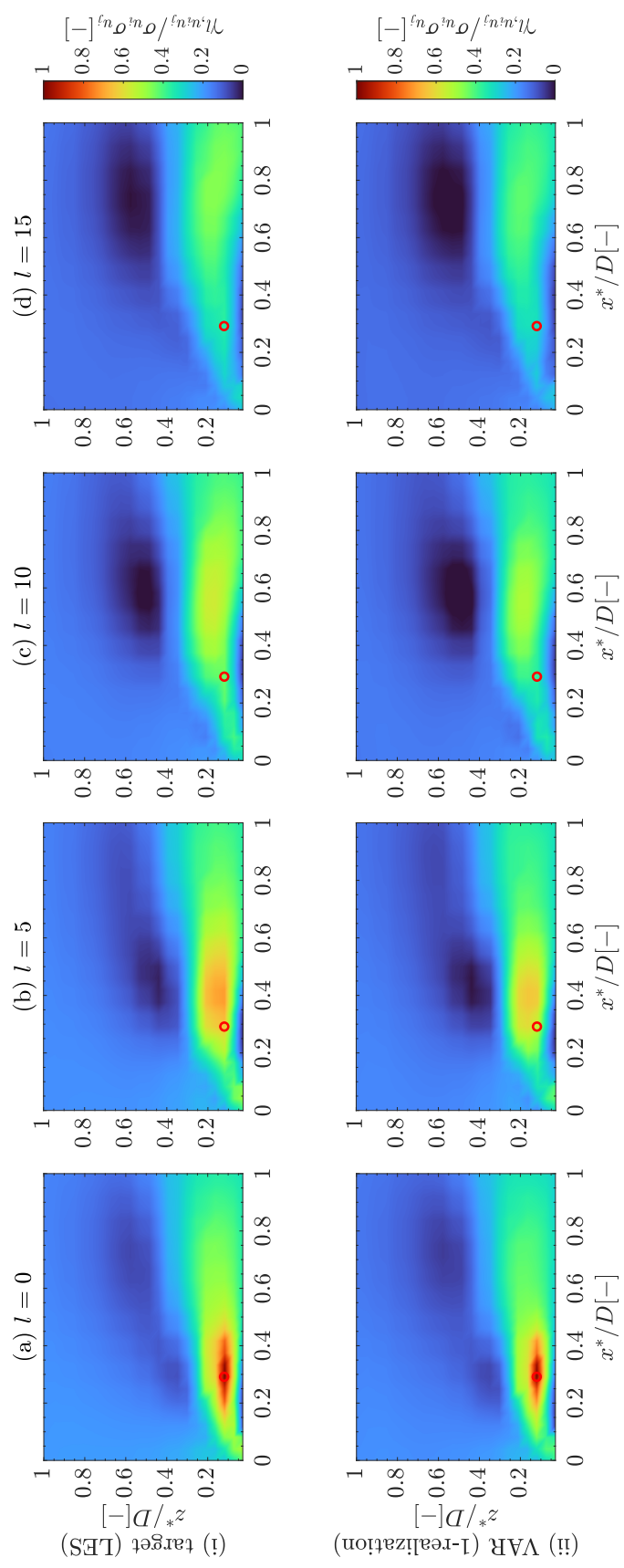

Figure 6.17: Correlation of the $u-$velocity component, $\gamma_{l,u_iu_j}/\sigma_{u_i}\sigma_{u_j}$ distribution on the $p-$plane with respect to the highlighted point (red circle) located at $(x^*/D, z^*/D) \approx (0.29, 0.12)$ (inside the recirculation bubble) at time lags $l = 0, 5, 10, 15$, computed for both the target data (top row) and a single sample generated by the VAR model (bottom row).

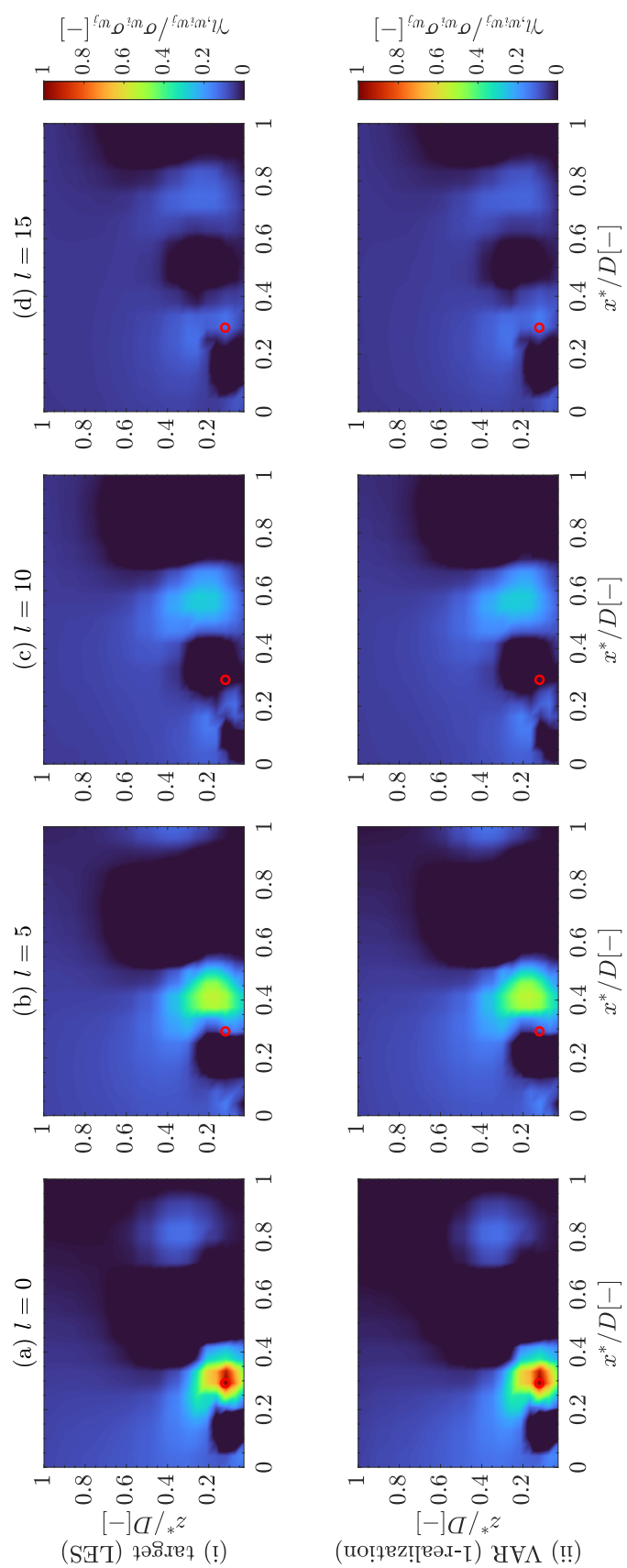

Figure 6.18: Correlation of the $w-$velocity component, $\gamma_{l,w_iw_j}/\sigma_{w_i}\sigma_{w_j}$ distribution on the $p-$plane with respect to the highlighted point (red circle) located at $(x^*/D, z^*/D) \approx (0.29, 0.12)$ (inside the recirculation bubble) at time lags $l = 0, 5, 10, 15$, computed for both the target data (top row) and a single sample generated by the VAR model (bottom row).

The non-dimensional standard deviation distributions on the $p-$plane for u and $w-$velocity components, σ_u/U_{ref} and σ_w/U_{ref}, respectively, are presented in Figure 6.19 for both the target and the sample of the velocity field generated by the VAR model. The u and $w-$velocity components of the synthetic wind field reproduce very well the variation in the standard deviation distribution compared to the target distribution, particularly the increased standard deviation values within the recirculation bubble region.

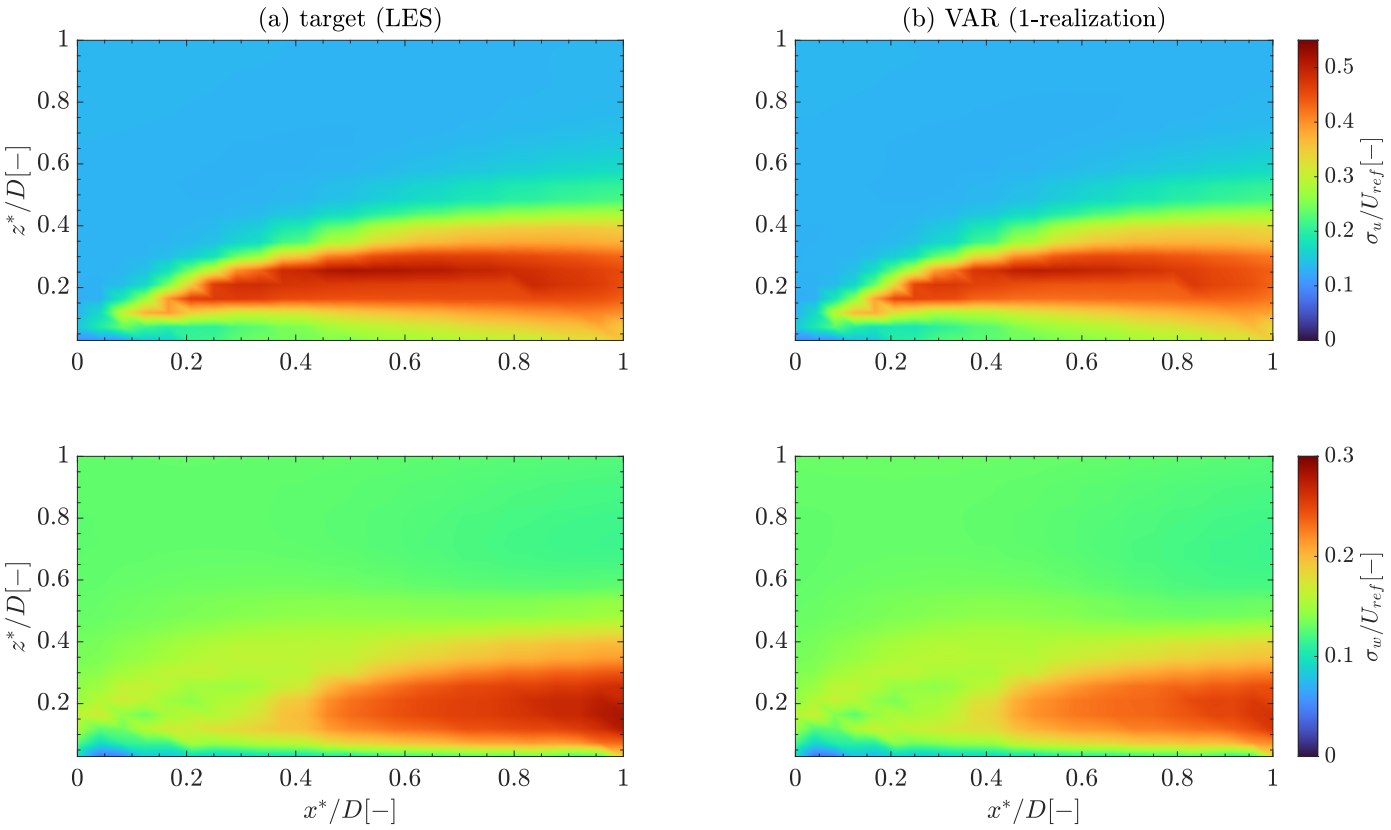

Figure 6.19: Non-dimensional standard deviation distribution for the longitudinal and vertical velocity components, σ_u/U_{ref} and σ_w/U_{ref}, over the $p-$plane, for (a) the target evaluated from the LES, and (b) a sample wind field generated by a VAR model.

In Figure 6.20, the non-dimensional instantaneous longitudinal velocity component, $\tilde{u}/U_{ref}$, is shown with the vector plot of both the longitudinal and vertical velocity components on the $p-$plane at various time instants for the target LES and one sample generated by VAR($N = 5$) model obtained using CG-CEO approach. The generated synthetic wind field effectively replicates the spatial turbulence structures presented in the LES resolved wind field.

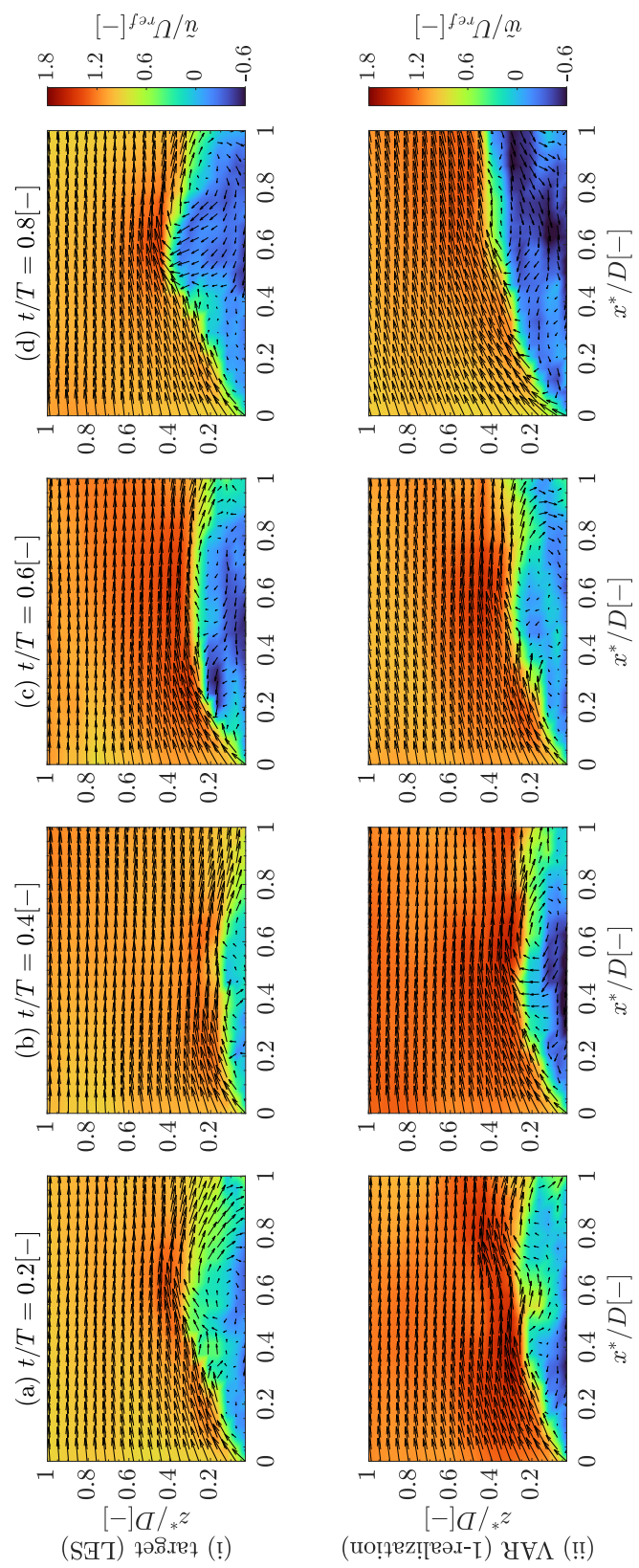

Figure 6.20: Non-dimensional instantaneous longitudinal velocity component, $\tilde{u}/U_{ref}$, with the vector plot of both the longitudinal and vertical velocity components on the $p-$plane at non-dimensional time instants $t/T = 0.2, 0.4, 0.6, 0.8$, for (i) target (LES), (ii) one sample generated by VAR($N = 5$) model obtained using CG-CEO approach.

6.3.3 Synthesis of the lateral and vertical velocity components within the $m-$plane using Veer-Shinozuka-eigendecomposition approach

The VSED was employed to synthetize the v and $w-$velocity components on the $m-$plane, which consisted of a grid of $N_y \times N_z = 28 \times 16$ points. The VSED was used to generate synthetic v and $w-$velocity components over a time period of $T = 2.513$ seconds, with a time step of $\Delta t = 0.0049$ seconds. The initial 20 eigenmodes were considered in the synthesis process due to memory limitations. The target CPSDM was computed using the Blackman and Tukey estimator (Marple Jr & Carey, 2019) to reduce the noise usually obtained in spectra.

In Figures 6.21a and 6.21b, both the target spectrum and the target spectrum multiplied by the frequency for the $v-$velocity component, at a given gird point, are shown together with the individual spectra corresponding to each eigenmode, along with the cumulative spectrum resulting from the summation of these individual spectra for the 20 most energetic eigenmodes. These spectra are evaluated at the grid point located in the bottom corner of the grid. Increasing the number of considered eigenmodes can reduce the difference between the target and cumulative spectra. It is worth mentioning that achieving a more accurate representation of the target spectra will result in a better reproduction of the variance since the variance is the integral of the spectrum along the frequency interval. Figure 6.21c shows the eigenvalues, λ, for each eigenmode against the normalized frequency fD/U_{ref}. This figure demonstrates the extent of each eigenvalue's contribution to the information present in the target CPSDM at various frequency. To assess the influence of including more eigenmodes to the energy contained in the target spectra, the computation of $E_{\boldsymbol{S}}$ (see Equation 4.24) was performed, and the results are illustrated in Figure 6.21d. Notably, it is evident from Figure 6.21 that the initial eigenmodes contains the majority of the energy contained in the target spectra, while subsequent eigenmodes have less contribution.

In Figure 6.22, the distribution of the non-dimensional standard deviation, σ_v/U_{ref}, is shown on $m-$plane for the target and various inclusions of eigenmodes in the cumulative spectrum. Increasing the number of eigenmodes results in a more accurate reproduction of the variance of the RP. Notably, the initial eigenmodes contribute significantly, as evident from the slight difference between the variances obtained for number of modes $N_m = 11$ and 16. Figure 6.23 shows the eigenvectors for the v and $w-$velocity components on the $m-$plane at various frequencies, focusing on the third and fourth eigenmodes. This figure provides insights into the contribution of the third and fourth eigenmodes to the spatial structures of the fluctuation velocity field.

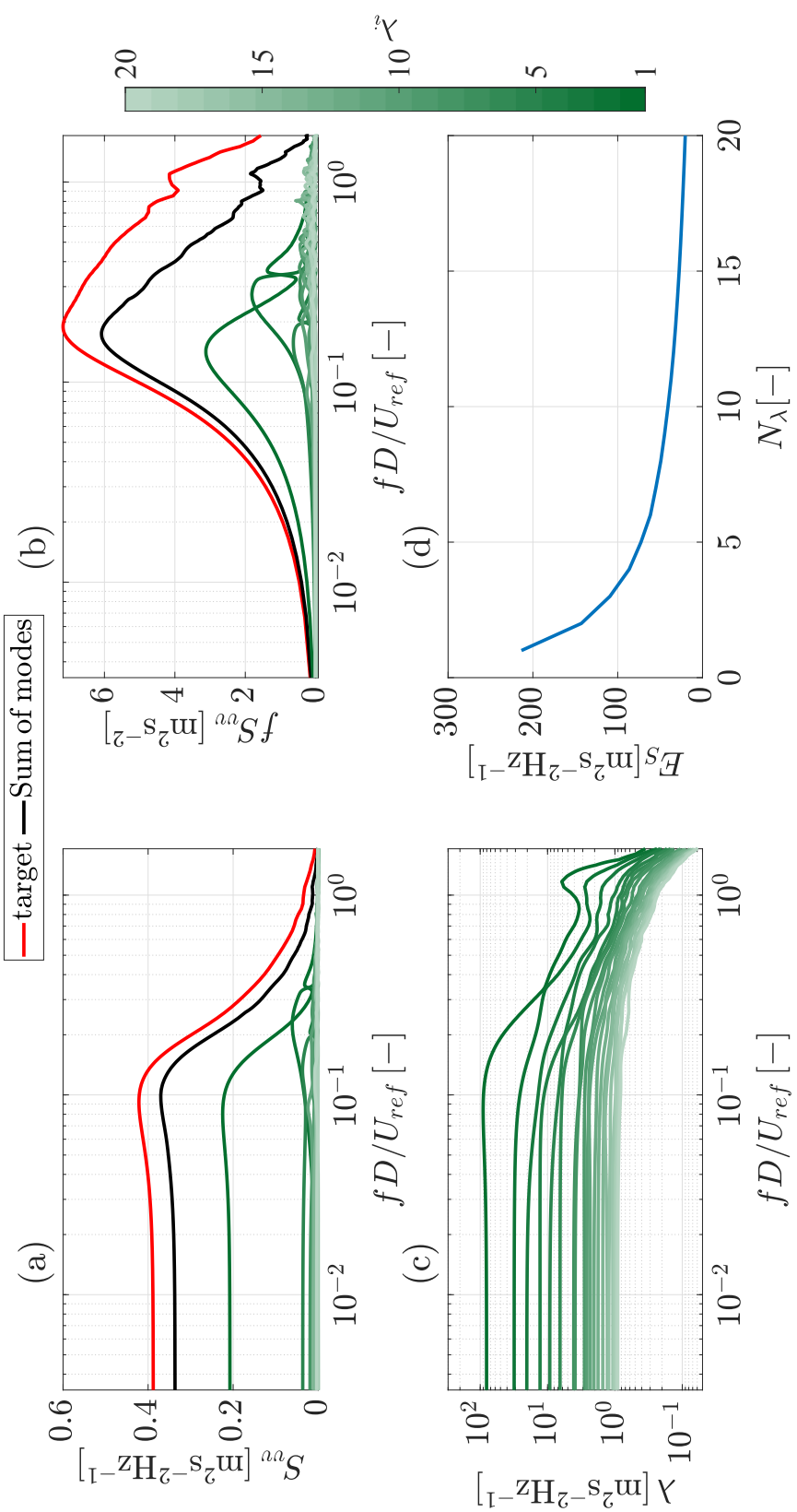

Figure 6.21: (a) Spectra for the lateral velocity component, S_{vv}, for the target (LES), together with the individual spectra corresponding to each eigenmode, along with the cumulative spectrum resulting from the summation of these individual spectra for the 20 most energetic eigenmodes, (b) the spectra multiplied to the frequency, fS_{vv}, for the target, together with the individual spectra corresponding to each eigenmode, along with the cumulative spectrum resulting from the summation of these individual spectra for the 20 most energetic eigenmodes, (c) the values of the eigenvalues, λ for each eigenmode against the normalized frequency fD/U_{ref}, and (d) error $E_{\boldsymbol{S}}$ evaluated between the target CPSDM with the computed CPSDM through the cumulative sum of the eigenmodes.

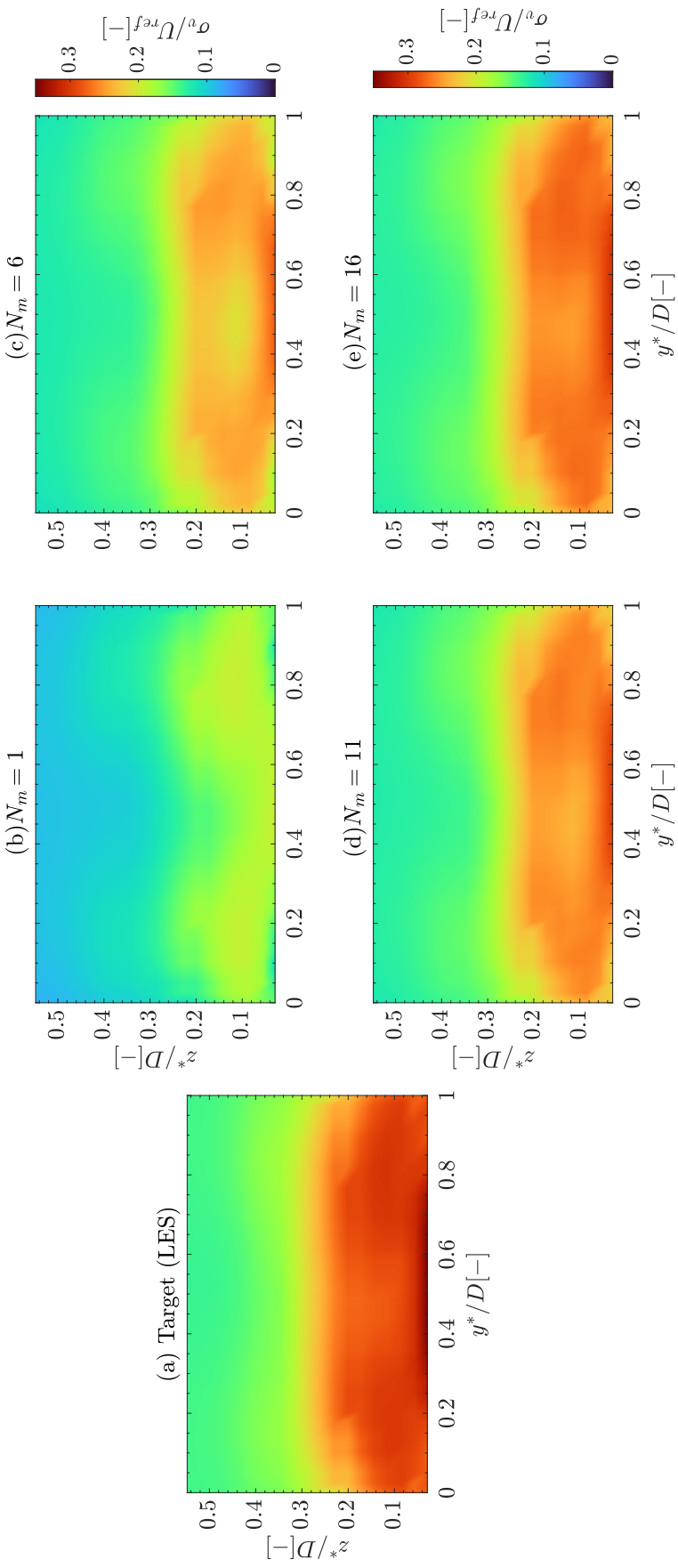

Figure 6.22: Distribution of the non-dimensional standard deviation of the lateral velocity component, σ_v/U_{ref}, over the $m-$plane for (a) target (LES), and fo considering number of eigmodes, N_m = (b)1, (c)6, (d)11, (e)16.

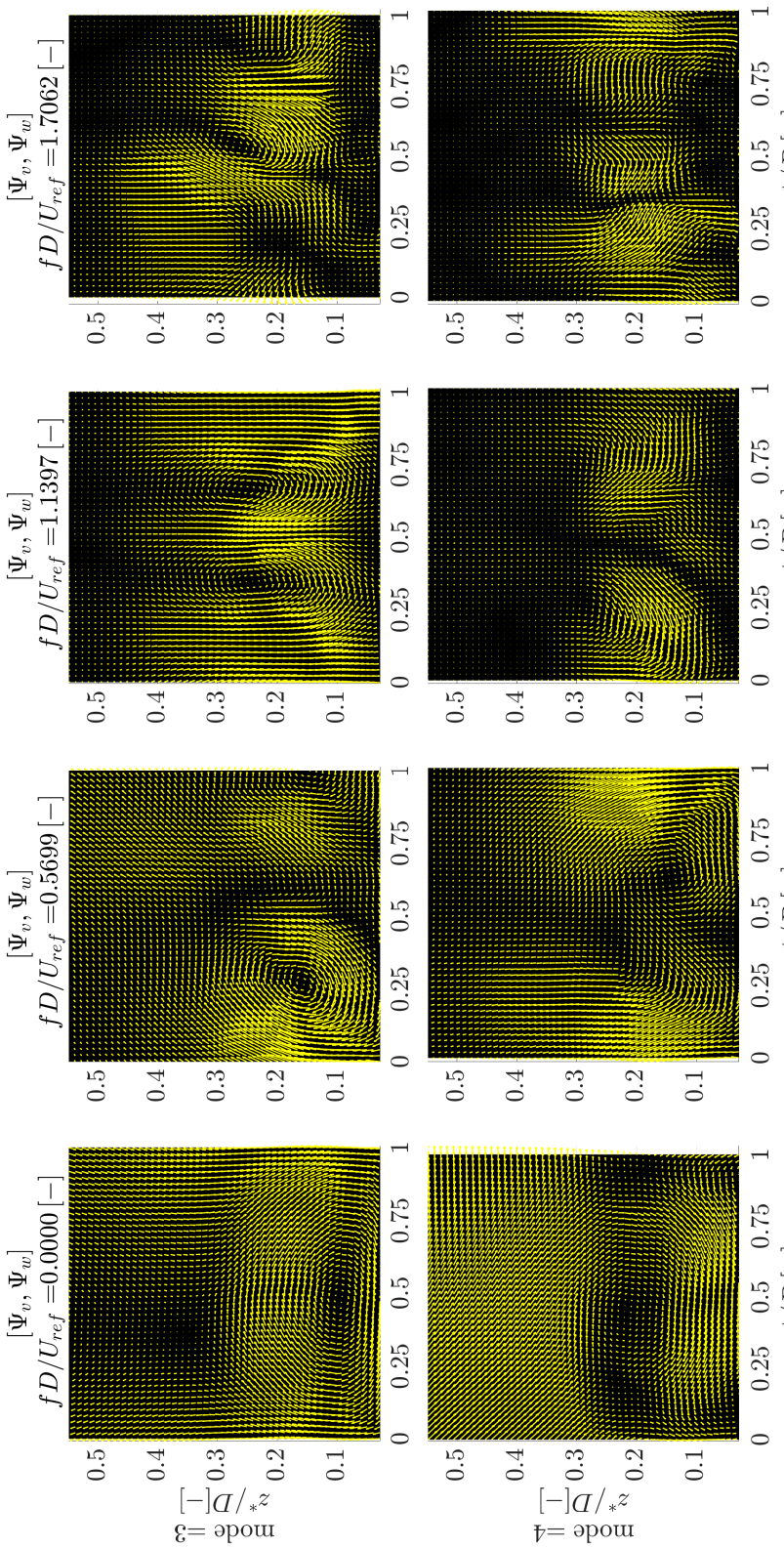

Figure 6.23: Eigenvectors $[\Psi_v, \Psi_w]$, for the third and fourth eigenmodes in terms of the normalized frequency, fD/U_{ref}, over the $m-$plane.

Figure 6.24 shows the two specific points selected within $m-$plane, point 1 within the recirculation bubble and point 2 outside the recirculation bubble, where the auto-spectra and the cross-spectra of the v and $w-$velocity components were computed. The spectra are presented in Figure 6.25, showing the target spectrum, the cumulative spectrum of the 20 most energetic eigenmodes, and an ensemble of the CPSDM of 10 samples. The S_{v_i,w_j}, for $i,j = 1,2$, exhibits lower values compared to the S_{v_i,v_j} and S_{w_i,w_j}. On the other hand, the auto-spectrum, S_{v_1,v_1}, shows the highest energy content compared to the other auto-spectra. In general, the ensemble CPDSM evidences a good match to the cumulative spectrum of the 20 eigenmodes. The ensemble and cumulative CPSDMs will better represent the target CPSDM and the variances by including more eigenmodes during synthesis. Nevertheless, this enhancement comes at the cost of more significant computational costs and higher memory demands.

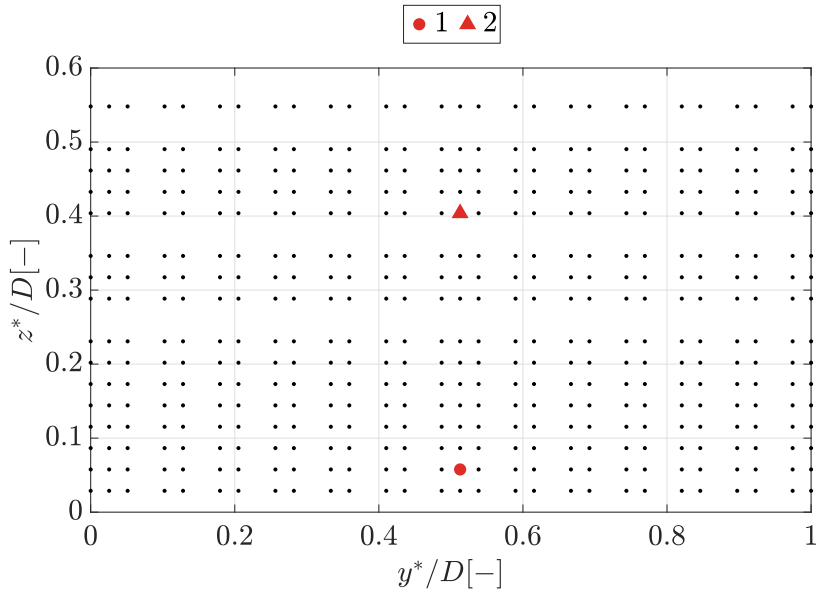

Figure 6.24: Scheme of the $N_y \times N_z = 28 \times 16$ grid points distributed across the $m-$plane, highlighting specific grid points (circle and triangle) located at $y^*/D \approx 0.513$ and $z^*/D \approx 0.058, 0.404$, which are considered for the CPSDM computation, shown in Figure 6.25.

In Figure 6.26, the non-dimensional instantaneous lateral velocity component, $\tilde{v}_{\mathcal{N}}/U_{ref}$, is shown with the vector plot of both the lateral and vertical velocity components over the $m-$plane at various time instants for the target LES and one sample generated by VSED approach. The generated synthetic wind field reproduces well the spatial turbulence structures depicted in the target.

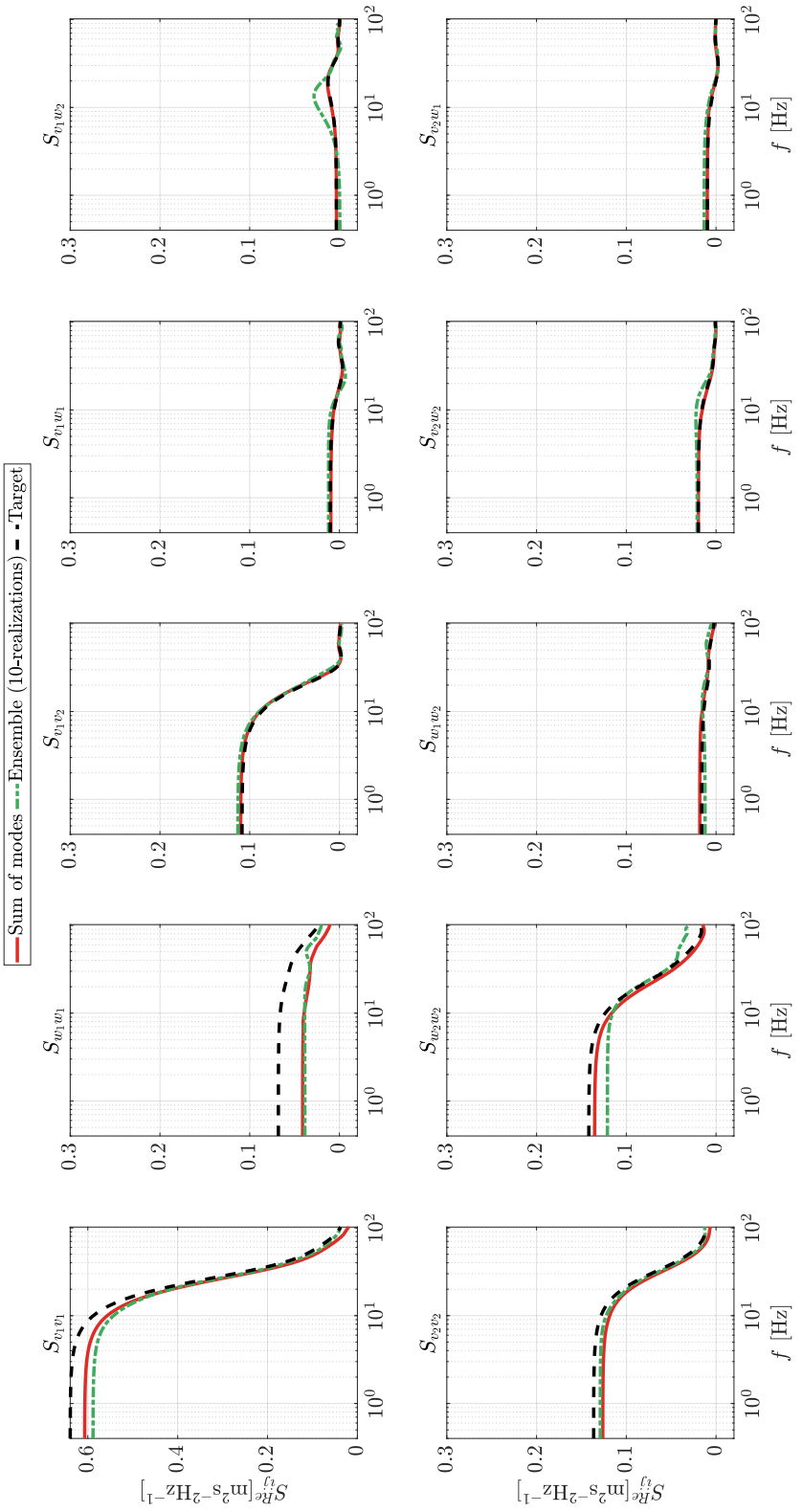

Figure 6.25: Real part of the one-sided CPSDM, S_{ij}^{Re}, for the v and $w-$velocity components, in terms of frequency f, for (a) the cumulative spectrum of the initial 20 eigenmodes (red), (b) the CPSDM of the synthetic wind field generated by VSED approach (green)and (c) target CPSDM (black), between two grid points located on a vertical line depicted in Figure 6.24.

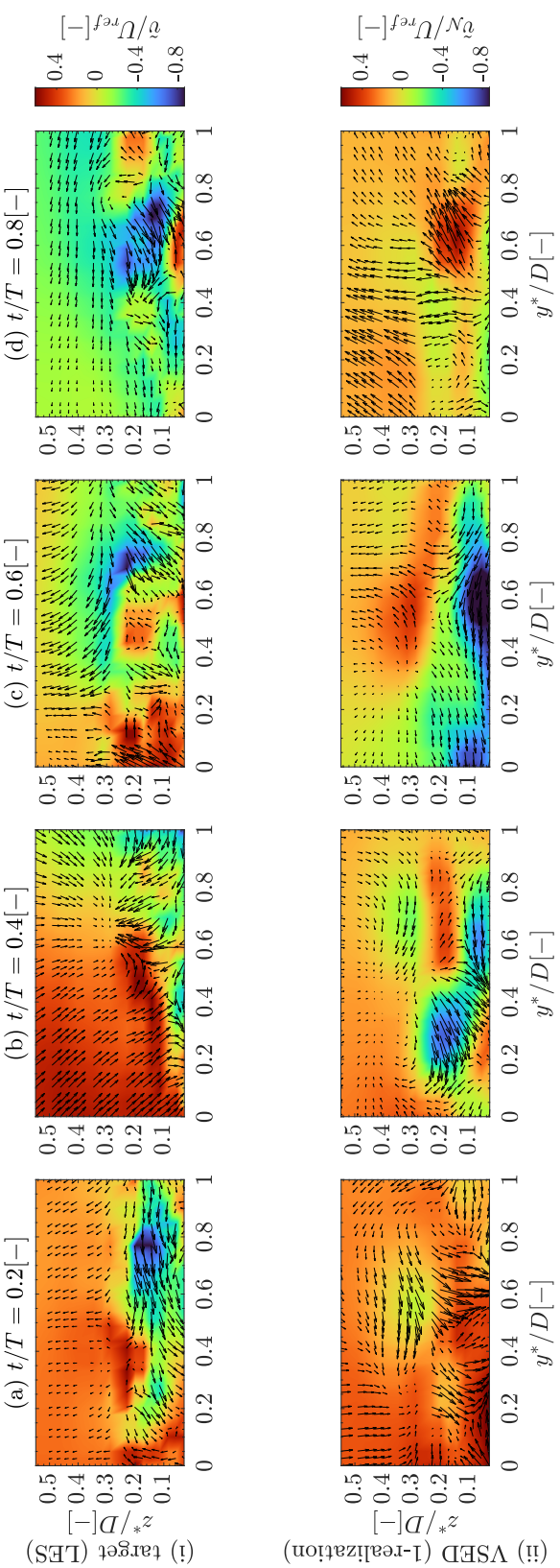

Figure 6.26: Non-dimensional instantaneous lateral velocity component, $\tilde{v}_{\mathcal{N}}/U_{ref}$, with the vector plot of both the lateral and vertical velocity components on the $m-$plane at non-dimensional time instants $t/T = 0.2, 0.4, 0.6, 0.8$, for (i) target (LES), (ii) one Gaussian sample generated by VSED approach.

6.4 Conclusions

The objective of this chapter is to assess the effectiveness of various Numeric Generation (NG) methods in synthesizing complex wind fields characterized by high non-homogeneity, non-Gaussianity, and anisotropy over a High-Rise Building (HRB) exposed to an atmospheric turbulent inflow. Additionally, this chapter aims to reveal the strengths and limitations of each approach in generating such complex wind patterns across different planes over the HRB. The impact of utilizing time and frequency representation of the second-order statistics as an input to the synthesis process was exploited. The investigation also included an exploration of a proposed strategy to synthesis non-Gaussian velocity fields, which involves a statistical method and the quantile-to-quantile transformation. The statistical characteristics obtained from the LES study of the wind field over the HRB's rooftop were provided as inputs to the VSED, OCEAN, and CG-CEO to synthesize urban wind fields. This synthesis process was undertaken in three distinct case studies, each corresponding to a different approach. The OCEAN approach was employed to synthesize the longitudinal velocity component along a vertical line at the middle of the HRB rooftop, and the CG-CEO was applied to synthesize the longitudinal and vertical velocity components on a plane parallel to the mean wind speed direction. Furthermore, the VSED was utilized to synthesize the lateral and vertical velocity components on a plane perpendicular to the mean wind speed direction.

The optimal VAR model obtained from the OCEAN approach reproduced very well the target (LES) CPSDM, providing an accurate representation of the significant non-homogeneity present in the target CPSDM. While the optimal VAR model appropriately reproduced the target variance along the vertical line, a slight overestimation was observed at higher levels. This issue can be addressed by increasing the order of the VAR model. Despite the urban wind field exhibited a highly non-Gaussian distribution, especially in the shear region, the synthetic longitudinal velocity component along the vertical line followed, as expected, a Gaussian distribution. The CG-CEO was employed to obtain an optimal VAR model from a target CMF, successfully incorporating the quantile-to-quantile transformation to acquire a non-Gaussian synthetic wind field, more representative of the actual LES wind field. The performance of the CG-CEO was examined by checking the spatial correlation at various time lags between the wind field generated over the plane and three different locations. The synthetic wind fields generated by the VAR model reproduces accurately the spatial correlation of the velocity components resolved by the LES, effectively reproducing the strong correlation near selected points. The generated synthetic wind field correctly replicates the non-Gaussian characteristics shown by the LES resolved wind velocity field.

The twenty most energetic eigenmodes were considered in the VSED approach to synthesize the wind field on the $m-$plane. The contribution of each eigenmode to the target CPSDM was analyzed; additionally, the spatial patterns of the eigenvectors for different frequencies were examined. The first eigenmodes comprise the majority of the information present in the target CPSDM compared to the subsequent eigenmodes. The spectra of the synthetic wind field were compared to the target CPSDM at two grid points locations. The features of the target (LES) CPSDM are well-reproduced in the synthetic wind field, accurately replicating the non-homogeneity existing in the actual urban wind field. A satisfactory fitting to the

target CPSDM within the defined frequency range was achieved without requiring optimal calibration of the coefficients in the VSED approach.

Non-stationarity was not accounted for in this study, despite the known non-stationary nature of urban wind fields, thus non-stationarity needs to be considered in future work. Nonetheless, it is worth noting that the VAR approach can be readily extended to accommodate non-stationarity in synthesized wind fields using the concept of evolutionary spectra (where the spectra become time-dependent) (Deodatis & Shinozuka, 1988). This concept would involve time-dependent parameters within the VAR framework.

The advantages and disadvantages of each approach's performance are summarized in Table 6.1.

Approach	Advantages	Limitations
SM (VAR)	• Has theoretical expressions for CMF and CPSDM, facilitating the model's reliability assessment. • Simulation can be readily restarted. • Can be easily extended to synthesize non-stationary wind fields.	• CMF-based approaches are prone to aliasing for high value time step. • Optimal models are computationally costly for high number of variables.
SRM (VSED)	• The computational cost of the synthesis process can be decreased by neglecting the low energy modes. • A satisfactory fit to a specified target CPSDM within a defined frequency range can be achieved without the need for optimal calibration.	• CPSDM estimations are required for the reproduced CPSDM assessment. • The simulation time is predetermined initially and the simulation can not be restarted. • Requires the calculation of the eigen-properties of the CPSDM at each frequency. • Requires a substantial amount of memory to synthesis wind fields for large time periods.

Table 6.1: Advantages and limitations of the VAR and the VSED approaches.

Chapter 7

Conclusions and future work

To meet the massive demands for renewable power capacity, it is essential to systematically incorporate other types of locations different from natural flat onshore sites and offshore sites, such as highly complex mountainous terrains and urban environments, as potential locations for wind turbine installations. Urban environments have been chosen as preferred sites for Small Wind Turbines (SWT) due to their minimal space requirements; therefore, they can be installed near high-demand areas (such as cities). In the aeroelastic design process of SWTs, a set of load cases specified by the International Electrotechnical Commission (IEC) 61400-2 standards need to be simulated to ensure the safety of operation. The IEC 61400-2 standards utilize semi-empirical turbulence models primarily developed for open and flat terrain for the aeroelastic design of urban wind turbines. However, wind fields in urban environments exhibit different characteristics than the ones in open and flat terrain as they are affected by factors such as the shape and the arrangement of buildings and urban infrastructure. Consequently, using the current IEC 61400-2 standards for the aeroelastic design of urban SWTs might lead to ill-prediction of the loads experienced by the SWT in such a complex environment. Eventually, this would lead to low performance of urban SWTs and reduced energy yield.

In this doctoral thesis, the problem of generating synthetic wind velocity fields, representative of the urban environment, is addressed. The methods proposed in the IEC standards for generating wind velocity fields do not consider the specific characteristics of urban wind flows, such as high non-homogeneity, non-Gaussianity and anisotropy. In the present research, a strategy to deal with these characteristics of the urban ABL is presented, laying the groundwork for a methodology to synthesize random processes representative of realistic urban wind velocity fields to be used in the aeroelastic simulations of SWTs operating in the built environment. This methodology includes the use of wind velocity field databases generated with LES for resolving the statistical features of urban wind fields to provide a reliable representation of the statistical characteristics of urban wind fields compared to the current IEC 61400-2 standards. These realistic statistical characteristics are quantified as the mean wind velocity field and the two-point two-times second-order statistical objects, that are, the Covariance Matrix Function (CMF) and the Cross Power Spectral Density Matrix (CPSDM). In this context, the Spectral Representation Methods (SRMs) and the Sequential Methods (SMs) have been employed and developed to utilize the statistical characteristics

resolved from LES studies as inputs for the numeric generation approaches. This was done to synthesize urban wind fields for aeroelastic simulations of urban SWT.

Different methodologies were proposed to optimally calibrate the parameters of the SMs, particularly for the Autoregressive (AR) model and its vector version (VAR), from a predefined second-order statistical information described in the time (AutoCovariance Function (ACF) and CMF) and in the frequency domain (auto-Power Spectral Density (PSD) and CPSDM). In the case of the AR model, the proposed spectra-based approach employs the pole-placement approach to fit an AR spectrum to a target spectrum within a frequency range. This is done by using the relationship between the AR model parameters and the poles of the AR model. An optimization algorithm is utilized to identify the pole positions that result in the closest match to the target PSD. The autocovariance-based approach uses the relationship between the AR model parameters and the theoretical ACF equations. It employs a systematic exploration of regression coefficients, by utilizing a genetic algorithm-based optimization approach, to identify the optimal selection of coefficients and lag values, aiming to achieve the closest match to a target ACF.

A case study was analyzed using the von Karman turbulence model to provide the Fourier pairs, the ACF and PSD targets for the ACF-based approaches (state-of-the-art), and the proposed approach, respectively, for a single velocity component at one point. The ACF-based approaches reproduced very well the target ACF, although aliasing was observed in the reproduced PSD, due to the coarse discretization of the ACF. The proposed PSD-based approach showed a perfect fitting to the target spectrum. However, the obtained AR model can only reproduce a fraction of the target variance, as the AR PSD fitting is constrained to a specific frequency range, defined by the target PSD. In contrast, the ACF-based approach does not present this limitation, as it requires matching the target ACF at zero lag only to reproduce the variance. Consequently, this study outlines the implications of each approach. It presents the groundwork for a discussion on the most suitable method to employ, depending on the application of the generated wind field. These arguments assisted in the selection process of specific parameters, such as the time step, which was employed in the conducted LES study to properly determine the CMF and the CPSDM.

The proposed approach was extended to a multivariate scenario, including multiple grid points and one or several velocity components, which requires the fitting of a target CMF or CPSDM instead of just an ACF or PSD. To perform this extension, the eigenanalysis of the companion matrix of a VAR model was required. This approach is referred to as the OCEAN approach. In this context, the eigenvalues represent the poles of the VAR model and the eigenvectors provide insights into the assigned eigenvalue to the auto-spectra and the cross-spectra. Mann's turbulence model was utilized to obtain target CPSDMs for wind fields with different statistical characteristics to check the reliability of the proposed method. Three distinct cases were considered. In two instances, target CPSDMs were considered for stationary-homogeneous-anisotropic wind fields, including various combinations of velocity components and different grid point numbers. In one case, a target CPSDM was utilized for a stationary-homogeneous-isotropic wind field, considering only the longitudinal velocity component at four grid points. The Fourier pair of one of the target CPSDMs, CMF, was computed to compare the OCEAN with the state-of-the-art CMF-based approaches. Similar

implications were derived as those obtained in the AR model case (the univariate case). The OCEAN approach demonstrated a good match to the target CPSDM for all three considered instances. The CMF-based approaches showed a better fitting to the target CMF compared to the OCEAN approach. The proposed OCEAN approach is applicable for the numerical generation of synthetic stationary, homogeneous/non-homogeneous and isotropic/anisotropic turbulent wind fields, since the fitting process to the target CPSDM is independent of the statistical information represented in the predefined CPSDM. Furthermore, this approach takes into account both the real and imaginary parts of the target CPSDM, which is neglected in some studies. Including the imaginary parts of the spectra is crucial to ensure an accurate representation of non-symmetric (in the time lag domain) cross-covariances.

Once the considered approaches for generating synthetic wind fields were tested in the mentioned canonical cases (using standard forms of the CMF and the CPSDM, derived from well-known turbulence models), the next step was to analyze the turbulent wind characteristics in urban areas to gather the necessary statistical objects to be used as inputs in the numeric generation methods. In the following step, data obtained from LES, a resolved wind field, was utilized with the developed numeric generation approaches. A LES study was conducted on a particular case of an isolated High-Rise Building (HRB). In addition to this objective, the study aimed to provide second-order statistical information on the urban wind field over the HRB to be utilized as inputs for the synthesis of urban wind fields. The conducted LES study replicates a wind tunnel experiment (Šarkić Glumac et al., 2020; Vita et al., 2020), where the turbulent inflow is characterized by Eurocode Terrain category II. The turbulent inflow at the LES domain inlet was numerically generated by using Mann's approach. With this regard, a parametric study was conducted to assess the necessary parameter values to replicate the turbulent inflow obtained in the mentioned wind tunnel experiment used as a reference. The mean velocity, turbulence intensities, and integral length scales at the rooftop of the HRB were analyzed. The values of these parameters exhibited an expected strong dependency on their proximity to the rooftop, which is expected due to the formulation of a recirculation bubble at the rooftop of the HRB. This evidenced the necessity to deal with highly non-homogeneous velocity fields. Furthermore, the second-order statistics, such as the ACF and PSD, were analyzed atop the HRB. A faster decay was observed in the ACF in the region (inside the recirculation bubble) in close proximity to the rooftop surface. Additionally, a shift in the peak of the normalized PSD to high frequencies was noticed as the rooftop surface approached. Unveiling these effects of the urban environment on spectral features is essential for generating synthetic wind fields. Addressing each specific case would need a specific LES study to capture these statistical features accurately.

The second-order statistical information determined from the LES study was provided to the SRM (particularly Veer-Shizuoka combined with the eigendecomposition of the CPSDM referred to as VSED) and the SMs methods (the OCEAN approach and an optimal CMF-based approach referred to as CG-CEO). Three case studies were conducted to check the capability of such statistical methods to reproduce such highly non-homogeneous, non-Gaussian, and anisotropic wind fields. The OCEAN approach was employed to synthesize the longitudinal velocity component along a vertical line at the center of the HRB's rooftop. The VAR model effectively reproduces the target CPSDM, accurately capturing the increased energy content in the CPSDM near the rooftop surface. The variation in the variance along the vertical line is

well reproduced by the VAR model, although, an overestimation in the variance in the upper region was observed. However, this can be addressed by increasing the VAR model in order to acquire a more accurate representation. Furthermore, the time series of the wind velocity components generated by the OCEAN method show Gaussian PDFs, as expected, although, the urban wind field is characterized by a highly non-Gaussian nature. The CMF-based approach (CG-CEO) was employed to generate a synthetic wind field on a vertical plane, considering the longitudinal and the vertical velocity components. This plane is located in the middle of the rooftop surface and is aligned parallel to the mean wind direction. The reliability of the CG-CEO approach in reproducing the target CMF was assessed by computing the spatial correlation between the wind field over the plane and three distinct locations: one within the recirculation bubble, one in the region of the shear layer, and one outside the recirculation bubble. The spatial correlations of the synthetically generated wind fields effectively replicate the variations observed in the spatial correlation distributions resolved from the LES, accurately capturing the strong correlations in the proximity of these selected points. The application of the quantile-to-quantile transformation resulted in an accurate reproduction of the non-Gaussian characteristics of the target (LES) wind velocity field within the synthetic wind field. The VSED approach was applied to synthetically generate the lateral and vertical velocity components of the wind field on a vertical plane located in the middle of the rooftop surface and perpendicular to the wind flow direction. A limitation on memory capacity restricted the consideration of only the twenty most energetic eigenmodes for synthesizing the wind field on the plane. Each eigenmode's contribution to the information in the target CPSDM was analyzed. This analysis involved examining the direction of the eigenvectors and visualizing the spatial patterns within the frequency interval represented by each mode. The considered eigenmodes exhibit a significant impact on the synthesized field, as the first eigenmodes contain most of the information in the target CPSDM. Further improvement in representation can be achieved by including additional eigenmodes in the synthesis process. The synthetic wind field obtained by the VSED captures very well the non-homogeneity represented in the LES-resolved urban wind field.

In future research, it is essential to extend the scope of the LES study to include various wind directions and building configurations. This will allow for the generation of diverse second-order statistics that can be tested with statistical methods, such as SRMs and SMs, to assess their ability to replicate various environmental conditions. Moreover, a comprehensive analysis is needed to determine whether existing turbulence models are suitable for reproducing the second-order statistics generated by the LES for multiple wind directions and urban configurations. This evaluation will provide insights into the applicability of these models under different conditions. The non-stationarity of the wind field needs to be considered, as actual wind fields in urban environments are non-stationary due to various factors. The non-stationarity can be represented in the synthesis wind field by considering the concept of evolutionary spectra and autocovariance. In the case of a non-stationary wind field, the statistical characteristics of wind fields exhibit temporal dependence. This leads to the generation of time-dependent CMFs and CPSDMs. In this context, varying coefficient models play a crucial role as they enable modeling dependencies of the VAR coefficients on additional variables, such as time and wind direction. In the case of spectra-based approaches, additional analysis is necessary to examine how the location of poles/eigenvalues changes when time-

dependent target spectra are provided. For covariance-based approaches, a study is needed to investigate how the **j** and **l** vectors change for each optimal AR/VAR model as time-dependent target ACF/CMF are considered. This analysis will help determine the dynamics of these vectors under varying conditions. Additional future research efforts are required to adapt these type of methodologies to the IEC standard grammar.

This Doctoral Thesis was a part of the zEPHYR European research project, focusing on enhancing and developing wind turbines efficiency within complex terrains and urban terrains. This study contributed to the large wind turbine, complex terrain, and urban canopy benchmarks outlined in the zEPHYR project. The methodologies developed in this research are provided in an open-source toolbox named "mVARbox". Furthermore, the datasets derived from the conducted LES study will be made publicly available through Zenodo. Part of the research finding of this document has been disseminated in two JCR-Q1 papers (Gallego-Castillo et al., 2022; Elagamy et al., 2023) and four conference contributions (Elagamy et al., 2021a, 2021b, 2022; Gallego-Castillo et al., 2024).

References

Abohela, I., Hamza, N., & Dudek, S. (2013). Effect of roof shape, wind direction, building height and urban configuration on the energy yield and positioning of roof mounted wind turbines. *Renewable Energy*, *50*, 1106–1118. Retrieved from https://www.sciencedirect.com/science/article/pii/S0960148112005381 doi: 10.1016/j.renene.2012.08.068

Aboshosha, H., Elshaer, A., Bitsuamlak, G. T., & El Damatty, A. (2015). Consistent inflow turbulence generator for LES evaluation of wind-induced responses for tall buildings. *Journal of Wind Engineering and Industrial Aerodynamics*, *142*, 198-216. Retrieved from https://www.sciencedirect.com/science/article/pii/S0167610515000872 doi: 10.1016/j.jweia.2015.04.004

Ahmadianfar, I., Gong, W., Heidari, A., Golilarz, N., Samadi-Koucheksaraee, A., & Chen, H. (2021). Gradient-based optimization with ranking mechanisms for parameter identification of photovoltaic systems. *Energy Reports*, *7*, 3979–3997. Retrieved from https://www.sciencedirect.com/science/article/pii/S2352484721004315 doi: 10.1016/j.egyr.2021.06.064

AIJ. (2007). *Architectural institute of Japan, guidebook for CFD predictions of urban wind environment.* Retrieved from https://www.aij.or.jp/jpn/publish/cfdguide/index_e.htm

Bazdidi-Tehrani, F., Kiamansouri, M., & Jadidi, M. (2016). Inflow turbulence generation techniques for large eddy simulation of flow and dispersion around a model building in a turbulent atmospheric boundary layer. *Journal of Building Performance Simulation*, *9*(6), 680-698. Retrieved from https://doi.org/10.1080/19401493.2016.1196729 doi: 10.1080/19401493.2016.1196729

Bendat, J., & Piersol, A. (2011). *Random data: analysis and measurement procedures* (Vol. 729). John Wiley & Sons.

Benowitz, B. A., & Deodatis, G. (2015). Simulation of wind velocities on long span structures: a novel stochastic wave based model. *Journal of wind engineering and industrial aerodynamics*, *147*, 154–163. Retrieved from https://www.sciencedirect.com/science/article/pii/S0167610515002457 doi: 10.1016/j.jweia.2015.10.004

Berg, J., Natarajan, A., Mann, J., & Patton, E. G. (2016). Gaussian vs non-gaussian turbulence: impact on wind turbine loads. *Wind Energy*, *19*(11), 1975–1989.

Blocken, B. (2015). Computational Fluid Dynamics for urban physics: Importance, scales, possibilities, limitations and ten tips and tricks towards accurate and reliable simulations. *Building and Environment*, *91*, 219-245. Retrieved from https://www.sciencedirect

.com/science/article/pii/S0360132315000724 doi: 10.1016/j.buildenv.2015.02.015

Blocken, B. (2018). LES over RANS in building simulation for outdoor and indoor applications: A foregone conclusion? *Building Simulation*, *11*(4), 821–870. doi: 10.1007/s12273-018-0459-3

Box, G. E., Jenkins, G. M., Reinsel, G. C., & Ljung, G. M. (2016). *Time series analysis: forecasting and control* (5th ed.). Wiley.

Brook, R. (1972). The measurement of turbulence in a city environment. *Journal of Applied Meteorology and Climatology*, *11*(3), 443–450. Retrieved from http://www.jstor.org/stable/26175738

Burton, T., Jenkins, N., Sharpe, D., & Bossanyi, E. (2011). *Wind energy handbook*. John Wiley & Sons, Ltd. doi: 10.1002/9781119992714

Castro, H. G., & Paz, R. R. (2013). A time and space correlated turbulence synthesis method for Large Eddy Simulations. *Journal of Computational Physics*, *235*, 742-763. Retrieved from https://www.sciencedirect.com/science/article/pii/S0021999112006389 doi: 10.1016/j.jcp.2012.10.035

Castro, H. G., Paz, R. R., Mroginski, J. L., & Storti, M. A. (2017). Evaluation of the proper coherence representation in random flow generation based methods. *Journal of Wind Engineering and Industrial Aerodynamics*, *168*, 211-227. Retrieved from https://www.sciencedirect.com/science/article/pii/S0167610517301344 doi: 10.1016/j.jweia.2017.06.009

CEDVAL. (2006). *Compilation of experimental data for validation of microscale dispersion models.* Hamburg, Germany.

Chang, M. K., Kwiatkowski, J. W., Nau, R. F., Oliver, R. M., & Pister, K. S. (1981). ARMA models for earthquake ground motions. Seismic safety margins research program.. Retrieved from https://api.semanticscholar.org/CorpusID:131265626

Chao, B. F. (1984). *On the maximum-entropy/autoregressive modeling of time series*. National Aeronautics and Space Administration, Goddard Space Flight Center.

Chen, J., Song, Y., Peng, Y., & Spanos, P. D. (2018). Simulation of homogeneous fluctuating wind field in two spatial dimensions via a joint wave number–frequency power spectrum. *Journal of Engineering Mechanics*, *144*(11), 04018100. Retrieved from https://ascelibrary.org/doi/abs/10.1061/%28ASCE%29EM.1943-7889.0001525 doi: 10.1061/(ASCE)EM.1943-7889.0001525

Chen, X., & Kareem, A. (2002). Advances in modeling of aerodynamic forces on bridge decks. *Journal of Engineering Mechanics*, *128*(11), 1193-1205. Retrieved from https://ascelibrary.org/doi/abs/10.1061/%28ASCE%290733-9399%282002%29128%3A11%281193%29 doi: 10.1061/(ASCE)0733-9399(2002)128:11(1193)

Christen, A., van Gorsel, E., & Vogt, R. (2007). Coherent structures in urban roughness sublayer turbulence. *International Journal of Climatology*, *27*(14), 1955–1968. Retrieved from https://rmets.onlinelibrary.wiley.com/doi/abs/10.1002/joc.1625 doi: 10.1002/joc.1625

Christen, A., Vogt, R., & Rotach, M. W. (2003). Profile measurements of selected turbulence characteristics over different urban surfaces. In *Proc. 4th international conference on urban air quality* (pp. 408–411).

Cottone, G., & Di Paola, M. (2011). Fractional spectral moments for digital simulation

of multivariate wind velocity fields. *Journal of Wind Engineering and Industrial Aerodynamics*, *99*(6-7), 741–747. Retrieved from https://www.sciencedirect.com/science/article/pii/S0167610511000511 (The Eleventh Italian National Conference on Wind Engineering, IN-VENTO-2010, Spoleto, Italy, June 30th - July 3rd 2010) doi: 10.1016/j.jweia.2011.03.006

Deodatis, G., & Shinozuka, M. (1988). Autoregressive model for nonstationary stochastic processes. *Journal of Engineering Mechanics*, *114*(11), 1995-2012. Retrieved from https://ascelibrary.org/doi/abs/10.1061/%28ASCE%290733-9399%281988%29114%3A11%281995%29 doi: 10.1061/(ASCE)0733-9399(1988)114:11(1995)

di Mare, L., Klein, M., Jones, W. P., & Janicka, J. (2006, 02). Synthetic turbulence inflow conditions for large-eddy simulation. *Physics of Fluids*, *18*(2), 025107. Retrieved from https://doi.org/10.1063/1.2130744 doi: 10.1063/1.2130744

Dimitrov, N., Natarajan, A., & Mann, J. (2017). Effects of normal and extreme turbulence spectral parameters on wind turbine loads. *Renewable Energy*, *101*, 1180-1193. Retrieved from https://www.sciencedirect.com/science/article/pii/S0960148116308655 doi: 10.1016/j.renene.2016.10.001

Di Paola, M., & Gullo, I. (2001). Digital generation of multivariate wind field processes. *Probabilistic Engineering Mechanics*, *16*(1), 1–10. Retrieved from https://www.sciencedirect.com/science/article/pii/S0266892099000326 doi: 10.1016/S0266-8920(99)00032-6

Di Paola, M., & Zingales, M. (2008). Stochastic differential calculus for wind-exposed structures with autoregressive continuous (ARC) filters. *Journal of wind engineering and industrial aerodynamics*, *96*(12), 2403–2417. Retrieved from https://www.sciencedirect.com/science/article/pii/S0167610508001104 doi: 10.1016/j.jweia.2008.04.003

Elagamy, M., Gallego-Castillo, C., Cuerva-Tejero, A., Lopez-Garcia, O., & Avila-Sanchez, S. (2021a, November). Optimal autoregressive models for synthetic generation of turbulence. Implications of reproducing the spectrum or the autocovariance function. In *17th European Academy of Wind Energy Conference (PhD seminar)*. Porto, Portugal.

Elagamy, M., Gallego-Castillo, C., Cuerva-Tejero, A., Lopez-Garcia, O., & Avila-Sanchez, S. (2021b, September). Restricted autoregressive models for synthetic generation of stationary homogeneous isotropic turbulence. A methodology based on multi-point spectrum fitting. In *17th International Conference of Computational Methods in Sciences and Engineering*. Heraklion, Greece.

Elagamy, M., Gallego-Castillo, C., Cuerva-Tejero, A., Lopez-Garcia, O., & Avila-Sanchez, S. (2023). Eigenanalysis of vector autoregressive model for optimal fitting of a predefined cross power spectral density matrix: Application to numeric generation of stationary homogeneous isotropic/anisotropic turbulent wind fields. *Journal of Wind Engineering and Industrial Aerodynamics*, *238*, 105420. Retrieved from https://www.sciencedirect.com/science/article/pii/S016761052300123X doi: 10.1016/j.jweia.2023.105420

Elagamy, M., Kale, B., Gallego-Castillo, C., Cuerva-Tejero, A., Buckingham, S., van Beeck, J., ... Avila-Sanchez, S. (2022, November). Statistical characteristics of turbulent wind inflow obtained from WRF-LES simulations for the SWiFT test site. In *18th European Academy of Wind Energy Conference (PhD Seminar)*. Bruges, Belgium. Retrieved from https://phd2022.eawe.eu/program/book-of-abstracts/

Elagamy, M., Tiwari, N., Gallego-Castillo, C., Cuerva-Tejero, A., Lopez-Garcia, O., & Avila-Sanchez, S. (n.d.). *Large eddy simulation of the flow around a high-rise building with special focus on the two-points two-times second order statistics of the velocity vield.* (Under Review)

El Bahlouli, A., Rautenberg, A., Schön, M., zum Berge, K., Bange, J., & Knaus, H. (2019). Comparison of CFD simulation to UAS measurements for wind flows in complex terrain: application to the WINSENT test site. *Energies*, *12*(10), 1992.

Eliasson, I., Offerle, B., Grimmond, C., & Lindqvist, S. (2006). Wind fields and turbulence statistics in an urban street canyon. *Atmospheric environment*, *40*(1), 1–16. Retrieved from https://www.sciencedirect.com/science/article/pii/S1352231005002967 doi: 10.1016/j.atmosenv.2005.03.031

Emes, M., Arjomandi, M., Kelso, R., & Ghanadi, F. (2016, July 6–8). Integral length scales in a low-roughness atmospheric boundary layer. In *Proceedings of the 18th Australasian Wind Engineering Society Workshop* (pp. 1–4). McLaren Vale, South Australia: Australasian Wind Engineering Society. Retrieved from https://hdl.handle.net/2440/109454

Encraft. (2009). Encraft warwick wind trials project. *http://www.bwea.com/pdf/small/wineur.pdf*.

ETIPWind. (2023). *European wind energy competitiveness report.* Retrieved from https://etipwind.eu/publications/ (Latest ETIPWind report, June 2023)

Eurocode. (2005). *Eurocode 1: actions on structures - Part 1-4: general actions - wind actions* (Tech. Rep. No. EN 1991-1-4). Brussels, Belgium: CEN.

Evans, S., KC, A., Bradney, D., Urmee, T., Whale, J., & Clausen, P. (2017). The suitability of the IEC 61400-2 wind model for small wind turbines operating in the built environment. *Renewable Energy and Environmental Sustainability*, *2*, 31. Retrieved from https://doi.org/10.1051/rees/2017022 doi: 10.1051/rees/2017022

Feigenwinter, C., Vogt, R., & Parlow, E. (1999). Vertical structure of selected turbulence characteristics above an urban canopy. *Theoretical and Applied Climatology*, *62*(1), 51–63. Retrieved from 10.1007/s007040050074 doi: 10.1007/s007040050074

Fischer, R., Bastigkeit, I., Leitl, B., & Schatzmann, M. (2010). Generation of spatio-temporally high resolved datasets for the validation of LES-models simulating flow and dispersion phenomena within the lower atmospheric boundary layer. In *Proc. 5th international symposium on computational wind engineering (cwe2010), chapel hill, north carolina, usa.* Retrieved from https://api.semanticscholar.org/CorpusID:62126728

Forsyth, T., Baranowski, R., Whale, J., Tabrizi, A., KC, A., Peppoloni, M., ... Kelley, N. (2018). *International Energy Agency wind technology collaboration Programme Task 27 small wind turbine technical report* (Tech. Rep.). Retrieved from https://usercontent.one/wp/iea-wind.org/wp-content/uploads/2021/06/IEA-Wind-TCP-Task-27-Draft-Small-Wind-Turbine-Technical-Report.pdf

Fortuniak, K., & Pawlak, W. (2015). Selected spectral characteristics of turbulence over an urbanized area in the centre of Łódź, Poland. *Boundary-Layer Meteorology*, *154*(1), 137–156. Retrieved from https://doi.org/10.1007/s10546-014-9966-7 doi: 10.1007/s10546-014-9966-7

Franke, J., Hellsten, A., Schlünzen, H., & Carissimo, B. (2007). *Best practice guideline for the CFD simulation of flows in the urban environment: COST action 732 quality assurance and improvement of microscale meteorological models.* Meteorological Institute.

Gallego-Castillo, C., Cuerva-Tejero, A., Elagamy, M., Lopez-Garcia, O., & Avila-Sanchez, S. (2022). A tutorial on reproducing a predefined autocovariance function through AR models: application to stationary homogeneous isotropic turbulence. *Stochastic Environmental Research and Risk Assessment*, *36*(9), 2711-2736. Retrieved from https://doi.org/10.1007/s00477-021-02156-0 doi: 10.1007/s00477-021-02156-0

Gallego-Castillo, C., Cuerva-Tejero, A., Lopez-Garcia, O., & Avila, S. (2020). A comparison of spectral and time series based methods for synthesis of homogeneous and stationary stochastic velocity fields WindEurope Technology Workshop 2020. *Resource Assessment & Analysis of Operating Wind Farms (Online event)*.

Gallego-Castillo, C., Elagamy, M., Cuerva-Tejero, A., Lopez-Garcia, O., & Avila-Sanchez, S. (2024, May). Synthesis of realistic non-homogeneous non-gaussian turbulent wind fields. In *TORQUE conference*. Florence, Italy. (Accepted-to be published)

Giannini, C., & Mosconi, R. (1987). Predictions from unrestricted and restricted var models. *Giornale degli Economisti e Annali di Economia*, *46*, 291–316. Retrieved from http://www.jstor.org/stable/23247093

Grigoriu, M. (1984). Crossings of non-Gaussian translation processes. *Journal of Engineering Mechanics*, *110*(4), 610-620. Retrieved from https://ascelibrary.org/doi/abs/10.1061/%28ASCE%290733-9399%281984%29110%3A4%28610%29 doi: 10.1061/(ASCE)0733-9399(1984)110:4(610)

Grigoriu, M. (2002). *Stochastic calculus: applications in science and engineering* (1st ed.). Birkhäuser Boston, MA. Retrieved from https://doi.org/10.1007/978-0-8176-8228-6

Guo, F., & Mann, J. (2022, Feb 22). *Mannturb4d_v1 (version v1.0)*. Zenodo. (Initial release of the 4D Mann Turbulence Generator) doi: 10.5281/zenodo.6223785

Hemida, H., & Šarkić, A. (2014). *Final report of a short term scientific mission COST action TU1304: wind tunnel tests–air flow around buildings* (Tech. Rep.). WINERCOST. Retrieved from http://winercost.com/cost_files/STSM_report-Sarkic_Hemida.pdf

Hemida, H., Šarkić Glumac, A., Vita, G., Kostadinović Vranešević, K., & Höffer, R. (2020). On the flow over high-rise building for wind energy harvesting: An experimental investigation of wind speed and surface pressure. *Applied Sciences*, *10*(15). doi: 10.3390/app10155283

Huang, S., Li, Q., & Wu, J. (2010). A general inflow turbulence generator for large eddy simulation. *Journal of Wind Engineering and Industrial Aerodynamics*, *98*(10), 600-617. Retrieved from https://www.sciencedirect.com/science/article/pii/S0167610510000644 doi: 10.1016/j.jweia.2010.06.002

Huo, T., Tong, L. W., & Mashiri, F. R. (2018). Turbulent wind field simulation of wind turbine structures with consideration of the effect of rotating blades. *Advanced Steel Construction*, *15*(1), 82–92. doi: 10.18057/IJASC.2019.15.1.11

Hytti, H., Takalo, R., & Ihalainen, H. (2006). Tutorial on multivariate autoregressive modelling. *Journal of clinical monitoring and computing*, *20*(2), 101–108. Retrieved from https://doi.org/10.1007/s10877-006-9013-4 doi: 10.1007/s10877-006-9013-4

IEA. (2023). *Renewable energy market update - june 2023*. Retrieved from https://www.iea.org/reports/renewable-energy-market-update-june-2023 (License: CC BY 4.0)

IEC 61400-1. (2019). Part 1: safety requirements. Wind turbine generator systems. *Edition*

4, International Electrotechnical Commission.

IEC 61400-2. (2019). Wind turbines Part 2: design requirements for small wind turbines-annex M. *Edition 3, International Electrotechnical Commission.*

IRENA. (2020). *Rise of renewables in cities: energy solutions for the urban future.* Abu Dhabi, United Arab Emirates: International Renewable Energy Agency. Retrieved from https://www.irena.org/-/media/Files/IRENA/Agency/Publication/2020/Oct/IRENA_Renewables_in_cities_2020.pdf

Issa, R. (1986). Solution of the implicitly discretized fluid flow equations by operator-splitting. *Journal of Computational Physics*, *62*(1), 40-65. doi: 10.1016/0021-9991(86)90099-9

Jacob, J., & Sagaut, P. (2018). Wind comfort assessment by means of large eddy simulation with lattice Boltzmann method in full scale city area. *Building and Environment*, *139*, 110-124. Retrieved from https://www.sciencedirect.com/science/article/pii/S0360132318302750 doi: 10.1016/j.buildenv.2018.05.015

Kaimal, J., Wyngaard, J., Izumi, Y., & Coté, O. (1972). Spectral characteristics of surface-layer turbulence. *Quarterly Journal of the Royal Meteorological Society*, *98*(417), 563–589. Retrieved from https://api.semanticscholar.org/CorpusID:123560157

Kaimal, J. C., & Finnigan, J. J. (1994). *Atmospheric boundary layer flows: their structure and measurement.* Oxford university press.

Kareem, A. (2008). Numerical simulation of wind effects: a probabilistic perspective. *Journal of Wind Engineering and Industrial Aerodynamics*, *96*(10-11), 1472–1497. Retrieved from https://www.sciencedirect.com/science/article/pii/S0167610508000275 (4th International Symposium on Computational Wind Engineering (CWE2006)) doi: 10.1016/j.jweia.2008.02.048

KC, A., Whale, J., & Urmee, T. (2019). Urban wind conditions and small wind turbines in the built environment: a review. *Renewable Energy*, *131*, 268-283. Retrieved from https://www.sciencedirect.com/science/article/pii/S0960148118308474 doi: 10.1016/j.renene.2018.07.050

Kirkegaard, J. K., Rudolph, D. P., Nyborg, S., Solman, H., Gill, E., Cronin, T., & Hallisey, M. (2023, July). Tackling grand challenges in wind energy through a socio-technical perspective. *Nature Energy*, *8*(7), 655-664. Retrieved from https://doi.org/10.1038/s41560-023-01266-z doi: 10.1038/s41560-023-01266-z

Kleinhans, D., Friedrich, R., Schaffarczyk, A., & Peinke, J. (2009). Synthetic turbulence models for wind turbine applications. In *Progress in Turbulence III* (Vol. 131, pp. 111–114). Berlin, Heidelberg: Springer Berlin Heidelberg. doi: 10.1007/978-3-642-02225-8_26

Kono, T., Kogaki, T., & Kiwata, T. (2016). Numerical investigation of wind conditions for roof-mounted wind turbines: effects of wind direction and horizontal aspect ratio of a high-rise cuboid building. *Energies*, *9*(11), 907. Retrieved from https://www.mdpi.com/1996-1073/9/11/907 doi: 10.3390/en9110907

Krenk, S. (1996). Wind field coherence and dynamic wind forces. In A. Naess & S. Krenk (Eds.), *IUTAM Symposium on Advances in Nonlinear Stochastic Mechanics* (pp. 269–278). Dordrecht: Springer Netherlands.

Krenk, S. (2011, May). Explicit calibration and simulation of stochastic fields by low-order ARMA processes. In *3rd international conference on computational methods in structural dynamics and earthquake engineering.* Corfu, Greece.

Krenk, S., & Møller, R. (2019). Turbulent wind field representation and conditional mean-field

simulation. *Proceedings of the Royal Society A*, *475*(2223), 20180887. Retrieved from https://royalsocietypublishing.org/doi/abs/10.1098/rspa.2018.0887 doi: 10.1098/rspa.2018.0887

Kristensen, L., & Jensen, N. (1979). Lateral coherence in isotropic turbulence and in the natural wind. *Boundary-Layer Meteorology*, *17*(3), 353–373. Retrieved from https://doi.org/10.1007/BF00117924 doi: 10.1007/BF00117924

Kristensen, L., & Kirkegaard, P. (1986). *Sampling problems with spectral coherence* (No. 526). Risø National Laboratory. Retrieved from https://orbit.dtu.dk/en/publications/sampling-problems-with-spectral-coherence

Landau, L. D., & Lifshitz, E. M. (1987). *Theoretical Physics, vol. 6, Fluid Mechanics.* Pergamon, London.

Lathi, B. P. (2005). *Linear systems and signals, second edition.* Oxford University Press.

Lebrun, R., & Dutfoy, A. (2009). An innovating analysis of the Nataf transformation from the copula viewpoint. *Probabilistic Engineering Mechanics*, *24*(3), 312-320. Retrieved from https://www.sciencedirect.com/science/article/pii/S0266892008000660 doi: https://doi.org/10.1016/j.probengmech.2008.08.001

Ledo, L., Kosasih, P., & Cooper, P. (2011). Roof mounting site analysis for micro-wind turbines. *Renewable Energy*, *36*(5), 1379–1391. Retrieved from https://www.sciencedirect.com/science/article/pii/S096014811000501X doi: 10.1016/j.renene.2010.10.030

Li, Y., & Kareem, A. (1990). ARMA systems in wind engineering. *Probabilistic Engineering Mechanics*, *5*(2), 49-59. Retrieved from https://www.sciencedirect.com/science/article/pii/S026689200880001X doi: 10.1016/S0266-8920(08)80001-X

Li, Y., & Kareem, A. (1991). Simulation of multivariate nonstationary random processes by FFT. *Journal of Engineering Mechanics*, *117*(5), 1037-1058. Retrieved from https://ascelibrary.org/doi/abs/10.1061/%28ASCE%290733-9399%281991%29117%3A5%281037%29 doi: 10.1061/(ASCE)0733-9399(1991)117:5(1037)

Li, Y., & Kareem, A. (1993). Simulation of multivariate random processes: Hybrid DFT and digital filtering approach. *Journal of Engineering Mechanics*, *119*(5), 1078-1098. Retrieved from https://ascelibrary.org/doi/abs/10.1061/%28ASCE%290733-9399%281993%29119%3A5%281078%29 doi: 10.1061/(ASCE)0733-9399(1993)119:5(1078)

Li, Y., & Kareem, A. (1995). Stochastic decomposition and application to probabilistic dynamics. *Journal of Engineering Mechanics*, *121*(1), 162-174. Retrieved from https://ascelibrary.org/doi/abs/10.1061/%28ASCE%290733-9399%281995%29121%3A1%28162%29 doi: 10.1061/(ASCE)0733-9399(1995)121:1(162)

Li, Y., & Kareem, A. (1997). Simulation of multivariate nonstationary random processes: Hybrid DFT and digital filtering approach. *Journal of Engineering Mechanics*, *123*(12), 1302-1310. Retrieved from https://ascelibrary.org/doi/abs/10.1061/%28ASCE%290733-9399%281997%29123%3A12%281302%29 doi: 10.1061/(ASCE)0733-9399(1997)123:12(1302)

Li, Y., Togbenou, K., Xiang, H., & Chen, N. (2017a). Simulation of non-stationary wind velocity field on bridges based on Taylor series. *Journal of Wind Engineering and Industrial Aerodynamics*, *169*, 117–127. Retrieved from https://www.sciencedirect.com/science/article/pii/S0167610516302239 doi: 10.1016/j.jweia.2017.07.005

Li, Y., Togbenou, K., Xiang, H., & Chen, N. (2017b). Simulation of non-stationary wind velocity field on bridges based on taylor series. *Journal of Wind Engineering and*

Industrial Aerodynamics, *169*, 117-127. Retrieved from https://www.sciencedirect.com/science/article/pii/S0167610516302239 doi: 10.1016/j.jweia.2017.07.005

Lilly, D. K. (1962). On the numerical simulation of buoyant convection. *Tellus*, *14*(2), 148–172. Retrieved from https://doi.org/10.3402/tellusa.v14i2.9537 doi: 10.3402/tellusa.v14i2.9537

Lorenz, E. N. (1963). Deterministic nonperiodic flow. *Journal of Atmospheric Sciences*, *20*(2), 130 - 141. Retrieved from https://journals.ametsoc.org/view/journals/atsc/20/2/1520-0469_1963_020_0130_dnf_2_0_co_2.xml doi: 10.1175/1520-0469(1963)020<0130:DNF>2.0.CO;2

Lumley, J. L. (2007). *Stochastic tools in turbulence*. Courier Corporation.

Lütkepohl, H. (2013). *Introduction to multiple time series analysis*. Springer Science & Business Media.

Lyons, R. G. (2010). *Understanding digital signal processing* (3rd ed.). Pearson Education India.

Madsen, H. (2007). *Time series analysis* (1st ed.). Chapman and Hall/CRC. doi: 10.1201/9781420059687

Mann, J. (1994a). *Models in micrometeorology* (No. Risø-R-727). Risø National Laboratory.

Mann, J. (1994b). The spatial structure of neutral atmospheric surface-layer turbulence. *Journal of fluid mechanics*, *273*, 141–168. doi: 10.1017/S0022112094001886

Mann, J. (1998). Wind field simulation. *Probabilistic engineering mechanics*, *13*(4), 269–282. Retrieved from https://www.sciencedirect.com/science/article/pii/S0266892097000362 doi: 10.1016/S0266-8920(97)00036-2

Marple Jr, S., & Carey, W. (2019). *Digital spectral analysis with applications* (second ed.). Acoustical Society of America.

Meirovitch, L. (1986). *Elements of vibration analysis*. McGraw-Hill Book Company.

Melaku, A. F., & Bitsuamlak, G. T. (2021). A divergence-free inflow turbulence generator using spectral representation method for large-eddy simulation of ABL flows. *Journal of Wind Engineering and Industrial Aerodynamics*, *212*, 104580. Retrieved from https://www.sciencedirect.com/science/article/pii/S0167610521000660 doi: 10.1016/j.jweia.2021.104580

Meng, Y., & Hibi, K. (1998). Turbulent measurments of the flow field around a high-rise building. *Wind Engineers, JAWE*, *1998*(76), 55-64. doi: 10.5359/jawe.1998.76_55

Merlier, L., Jacob, J., & Sagaut, P. (2019). Lattice-Boltzmann large-eddy simulation of pollutant dispersion in complex urban environment with dense gas effect: Model evaluation and flow analysis. *Building and Environment*, *148*, 634-652. Retrieved from https://www.sciencedirect.com/science/article/pii/S0360132318307042 doi: 10.1016/j.buildenv.2018.11.009

Micallef, D., & Van Bussel, G. (2018). A review of urban wind energy research: aerodynamics and other challenges. *Energies*, *11*(9). Retrieved from https://www.mdpi.com/1996-1073/11/9/2204 doi: 10.3390/en11092204

Mignolet, M., & Spanos, P. (1987). Recursive simulation of stationary multivariate random processes - Part I. *Journal of Applied Mechanics*, *54*(3), 674-680. doi: 10.1115/1.3173087

Mignolet, M. P., & Spanos, P. D. (1992). Simulation of homogeneous two-dimensional random fields: Part I—AR and ARMA models. *Journal of Applied Mechanics*, *59*(2S), S260-S269. Retrieved from https://doi.org/10.1115/1.2899499 doi: 10.1115/1.2899499

Musial, W., & Ram, B. (2010). *Large-scale offshore wind power in the United States: assessment of opportunities and barriers* (Tech. Rep. No. NREL/TP-500-40745). National Renewable Energy Lab.(NREL), Golden, CO (United States). Retrieved from https://www.nrel.gov/docs/fy10osti/40745.pdf doi: 10.2172/990101

Nelson, M. A., Brown, M. J., Pardyjak, E. R., & Klewicki, J. (2004). *Turbulence within and above real and artificial urban canopies* (Tech. Rep.). Los Alamos National Laboratory.

Nelson, M. A., Pardyjak, E. R., Brown, M. J., & Klewicki, J. (2007b). Properties of the wind field within the Oklahoma City Park Avenue street canyon. Part II: Spectra, cospectra, and quadrant analyses. *Journal of Applied Meteorology and Climatology*, *46*(12), 2055–2073. Retrieved from https://journals.ametsoc.org/view/journals/apme/46/12/2006jamc1427.1.xml doi: 10.1175/2006JAMC1427.1

Nelson, M. A., Pardyjak, E. R., Klewicki, J., Pol, S., & Brown, M. J. (2007a). Properties of the wind field within the Oklahoma City Park Avenue street canyon. Part I: Mean flow and turbulence statistics. *Journal of Applied Meteorology and Climatology*, *46*(12), 2038–2054. Retrieved from https://journals.ametsoc.org/view/journals/apme/46/12/2006jamc1427.1.xml doi: 10.1175/2006JAMC1427.1

Nicoud, F., & Ducros, F. (1999). Subgrid-Scale stress modelling based on the square of the velocity gradient tensor. *Flow, Turbulence and Combustion*, *62*(3), 183-200. doi: 10.1023/A:1009995426001

Oke, T. R. (1987). *Boundary layer climates* (2nd ed.). London: Routledge. doi: 10.4324/9780203407219

Oke, T. R., Mills, G., Christen, A., & Voogt, J. A. (2017). Airflow. In *Urban climates.* Cambridge University Press. doi: 10.1017/9781139016476

Ono, Y., Tamura, T., & Kataoka, H. (2008). LES analysis of unsteady characteristics of conical vortex on a flat roof. *Journal of Wind engineering and Industrial aerodynamics*, *96*(10), 2007–2018. Retrieved from https://www.sciencedirect.com/science/article/pii/S0167610508000780 doi: 10.1016/j.jweia.2008.02.021

Panofsky, H. A., & Dutton, J. A. (1984). *Atmospheric turbulence.* New York: John Wiley & Sons.

Patankar, S., & Spalding, D. (1972). A calculation procedure for heat, mass and momentum transfer in three-dimensional parabolic flows. *International Journal of Heat and Mass Transfer*, *15*(10), 1787-1806. doi: 10.1016/0017-9310(72)90054-3

Patruno, L., & Ricci, M. (2017). On the generation of synthetic divergence-free homogeneous anisotropic turbulence. *Computer Methods in Applied Mechanics and Engineering*, *315*, 396-417. Retrieved from https://www.sciencedirect.com/science/article/pii/S0045782516308581 doi: 10.1016/j.cma.2016.11.005

Peng, H., Dai, S., Lin, K., Hu, G., & Liu, H. (2020). Experimental investigation of wind characteristics and wind energy potential over rooftops: Effects of building parameters. *Journal of Wind Engineering and Industrial Aerodynamics*, *205*, 104304. Retrieved from https://www.sciencedirect.com/science/article/pii/S0167610520302142 doi: 10.1016/j.jweia.2020.104304

Phillips, C. L., Nagle, H. T., & Chakrabortty, A. (2015). *Digital control system analysis and design* (4th ed.). Pearson.

Pope, S. B. (2000). *Turbulent flows.* Cambridge University Press. doi: 10.1017/CBO9780511840531

Reed, D., & Scanlan, R. (1983). Time series analysis of cooling tower wind loading. *Journal of structural engineering*, *109*(2), 538–554. Retrieved from https://ascelibrary.org/doi/abs/10.1061/%28ASCE%290733-9445%281983%29109%3A2%28538%29 doi: 10.1061/(ASCE)0733-9445(1983)109:2(538)

Reif, B. P., & Durbin, P. (2010). *Statistical theory and modeling for turbulent flows*. John Wiley & Sons. doi: 10.1002/9780470972076

Ricciardelli, F., & Polimeno, S. (2006). Some characteristics of the wind flow in the lower urban boundary layer. *Journal of Wind Engineering and Industrial Aerodynamics*, *94*(11), 815–832. Retrieved from https://www.sciencedirect.com/science/article/pii/S0167610506000894 doi: 10.1016/j.jweia.2006.06.003

Rotach, M. (1991). *Turbulence within and above an urban canopy* (Doctoral dissertation, ETH Zurich). doi: 10.3929/ethz-a-000599740

Rotach, M. (1995). Profiles of turbulence statistics in and above an urban street canyon. *Atmospheric Environment*, *29*(13), 1473–1486. Retrieved from https://www.sciencedirect.com/science/article/pii/135223109500084C doi: 10.1016/1352-2310(95)00084-C

Roth, M. (2000). Review of atmospheric turbulence over cities. *Quarterly Journal of the Royal Meteorological Society*, *126*(564), 941–990. Retrieved from https://rmets.onlinelibrary.wiley.com/doi/abs/10.1002/qj.49712656409 doi: 10.1002/qj.49712656409

Samaras, E., Shinzuka, M., & Tsurui, A. (1985). ARMA representation of random processes. *Journal of Engineering Mechanics*, *111*(3), 449–461. Retrieved from https://ascelibrary.org/doi/abs/10.1061/%28ASCE%290733-9399%281985%29111%3A3%28449%29 doi: 10.1061/(ASCE)0733-9399(1985)111:3(449)

Samii, K., & Vandiver, J. (1984, 05). *A numerically efficient technique for the simulation of random wave forces on offshore structures* (Vol. All Days). Retrieved from https://doi.org/10.4043/4811-MS doi: 10.4043/4811-MS

Schottler, J., Reinke, N., Hölling, A., Whale, J., Peinke, J., & Hölling, M. (2017). On the impact of non-gaussian wind statistics on wind turbines an experimental approach. *Wind Energy Science*, *2*(1), 1–13. Retrieved from https://wes.copernicus.org/articles/2/1/2017/ doi: 10.5194/wes-2-1-2017

Shaler, K., Jonkman, J., Doubrawa Moreira, P., & Hamilton, N. (2019, January 7–11). FAST.Farm response to varying wind inflow techniques. In *Aiaa scitech 2019 forum*. San Diego, California. Retrieved from https://doi.org/10.2514/6.2019-2086 doi: 10.2514/6.2019-2086

Shinozuka, M. (1971). Simulation of multivariate and multidimensional random processes. *The Journal of the Acoustical Society of America*, *49*(1B), 357–368. Retrieved from https://doi.org/10.1121/1.1912338 doi: 10.1121/1.1912338

Shinozuka, M. (1972). Monte carlo solution of structural dynamics. *Computers & Structures*, *2*(5), 855-874. Retrieved from https://www.sciencedirect.com/science/article/pii/0045794972900430 doi: 10.1016/0045-7949(72)90043-0

Shinozuka, M., & Deodatis, G. (1991). Simulation of stochastic processes by spectral representation. *Applied Mechanics Reviews*, *44*(4), 191-204. Retrieved from https://doi.org/10.1115/1.3119501 doi: 10.1115/1.3119501

Shinozuka, M., & Deodatis, G. (1996). Simulation of multi-dimensional gaussian stochastic fields by spectral representation. *Applied Mechanics Reviews*, *49*(1), 29-53. Retrieved

from https://doi.org/10.1115/1.3101883 doi: 10.1115/1.3101883

Shinozuka, M., & Jan, C.-M. (1972). Digital simulation of random processes and its applications. *Journal of Sound and Vibration*, *25*(1), 111-128. Retrieved from https://www.sciencedirect.com/science/article/pii/0022460X72906001 doi: 10.1016/0022-460X(72)90600-1

Shinozuka, M., Yun, C.-B., & Seya, H. (1990). Stochastic methods in wind engineering. *Journal of Wind Engineering and Industrial Aerodynamics*, *36*, 829-843. Retrieved from https://www.sciencedirect.com/science/article/pii/016761059090080V doi: 10.1016/0167-6105(90)90080-V

Shur, M. L., Spalart, P. R., Strelets, M. K., & Travin, A. K. (2014, 07 01). Synthetic turbulence generators for RANS-LES interfaces in zonal simulations of aerodynamic and aeroacoustic problems. *Flow, Turbulence and Combustion*, *93*(1), 63–92. Retrieved from https://doi.org/10.1007/s10494-014-9534-8 doi: 10.1007/s10494-014-9534-8

Smagorinsky, J. (1963). General circulation experiments with the primitive equations. Part I: the basic experiment. *Monthly Weather Review*, *91*, 99-164. doi: 10.1175/1520-0493(1963)091\textless0099:GCEWTP\textgreater2.3.CO;2

Smith, J., Forsyth, T., Sinclair, K., & Oteri, F. (2012). *Built-environment wind turbine roadmap* (Tech. Rep. No. NREL/TP-5000-50499). National Renewable Energy Lab.(NREL), Golden, CO (United States). Retrieved from https://doi.org/10.2172/1054820 doi: 10.2172/1054820

Spanos, P. (1983, 09). ARMA algorithms for ocean wave modeling. *Journal of Energy Resources Technology*, *105*(3), 300-309. Retrieved from https://doi.org/10.1115/1.3230919 doi: 10.1115/1.3230919

Spanos, P. D. (1983). ARMA Algorithms for ocean wave modeling. *ASME Journal Energy Resources Technology*, *105*(3), 300–309. Retrieved from https://doi.org/10.1115/1.3230919 doi: 10.1115/1.3230919

Spanos, P. D., & Hansen, J. (1981). Linear prediction theory for digital simulation of sea waves. *ASME Journal Energy Resources Technology*, *103*(3), 243–249. Retrieved from https://doi.org/10.1115/1.3230845 doi: 10.1115/1.3230845

Spanos, P. D., & Mignolet, M. P. (1992). Simulation of homogeneous two-dimensional random fields: Part II—MA and ARMA models. *Journal of Applied Mechanics*, *59*(2S), S270-S277. Retrieved from https://doi.org/10.1115/1.2899500 doi: 10.1115/1.2899500

Stathopoulos, T., Alrawashdeh, H., Al-Quraan, A., Blocken, B., Dilimulati, A., Paraschivoiu, M., & Pilay, P. (2018). Urban wind energy: Some views on potential and challenges. *Journal of Wind Engineering and Industrial Aerodynamics*, *179*, 146-157. Retrieved from https://www.sciencedirect.com/science/article/pii/S0167610517304774 doi: 10.1016/j.jweia.2018.05.018

Tabrizi, A., Whale, J., Lyons, T., & Urmee, T. (2015). Extent to which international wind turbine design standard, IEC 61400-2 is valid for a rooftop wind installation. *Journal of Wind Engineering and Industrial Aerodynamics*, *139*, 50–61. Retrieved from https://www.sciencedirect.com/science/article/pii/S016761051500015X doi: 10.1016/j.jweia.2015.01.006

Takalo, R., Hytti, H., & Ihalainen, H. (2005). Tutorial on univariate autoregressive spectral analysis. *Journal of clinical monitoring and computing*, *19*(6), 401–410. Retrieved from https://doi.org/10.1007/s10877-005-7089-x doi: 10.1007/s10877-005-7089-x

Taylor, G. I. (1938). The spectrum of turbulence. *Proceedings of the Royal Society of London. Series A, Mathematical and Physical Sciences*, *164*(919), 476–490. Retrieved from http://doi.org/10.1098/rspa.1938.0032 doi: 10.1098/rspa.1938.0032

Toja-Silva, F., Kono, T., Peralta, C., Lopez-Garcia, O., & Chen, J. (2018). A review of computational fluid dynamics (CFD) simulations of the wind flow around buildings for urban wind energy exploitation. *Journal of Wind Engineering and Industrial Aerodynamics*, *180*, 66-87. Retrieved from https://www.sciencedirect.com/science/article/pii/S0167610518302277 doi: 10.1016/j.jweia.2018.07.010

Toja-Silva, F., Peralta, C., Lopez-Garcia, O., Navarro, J., & Cruz, I. (2015). On roof geometry for urban wind energy exploitation in high-rise buildings. *computation*, *3*(2), 299–325. Retrieved from https://www.mdpi.com/2079-3197/3/2/299 doi: 10.3390/computation3020299

Tolias, I., Koutsourakis, N., Hertwig, D., Efthimiou, G., Venetsanos, A., & Bartzis, J. (2018a). Large Eddy Simulation study on the structure of turbulent flow in a complex city. *Journal of Wind Engineering and Industrial Aerodynamics*, *177*, 101-116. Retrieved from https://www.sciencedirect.com/science/article/pii/S0167610517309765 doi: 10.1016/j.jweia.2018.03.017

Tolias, I., Koutsourakis, N., Hertwig, D., Efthimiou, G., Venetsanos, A., & Bartzis, J. (2018b). Large Eddy Simulation study on the structure of turbulent flow in a complex city. *Journal of Wind Engineering and Industrial Aerodynamics*, *177*, 101–116. Retrieved from https://www.sciencedirect.com/science/article/pii/S0167610517309765 doi: 10.1016/j.jweia.2018.03.017

Tominaga, Y., Mochida, A., Yoshie, R., Kataoka, H., Nozu, T., Yoshikawa, M., & Shirasawa, T. (2008). AIJ guidelines for practical applications of CFD to pedestrian wind environment around buildings. *Journal of Wind Engineering and Industrial Aerodynamics*, *96*(10), 1749-1761. Retrieved from https://www.sciencedirect.com/science/article/pii/S0167610508000445 doi: 10.1016/j.jweia.2008.02.058

Tsay, R. S. (2013). *Multivariate time series analysis: with R and financial applications*. John Wiley & Sons.

Vasaturo, R., Kalkman, I., Blocken, B., & van Wesemael, P. (2018). Large eddy simulation of the neutral atmospheric boundary layer: performance evaluation of three inflow methods for terrains with different roughness. *Journal of Wind Engineering and Industrial Aerodynamics*, *173*, 241-261. Retrieved from https://www.sciencedirect.com/science/article/pii/S0167610517300168 doi: 10.1016/j.jweia.2017.11.025

Veers, P. S. (1988). *Three-dimensional wind simulation* (Tech. Rep. No. SAND-88-0152C). Sandia National Labs., Albuquerque, NM (USA).

Vita, G. (2020). *The effect of turbulence in the built environment on wind turbine aerodynamics (doctoral thesis)* (Unpublished doctoral dissertation). University of Birmingham.

Vita, G., Šarkić Glumac, A., Hemida, H., Salvadori, S., & Baniotopoulos, C. (2020). On the wind energy resource above high-rise buildings. *Energies*, *13*(14). doi: 10.3390/en13143641

Vogel, C. (2009). Spectral characteristics of turbulence from rooftop meteorological stations in Washington, DC. In *Eighth symposium on the urban environment*. Retrieved from https://ams.confex.com/ams/89annual/techprogram/paper_146886.htm

Von Karman, T. (1948). Progress in the statistical theory of turbulence. *Proceedings*

of the National Academy of Sciences of the United States of America, *34*(11), 530-539. Retrieved from https://www.pnas.org/doi/abs/10.1073/pnas.34.11.530 doi: 10.1073/pnas.34.11.530

Vranešević, K. K., Vita, G., & Bordas, A., Stephane P.A.and Šarkić Glumac. (2022). Furthering knowledge on the flow pattern around high-rise buildings: LES investigation of the wind energy potential. *Journal of Wind Engineering and Industrial Aerodynamics*, *226*, 105029. doi: 10.1016/j.jweia.2022.105029

Šarkić Glumac, A., Hemida, H., & Höffer, R. (2018a). Wind energy potential above a high-rise building influenced by neighboring buildings: An experimental investigation. *Journal of Wind Engineering and Industrial Aerodynamics*, *175*, 32-42. doi: 10.1016/j.jweia.2018.01.022

Šarkić Glumac, A., Hemida, H., & Höffer, R. (2018b). *Wind tunnel experimental data for flow characteristics above the roof of high-rise buildings in group arrangement for wind energy harvesting.* Mendeley Data. doi: 10.17632/cxc4w2myyw.2

Šarkić Glumac, A., Hemida, H., Vita, G., Kostadinović Vranešević, K., & Höffer, R. (2020). *Wind tunnel experimental data for flow characteristics above the roof of isolated high-rise building for wind energy harvesting considering two shapes of the roof, flat roof and deck roof.* Mendeley Data. doi: 10.17632/jp7vc8tf7w.1

Wang, H., & Wu, T. (2018). Hilbert-Wavelet-Based nonstationary wind field simulation: a multiscale spatial correlation scheme. *Journal of Engineering Mechanics*, *144*(8), 04018063. Retrieved from https://ascelibrary.org/doi/abs/10.1061/%28ASCE%29EM.1943-7889.0001490 doi: 10.1061/(ASCE)EM.1943-7889.0001490

Wang, H., Zong, Z.-h., Li, A.-q., Tong, T., Niu, J., & Deng, W.-p. (2012). Digital simulation of 3D turbulence wind field of Sutong Bridge based on measured wind spectra. *Journal of Zhejiang University SCIENCE A*, *13*(2), 91–104. Retrieved from https://doi.org/10.1631/jzus.A1100177 doi: 10.1631/jzus.A1100177

Wang, J. (1992). Turbulence characteristics in an urban atmosphere of complex terrain. *Atmospheric Environment. Part A. General Topics*, *26*(15), 2717–2724. Retrieved from https://www.sciencedirect.com/science/article/pii/0960168692900067 doi: 10.1016/0960-1686(92)90006-7

WINEUR. (2007). Wind energy integration in the urban environment: report on resource assessment. *European Commission. http://www.bwea.com/pdf/small/wineur.pdf*.

Wise, A. (1971). Effects due to groups of buildings. *Philosophical Transactions of the Royal Society of London. Series A, Mathematical and Physical Sciences*, *269*(1199), 469–485.

Wyngaard, J. C. (2010). *Turbulence in the atmosphere.* Cambridge University Press.

Xiong, M., Chen, B., Zhang, H., & Qian, Y. (2022). Study on accuracy of CFD simulations of wind environment around high-rise buildings: a comparative study of $k-\epsilon$; turbulence models based on polyhedral meshes and wind tunnel experiments. *Applied Sciences*, *12*(14). Retrieved from https://www.mdpi.com/2076-3417/12/14/7105 doi: 10.3390/app12147105

Yakhot, A., Liu, H., & Nikitin, N. (2006). Turbulent flow around a wall-mounted cube: A direct numerical simulation. *International journal of heat and fluid flow*, *27*(6), 994–1009. Retrieved from https://www.sciencedirect.com/science/article/pii/S0142727X06000476 doi: 10.1016/j.ijheatfluidflow.2006.02.026

Zhao, N., & Huang, G. (2020). Wind velocity field simulation based on enhanced closed-

form solution of Cholesky decomposition. *Journal of Engineering Mechanics*, *146*(2), 04019128. Retrieved from https://ascelibrary.org/doi/abs/10.1061/%28ASCE%29EM.1943-7889.0001712 doi: 10.1061/(ASCE)EM.1943-7889.0001712

Zivot, E., & Wang, J. (2006). *Modeling financial time series with S-PLUS* (Vol. 2). Springer. doi: 10.1007/978-0-387-32348-0

Annexes

1 Changing independent variable of a function

Two methods to change an independent variable in a function are presented in this section. The first method is to change the variable while preserving the integral of the function and the second method is changing the variable by replacement.

First method: Change an independent variable while preserving the integral of the function

An independent variable x of a given function $g(x)$ can be replaced by another independent variable y, where $x = f(y)$ and $y = h(x)$, while preserving the integral of the function g by fulfilling the following relation:

$$g(y)dy = g(x)dx, \tag{1}$$

where $dx = \dfrac{df(y)}{dy}dy$, thus,

$$g(y)dy = g(x)\left[\frac{df(y)}{dy}dy\right] \rightarrow g(y) = g(x)\frac{df(y)}{dy}. \tag{2}$$

The main advantage of this method is that the integral area is preserved, therefore,

$$\int_{x_1}^{x_2} g(x)dx = \int_{y_1=h(x_1)}^{y_2=h(x_2)} g(y)dy.$$

Preserving the integral area of the function is essential for the AR spectrum analysis. The variance of the AR process is equivalent to the area under the AR spectrum, thus, it is crucial to preserve the area under the AR spectrum while dealing with different spectra in various frequency/wavenumber domains.

Second method: Replacement

Another method to change an independent variable x to another independent variable y, where $x = f(y)$, is by using the replacement approach. This method directly substitute the

independent variable x with $f(y)$, to obtain $g(y) = g(x = f(y))$. The demerit of this method is that the integral of the function is not preserved between the two independent variables, thus,

$$\int_{x_1}^{x_2} g(x)dx \neq \int_{y_1=h(x_1)}^{y_2=h(x_2)} g(y)dy.$$

To manifest the difference between both methods, consider a function $g(x) = ax + b$, where a, b are constants and x is an independent variable. To change the independent variable x to the independent variable y, where $x = cy$ and c is a constant, by using the first method the obtained $g(y)$ is equal to $g(y) = c(acy + b)$. Whilst, the obtained $g(y)$ by utilizing the second method is equal to $acy + b$. From the two methods, it can be observed that the only difference between the obtained functions $g(y)$ is a factor that preserves the area after changing the independent variable.

By applying the concept of changing an independent variable while preserving the integral of the function, the AR spectrum can be expressed in terms of various variables. The general form of AR spectrum is expressed as follows:

$$S^{\mathrm{AR}}(x) = C_{\mathrm{AR}} \frac{\sigma^2}{\left|1 - \sum_{j=1}^{p} \varphi_j \exp(-\mathrm{i}jg(x))\right|^2}, \quad x_a \leq x \leq x_b, \tag{3}$$

where C_{AR} is a scaling factor for the AR spectrum, $g(x)$ is a scaling function of the independent variable, and x_a and x_b represent the limits of the independent variable. The values of these parameters for different domains are presented in Table 1.

$S^{\mathrm{AR}}(x)$	x	C_{AR}	$g(x)$	x_a	x_b
$S^{\mathrm{AR}}(f)$	f	$\frac{1}{f_{\max}}$	$\frac{\pi f}{f_{\max}}$	0	$f_{\max}$
$S^{\mathrm{AR}}(\omega)$	ω	$\frac{1}{\omega_{\max}}$	$\frac{\pi \omega}{\omega_{\max}}$	0	$\omega_{\max}$
$S^{\mathrm{AR}}(k)$	k	$\frac{1}{k_{\max}}$	$\frac{\pi k}{k_{\max}}$	0	$k_{\max}$

Table 1: Coefficients for the general form of the AR spectrum equation (3).

By using the concept of changing an independent variable while preserving the integral of the function, similarly, the VAR CPSDM can be presented in a general form in terms of the independent variable x:

$$\boldsymbol{S}^{\mathrm{VAR}}(x) = C_{\mathrm{VAR}}[\boldsymbol{W}_1 \boldsymbol{W}_2(g(x))]^{-1} \boldsymbol{\Sigma}\boldsymbol{\Sigma}^T [\boldsymbol{W}_1 \boldsymbol{W}_2(g(x))]^{-H}, \quad x_a \leq x \leq x_b, \tag{4}$$

where

$$\boldsymbol{W}_1 = \begin{bmatrix} \boldsymbol{I} & \boldsymbol{\Phi}_1 & \boldsymbol{\Phi}_2 & \dots & \boldsymbol{\Phi}_p \end{bmatrix}, \tag{5}$$

and

$$\boldsymbol{W}_2(g(x)) = \begin{bmatrix} \boldsymbol{I} \\ \exp(-\mathrm{i}g(x))\boldsymbol{I} \\ \exp(-\mathrm{i}2g(x))\boldsymbol{I} \\ \vdots \\ \exp(-\mathrm{i}pg(x))\boldsymbol{I} \end{bmatrix}, \tag{6}$$

where C_{VAR} is a scaling factor for the VAR CPSDM. The values of the aforementioned parameters in terms of various domains are shown in Table 2.

$\boldsymbol{S}^{\mathrm{VAR}}(x)$	x	C_{VAR}	$g(x)$	x_a	x_b
$\boldsymbol{S}^{\mathrm{VAR}}(f)$	f	$\frac{1}{f_{\max}}$	$\frac{\pi f}{f_{\max}}$	0	$f_{\max}$
$\boldsymbol{S}^{\mathrm{VAR}}(\omega)$	ω	$\frac{1}{\omega_{\max}}$	$\frac{\pi \omega}{\omega_{\max}}$	0	$\omega_{\max}$
$\boldsymbol{S}^{\mathrm{VAR}}(k)$	k	$\frac{1}{k_{\max}}$	$\frac{\pi k}{k_{\max}}$	0	$k_{\max}$

Table 2: Coefficients for the general form of the VAR spectrum equation (4).

2 Influence of the discretization of the ACF on the reproduced PSD

The selection of the $\Delta\mathring{r}$ value for discretizing a predefined continuous ACF influences both the parsimony of the AR model and the spectrum reproduced by the AR model (P. D. Spanos, 1983). For small $\Delta\mathring{r}$ values, a higher number of AR model coefficients is necessary to reproduce reasonably well the target ACF. Whereas, large $\Delta\mathring{r}$ values may lead to an increase in high frequencies in the reproduced PSD. This increase in the PSD high frequencies is referred to as aliasing, which causes challenges in some engineering problems (Li & Kareem, 1990). In Figure 1, the non-dimensional ACF for $u-$ velocity component, $\mathring{\gamma}_u(\mathring{r})$, obtained from vK turbulence model (see Equation (3.32)) is shown together the target ACF obtained from the discretization of $\mathring{\gamma}_u(\mathring{r})$ with $\Delta\mathring{r} = 0.1245$ and assuming the TFTH as shown in Equation (3.33).

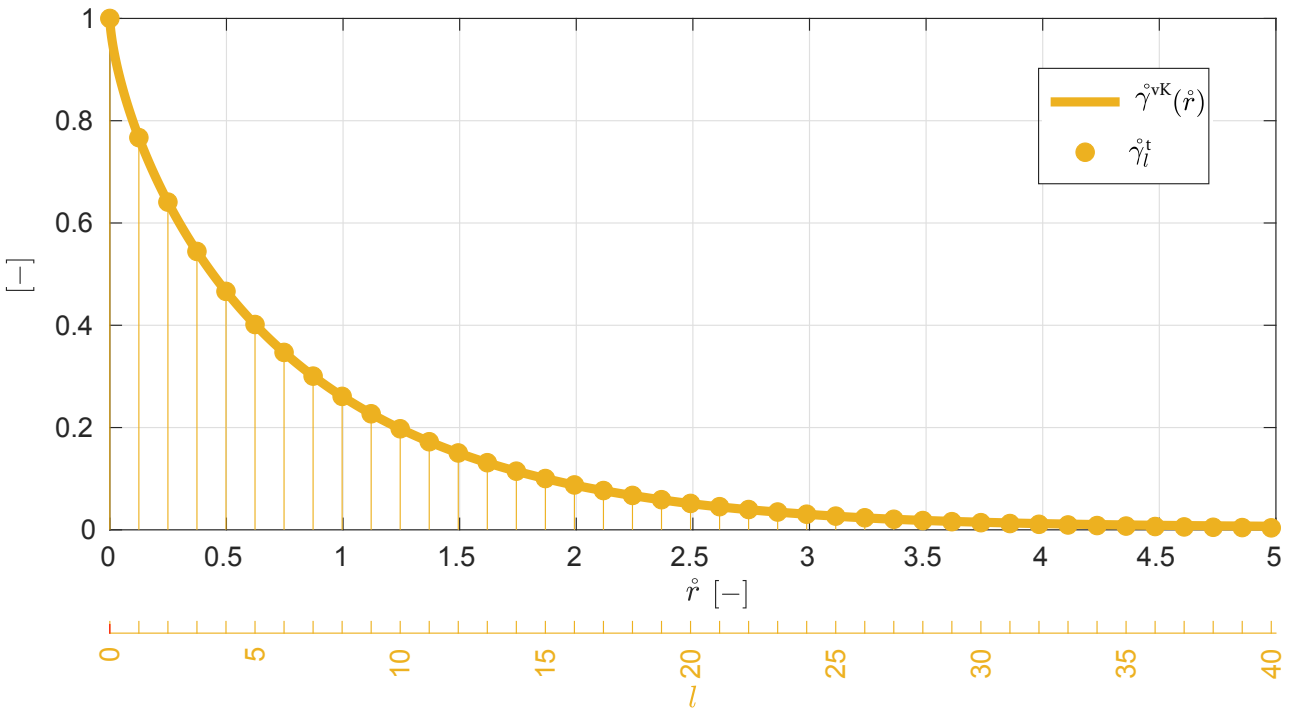

Figure 1: Non-dimensional ACF for $u-$velocity component, $\mathring{\gamma}_u(\mathring{r})$, obtained from vK turbulence model (continuous) together with the target ACF , $\mathring{\gamma}_l^{\mathrm{t}}$, for $\Delta\mathring{r} = 0.1245$ (discrete) (Figure is adapted from (Gallego-Castillo et al., 2022))

To analyze the influence of the $\Delta\mathring{r}$ value on the reproduced spectrum, three values for $\Delta\mathring{r} = 0.0622, 0.1245.0.2490$ were considered. The one-sided PSD of the obtained target ACF, for each $\Delta\mathring{r}$, is computed through the Discrete-Time Fourier Transform (DTFT) of each ACF. The computed PSD for each $\Delta\mathring{r}$ is shown in Figure 2 together with the PSD evaluated from the vk turbulence model in Equation (3.34). It is worth mentioning that the target PSDs are computed only up to the $\mathring{k}_{\max} = 2\pi/2\Delta\mathring{r}$ derived from the Nyquist theorem. As depicted in Figure 2, large $\Delta\mathring{r}$ values lead to aliasing in the target PSD.

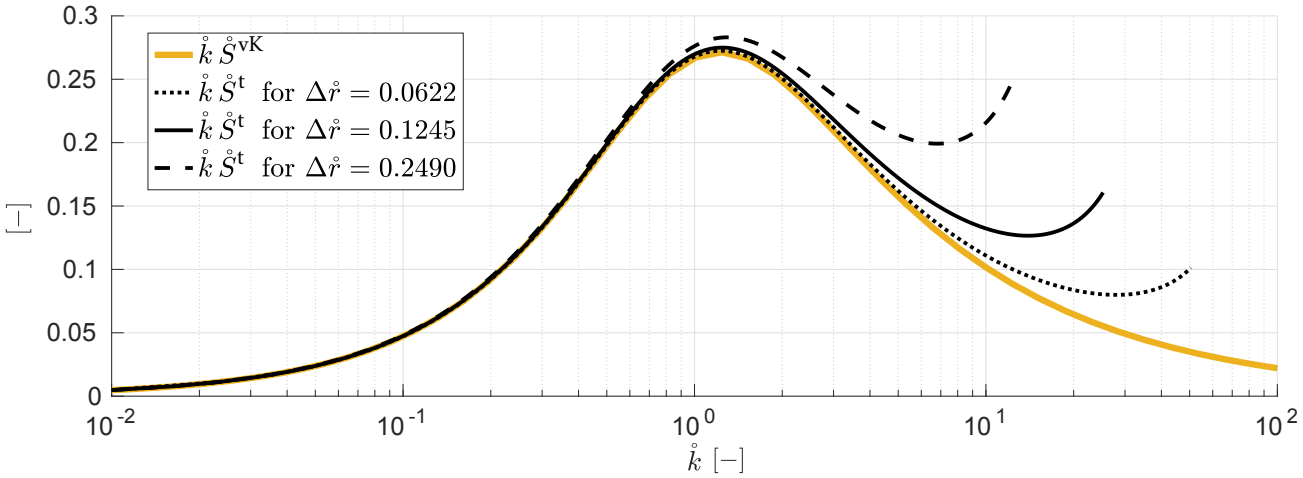

Figure 2: Non-dimensional vK spectrum, $\mathring{k}\mathring{S}^{\mathrm{vK}}$, together with the non-dimensional target spectrum, $\mathring{k}\mathring{S}^{\mathrm{t}}$, computed for $\Delta\mathring{r} = 0.0622, 0.1245.0.2490$ (Figure is acquired from (Gallego-Castillo et al., 2022)).

3 Relationship of the poles of an AR(p) model and the eigenvalues of the companion matrix of VAR(1) representation

In this section, the relation between the poles of an AR(p) model and the eigenvalues of the companion matrix is illustrated. This is illustrated by considering an AR(3) model and representing the AR(3) model by an AR(1) surrogate. The companion matrix of this AR(1) representation is defined as

$$\boldsymbol{\Phi}_* = \begin{bmatrix} \Phi_1 & \Phi_2 & \Phi_3 \\ 1 & 0 & 0 \\ 0 & 1 & 0 \end{bmatrix}. \tag{7}$$

The eigenvalues of the companion matrix can be evaluated from

$$\det(\boldsymbol{\Phi}_* - \lambda \boldsymbol{I}) = 0, \tag{8}$$

and expanding the previous expressions, to get the following

$$1 - \Phi_1\lambda^{-1} - \Phi_2\lambda^{-2} - \Phi_3\lambda^{-3} = 0, \tag{9}$$

the previous equation is similar to the characteristics equation of the AR model (Elagamy et al., 2021a), where the AR(3) model, it is represented in terms of the backshift operator as

$$1 - \Phi_1 B - \Phi_2 B^2 - \Phi_3 B^3 = 0, \tag{10}$$

which can be factorized as

$$(1 - G_1 B_1)(1 - G_2 B_2)(1 - G_3 B_3) = 0, \tag{11}$$

where G_1, G_2, G_3 are the poles of the AR(3) model (Elagamy et al., 2021a). By substituting B with λ^{-1} in Equation (11), thus, $G_i = \lambda_i$, for $i = 1, 2, 3$.

4 Derivation of the eigenvector matrix of the companion matrix of VAR(1) representation

The particular shape of the companion matrix, $\mathbf{\Phi}_*$, as shown in Equation (4.4), is reflected on its eigenvectors matrix, $\boldsymbol{V}$. To comprehend this relation, consider a VAR(3) model with 2-variates, where the companion matrix for this VAR(3) process is defined as:

$$\mathbf{\Phi}_* = \begin{bmatrix} \mathbf{\Phi}_1 & \mathbf{\Phi}_2 & \mathbf{\Phi}_3 \\ \mathbf{I} & \mathbf{0} & \mathbf{0} \\ \mathbf{0} & \mathbf{I} & \mathbf{0} \end{bmatrix}, \tag{12}$$

where the regression coefficient matrix $\mathbf{\Phi}_i$ is

$$\mathbf{\Phi}_i = \begin{bmatrix} \Phi_{11,i} & \Phi_{12,i} \\ \Phi_{21,i} & \Phi_{22,i} \end{bmatrix}. \tag{13}$$

The companion matrix can be decomposed by using eigendecomposition, as shown in Equation (4.22), to get that the eigenvalues matrix $\text{diag}(\boldsymbol{D}) = [\lambda_1, \ldots, \lambda_6]$ and $\boldsymbol{V} = [\boldsymbol{v}_1, \ldots, \boldsymbol{v}_6]$, where $\boldsymbol{v}_i = [v_{1i}, \ldots, v_{6i}]^T$. By considering the first eigenvalue λ_1 and its corresponding eigenvector $\boldsymbol{v}_1$, in Equation (4.22), to get the following:

$$\mathbf{\Phi}_* \boldsymbol{v}_1 = \lambda_1 \boldsymbol{v}_1. \tag{14}$$

By multiplying the companion matrix by the eigenvector $\boldsymbol{v}_1$, then,

$$\begin{bmatrix} f(v_{j1}, \Phi_{1j,1}, \Phi_{1j,2}, \Phi_{1j,3}) \\ f(v_{j1}, \Phi_{2j,1}, \Phi_{2j,2}, \Phi_{2j,3}) \\ v_{11} \\ v_{21} \\ v_{31} \\ v_{41} \end{bmatrix} = \lambda_1 \begin{bmatrix} v_{11} \\ v_{21} \\ v_{31} \\ v_{41} \\ v_{51} \\ v_{61} \end{bmatrix}. \tag{15}$$

From Equation (15), it can be noted that,

$$v_{31} = \frac{1}{\lambda_1} v_{11}, \;\; v_{41} = \frac{1}{\lambda_1} v_{21}, \;\; v_{51} = \frac{1}{\lambda_1} v_{31} \text{ and } v_{61} = \frac{1}{\lambda_1} v_{41}, \tag{16}$$

and by substituting the values of v_{31} and v_{41} in the expressions for v_{51} and v_{61} in Expression (16), respectively, then

$$v_{51} = \frac{1}{\lambda_1^2} v_{11} \text{ and } v_{61} = \frac{1}{\lambda_1^2} v_{21}. \tag{17}$$

Thus, by using the values of v_{31} and v_{41} from Equation (16) and the values of v_{51} and v_{61} from Equation (17), then the eigenvector $\boldsymbol{v}_1$ can be written as

$$\boldsymbol{v}_1 = \begin{bmatrix} v_{11} & v_{21} & \frac{1}{\lambda_1}v_{11} & \frac{1}{\lambda_1}v_{21} & \frac{1}{\lambda_1^2}v_{11} & \frac{1}{\lambda_1^2}v_{21} \end{bmatrix}^T.$$

It can be concluded that the eigenvector $\boldsymbol{v}_1$ contains independent variables (first h-rows components) v_{11} and v_{21}, where the rest of the components in the eigenvector $\boldsymbol{v}_1$ can be deduced from the identified $h(=2)$ independent variables and the corresponding eigenvalue of the eigenvector, λ_1. From the previous example and after applying the same procedures for the rest of the eigenvectors, the general form of the eigenvectors matrix $\boldsymbol{V}$ for a VAR(p) model with h-variates can be expressed as:

$$\boldsymbol{V} = \begin{bmatrix} (\lambda_1^0)^{-1}v_{11} & (\lambda_2^0)^{-1}v_{12} & \dots & (\lambda_{ph}^0)^{-1}v_{1(ph)} \\ \vdots & \vdots & \ddots & \vdots \\ (\lambda_1^0)^{-1}v_{h1} & (\lambda_2^0)^{-1}v_{h2} & \dots & (\lambda_{ph}^0)^{-1}v_{h(ph)} \\ \vdots & \vdots & & \vdots \\ (\lambda_1^{p-1})^{-1}v_{11} & (\lambda_2^{p-1})^{-1}v_{12} & \dots & (\lambda_{ph}^{p-1})^{-1}v_{1(ph)} \\ \vdots & \vdots & \ddots & \vdots \\ (\lambda_1^{p-1})^{-1}v_{h1} & (\lambda_2^{p-1})^{-1}v_{h2} & \dots & (\lambda_{ph}^{p-1})^{-1}v_{h(ph)} \end{bmatrix}_{ph\times ph}. \tag{18}$$

5 Mann's turbulence model

The von Karman three-dimensional energy spectrum (Von Karman, 1948), as proposed in (Reif & Durbin, 2010), is expressed as:

$$E(k) = 3\overline{u_{iso}^2}C_{\text{vK}}L\frac{(kL)^4}{[1+(kL)^2]^m},$$

where k is magnitude of the vector wavenumber $\boldsymbol{k}$, L is the length scale of the three dimensional energy spectrum, $3\overline{u_{iso}^2} = 2$ TKE (Turbulence Kinetic Energy), $\overline{u_{iso}^2}$ is the isotropic variance, von Karman proposed the value $m = 17/6$ and C_{vK} is a parameter expressed as:

$$C_{\text{vK}} = \frac{\Gamma(m)}{\Gamma(5/2)\Gamma(m-5/2)}.$$

The final formulation of the Mann's US-SVT, $\phi_{ij}(\boldsymbol{k})$, is defined as (Mann, 1994a, 1994b, 1998):

$$\phi_{11}(\boldsymbol{k}) = \frac{E(k_0)}{4\pi k_0^4}[k_0^2 - k_1^2 - 2k_1k_{30}\zeta_1 + (k_1^2+k_2^2)\zeta_1^2],$$
$$\phi_{22}(\boldsymbol{k}) = \frac{E(k_0)}{4\pi k_0^4}[k_0^2 - k_2^2 - 2k_2k_{30}\zeta_2 + (k_1^2+k_2^2)\zeta_2^2],$$
$$\phi_{33}(\boldsymbol{k}) = \frac{E(k_0)}{4\pi k^4}[k_1^2+k_2^2],$$
$$\phi_{12}(\boldsymbol{k}) = \frac{E(k_0)}{4\pi k_0^4}[-k_1k_2 - k_2k_{30}\zeta_1 - k_1k_{30}\zeta_2 + (k_1^2+k_2^2)\zeta_1\zeta_2],$$
$$\phi_{13}(\boldsymbol{k}) = \frac{E(k_0)}{4\pi k_0^2k^2}[-k_1k_{30} + (k_1^2+k_2^2)\zeta_1],$$
$$\phi_{23}(\boldsymbol{k}) = \frac{E(k_0)}{4\pi k_0^2k^2}[-k_2k_{30} + (k_1^2+k_2^2)\zeta_2],$$

where

$$\zeta_1 = C_1 - \frac{k_2}{k_1}C_2 \quad , \quad \zeta_2 = \frac{k_2}{k_1}C_1 + C_2,$$
$$C_1 = \frac{\beta k_1^2(k_0^2 - 2k_{30}^2 + \beta k_1k_{30})}{k^2(k_1^2+k_2^2)} \quad , \quad C_2 = \frac{k_2k_0^2}{(k_1^2+k_2^2)^{3/2}}\ \arctan\left[\frac{\beta k_1(k_1^2+k_2^2)^{1/2}}{k_0^2 - k_{30}k_1\beta}\right],$$

where $\beta(=\Gamma(kL)^{-2/3})$ is the non-dimensional time, $k_{30} = k_3 + \beta k_1$ and $k_0 = |\boldsymbol{k}_0| = \sqrt{k_1^2+k_2^2+k_{30}^2}$. Note that $\phi_{ji} = \phi_{ij}^*$.

6 Effect of negative ACF values on its Fourier pair

In this section, the predefined targets, CMF and CPSDM, are analyzed. A decrease in the CPSDM, at low frequencies, was observed in the generated target CPSDM from Mann's turbulence model with the simplified eddy lifetime selected. This is associated with the fact that the generated CMF target has negative values at high time lags l. In Figure 3, the effect of the negative value of the ACF on the obtained PSD is shown, where the analyzed ACF is the ACF for the longitudinal velocity component, γ_{11}^{t}, obtained from Mann's turbulence model. The PSD is obtained by calculating the DTFT of the ACF, γ_{11}^{t}. Three cases of the target ACF, γ_{11}^{t}, corresponding to three different maximum time lags, $l_{\max}$ have been considered. For the first case of target ACF (Case 1), a maximum time lag $l_{\max} = 205$ has been considered, taking into account that the ACF is negative for $l > 205$. The second and third cases of the target ACF have maximum time lags $l_{\max} = 500$ and $l_{\max} = 800$, respectively. As shown in Figure 3, adding more negative values of ACF leads to a decrease in the corresponding PSD obtained for the lower frequency range.

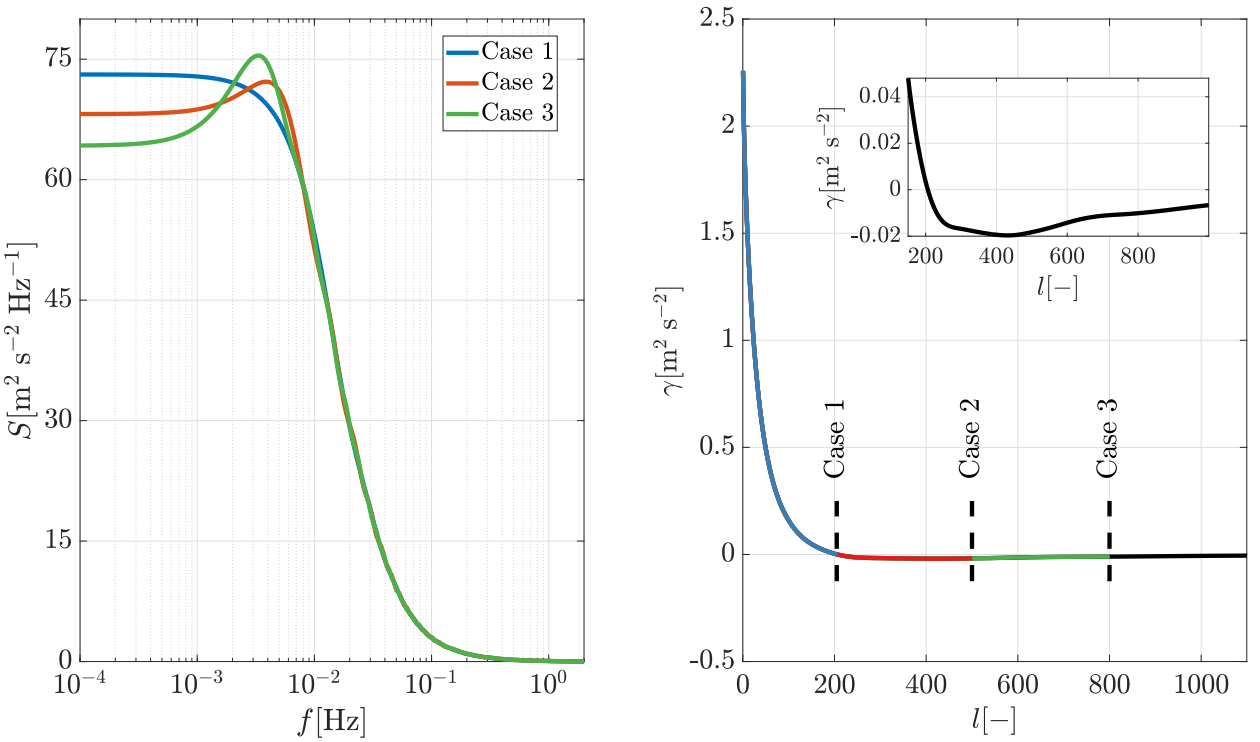

Figure 3: One-sided PSD (left side), S, obtained by calculating the DTFT of the ACF (right side), γ: (a) ACF with $l_{\max} = 205$ (Case 1), (b) ACF with $l_{\max} = 500$ (Case 2), and (c) ACF with $l_{\max} = 800$ (Case 3).

Note that, the negative values obtained in the generated target ACF is due to utilizing the eddy lifetime formulation proposed by (Landau & Lifshitz, 1987), for calculating the SVT, instead of using the eddy lifetime model proposed by Mann (Mann, 1994a).

7 Mesh independence study for the LES study

In Figure 4, the non-dimensional longitudinal velocity profile, U/U_{ref}, for coarse, intermediate, and fine were compared for the grid independency study. It was observed that the "fine" mesh is sufficiently refined and the discrepancy between the intermediate and the fine mesh is negligible. The velocity components are compared at six different locations and the trend is consistent. The difference between the maximum $U_{\max}/U_{ref}$ in the fine and the intermediate grids is 0.38% and 0.3% for locations e_1 and m_1, respectively. Whilst, the difference between the $U_{\max}/U_{ref}$ in the fine and the coarse grids is 1.92% and 1.36% for locations e_1 and m_1, respectively.

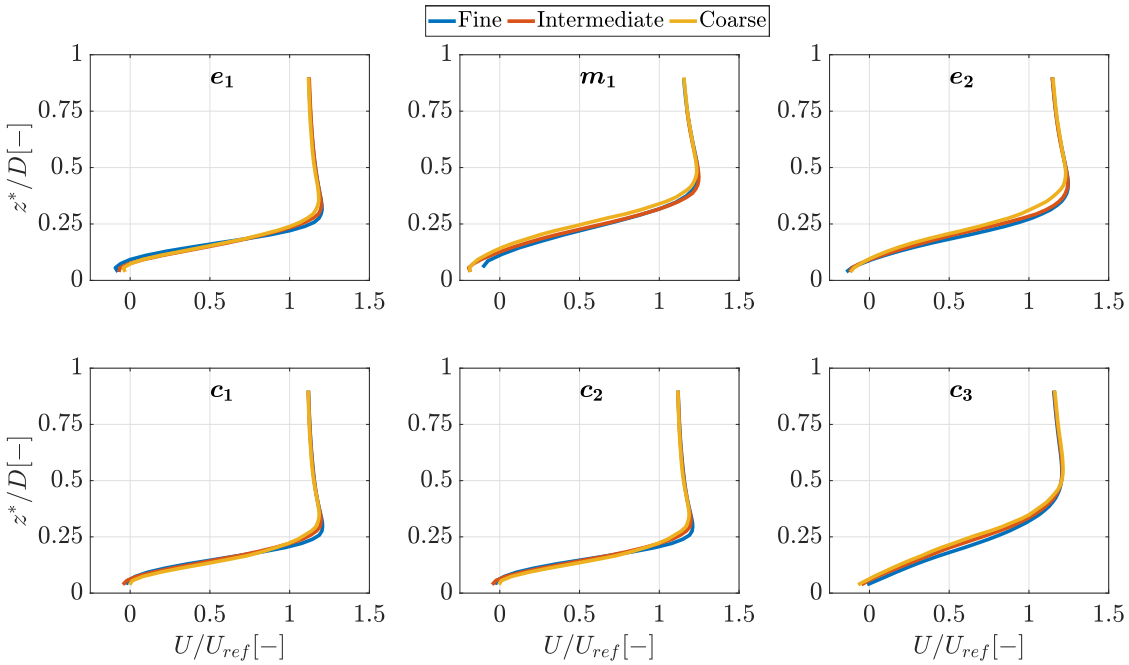

Figure 4: Non-dimensional mean longitudinal velocity component, U/U_{ref}, against the non-dimensional height, z^*/D, for coarse, intermediate and fine mesh grids (see Table 5.1), along different vertical lines over the rooftop locations shown in Figure 5.1b.